Title	Studies of tensor interactions and reaction mechanism of short-range correlated-nucleon pairs through 16O(p,pd) reactions
Author(s)	Wang, Xuan
Citation	大阪大学, 2024, 博士論文
Version Type	VoR
URL	https://doi.org/10.18910/96379
rights	
Note	

OSAKA UNIVERSITY

Graduate School of Science

Studies of tensor interactions and reaction mechanism of short-range correlated-nucleon pairs through ^{16}O(p,pd) reactions

Author:
Xuan WANG

Supervisor:
Nori AOI
Isao TANIHATA

Submit date: February, 2024

Abstract

We investigate short-range correlated-nucleon pairs in ^{16}O induced by tensor interactions by measuring pick-up reactions of high-momentum neutrons, in coincidence with high-momentum protons emitted at opposite angles. The nuclear tensor interaction is a major part of nucleon-nucleon interactions, and it was originally found in understanding the properties of deuteron, such as binding energy and non-zero quadrupole moment. However, its role in heavier nuclei is elusive, because explicit treatment of tensor interactions is difficult in nuclear structure models and the effect of tensor interactions is not easy to isolate experimentally from others. Recently theoretical and experimental studies have shown the necessity of tensor interactions in inducing high-relative-momentum nucleon pairs, which are formerly considered due to short-range central interactions. Pioneering work has shown the existence of high-momentum nucleon pairs induced by tensor interactions, by comparing the cross sections to different final states in ^{16}O(p, pd) reactions. However, the discussion in this work suffered from the influence of competing reaction mechanism. Therefore, we performed systematical measurements on ^{16}O(p, pd) reactions at various incident energies and scattering angles to study effects of tensor interactions without ambiguity of reaction mechanisms.

In this thesis, we present a systematic study on the high-relative-momentum pn pairs with specific spin and isospin configurations. We measured the pick-up domain ^{16}O(p, pd) reactions at 230 and 392 MeV incident energies and several scattering angles at Research Center for Nuclear Physics, Osaka University. We measured deuterons by the Grand Raiden spectrometer and protons in coincidence by a plastic scintillator array. From the energies and scattering angles of deuterons and protons, we constructed the missing mass spectrum of ^{14}N and obtained the cross section of reactions populating to the 3.95 MeV state ($J^\pi = 1^+$, $T = 0$) and 2.31 MeV state ($J^\pi = 0^+$, $T = 1$) in ^{14}N. We deduced the cross section ratio between reactions populating to two final states, corresponding to the removal of $(S, T) = (0,1)$ and $(1,0)$ pn pairs from ^{16}O. We discuss the dependence of the cross section ratio on the relative-momentum of the correlated nucleon pairs from the data at different incident energies but the same scattering angle, where the effect of competing reaction mechanism cancel. Observed ratio difference shows an effect of tensor interactions clearly. We also discuss effects of other reaction mechanism, which is confirmed to reduce the observed effects of tensor interactions.

Abbreviations

ADC	Analogue-to-digital converter
Al	Aluminum
AVF	Azimuthally-Varying-Field
BLP	Beam Line Polarimeter
BOS4	Beihang-Osaka university Stack Structure Solid organic Scintillator
DAQ	Data acquisition system
DWIA	distorted-wave impulse-approximation
CFD	Constant fraction discriminator
FWHM	Full width at half maximum
GR	Grand Raiden spectrometer
HODO	Plastic Hodoscope detecor used for detecting protons
LAS	Large Acceptance Spectrometer
LN_2	Liquid nitrigen
NN	Nucleon-nucleon
PMT	Photo-multiplier tube
QCD	Quantum Chromo Dynamics (QCD)
QDC	Charge-to-digital converter
RCNP	Research Center for Nuclear Physics
SC	Scattering chamber
ScFc	Scattering chamber Faraday cup
TDC	Time-to-digital converter
TNMD	Two-nucleon momentum distriburion
TOF	Time of flight
UCOM	Unitory correlation operator method
VDC	Vertical Drift Chamber
VMC	Variational Monte Carlo method
WallFc	Wall Faraday cup

Contents

List of Figures

List of Tables

Chapter 1

Introduction

Atomic nuclei are made of protons and neutrons that we call nucleons. Even though it is established that nucleons are not fundamental particles, it is considered as "fundamental" objects in nuclear physics, with the energy scale of MeV. Therefore, describing nuclear property in terms of nucleon–nucleon (NN) interactions is the main subject in nuclear physics. Great achievements have been made in describing nuclei with NN interaction models but there are still some mysteries.

One unsolved question is how to treat tensor interactions in nuclear structure models. The nuclear tensor interaction is the rank two tensor term in NN interactions. The tensor operator (S_{12}) in momentum space is conventionally defined as [1]:

$$S_{12} \equiv \frac{3}{\vec{k}^2}(\vec{\sigma_1} \cdot \vec{k})(\vec{\sigma_2} \cdot \vec{k}) - \vec{\sigma_1} \cdot \vec{\sigma_2} , \tag{1.1}$$

$$= \frac{6}{\vec{k}^2}(\vec{S} \cdot \vec{k})^2 - 2(\vec{S})^2 , \tag{1.2}$$

where $\vec{k}$ denotes the relative momentum of two nucleon, $\vec{\sigma_1}$ and $\vec{\sigma_2}$ denote the spin of nucleon 1 and nucleon 2, respectively.

Even though it has been established that tensor interactions are necessary in understanding light nuclei such as deuteron and ^{4}He, the effect in heavier nuclei is still illusive. Due to the difficulty to treat it explicitly, tensor interaction has been included in conventional nuclear structure models as residual interactions. Ab-initio type calculations can provide accurate calculations with realistic NN interactions, but it is not possible yet to calculate for $A > 12$ nuclei. Approximation is somehow necessary for global understanding for nuclei in a wide range of mass. Then the key point, from experimental points of view, is to find out and understand the effect of tensor interactions in heavy nuclei experimentally.

Another important question left over is the inclusion of high-momentum nucleons in nuclei. Even though low-momentum component dominants in nucleon momentum distribution inside nuclei, the high-momentum component can not be ignored for a complete and consistent understanding of nuclear structure. For instance, it is found that high-momentum component of nucleons is extremely important in gaining binding energies of deuteron and ^{4}He. Mean-field type models have succeeded in describing many nuclear properties phenomenologically, but the limitation is reached in understand-

ing the high-momentum component. Conventionally, high-momentum component is understood as mainly from short-range central repulsion, which is treated phenomenologically with parameterizations in most NN interaction models. Tensor interactions, without a hard core, were regarded as important in medium and long range part. However, tensor interactions also give a characteristic range and contribute to the high-momentum component. Recently it is found that tensor interactions play an essential role in reproducing the momentum distribution at around 2 fm^{-1}.

Therefore, two remaining questions have joint together and drawn special interest recently. Several experiments measuring (p, d) and (p, Nd) reactions ($N = p$ or n) have shown the feasibility in studying high-momentum nucleons induced by tensor interactions selectively. In this work, we aim to study the effect of tensor interactions that induce short-range correlated-nucleon pairs inside ^{16}O. ^{16}O(p, pd) reactions have been measured systematically changing incident energy and scattering angle.

In this chapter, we firstly introduce the effective meson theory in Sec. 1.1, where one can see that tensor interactions are automatically included. After brief derivation, we discuss the feature of tensor interactions predicted by meson theory. In Sec. 1.2, we discuss the importance of tensor interactions experimentally and how tensor interactions were studied historically. Some difficulties are also discussed. At the end of Sec. 1.2, we also present recent achievements in understanding effects of tensor interactions in creating high-momentum component in nucleons. Following that we discuss studies of high-momentum nucleons in several nuclei in Sec. 1.3. After that we discuss in details about the experimental approach of present work in Sec. 1.4. Finally we present the objective of this thesis in Sec. 1.5.
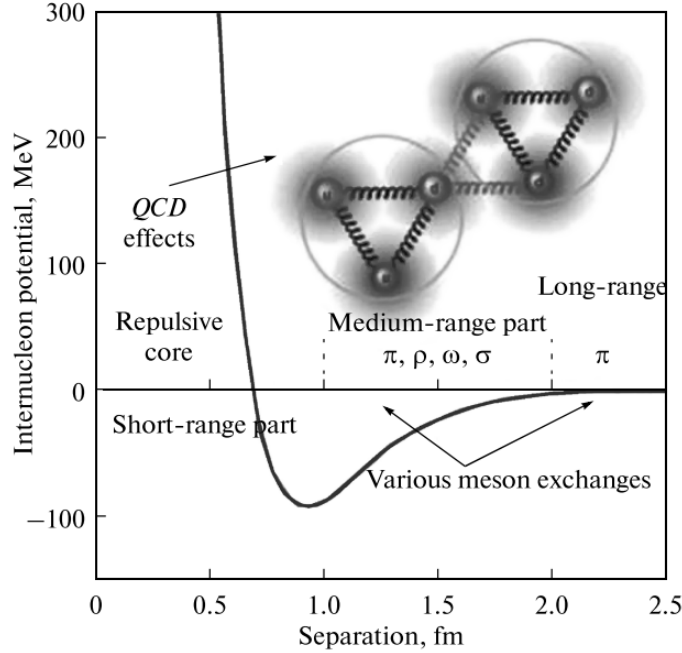
Figure 1.1: A general scheme for nucleon-nucleon potential is shown [3].

1.1 Tensor interactions in meson theory

Nowadays it is widely accepted that quantum chromodynamics (QCD) is the fundamental theory of strong interactions. The NN interactions has to be considered as completely determined by the underlying quark-gluon dynamics. However, due to the mathematical problems, we are still far from a quantitative understanding of NN force for all nuclei from this point of view. An effective meson theory can be understood as an appropriate approximation to the low energy QCD and it may very well be the appropriate representation for the NN interactions in the domain of nuclear physics. In fact, it is the only quantitative model for NN interactions [2].

Nucleon-nucleon potential is usually divided into three parts: long range, intermediate range and short range. A general scheme for NN potential is shown in Fig. 1.1 [3]. The long range part, in most of NN interaction models, is considered as one-pion-exchange potential. The medium range part is often treated by various single-meson exchanges. The short-range part is treated by exchanges of vector bosons as well as the QCD effects.

In the following part, we follow the formulation in Ref. [2], to present how tensor interactions are generated in meson theory and then summarize the feature of tensor interactions.

Following the conventional treatment, the Feynman diagrams for one-boson-exchange is shown in Fig. 1.2. E, $\vec{q}$ and E, $-\vec{q}$ are total energies and momenta of two incoming particles and E', $\vec{q}'$ and E', $-\vec{q}'$ are energies and momenta of two outgoing particles, respectively. According to the "Feynman rules", the formula for Fig. 1.2 is:

$$\frac{g_1\bar{u}_1(\vec{q}')\Gamma_1 u_1(\vec{q})P_\alpha g_2\bar{u}_2(-\vec{q}')\Gamma_2 u_2(-\vec{q})}{q^2 - m_\alpha^2} \ . \tag{1.3}$$
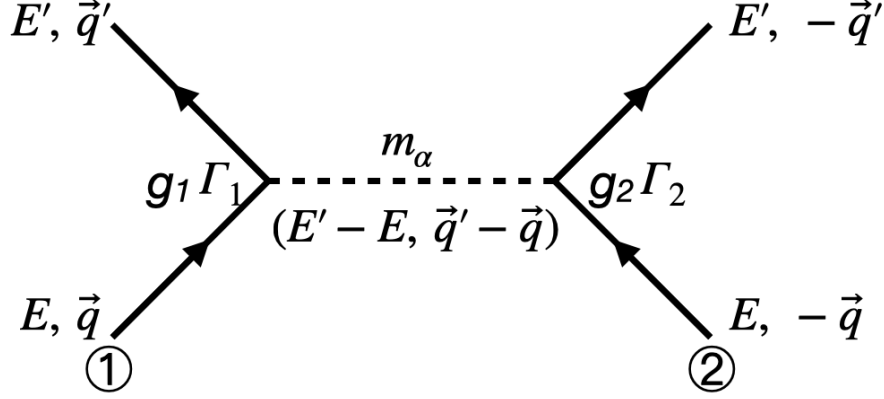
Figure 1.2: Feynman diagram for one-boson-exchange contribution to NN scattering is shown. Solid lines denote nucleons, and dashed line denotes a boson with mass m_α. The underlying time axis is vertical, pointing upwards into the future. The figure is from Ref. [2].

An outgoing nucleon is represented by a Dirac spinor (u) and an adjoint Dirac spinor ($\bar{u}$), e.g. for particle 1:

$$u_1(\vec{q}) \quad = \sqrt{\frac{E+M}{2E}} \begin{pmatrix} 1 \\ \frac{\vec{\sigma}_1 \cdot \vec{q}}{E+M} \end{pmatrix} \tag{1.4}$$

$$\bar{u}_1(\vec{q}\,') \quad = \sqrt{\frac{E'+M}{2E'}} \begin{pmatrix} 1 & -\frac{\vec{\sigma}_1 \cdot \vec{q}\,'}{E'+M} \end{pmatrix} , \tag{1.5}$$

where M is the mass of the nucleon. $\vec{\sigma}_1$ and $\vec{\sigma}_2$ are spin of nucleon 1 and 2, respectively. The normalization of the Dirac spinors is:

$$u^\dagger(\vec{q})u(\vec{q}) = 1 . \tag{1.6}$$

"$g_1\Gamma_1$" and "$g_2\Gamma_2$" are the vertices. The dashed (meson) line represents the propagator which appears as:

$$\frac{P_\alpha}{q^2 - m_\alpha^2} , \tag{1.7}$$

where $q^2 = (E'-E)^2 - (\vec{q}\,' - \vec{q})^2$, is the square of the four-momentum transferred by the meson. The process takes place "on the energy shell", i.e. energy is conserved. Consequently the energy of the nucleons before and after the scattering process must be the same: $E' = E$. Therefore, $q^2 = -(\vec{q}\,' - \vec{q})^2$. The propagator is:

$$\frac{P_\alpha}{-(\vec{q}\,' - \vec{q})^2 - m_\alpha^2} . \tag{1.8}$$

P_α is the propagator factor. In the simplest case it is "1". In following section, some of boson fields are presented with their couplings and how it predicts for the NN

interaction is discussed.

The pseudoscalar field

Pseudoscalar (ps) means that the field (ϕ_{ps}) switches sign in the case of either a space or a time reflection. Particles with negative intrinsic parity (e.g. π and η) have this property. Replacing vertexes $g_1\Gamma_1$ and $g_2\Gamma_2$ into $g_{\text{ps}}i\gamma_5$, Eq. 1.3 becomes:

$$g_{\text{ps}}^2 \frac{\bar{u}_1(\vec{q'})i\gamma_5 u_1(\vec{q})\bar{u}_2(-\vec{q'})i\gamma_5 u_2(-\vec{q})}{-(\vec{q'}-\vec{q})^2 - m_{\text{ps}}^2} \ , \tag{1.9}$$

where m_{ps}^2 is the mass of pseudoscalar meson.

The process takes place "on the energy shell", so we have $E' = E$. Skip the evaluation, we show the potential in momentum space:

$$\widehat{V}_{\text{ps}}(\vec{k}) = -\frac{g_{\text{ps}}^2}{4M^2} \frac{\vec{\sigma}_1 \cdot \vec{k} \ \vec{\sigma}_2 \cdot \vec{k}}{\vec{k}^2 + m_{\text{ps}}^2} \ , \tag{1.10}$$

where $\vec{k} \equiv \vec{q'} - \vec{q}$ and the approximation, $E \approx M$, is assumed. This potential is usually rewritten as:

$$\widehat{V}_{\text{ps}}(\vec{k}) = -\frac{1}{12M^2} \frac{g_{\text{ps}}^2 \cdot \vec{k}^2}{\vec{k}^2 + m_{\text{ps}}^2} \left(\vec{\sigma}_1 \cdot \vec{\sigma}_2 + S_{12}(\widehat{k}) \right) \ , \tag{1.11}$$

with

$$S_{12}(\widehat{k}) \equiv 3\vec{\sigma}_1 \cdot \widehat{k} \ \vec{\sigma}_2 \cdot \widehat{k} - \vec{\sigma}_1 \cdot \vec{\sigma}_2 \tag{1.12}$$

$$\widehat{k} \equiv \frac{\vec{k}}{|\vec{k}|} \ , \tag{1.13}$$

where S_{12} is known as the tensor operator (here in momentum space). Fourier transform into coordinate space:

$$V_{\text{ps}}(\vec{x}) = \frac{g_{\text{ps}}^2}{4\pi} \frac{g_{\text{ps}}^2}{12M^2} \{\vec{\sigma}_1 \cdot \vec{\sigma}_2 + S_{12}(\widehat{x})[1 + \frac{3}{m_{\text{ps}}r} + \frac{3}{(m_{\text{ps}}r)^2}]\} \frac{e^{-m_{\text{ps}}r}}{r} \ , \tag{1.14}$$

with

$$S_{12}(\widehat{x}) \equiv 3\vec{\sigma}_1 \cdot \widehat{x} \ \vec{\sigma}_2 \cdot \widehat{x} - \vec{\sigma}_1 \cdot \vec{\sigma}_2 \ , \tag{1.15}$$

$$r \equiv |\vec{x}|, \ \widehat{x} = \frac{\vec{x}}{r} \ . \tag{1.16}$$

For a ps-field, a derivative coupling is also commonly considered, the pseudovector (pv) coupling can be obtained by replacing the vertex into "$\frac{f_{\text{pv}}}{m_{\text{ps}}}\gamma_5$". The contribution

is exactly the same as for ps coupling, with the relationship of coupling constant:

$$g_{\mathrm{ps}} = f_{\mathrm{ps}} \, \frac{2M}{m_{\mathrm{ps}}} \; . \tag{1.17}$$

As the nucleons are on their mass shell, the ps and pv coupling are equivalent. (It is not true in the case of off-shell.)

The scalar field

Replacing the vertex with g_{s}, the one-scalar-boson exchange contribution is:

$$g_{\mathrm{s}}^2 \frac{\bar{u}_1(\vec{q'})u_1(\vec{q})\bar{u}_2(-\vec{q'})u_2(-\vec{q})}{-(\vec{q'}-\vec{q})^2 - m_{\mathrm{s}}^2} \tag{1.18}$$

Following similar evaluation, we obtain:

$$\widehat{V}_{\mathrm{s}}(\vec{k}) = -\frac{g_{\mathrm{s}}^2}{\vec{k}^2 + m_{\mathrm{s}}^2} \left(1 + \frac{\frac{1}{2}(\vec{\sigma}_1 + \vec{\sigma}_2) \cdot (-i)(\vec{k} \times \vec{p})}{2M^2} \right) \;, \tag{1.19}$$

where $\vec{p} = \frac{1}{2}(\vec{q'} + \vec{q})$. In coordinate space:

$$V_{\mathrm{s}}(\widehat{x}) = -\frac{g_{\mathrm{s}}^2}{4\pi}\{1 + \vec{L} \cdot \vec{S}\frac{m_{\mathrm{s}}^2}{2M^2}[\frac{1}{m_{\mathrm{s}}r} + \frac{1}{(m_{\mathrm{s}}r)^2}]\}\frac{e^{-m_{\mathrm{s}}r}}{r} \; . \tag{1.20}$$

The scalar meson-exchange causes an attractive central force and a spin-orbit force.

The vector field

With $g_{\mathrm{v}}\gamma_\mu$, the one-vector-boson exchange then is:

$$g_{\mathrm{v}}^2 \frac{\bar{u}_1(\vec{q'})\gamma_\mu u_1(\vec{q})(-g^{\mu\nu})\bar{u}_2(-\vec{q'})\gamma_\nu u_2(-\vec{q})}{-(\vec{q'}-\vec{q})^2 - m_{\mathrm{v}}^2} \; . \tag{1.21}$$

The potential in momentum space is:

$$\widehat{V}_{\mathrm{v}}(\vec{k}) = \frac{g_{\mathrm{v}}^2}{\vec{k}^2 + m^2} \left(1 - 3\frac{\frac{1}{2}(\vec{\sigma}_1 + \vec{\sigma}_2) \cdot (-i)(\vec{k} \times \vec{p})}{2M^2} \right) \; . \tag{1.22}$$

In coordinate space:

$$V_{\mathrm{v}}(\widehat{x}) = \frac{g_{\mathrm{v}}^2}{4\pi}\{1 - \vec{L} \cdot \vec{S}\frac{3m_{\mathrm{v}}^2}{2M^2}[\frac{1}{m_{\mathrm{v}}r} + \frac{1}{(m_{\mathrm{v}}r)^2}]\}\frac{e^{-m_{\mathrm{v}}r}}{r} \; . \tag{1.23}$$

We find a repulsive central force and a spin-orbit force with the same sign as that in the scalar field, but is by a factor of 3 stronger (if $m_{\mathrm{s}} = m_{\mathrm{v}}$).

One can also consider tensor coupling (not tensor force S_{12}) in the case of the vector

boson with the vertex:

$$\Gamma_{t,\mu} = -i\frac{f_v}{2M}\sigma_{\mu\nu}(q'-q)^{\mu} \tag{1.24}$$

where $\sigma_{\mu\nu} \equiv \frac{i}{2}[\gamma_\mu, \gamma_\nu]$.

For the full one-boson-exchange diagram one finally obtains in the approximation considered here:

$$\widehat{V}_t(\vec{k}) = \frac{-f_v^2}{4M^2}\frac{(\vec{\sigma}_1 \times \vec{k}) \cdot (\vec{\sigma}_1 \times \vec{k})}{\vec{k}^2 + m_v^2} \ . \tag{1.25}$$

In coordinate space it is:

$$V_t(\vec{x}) = -\frac{f_v^2}{4\pi}\frac{m_v^2}{12M^2}\left[2\vec{\sigma}_1 \cdot \vec{\sigma}_2 - S_{12}(\hat{x})\left(1 + \frac{3}{m_v r} + \frac{3}{(m_v r)^2}\right)\right]\frac{e^{-m_v r}}{r} \ , \tag{1.26}$$

The tensor force obtained here has the opposite sign compared to the ps case.

Brief summary

It should be remembered that the isovector contributions from the π, δ and ρ bosons have a factor of $\vec{\tau}_1 \cdot \vec{\tau}_2$.

The qualitative results obtained by the discussion above are summarized in Table 1.1 [4]. Various simple fields create central, tensor, spin-spin and spin-orbit forces, which are confirmed experimentally. We see the potential of tensor interactions has a factor:

$$\frac{\vec{k}^2}{\vec{k}^2 + m^2} \ , \tag{1.27}$$

where $\vec{k}$ and m is the momentum transfer and mess of the boson. With large momentum transfer and lightest mass (π), tensor interactions are strong.

With the total spin operator defined as $\vec{S} = \frac{1}{2}(\vec{\sigma}_1 + \vec{\sigma}_2)$, the tensor operator is written as:

$$S_{12}(\hat{k}) = 2[3(\vec{S} \cdot \hat{k})^2 - \vec{S}^2] \ , \tag{1.28}$$
$$S_{12}(\hat{x}) = 2[3(\vec{S} \cdot \hat{x})^2 - \vec{S}^2] \ , \tag{1.29}$$

in momentum and coordinate space, respectively.

There are in total four channels for two-nucleon:

$$S = 0, \ T = 0, \ \text{odd } L; \tag{1.30}$$
$$S = 1, \ T = 0, \ \text{even } L; \tag{1.31}$$
$$S = 0, \ T = 1, \ \text{even } L; \tag{1.32}$$
$$S = 1, \ T = 1, \ \text{odd } L. \tag{1.33}$$

The selection rule relevant for this study is "$L = 0$" (short-range), thus only two

Table 1.1: Various meson-nucleon couplings and their consequences for the NN interaction as deduced from the OBE model

Coupling	Bosons	Type of force	Type of force
pseudoscalar	η and π	spin-spin	tensor
scalar	σ and δ	attractive central	spin-orbit
vector	ω and ρ	repulsive central	spin-orbit
tensor	ω and ρ	spin-spin	tensor (opposite sign to ps)

channels are left. From Eq. 1.28 and 1.29, the tensor interactions act only in the $S = 1$ channels. While in a contrast, the central interactions have strength in all channels. Therefore, identifying the spin information of two-nucleon pair helps to separate effects from tensor and central interactions.

Table 1.2: Breaking down of deuteron binding energy

Binding energy	-2.24 [MeV]
Kinetic	19.88
Central	-4.46
Tensor	-16.64
LS	-1.02

1.2 Importance of tensor interactions

In this section, we firstly introduce the historical studies of tensor interactions and discuss the difficulty of understanding tensor interactions in heavy nuclei in subsection 1.2.1. After that in subsection 1.2.2 we discuss recent development in studying tensor interactions both theoretically and experimentally.

1.2.1 Historical studies of tensor interactions

The nuclear tensor interactions, as a term in NN interactions, are found to be present firstly in a phase-shift analysis of NN scattering data [5]. Only the tensor operator has non-vanishing matrix elements for the transition from $\Delta L = 2$ states. The existence of tensor interactions is then, firmly proved by the analysis for deuteron, whose quadrupole moment is $Q_d = 0.2860$ $e$fm^2 [6]. Because the deuteron is in the $S = 1$, $T = 0$ channel, the ground state of deuteron (mainly ^{3}S$_1$) must have a admixture of ^{3}D$_1$ [7, 8]. Even with a small admixture of D-state $P_D = 4.25\%$ [7], it is essential to reproduce the quadrupole momentum as well as the binding energy of deuteron. The D-state admixture is also taken as a measure of the strength of tensor interactions.

Table 1.2 shows a result of calculation for deuteron using AV8' interactions [9]. Total binding energy, kinetic energy as well as the binding energy from central interactions, tensor interactions and LS coupling are listed. The tensor interactions contribute to the binding energy of deuteron (-2.24 MeV) with -16.64 MeV, while as a comparison, the central interactions give -4.46 MeV. The central and LS interaction are not enough to surpass the kinetic energy to make deuteron bound.

Even though many years have passed and much effort has been made to understand the NN interactions, the role of tensor interactions is still elusive in heavier nuclei. While some of the research consider a weaker strength of tensor interactions is needed (or even not needed to include), some of them emphasize the necessity of tensor interactions.

Many investigations have been made to understand the tensor contributions to static nuclear structure such as binding energies, excitation energies and magnetic moments. A detailed shell-model calculation for energy splitting between $J^\pi = 0^-$, $T = 0$ and $J^\pi = 0^-$, $T = 1$ state in ^{16}O was performed to investigate the effect of tensor interactions [5]. It is found that including larger model space in the shell model calculation has a similar effect with renormalizing the effective interactions by reducing the strength of tensor interactions, to explain the energy difference of two $T = 0$ and

$T = 1$ state. To the binding energy of a closed LS nucleus like ^{4}He and ^{16}O, tenser interactions have no contribution in the first-order in the framework of shell model. However, tensor interactions have important second-order contributions to them and first-order effect to systems with two quasi-particles. It was pointed out to explain the isoscalar magnetic moments of doubly LS closed shell ± 1 nucleon nuclei. Another study shows the necessity of including tensor interactions in the Skyrme interaction, to reproduce the spin-orbit splittings in $N = 82$ isotones and $N = 50$ isotopes [10].

Also there are many investigations that study reaction related structure information and its relationship with tensor interactions. One of the example is the study of spin-dependent observables. Some low energy measurements for Gamow-Teller transitions have been reported that polarization results are consistent with minimal tensor contribution at low energies, while some results at the incident energy range of 300-500 MeV leads to a conclusion that the effect of tensor contribution is important [5, 11].

1.2.2   Recent studies of tensor interactions

The toughness of understanding the role of tensor interactions in heavier nuclei comes from not only the theoretical difficulties in treating tensor interactions explicitly in nuclear structure models but also the experimental difficulties to isolate the effect of tensor interactions. It has been considered that some of the static structure information are not sensitive to tensor interactions and some reaction related properties show the connection with tensor interactions only at high energy/momentum region. However, recent studies are shedding new light in these topics.

On the one hand, modern theoretical calculations provide accurate results in static properties of light nuclei with realistic NN interactions including tensor interactions. Recently, it is shown by the ab-initio calculation called Quantum Monte Carlo (QMC) method that the tensor interactions are essential in binding light nuclei (with $A \leqslant 12$) [12, 13]. By optimizing two-particle two-hole states, tensor-optimized shell model [14] treats deuteron-like tensor interactions in a shell-model basis. The calculations succeeded in explaining several light nuclei such as He [15] and Li isotopes [16]. Such calculation shows great feasibility to extend the understanding of tensor interactions to heavier nuclei. Also great progress has been made for the study of exotic nuclei in recent years. As a consequence, new shell gaps and magic numbers are found fra from the stability line [17, 18]. It is found that the tensor interactions cause the shift of single-particle energy [19] and thus lead to the shell evolution [20].

On the other hand, for the reaction related properties, many calculations and experiments have shown the dominant role of tensor interactions at high-momentum region, namely around 2 fm^{-1}. Thus much attention has been drawn for the high-momentum component recently. Modern theoretical calculations predict the existence of high-momentum nucleons induced by tensor interactions [12, 21–25]. Electron and proton induced knock-out experiments show the dominant role of pn pairs in short-range correlated-nucleon pairs inside ^{4}He [26] and ^{12}C [27–29], suggesting dominant contribution from tensor interactions at high-momentum region. Proton induced high-momentum neutron pick-up (p, d) reaction studies [30–32] have shown the enhancement of a the positive parity final state in ^{15}O related with two-particle-two-hole configurations in the ground state of ^{16}O induced by tensor interactions. A pioneering work us-

ing (p, pd) [33] and (p, nd) [34, 35] reactions investigates short-range correlated-nucleon pairs in ^{16}O and separates the effect of tensor interactions from others via spin and isospin character for the first time. It is found that high-momentum neutron pick-up reactions provide a unique tool to investigate the high-momentum component from tensor interaction selectively. More efforts are demanded for further understanding. We present the discussion and summarized existing studies related with the high-momentum component and tensor interactions in following section.

1.3 High momentum nucleons

Since Mayer and Jensen, the shell structure has played a major role in understanding nuclear structure. By assuming that nucleons move inside a "mean potential" created by other nucleons of the nuclei, the nuclear shell model has succeed in explaining a lot of properties of nuclei, for instance the ground state properties and magic numbers. Its limitation is realized, as it can be seen from its assumption, when one considers something beyond the mean field, e.g. the short-range correlations. As a basic assumption of the shell model, nucleons occupy the single-particle states with momenta below the Fermi momentum ($p_\mathrm{F} \approx 1.4$ fm^{-1}). However, electron-induced quasi-elastic proton knockout reactions $(e, e'p)$ show that the number of valence proton is smaller than the predicted value by the shell model [36]. It is found that over a large range of nuclei, from ^{2}H to ^{208}Pb, the so-called spectroscopic factor has a quenching with around 30% from the shell model value. Such quenching is considered as the evidence of the existence of the nucleons with momenta near or higher than the Fermi momentum, which is beyond the mean field [37].

It is widely accepted that the high-momentum nucleons are attributed mainly to short-range central interactions and tensor interactions. Actually, the interactions at short range are usually considered phenomenologically in most NN interaction models, because it is technically difficult to treat this part. Many models assume only a central type hard core for short range interactions, because tensor interactions do not have a short range repulsive core. However, tensor interactions have important effects at short range, even though tensor interactions are famous for dominating at the long range of NN interactions. Therefore, we stress the importance of separating the contributions from the central and tensor interactions on the high-momentum nucleons inside nuclei. In the following section, we present the discussion on the high-momentum component and discuss the evidence that tensor interactions are responsible for that.

When the momentum distribution is evaluated from an experiment (e.g. the $(e, e'p)$ reactions), one actually consider the "total" momentum distribution $F_\mathrm{t}(p)$, which can be written as:

$$F_\mathrm{t}(p) = f_1 F_1(p) + f_2 F_2(p) + ... \tag{1.34}$$

where p is the momentum and $F_1(p)$ and $F_2(p)$ are the single particle momentum distribution and the momentum distribution inside two correlated nucleons, respectively. Correspondingly, f_1 and f_2 are the probability of single particle and two-nucleon pair, respectively. Since the contribution from higher order (three-body and four-body interactions) is small for $p > 0.5$ fm^{-1} [38], we simply ignore other terms here. For the region $p < p_\mathrm{F}$, the mean field model gives a good description on the momentum distribution (but with a spectroscopic factor around 0.6) [36] and the contribution of nucleon pair is relatively small. However, the correlation part dominates when $p > 2$ fm^{-1} [38].

1.3.1 The momentum distribution in deuteron

As we see the importance of correlation on high-momentum nucleons, we consider the relative-momentum distribution from now on. Firstly, we start with deuteron, the
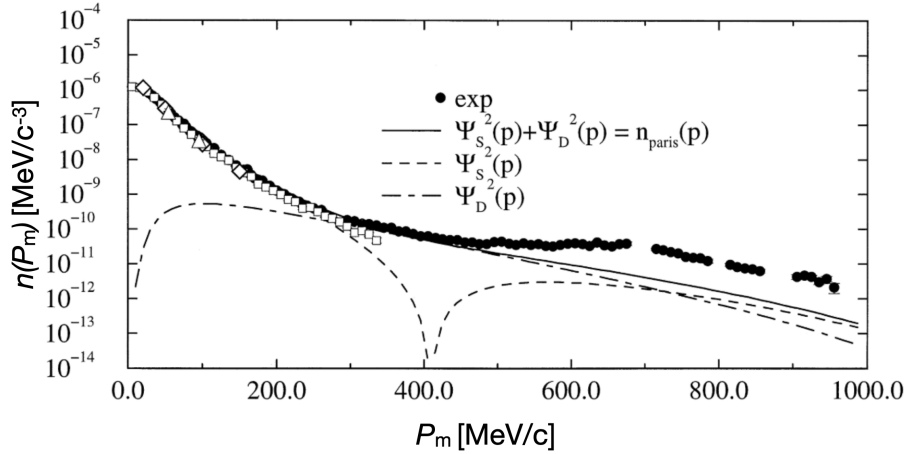
Figure 1.3: The reduced cross sections of $D(e, e'p)n$ reactions is shown in black dots. The momentum distribution calculated with the Paris potential is shown in lines. The open symbols are data from other experiments. The figure is from Ref. [39].

only bound two-nucleon system and the simplest case. As we mentioned in previous subsection, the tensor interactions play an essential role in reproducing the binding energy and quadrupole moment of deuteron, via a small amount of admixture of D-state.

Figure 1.3 shows the result of $D(e, e'p)n$ and the comparison with plane wave impulse approximation (PWIA) calculation [39]. Horizontal axis is the missing momentum (P_m) that corresponds to the nucleon momentum in the deuteron and the vertical axis is the reduced cross section (see [39] for definition). The reduced cross section of $D(e, e'p)n$ reactions is shown in black dots. The momentum distribution is shown in dashed lines, from the calculation using Paris potential, where tensor interactions have been included by meson-exchanges. The short and long dashed line shows the contribution of S- and D-state in the calculation, respectively. The reduced cross section of $D(e, e'p)n$ reactions are identical to the momentum distribution under the PWIA assumption. The calculation reproduces the data well up to 400 MeV/c, while for larger missing momentum, the cross section becomes increasingly larger than calculation, which is regarded as from meson exchange currents and isobar currents qualitatively [39].

At momentum around 400 MeV/c (corresponding to 2 fm^{-1}), the contribution of D-state become dominant and thus it is attributed to the tensor interactions. Thereafter, we refer the high-momentum as the region of momentum around 2 fm^{-1} in this thesis.

1.3.2 The momentum distribution in He

A calculation based on variational Monte Carlo (VMC) method has been performed to study light nuclei (up to $A = 8$) [21]. Figure 1.4 shows the two-nucleon momentum distribution of ^{4}He and deuteron. Horizontal axis is the relative-momentum of two nucleons ($P_{rel} = \frac{1}{2}|\vec{P}_1 - \vec{P}_2|$) and vertical axis is the density of the two-nucleon pair with zero total momentum ($P_{total} = |\vec{P}_1 + \vec{P}_2| = 0$) in ^{4}He. While the color lines show the
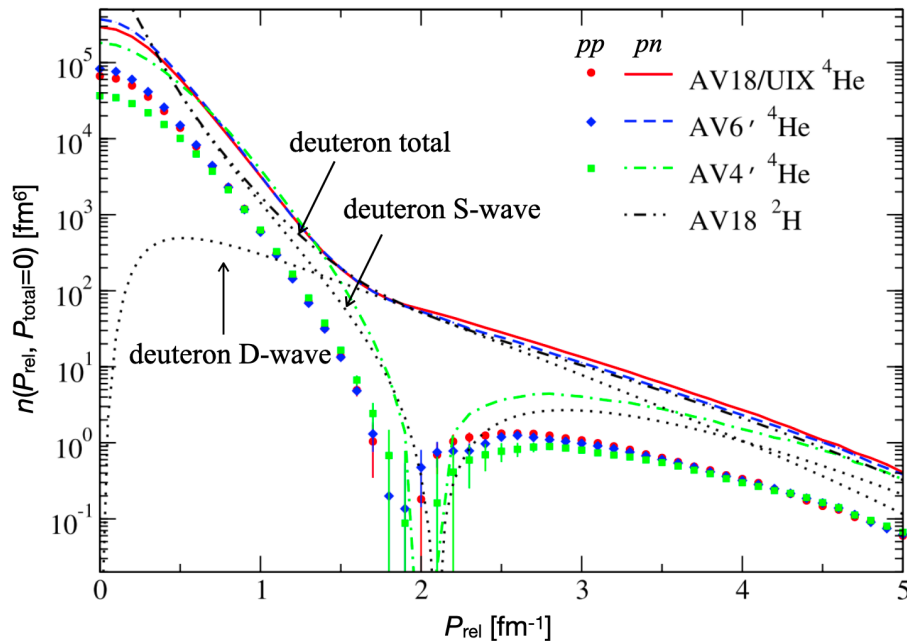
Figure 1.4: Two-nucleon momentum distribution of ^{4}He in VMC method is shown in color lines and symbols with various interactions. The black lines show the calculation for deuteron. The figure is from Ref. [21]

distribution of pn pairs, the color symbols show the distribution of pp pairs. Different colors represent results using different interactions. The black dotted line shows the scaled momentum distribution of deuteron calculated with AV18 interactions, where a clear S- and D-wave components are separately shown. The black dotted dashed line shows the total momentum distribution of deuteron. The calculation for ^{4}He using fully realistic AV18/UIX model (red) shows a very similar shape with deuteron, where the pp pair has a shape similar with S-wave component while pn pair has a similar shape with D-wave. As we discussed in Sec. 1.1, while central interactions act on all channels (different (S,T) configurations of two-nucleon), tensor interactions act only at the $(S,T) = (1,0)$ channel. Therefore, the difference of momentum distribution between pn ($T = 0$ or 1) and pp ($T = 1$) pairs indicates the relative change of the contribution from tensor interactions. The semi-realistic AV6' model (blue) shows similar result, but the AV4' model (green) shows large discrepancy of pn pair at around 2 fm^{-1}. It should be noted that, AV18 and AV6' include tensor interactions but AV4' does not. The green dashed line obtained by AV4' interactions differs with others at around 2 fm^{-1}, showing the contribution from tensor interactions. It is important to note that tensor interactions fill the dip at 2 fm^{-1} and show largest contribution there.

The different behavior of momentum distribution of pn and pp pairs can be seen more clearly in Fig. 1.5 [21]. The momentum distribution as functions of relative-momentum P_{rel} is shown in red lines, and that of total momentum P_{total} in blue lines. The solid and dashed line shows the distribution of pn and pp pairs, respectively. The distribution of pn and pp pairs behave similarly as functions of total momentum, but differently of relative-momentum. The inset shows the ratios of density between pn and
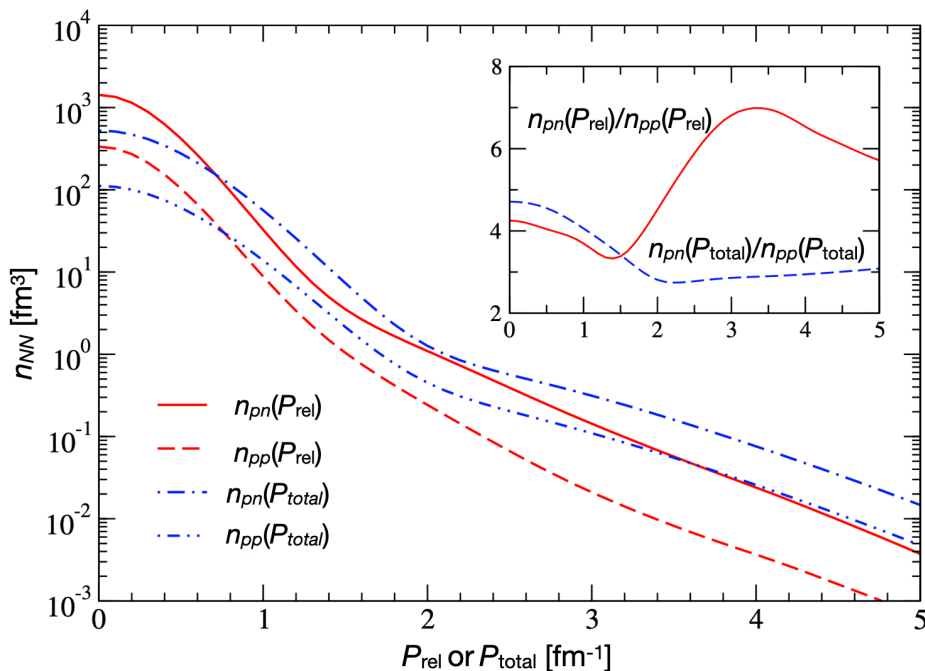
Figure 1.5: The momentum distributions $n_{NN}(P_{\text{rel}})$ and $n_{NN}(P_{\text{total}})$ in ^{4}He for pp and pp pairs. The inset shows the ratios $n_{pn}(P_{\text{rel}})/n_{pp}(P_{\text{rel}})$ and $n_{pn}(P_{\text{total}})/n_{pp}(P_{\text{total}})$. The figure is from Ref. [21].

pp pairs and we can see that the amount of pn pair becomes several times larger than pp pair at the momentum region from 1.4 to 4.0 fm^{-1} [21]. It should be noted that, from pair counting, the ratio of pn and pp in ^{4}He is 4, to which the $n_{pn}(P_{\text{total}})/n_{pp}(P_{\text{total}})$ is close.

The dominance of pn pair over pp pair at high-momentum region was experimentally confirmed by electron knock-out measurements at Jefferson Laboratory [26]. At around 500 MeV/c momentum region, the cross section ratio ^{4}He$(e, e'pn)/^4$He$(e, e'p)$ is around 90%.

The observation using electron probe only reports the isospin character but no spin character. One can see that both $T = 1$ and $T = 0$ configurations are allowed for a pn pair and central interactions contribute to both channels. The ideal method to separate effects from tensor and central interactions is to pin down both isospin and spin information of the correlated-nucleon pair. A hadron probe is then preferable due to much larger cross section, which makes the exclusive measurement possible. Measurement of ^{4}He(p, pd) has been reported to study high relative-momentum pn pair in ^{4}He [40].

The pn pair was investigated by (p, pd) reactions with 310 MeV/c relative-momentum. Preliminary result shows a pure $S = 1$ channel, indicating a very strong tensor interactions in ^{4}He [40]. Even though final conclusions have not been made for the study, it shows the high feasibility of (p, pd) reactions with sufficient amount of data accumulated within only few hours.
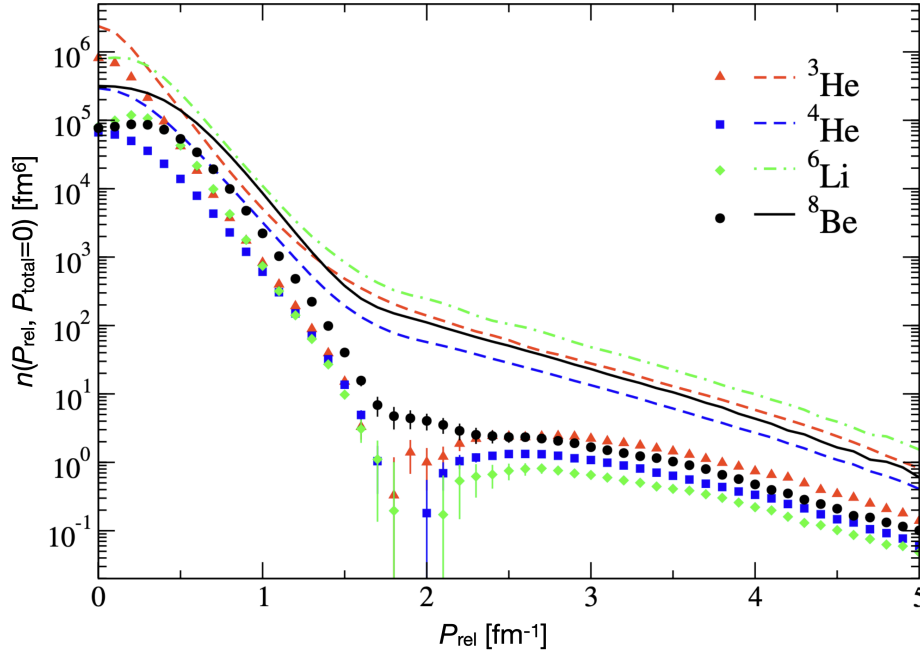
Figure 1.6: The *pn* (lines) and *pp* (symbols) momentum distributions in various nuclei as functions of the relative-momentum P_{rel} at vanishing total pair momentum P_{total} is shown. The figure is from Ref. [21].

1.3.3 The momentum distribution in heavier nuclei

Studies of high-momentum nucleons have been extended to nuclei heavier than ^{4}He as well. The variational Monte Carlo (VMC) calculations show similar results for several nuclei [21]. Figure 1.6 shows the two-nucleon distribution (ρ_{NN}) as functions of the relative-momentum P_{rel} at vanishing total pair momentum P_{total}. The lines show the distributions of *pn* pairs while the symbols show those of *pp* pairs. Similar with the calculation for ^{4}He, a dip is found at around 2 fm^{-1} in *pp* pairs distributions, but it is filled in *pn* pair distribution, which is mainly induced by tensor interactions [21]. Such feature is common for several light nuclei.

Even though great achievement has been seen in theoretical development with so called ab-initio calculations, it is difficult to perform such kind of calculation for mass number $A > 12$ nuclei. A linked and number conserving cluster expansion method has been developed to calculate medium-weight nuclei ($12 \leq A \leq 40$) [41]. In the calculation, the two-nucleon momentum distribution (TNMD) is obtained from the Fourier transform of two-body density matrix. The TNMD is integrated in different relative-momentum range with condition of zero sum momentum for *pn* and *pp* pairs in different nuclei. Results for ^{4}He, ^{12}C, ^{16}O and ^{40}Ca are shown in Table 1.3 [41]. The second and third column shows the percentage probability of *pp* and *pn* pairs in the whole relative-momentum range. The P_{pp} and P_{pn} value is proportional to the percentage of finding a *pp* and *pn* pairs in the nuclei by simple counting, which is also shown in VMC calculation [21]. The fourth and fifth column shows the percentage probability of *pp* and *pn* pairs in the relative-momentum range of $[1.5, 3.0]$ fm^{-1}, where

Table 1.3: The pp and pn percentage probability

A	P_{pp} [%] $[0,\infty]$	P_{pn} [%] $[0,\infty]$	P_{pp} [%] $[1.5,3.0]$	P_{pn} [%] $[1.5,3.0]$ fm^{-1}
4	19.7	81.3	2.9	97.1
12	30.6	69.4	13.3	86.7
16	29.5	70.5	10.8	89.2
40	31.0	69.0	24.0	76.0
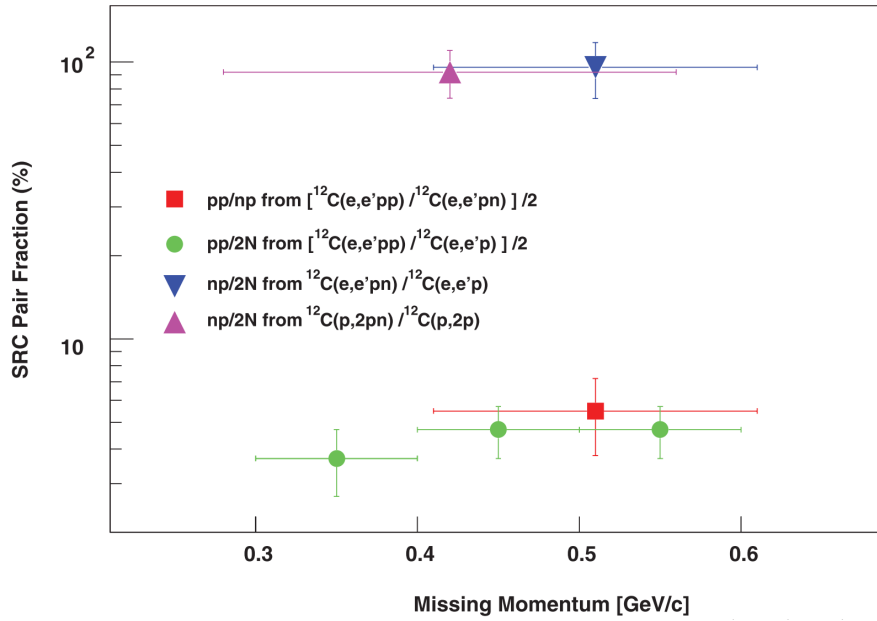
Figure 1.7: The fractions of correlated pair combinations in carbon as obtained from the $(e, e'pp)$ and $(e, e'pn)$ reactions, as well as from previous $(p, 2pn)$ data [28].

the tensor interactions dominate. P_{pn} is much larger than P_{pp} for all nuclei studied, which indicates that the tensor interactions dominate at this momentum region for nuclei from light to medium-weight.

Experimentally this has been examined by ^{12}C$(e, e'Np)$ reactions ($N = p$ or n) [28]. Measurements for $(e, e'pn)$ and $(e, e'pp)$ reactions were performed to study the correlated nucleon pairs inside ^{12}C and Fig. 1.7 shows the derived fractions of correlated pair combinations in ^{12}C obtained from $(e, e'pN)$ reactions [28], as well as from $(p, 2pn)$ data. The momentum region mentioned above ($[1.5, 3.0]$ fm^{-1}) corresponds to the missing momentum of 0.3 - 0.6 GeV/c, where the pn pairs dominate over pp pairs as shown in Fig. 1.7.

For heavier nuclei with $A > 12$, ab-initio calculations have not been achieved yet. A calculation with the unitary correlation operator method (UCOM) has been developed [25] and the result for ^{16}O is shown in Fig. 1.8. The momentum distribution of ^{16}O is shown, with different interactions in several lines. The thin solid line shows the mean field distribution. The dashed dotted line shows the distribution of central contribution (denoted as "radial"), extending to very large momentum. The calculations with tensor
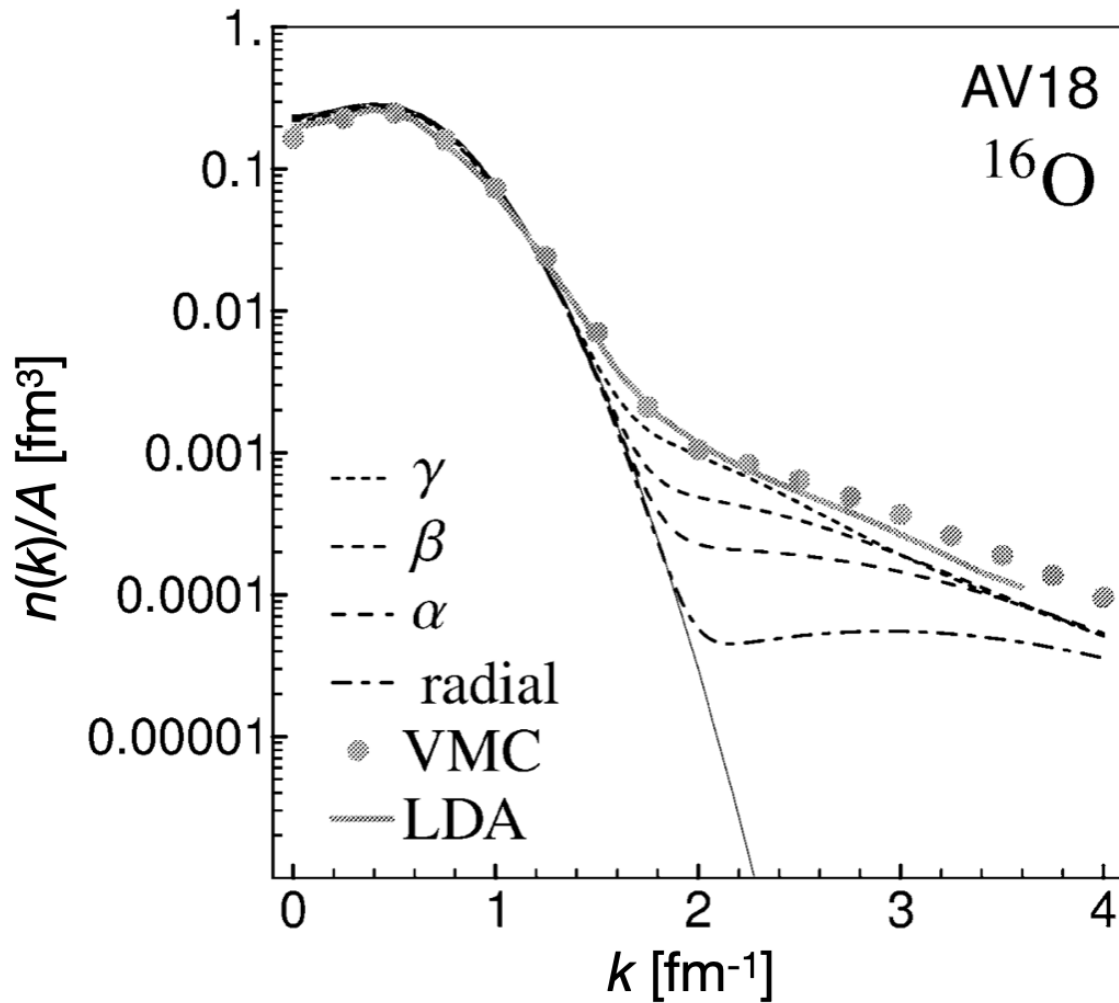
Figure 1.8: Momentum distribution of ^{16}O from UCOM calculation using AV18 interaction. The thin solid line shows the calculation for uncorrelated trial state and the dashed dotted line shows the one for two-body optimized radial correlators. The calculation with tensor correlators with restricted range (α, β and γ) is shown in dashed line. Result of VMC calculation using AV14 + Urbana VII three nucleon interaction and a spectral function analysis (LDA) is shown in grey dots and grey line, respectively. The figure is from Ref. [25].
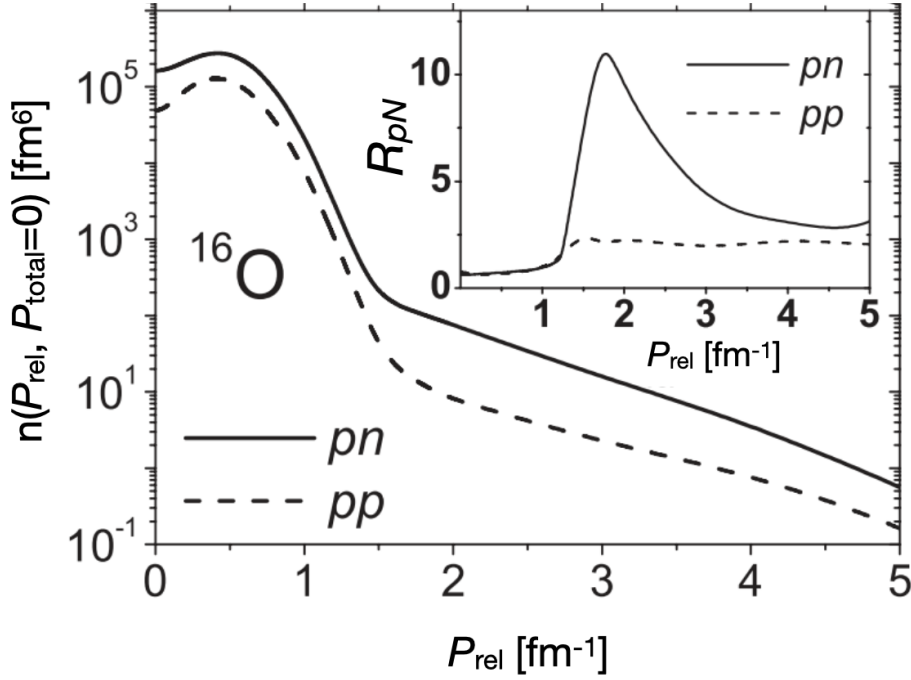
Figure 1.9: The TNMD is shown for ^{16}O at zero total momentum (back-to-back condition). The solid and dashed line shows the distribution of *pn* and *pp* pair, respectively. The inset shows the ration of the R_{pN}, see text for details. The figure is from Ref. [41].

interactions with different range parameters (α, β and γ) are shown in dashed lines, which induce a substantial enhancement at around 2 fm^{-1}. Similar results are shown in grey dot and grey line for VMC calculation and spectral function analysis (denoted as "LDA"), indicating the parameter γ is the most reasonable. Complete reference list can be found in [25].

The same calculation with Table 1.3 shows the contribution from different interactions for ^{16}O in an explicit way. Figure 1.9 shows the TNMD ($n(P_{\text{rel}})$) for back-to-back case (zero total momentum P_{total}) as a function of relative-momentum p_{rel}. The inset shows the ratio which is obtained by:

$$R_{pN} = \frac{n_{pN}(P_{\text{rel}}, P_{\text{total}} = 0)}{n_{pN}^{\text{central}}(P_{\text{rel}}, P_{\text{total}} = 0)} \tag{1.35}$$

where $N = p$ or n. The ratio mainly present the effect of tensor interactions [41]. The ratio increases drastically from 1.5 to 2 fm^{-1} and reaches the maximum, showing the dominant role of tensor interactions at momentum region around 2 fm^{-1}.

1.3.4 Summary

As a brief summary, we have presented several experimental and theoretical studies that show the crucial role of tensor interactions on high-momentum nucleons (~ 2 fm^{-1}), for several light nuclei.

In the theoretical side, on the one hand, for $A \leq 12$ nuclei, ab-initio type calculations provide detailed structure information to understand effects of tensor interactions, which are confirmed by experiments. On the other hand, for $A > 12$ nuclei, it is difficult to perform ab-initio type calculation yet. Several calculations have been developed with different assumptions and show results similar to ab-initio calculations. They predict the effect of tensor interactions in heavier nuclei.

In the experimental side, electron knock-out experiments provide a good method to study the momentum distribution of nucleon-nucleon pairs. However, the cross section of electron knock-out reactions is very small. It is difficult for double and triple coincident measurement on such small cross section reactions, even for stable target nuclei, not to mention for exotic nuclei. Therefore, the complete spin and isospin character is difficult to be pinned down in inclusive measurement of electron knock-out reactions, which causes the mixing of effect from tensor and central interactions. In addition, the amplitude of the high-momentum component is typically two or three orders smaller than the low-momentum part. As a consequence, the initial or final state interactions as well as many-body terms in the transition operators have to be taken into consideration in the analysis of these experiments. These corrections make it difficult to isolate the effect of tensor interactions [21].

Different from central interactions, tensor interactions have spin and isospin dependence. The unique feature of tensor interactions may help to distinguish the effect. As indicated by the work reported in Ref. [40], hadron probe is preferable since it is easier to perform exclusive measurement to extract spin and isospin character, owing to larger cross sections. In addition an important advantage of hadron probe lies in the ability to extend into inverse kinematics for exotic nuclei study. In next section, Sec. 1.4, we introduce several hadron probe experiments to study the high-momentum nucleon to explore effects of tensor interactions in details.
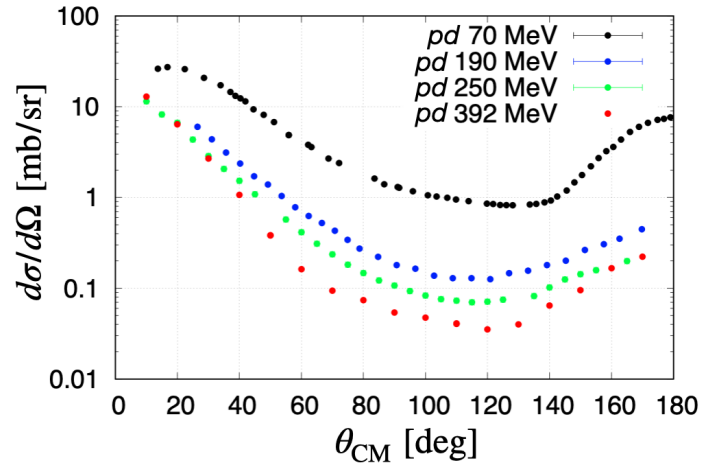
Figure 1.10: Figure shows the angular distribution of $p + d$ elastic scattering cross section at several incident energies. The data at 70, 190, 250 and 392 MeV is from [42–45], respectively.

1.4 Experimental method to study tensor interactions

Following the discussion in the previous sections, study of high-momentum nucleons is suitable to observe the effect of tensor interaction in nuclei. In this section we present the experimental methods, neutron pick-up reactions to explore the high-momentum nucleon induced by tensor interactions selectively.

Figure 1.10 shows the angular distribution of $p + d$ elastics scattering at various incident energies. The horizontal axis is the center of mass scattering angle. In normal kinematics the incident beam is proton, and the backward proton scattering angle in laboratory system corresponds to the forward deuteron scattering angle in laboratory system. The peak of cross section at large angle is understood as from a pick-up mechanism [46], where the momentum transfer is identical with the internal momentum of picked-up neutron.

Measurements for $^{16}O(p, d)$ reactions with deuterons detected at forward angle have been performed to study the high-momentum nucleons induced by tensor interactions [30–32]. It is found that the cross sections populating to different final states of the residual nuclei, ^{15}O, behave differently with the transfer momentum of the reaction. Figure 1.11 shows the ratios of cross sections of $^{16}O(p, d)$ reactions populating to different final states of ^{15}O [32]. The ratio $R_{g.s.}^+$ (shown in panel (a)) is taken from the cross sections of $^{16}O(p, d)$ populating to the 5.24 MeV excited state over that to the ground state of ^{15}O, while the ratio $R_{g.s.}^-$ (shown in panel (b)) is taken from the cross section of $^{16}O(p, d)$ populating to the 6.18 MeV excited state over that to the ground state of ^{15}O. Note that the spin and parity of the ground state and the 6.18 MeV excited state are $1/2^-$ and $3/2^-$, respectively. The one near 5.24 MeV includes $5/2^+$ and $1/2^+$ states, which are not separated, but both are positive parity states.

The tensor operator, in momentum space shown in Eq. 1.12 and coordinate space in Eq. 1.15, indicates the selection rules with $\Delta L = \Delta S = 2$. In the shell model framework, two-particle-two-hole (2p2h) excitation can be induced by tensor interactions,
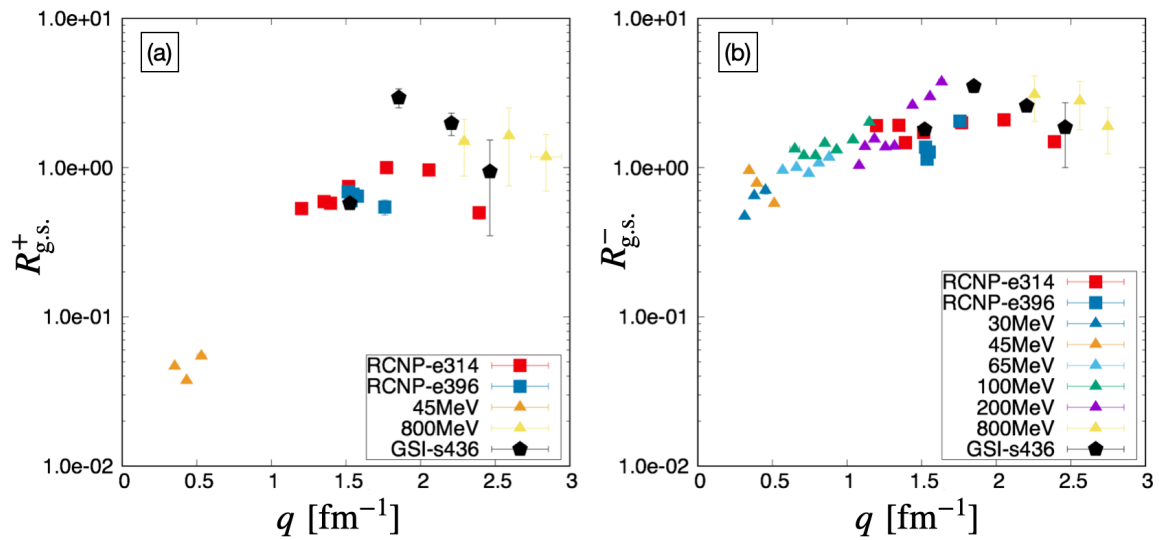
Figure 1.11: Ratios of cross sections of reactions populating to different final states are shown. The figure is from Ref. [32].
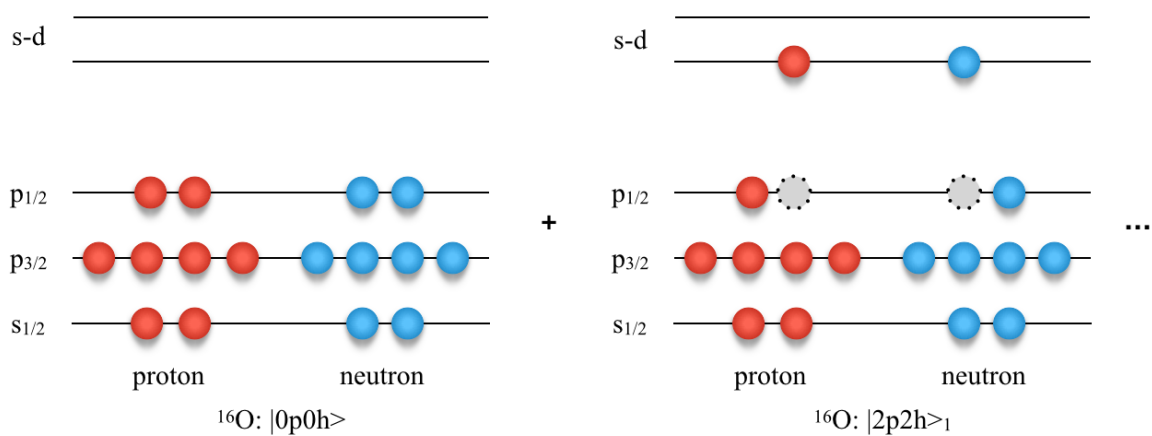
Figure 1.12: The first one shows the 0p0h configuration while the second one shows the 2p2h configuration. The figure is from Ref. [32].
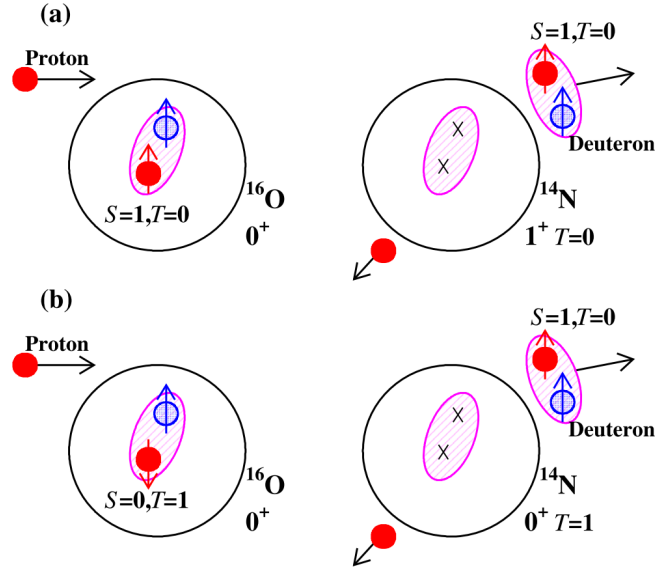
Figure 1.13: Schematic view of neutron pickup reaction with coincidence with a proton assuming (a) a $(S,T)=(1,0)$ correlated pair and (b) a $(S,T)=(0,1)$ correlated pair at the initial states in the (p,pd) reactions. The figure is from Ref. [33].

and thus high-momentum component is included [47]. The ground state of ^{16}O can be regarded as the sum of different configurations. As shown in Fig. 1.12, the lowest order configuration is the "zero-particle-zero-hole" (0p0h) configuration. Nucleons may be excited to upper orbital, causing "two-particle-two-hole" (2p2h) configurations or others. The "one-particle-one-hole (1p1h)" configurations cannot be mixed in the ground state of ^{16}O due to the spin and parity conservation. The "^{16}O:$|$2p2h$>_1$" in Figure 1.12 shows one of $|$2p2h$>$ configurations as an example. Obeying the selection rules of tensor operator, this configuration is induced by tensor interactions. ^{15}O can be regarded as a neutron removed from ^{16}O. One can remove a neutron from p shell to populate negative parity final state of ^{15}O. However, to populate positive parity state (e.g. the 5.24 MeV excited state), the neutron should be removed from s-d shell, which is in the 2p2h configurations. Therefore, $R_{\text{g.s.}}^{+}$ is related with tensor interactions while $R_{\text{g.s.}}^{-}$ is not. As shown in Figure 1.11, the tensor related ratio, $R_{\text{g.s.}}^{+}$, increases by about two orders of magnitude from small momentum transfer to large momentum transfer. In contrast, the non-tensor related ratio, $R_{\text{g.s.}}^{-}$, changes within one order of magnitude varying the same momentum transfer range. The different behavior of two ratios along different momentum transfer shows an effect of tensor interactions in ^{16}O ground state wave function.

As we discussed in subsection 1.3, the correlation part dominates in momentum distribution at high-momentum. If the incoming proton picks up a high-momentum neutron which is strongly correlated with another nucleon, the other correlated nucleon may be emitted simultaneously. Therefore, (p,Nd) reactions ($N = n$ or p) is an useful tool to study correlated pairs with large relative-momentum. A pioneering experiment has been reported in Ref. [33, 34]. The deuterons were detected at small forward scattering angle and the protons or neutrons were detected at backward angle
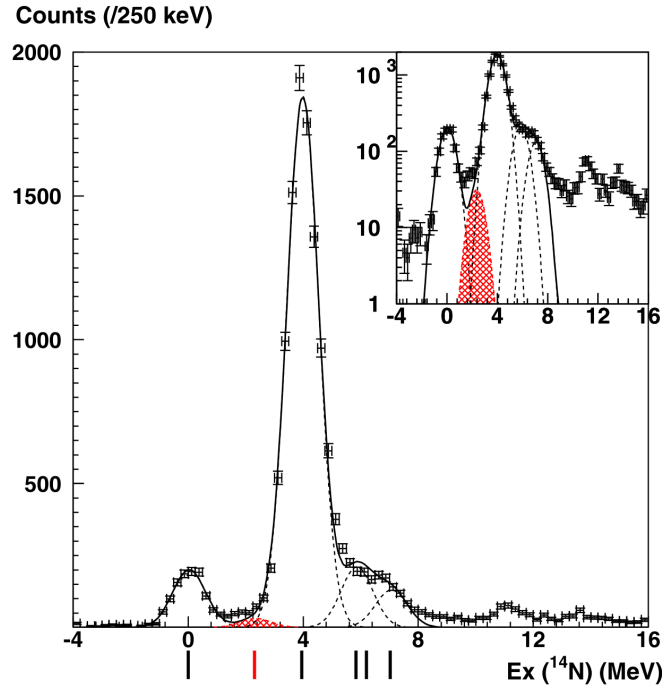
Figure 1.14: Excitation energy spectrum of $^{16}O(p,pd)^{14}N$ reactions with the total and individual fitting results shown by the solid and dashed lines, respectively. The figure is from Ref. [33].

in coincidence. For $^{16}O(p,pd)^{14}N$, if the reaction populates a $J^\pi = 1^+$, $T = 0$ state of ^{14}N, as shown in panel (a) of Fig. 1.13, the nucleon pair inside ^{16}O should be a pn pair with $(S,T)=(1,0)$ in the initial state, since the deuteron with $(S,T)=(1,0)$ is in the final state. For the pn pair with $(S,T) = (0,1)$, the final state should has $J^\pi = 0^+$, $T = 1$, as shown in panel (b). Similarly, for $^{16}O(p,nd)^{14}O$, the pair should be a n-n pair with $(S,T) = (0,1)$, for the final state of $T = 1$ ^{14}O. By this method, nucleon pairs of different (S,T) configurations are studied by selecting the final state of the residual nucleus.

The spectrum of the residual nucleus was reconstructed from the energies and scattering angles of deuterons and protons (or neutrons). Figure 1.14 shows an excitation energy spectrum of ^{14}N from (p,pd) reactions. The discussion focus on the first ($E_{ex} = 2.3$ MeV, $J^\pi = 0^+$) and second excited state ($E_{ex} = 3.9$ MeV, $J^\pi = 1^+$), where the $L = 0$ transition dominates [33, 49]. It is found that the cross section of reaction populating the 2.3 MeV state (marked as red in Fig. 1.14) is small compared with the 3.9 MeV excited state in 392 MeV data. In contrast, both states have similar strength in the spectrum taken at a smaller incident energy, 75 MeV, as shown in Fig. 1.15.

The DWIA (distorted-wave impulse approximations) calculation describe the shape of the three-body triple differential cross section of $^{16}O(p,pd)$ very well, and thus the spectroscopic amplitudes were deduced by reproducing the cross section. The ratio between 2.3 MeV excited state and 3.9 MeV excited state is shown in Fig. 1.16. The cross symbol shows the data with 75 MeV proton beam [48]. The blue hatch area shows the result of DWIA calculation, where the spectroscopic factor ratio of two
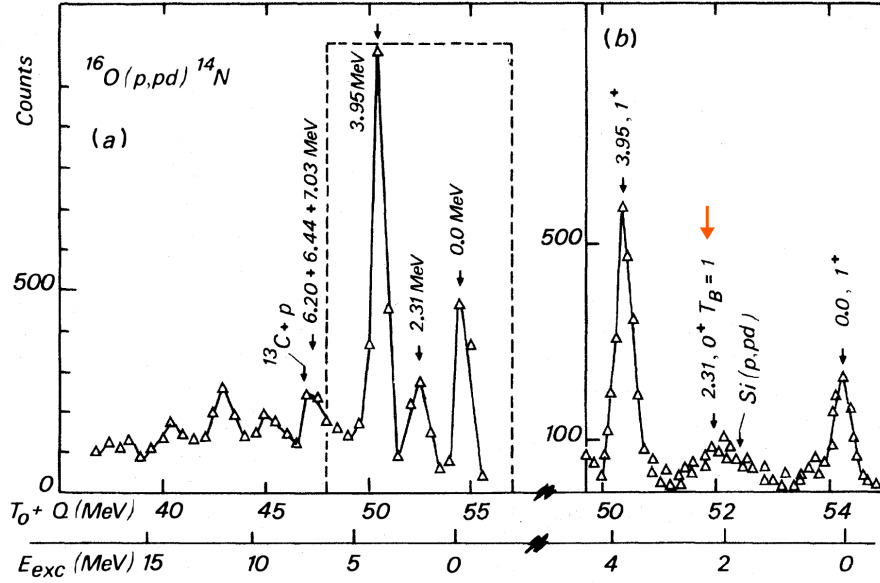
Figure 1.15: Excitation energy spectrum of ^{16}O$(p, pd)^{14}$N reactions with 75 MeV incident proton. Panel (a) shows an overview and panel (b) shows a detail representation of dashed line in panel (a). The figure is from Ref. [48].

states was determined to reproduce the data. The triangle symbols show the data with 392 MeV incident proton and three symbols represent three different spectrometer setting, covering different proton momenta range as shown in horizontal axis. DWIA and PWIA (plane-wave impulse approximation) calculations are shown in green and red areas, respectively, using the determined spectroscopic factor obtained from the calculation for 75 MeV data. They give roughly same results, indicating that the distorted wave effect is actually canceled out by taking the ratio. Therefore, it is expected that the ratio $R_{2.31/3.95}$ should reflect the spectroscopic amplitude of pn pairs with $(S, T) = (0, 1)$ and $(S, T) = (1, 0)$.

A strong relative reduction of the cross section ratio is expected to be due to tensor interactions. The DWIA calculation using two-body interactions including tensor interactions present a reduction of the ratio. However, the discrepancy between data and calculations can be seen. It requires more efforts in both experimental and theoretical studies.
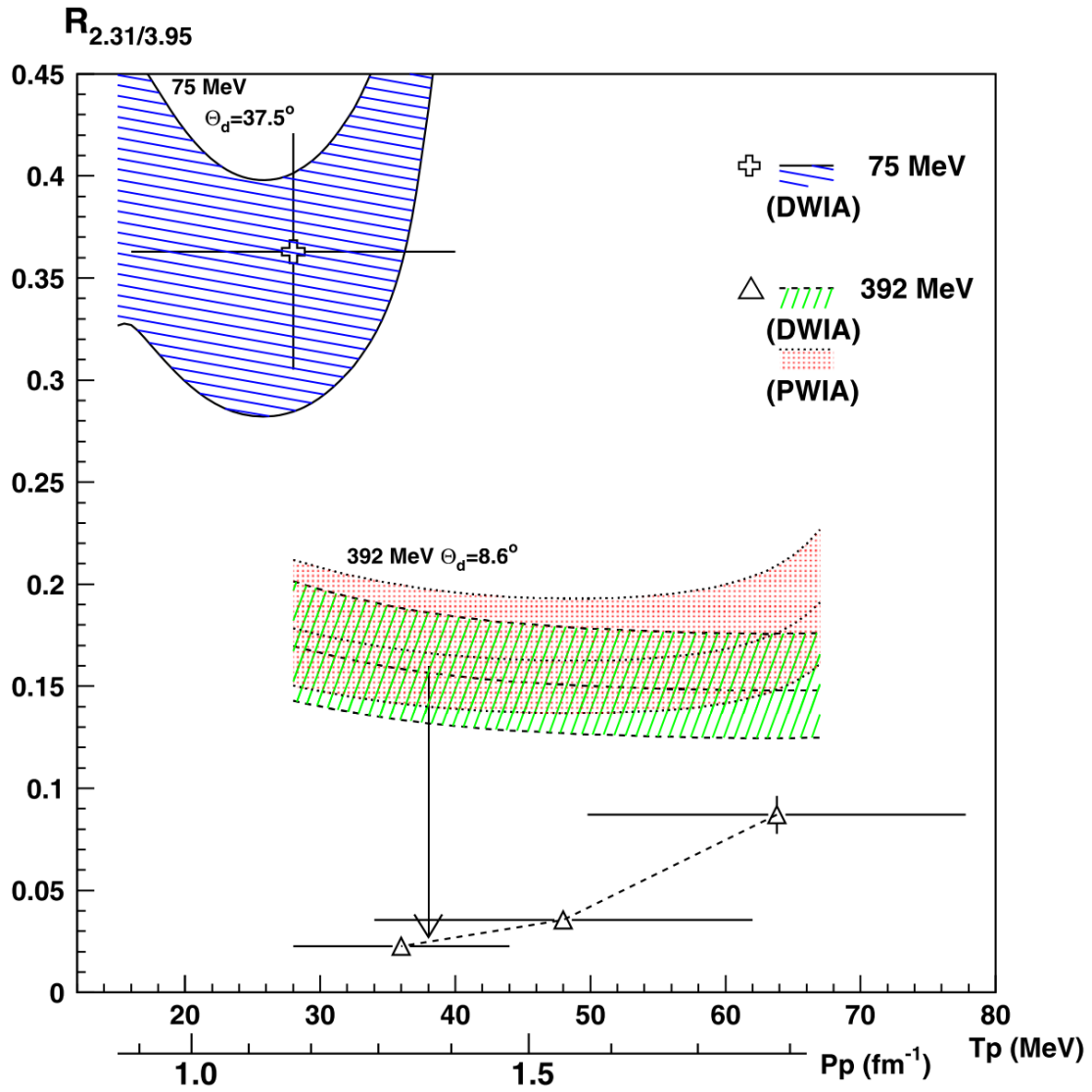
Figure 1.16: Ratio of cross section for 2.31 to 3.95 MeV excited state is shown as functions of proton energy [33].

1.5 Thesis objective

To complete the knowledge of nucleon-nucleon interactions, it is essential to under-standing effects of tensor interactions in nuclei heavier than ^{4}He. High-momentum nucleons in light nuclei have been been studied and it is found that tensor interactions play a dominate role at the momentum region around 2 fm^{-1}. Therefore, we aim to study the high-momentum nucleons to understand the effect of tensor interactions in nuclei.

Neutron pick-up reaction provides a unique tool to focus on the high-momentum nucleon selectively. Previous work have shown the existence of high-momentum nucleon pairs induced by tensor interactions, from the cross section ratio between different final states in ^{16}O(p, pd) reactions, which correspond to pn pair with $(S, T) =$(1,0) and (0,1) configuration in the initial state. In order to investigate effects of tensor interactions without ambiguity of reaction mechanism, we performed systematic measurements on ^{16}O(p, pd) reactions covering various momentum transfer, with various incident energies and scattering angles. Especially, we aim to seek for answers of following questions:
1) how much is the cross section ratio at various momentum transfer?
2) how does reaction mechanism affect the ratio? (does the cross section ratio change with incident energies and scattering angles or depend only on momentum transfer?)
3) is the strength of tensor interactions in ^{16}O same with that in deuteron?

In this thesis, we present the systematic study on ^{16}O(p, pd) reactions at Research Center for Nuclear Physics, Osaka. We measured the pick-up domain ^{16}O(p, pd) re-actions at 230 and 392 MeV incident energies and several scattering angles. Forward going deuterons were momentum-analyzed by the Grand Raiden spectrometer and de-tected by focal plane detectors. We developed a plastic scintillator array and used it to measure backward going protons, in coincidence with deuterons. The details about experimental setup and the detector system are presented in Chap. 2.

We analyzed ^{16}O(p, pd) channel to obtain the energies and scattering angles of coincident protons and deuterons. From the energies and scattering angles of deuterons and protons, we constructed the missing mass spectrum of ^{14}N. We also analyzed scaler data to estimate several efficiencies and obtained the differential cross sections. The procedures of data analysis are presented in Chap. 3.

In Chap. 4, we discuss the experimental results and present conclusions and dis-cussion. We deduced the cross section ratio between reactions populating to two final states of ^{14}N, corresponding to the removal of $(S, T) = $(0,1) and (1,0) pn pairs from ^{16}O. We discuss the dependence of the cross section ratio on the relative-momentum of the correlated nucleon pairs from the data at different incident energies but the same forward scattering angle, where the effect of competing reaction mechanism is small. Observed ratio difference shows an effect of tensor interactions clearly. We also discuss effects of competing reaction mechanism, which is found to reduce the observed effects of tensor interactions.

In Chap. 5, a summary of this work is presented and perspectives are discussed.

In addition, we prepare several appendixes related with present work. In Appendix A, we discuss kinematics of two-body and three-body final state reactions. Kinematical formula as well as the derivation used in this thesis is summarized there. In Appendix B, we present the result of Monte Carlo simulation, which was used to investigate tar-

get effect on energy resolution in the excitation energy spectrum. We have developed a neutron detector system called "BOS4" to measure $^{16}O(p, nd)$ channel in the same experiment. We present brief introduction in Appendix C. We found proton background originated from incident beam hitting at the beam line upstream than the scattering chamber. The treatment and effects of this background are discussed in Appendix D.

Chapter 2

Experiment

In order to study effects of tensor interactions, we performed RCNP-E552 experiment at WS Course in Research Center for Nuclear Physics (RCNP) to measure ^{16}O(p, pd) reactions systematically at various momentum transfer. We submitted the experimental proposal on January, 2021, and it was approved with "Grade A". During the machine commissioning we run E552 experiment, which is the first physics experiment after the few-year shutdown due to facility upgrade.

Proton beam with two incident energies were used in E552 (392 MeV on April, 2023 and 230 MeV on March, 2023), to bombard the ice target. The forward going deuterons were momentum-analyzed by Grand Raiden spectrometer (GR) and detected by the focal plane detectors, in coincidence with the backward going particle protons, detected by an array of plastic scintillators.

At the beginning of this chapter, we present the kinematics setting in E552 experiment as well as the considerations in Sec. 2.1. Secondly, we introduce the facility briefly in Sec. 2.2. Thirdly, we introduce the target system used in E552 in Sec. 2.3, including the cool target system and low profile target system. Fourthly we present a short introduction on the high-resolution magnetic spectrometer "Grain Raiden" (GR) including the focal plane detector system in Sec. 2.4. After that we show the detector setup around the scattering chamber in Sec. 2.5 as well as the data acquisition system (DAQ) in Sec. 2.6. Last but not least, we present the data summary in E552 experiment in Sec. 2.7.

2.1 Kinematics setting

In order to study effects of tensor interactions, we investigate ^{16}O(p, pd) reactions systematically at various momentum transfer. From kinematics, both incident energy and scattering angle affect the momentum transfer of the (p, pd) reactions. We calculated the kinematics of ^{16}O(p, pd) reactions, with the assumption of recoilless condition, which means the recoil particle (^{14}N) has zero-momentum after reaction. The main reason is that at recoilless condition the internal momentum of picked-up neutron (as well as the correlated proton) is identical to the momentum transfer in pick-up reaction (detailed explanation is presented in Appendix A). Therefore, by changing incident energy and scattering angle, we are able to probe the pn pair with different relative momenta.
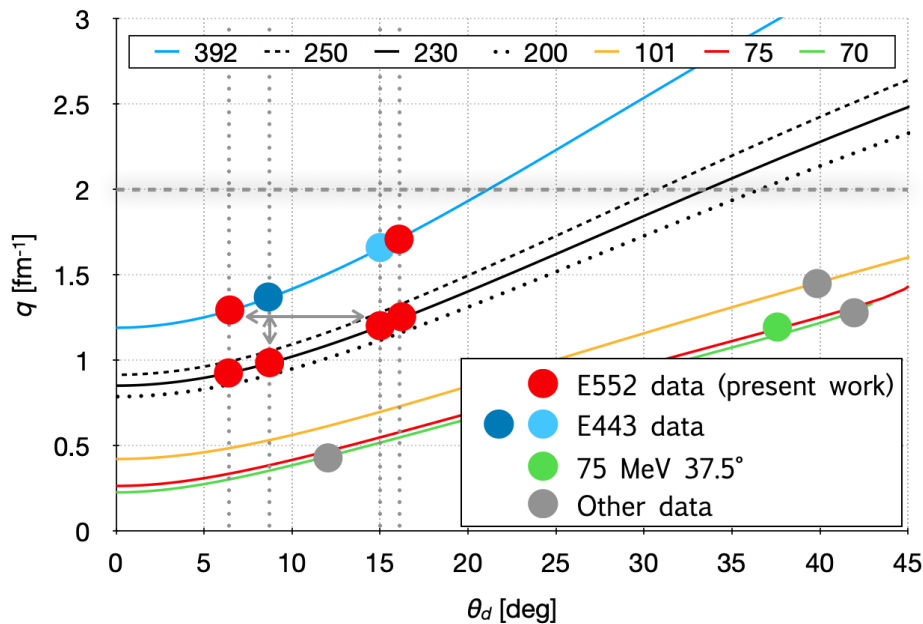
Figure 2.1: Momentum transfer of ^{16}O(p, pd) reaction is shown for various incident energies and scattering angles of deuteron.

In addition, the cross section is expected to be maximum at recoilless condition.

Figure 2.1 shows the momentum transfer in ^{16}O(p, pd) reactions as a function of scattering angle of deuterons at various incident energies. Formulas are presented in Appendix A. With certain incident energy, scattering angle of deuterons and the excitation energy of residual nuclei, the momentum transfer is calculated. Lines with different colors show the kinematics at different incident energies. In previous experiment (E443 [33]), the reaction was studied at 392 MeV proton incident energy and 8.7 and 15 degree of deuteron scattering angles, as shown in blue circle along blue line. The horizontal dash line shows the 2 fm^{-1} line, where tensor interactions are expected to have the largest effect. In order to approach that, we proposed to use the largest beam energy at RCNP, 392 MeV, and measure the deuteron at the maximum scattering angle. In transfer reaction, more forward angle of the deuteron is detected, purer the pick-up reaction mechanism is. Therefore, it is desirable to measure the deuteron at most forward angle also. The maximum and minimum angle of Grand Raiden (GR) spectrometer was determined accordingly from the backward particle detection by "BAckward Nucleon Detector" (BAND). The restriction came from the space limitation around scattering chamber. As a result, the maximum and minimum angle (center value) of deuteron is fixed as 16.1° and 6.4°, respectively.

To investigate effects of tensor interactions and reaction mechanism, it is desirable to measure the same reaction with lower incident energy at the same scattering angles of deuteron. We performed measurement at 230 MeV incident energy because at this energy and 16.1° and 15°, the momentum transfer is similar with that at 8.7° and 6.4° and 392 MeV, respectively. Therefore, two comparisons can be made to study different effects independently: for data at the same angles but different incident energies, we can explore the effect of tensor interactions at different momentum regions, free from

Table 2.1: Kinematics summary

T_{b} [MeV]	θ_d	q [fm^{-1}]	Proton angle (HODO)
392	6.4°	1.29	132.8°-158.7°
	16.1°	1.71	107.5°-133.8°
230	6.4°	0.94	132.8°-158.7°
	8.7°	1.00	123.5°-149.4°
	15.0°	1.22	110.3°-136.7°
	16.1°	1.26	107.5°-133.8°

the influence of reaction mechanism; for data at the same momentum but different energies and angles, we can study the effect of reaction mechanism, assuming the same effect from tensor interactions.

As a result, we performed RCNP-E552 experiment to measure ^{16}O(p, pd) reactions at 392 MeV incident energy (T_{b}) with 2 scattering angles of deuterons (θ_d) and 230 MeV with 4 angles, respectively. The angle of BAND for backward particles was adjusted accordingly with GR for forward particles. With a specially designed holder frame, BAND was installed on Large Acceptance Spectrometer (LAS) rotational base and adjusted by LAS rotation. In addition, the proton hodoscope detector (HODO) was equipped with a rail system and was shifted for different angular settings to avoid interference. Table 2.1 shows the summary of kinematics condition of E552 experiment. The momentum transfer, identical with the internal momentum of probed nucleons, was calculated for each deuteron angle and incident energy with recoilless condition.

2.2 Experimental facility

In this section we first present an overview of RCNP in subsection 2.2.1, then we introduce the beam line up to WS Course in subsection 2.2.2. After that we present the setup of beam line polarimeters in subsection 2.2.3. Finally we discuss the "Grand RAiden Forward" (GRAF) beam line in subsection 2.2.4.

2.2.1 Overview

RCNP is a joint research center with the largest accelerator facility on a university campus in Japan. Figure 2.2 shows a bird view of RCNP. Equipped with a K140 Azimuthally-Varying-Field (AVF) Cyclotron and a K400 Ring Cyclotron, it has the capability to accelerate proton beams up to 400 MeV, which is suitable for our experiment. There are several experimental terminals in RCNP, such as WS Course (equipped with high-resolution spectrometer), EN Course (capable for radioactive beam experiment) and so on.

2.2.2 Beam line

The unpolarized proton beam is generated from the Electron Cyclotron Resonance (ECR) source and accelerated to 65 MeV by AVF Cyclotron and 392 MeV by Ring
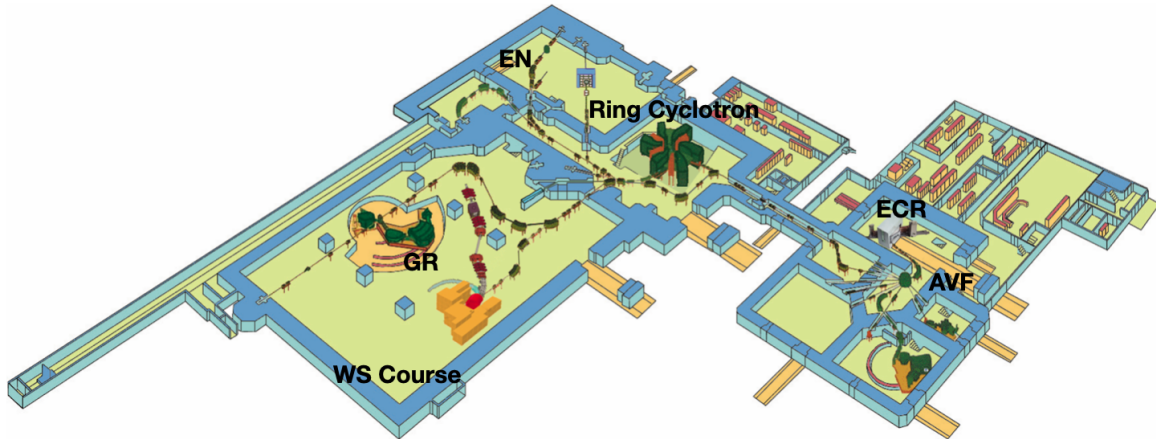
Figure 2.2: A schematic overview of RCNP cyclotron facility is shown. The figure is from RCNP wiki page.

Cyclotron, or 44 MeV by AVF Cyclotron and 230 MeV by Ring Cyclotron. It was delivered achromatically to the scattering chamber by the WS beam line, as shown in Fig. 2.3.

The WS beam line is operated mainly in two mode, dispersive and achromatic mode. The dispersive mode is used for dispersion matching by using Grand Raiden (GR) spectrometer, in order to reach the best energy resolution, while the achromatic mode provides the double-achromatic beam transport. In E522 experiment, because we aim to have large beam intensity and focusing condition instead of the best energy resolution for the forward particles, we used the achromatic mode instead of dispersive mode.

Figure 2.4 shows the beam envelops for the WS beam line and GR in the achromatic mode [50]. Two Beam Line Polarimeters (BLPs) are placed at the first and second doubly-focusing point. Originally designed for beam line polarization measurement, in E552 BLPs were used as the beam intensity monitor, which is discussed in next subsection 2.2.3. Section III and IV act as one ion-optical unit, to compensate the lateral and angular dispersion produced at Section I and II. The beam is doubly focused at the position slightly upstream of QM9S and focused both horizontally and vertically to target position by Section V.

In E552 experiment, the typical beam intensity in average was few tens nA, and the maximum intensity achieved was around 300 nA. The beam energy resolution was from 170 to 400 keV (full width at half maximum (FWHM)) and the typical emittance is around 0.1 degree.

2.2.3 Beam Line Polarimeter

Two sets of Beam Line Polarimeters BLP1 and BLP2 are placed in the first two doubly-focusing point of WS beam line to measure the beam polarization. In E552 experiment, we used unpolarized beam and they were used to monitor the beam intensity. Both of them consist of four pair of plastic scintillation counters to measure p+H elastic scattering from an Aramid target. Figure 2.5 shows the configuration of left (L and L')
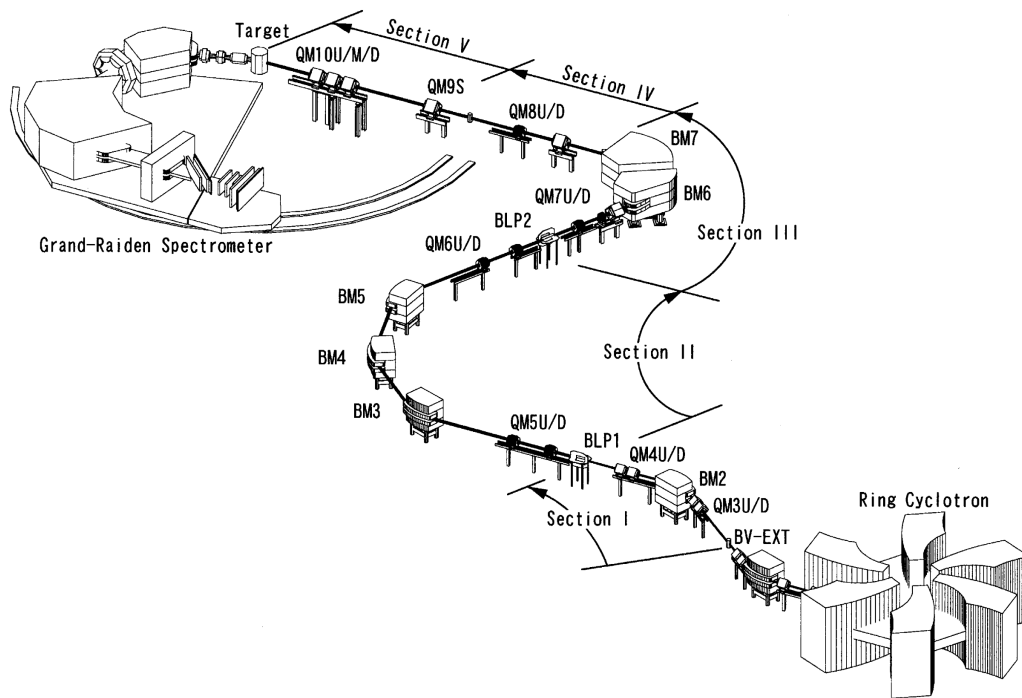
Figure 2.3: A schematic overview of WS beam line is shown. In a achromatic mode, the WS beam line is able to deliver a double-achromatic beam with zero lateral and angular dispersions at the target position. The figure is from Ref. [50].
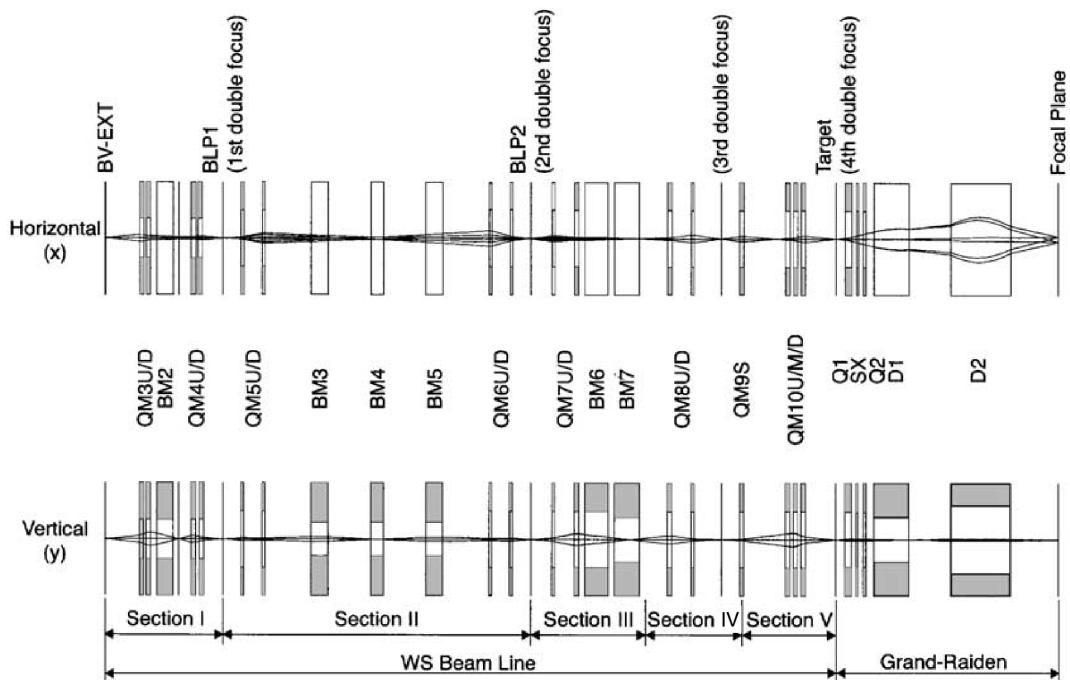
Figure 2.4: WS beam line and GR in achromatic mode. The figure is from Ref. [50].
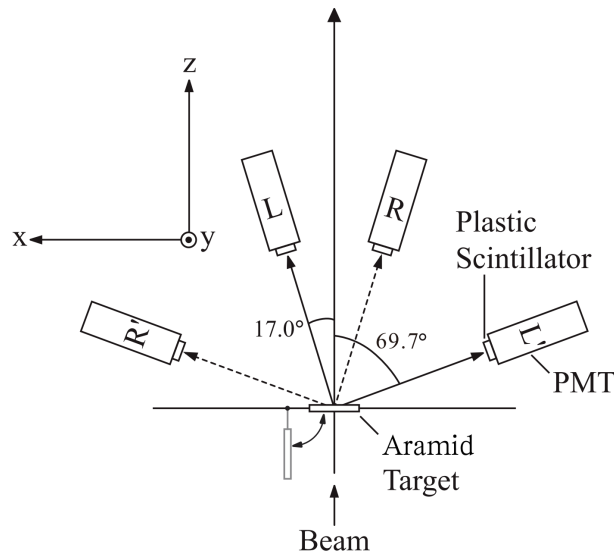
Figure 2.5: The top view of BLP is shown. Left (L and L') and right (R and R') pairs are shown while the up and down pairs locating in the vertical plane are not shown in this figure. Figure is modified from [34].

Table 2.2: BLP setting

Incident beam energy [MeV]	Target thickness of BLP1 [μm]	Target thickness of BLP2 [μm]	Angle [deg]
392	4	12	17.0, 69.7
230	12	12	17.0, 71.1

and right (R and R') pairs in the horizontal plane (z-x), while the up and down pairs with similar geometry in the vertical plane (z-y) are not shown. Each pair measure two protons from the same p+H scattering in coincidence. Table 2.2 shows a summary for the BLP target thickness and angle of pair counters at two incident energies.

2.2.4 Grand Raiden forward beam line

The beam was transported to the target position inside the scattering chamber (SC). The unreacted beam was transported to a wall Faraday cup (WallFc) by the "Grand RAiden Forward" (GRAF) beam line. The top view of GRAF beam line is shown in Fig. 2.6, as well as the GR and the "Large Acceptance Spectrometer" (LAS). With the help of GRAF, the beam is collected at the well-shielded WallFc at 25-meters downstream of the target, which significantly decreases the background level around the target and the maximum beam intensity is increased up to 1 μA [51]. To avoid interference, GR-SX (the sextupole of GR) is shifted outside of the beam line. When the GR angle is smaller than 10°, the beam line is affected by GR-Q1 magnet, as shown in the insert of Fig. 2.6. In such case the position of BM1 was adjusted for each GR angle. In addition, the magnetic field of GRAF was adjusted according to the magnetic rigidity of GR central trajectory to transport the beam to WallFc. The
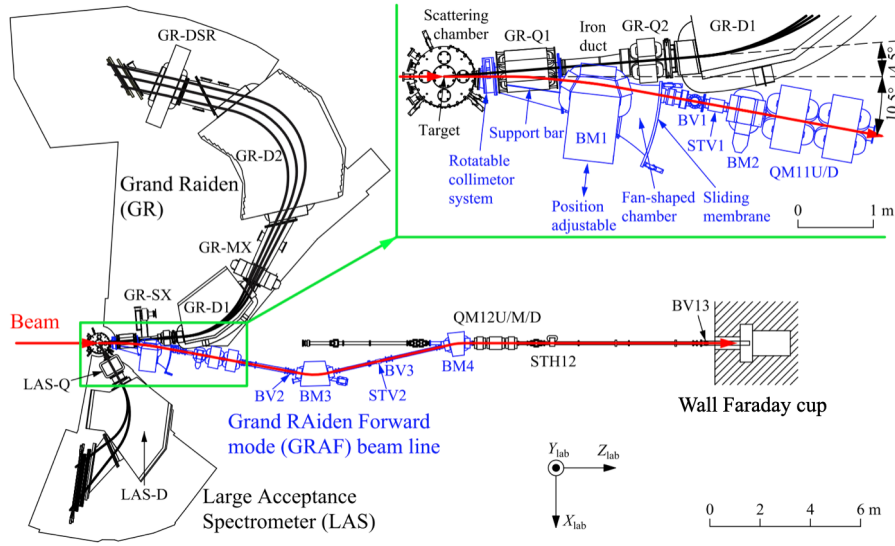
Figure 2.6: The top view of GRAF beam line, GR and LAS is shown [51]. The inset represents a zoomed view of the GRAF beam line around the target.

typical transmission efficiency of GRAF is around 99% in the calibration run of E552.

2.3 Target

In E552, a windowless self-supporting ice target was used as oxygen target, which is introduced in subsection 2.3.1. Besides, in subsection 2.3.2 we discuss several reference targets: A carbon target was used for energy calibration; A deuterated polyethylene (CD$_2$) target was used as a deuteron target for setup and calibration of detector systems. In addition, a viewer made by zinc sulfide was used for beam tuning.

2.3.1 Ice target

There are several advantages to use the ice as the oxygen target in E552 experiment:

- As a solid target, it has large density compared with gas or liquid target;

- Solid target can hold itself without a window, which make it possible to be free of background;

- Compare with other solid oxygen target, the ice (H$_2$O) has the largest oxygen atomic ratio;

- Hydrogen does not contribute to the background in deuteron channel.

There are also several challenges in using the ice target:

- It is difficult to make and handle thin ice;

- It is difficult to control the thickness as well as the uniformity;
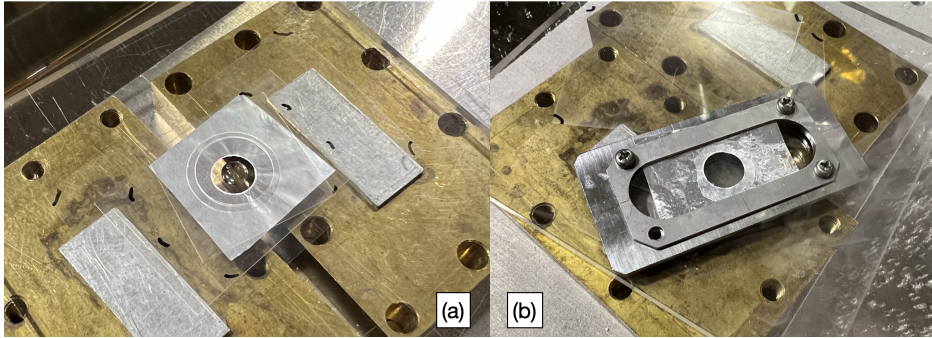
Figure 2.7: Photos before and after making an ice target are shown in panel (a) and (b), respectively.

- To keep the ice target, it is necessary to use cooling system.

Besides ^{16}O(p, pd) reactions, we also measured ^{16}O(p, nd) reactions in E552. Due to the yield and resolution difference of two channels, we used different thickness of ice targets for different channels. The target thickness effect was studied by Monte Carlo simulation, which is presented in Appendix B. In short, the ice target thickness was determined by the maximum thickness that does not make the energy resolution worse in the excitation energy spectrum of the residual nuclei. As a result, we determined to use around 20 and 200 mg/cm^2 for (p, pd) and (p, nd) channel, respectively.

Based on the method developed in Ref. [52], we made thin ice target before beam time. On top of a resin panel, we prepared a OHP (overhead projector) film as the substrate. An aluminum (Al) foil with a thickness of 11 μm and a 9 mm $\emptyset$ hole was used to hold the ice sheet. A drop of pure water was carefully placed at the center of the hole. On top on the Al foil, we placed OHP films as the pacer with holes larger than that on the Al foil. The thickness depends on the thickness of the ice target we need. Then another OHP film was placed and pressed by copper blocks.

We used liquid nitrogen (LN$_2$) to cool down all the parts and removed OHP films carefully after the ice was made. After that, the Al foil was mounted to the target frame and installed to the target ladder. The ice was protected by nitrogen atmosphere, so that it was kept at low temperature and away from vapor in the air.

Figure 2.7 shows two photos of making an ice target. Panel (a) shows a photo before cooling. Panel (b) shows a photo after mounting the Al foil in the target frame.

During the experiment preparation before the beam time, whether stable and uniform ice targets with desired thickness can be made or not became the largest uncertain step. Based on the method developed in [52], together with previous experience, we summarize several important points in making thin ice for people who may want to use this system in the future:

- The thickness of the substrate aluminum (Al) foil should be thin enough, because thick Al foil will break the thin ice easily when it is deformed due to the temperature change. In E552 experiment, 11 μm Al foil was used as the substrate.

- The diameter of the hole of spacer polyester should be chosen properly. It should be enough larger than the diameter of hole of Al foil, because once the water drop

Table 2.3: Target summary

Name	Thickness [mg/cm^2]	Purpose
Thin ice	$\sim$20	Physics
Thick ice	$\sim$200	Physics
Carbon	42	Reference
CD$_2$	24	Reference
ZnS	–	Viewer

(before cooling) touch the edge of spacer, the water will spread and escape easily. However, the diameter should not be too large, otherwise due to the bending of the covering polyester, the thickness of the ice would be much smaller than that of the spacer. In E552, we use the Al foil with a 9 mm ∅ hole and one layer of polyester spacer with a 16 mm ∅ hole and another one with a 19 mm ∅ hole. Both spacers are0.1 mm thick.

- Since we use liquid nitrogen (LN$_2$) to cool the system, as well as to make the ice, the temperature decreased drastically. While making the ice, if the temperature is too low, the ice appears to be sticky and it is difficult to remove the polyester films without breaking the ice. Therefore, it is easier to remove the polyester films when the ice is just formed.

Figure 2.8 shows a schematic vie of the target cooling system [52]. Liquid nitrogen (LN$_2$) from a LN$_2$ tank was fed into the reservoir from the top, by supplying high pressure nitrogen gas from a nitrogen gas bottle to the LN$_2$ tank. The reservoir and the target ladder were cooled down by LN$_2$ to around 90 K. Two thermometers were used as temperature sensors, attaching on the surface of the reservoir and the target ladder, respectively. The vertical position of the cool target ladder was changed by a stepping motor with remote control.

The target tilted angle was fixed as 45 degree as shown in Fig. 2.9, based on the study of target effect by using Monte Carlo simulation, discussed in Appendix B.

During E552, we monitored the weight of the LN$_2$ tank, the temperature and the pressure of nitrogen gas bottle to insure a stable condition for the cooling system. As a result, all ice targets used in E552 survived until the end without significant thickness change during the whole beam time. The analysis of thickness measurement is discussed in subsection 3.3.5. Figure 2.10 shows photos of the condition of the thin ice target used before and after beam time on May in panel (a) and (b), respectively. The ice target in panel (b) was frosted because the photo was taken after the target was removed from cooling system and exposed in the air.

2.3.2 Reference target

Besides the ice target for physics channel, several reference targets were used for various purposes in E552. Table 2.3 shows a summary of targets used in E552.

A carbon target was installed in the cool target ladder as well. With a sieve slit at the entrance of GR we used the data of $p+^{12}$C elastic scattering to calibrate the GR
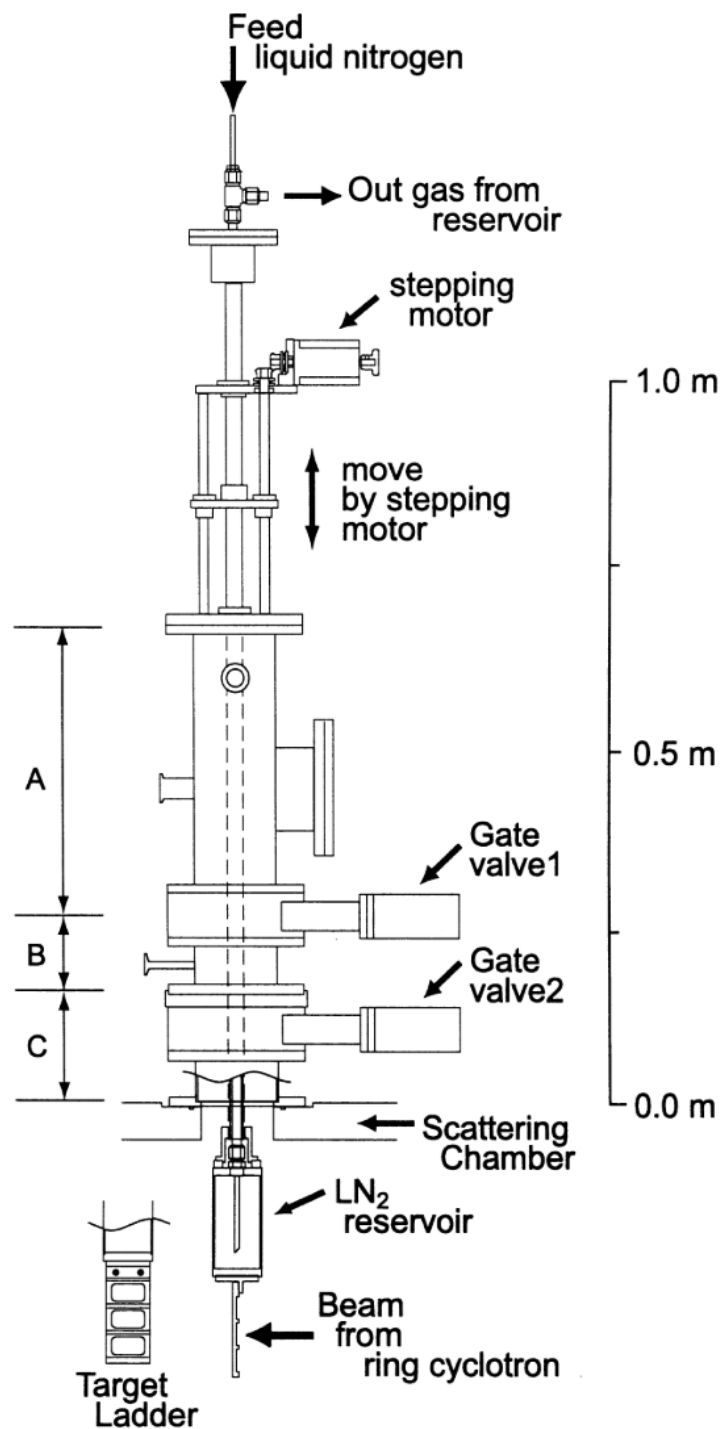
Figure 2.8: The schematic view of the target cooling system is shown [52].
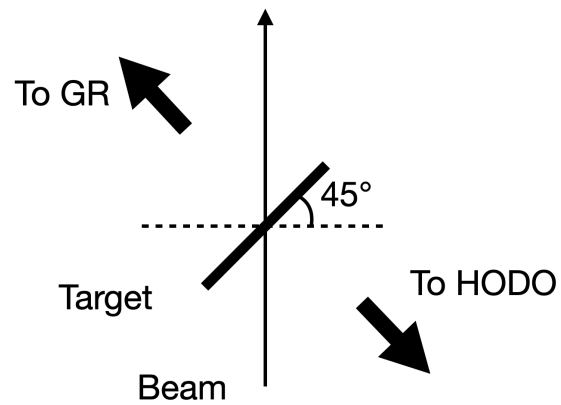
Figure 2.9: The target was tilted with 45 degree in E552 experiment.
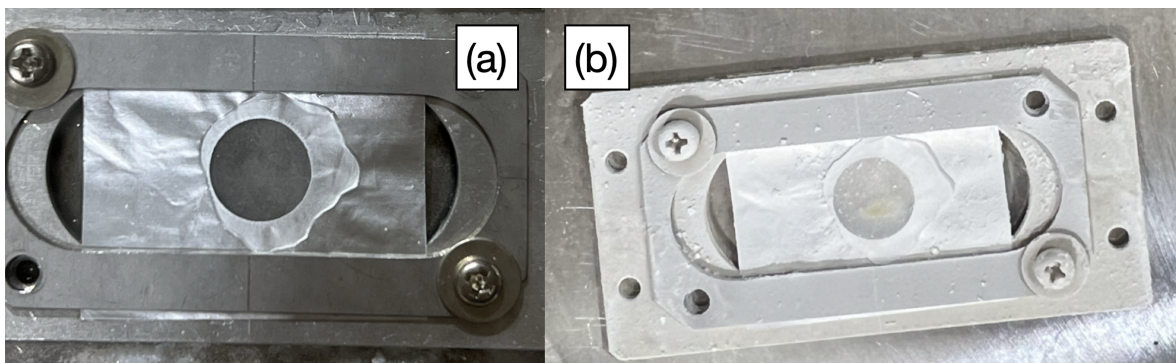
Figure 2.10: The photo of the ice target is shown in panel (a) and (b) for condition before and after beam time on May, respectively. The ice target in panel(b) was frosted because the photo was taken after the target was removed from cooling system and exposed in the air.
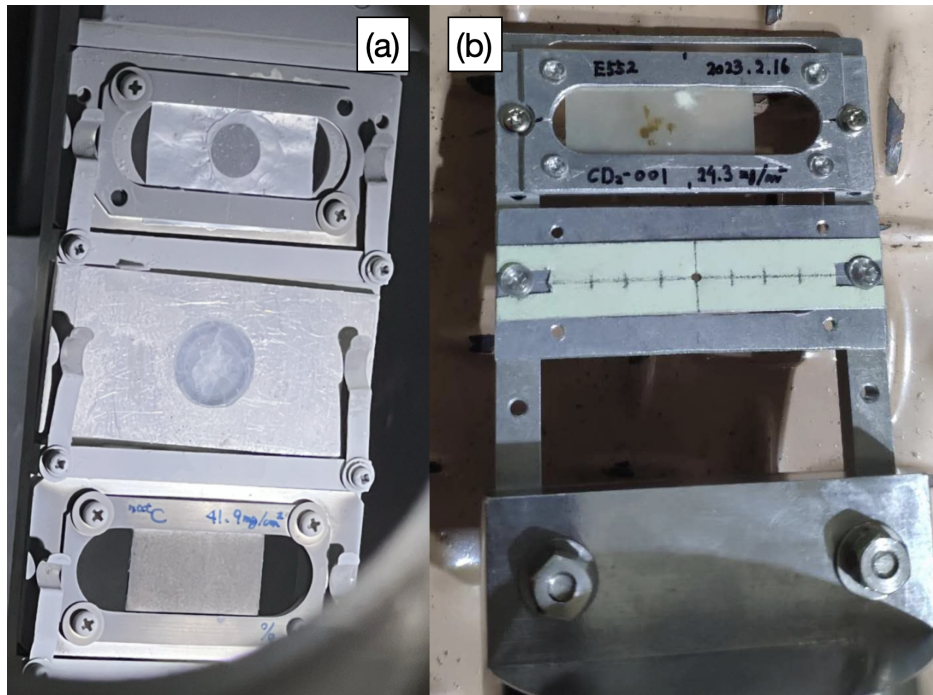
Figure 2.11: Photos of all targets used in E552 experiment is shown. Panel (a) shows thin ice, thick ice and carbon target on the cool target ladder from top to bottom, respectively. Panel (b) shows the CD_2 target and viewer in the low target profile, respectively.

optics, which is discussed in detail in subsection 3.1.3 and 3.1.4. With known thickness and better uniformity, we measured p+C elastic scattering to confirm the detector performance as well as scaler analysis, presented in subsection 3.3.4. A deuterated polyethylene (CD_2) target was used as carbon and deuteron target. Deuteron target is convenient in backward detector setup as well as energy and angle calibration, because the kinematics of $p + d$ scattering is similar with that of our aim channel (p, pd). In addition, a viewer made by zinc sulfide (ZnS) was used for beam tuning.

In E552, we used two target ladders: a cool target ladder from the top controlled by the cooling target system and a low profile target sit on a movable table inside the scattering chamber (SC). Figure 2.11 shows photos of all targets used in E552 experiment. Panel (a) shows thin ice, thick ice and carbon target on the cool target ladder from top to bottom, respectively. Panel (b) shows the CD_2 target and viewer in the low target profile ladder. To avoid interference with the cool target ladder, the size of the low target profile ladder and the holder were optimized from the stander one commonly used in RCNP [53].

Figure 2.12 shows a photo taken during beam tuning. We set up a camera around SC to monitor the target and beam condition. During beam tuning, accelerator operators used the viewer to check and adjust the beam profile.
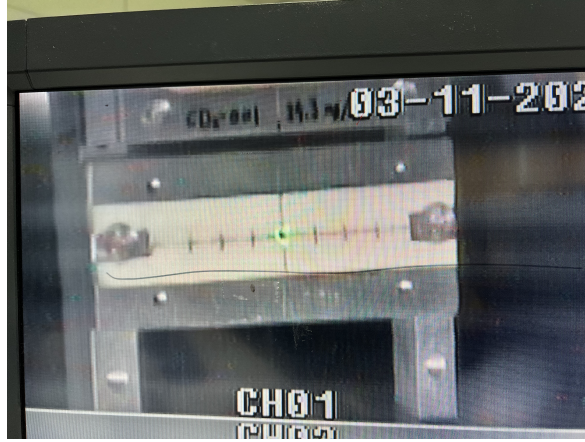
Figure 2.12: A photo of the beam spot checked by the viewer during beam tuning is shown. The diameter of the hole at the center of the viewer is 1 mm. The photo shows that the beam spot size is slightly larger than 1 mm at that momentum.

Table 2.4: GR specifications

Mean orbit radius	3 m
Total deflection angle	162°
Focal plane length	150 cm
Focal plane tilting angle	45.0°
Maximum magnetic rigidity	5.4 Tm
Vertical magnification	5.98
Horizontal magnification	-0.417
Momentum dispersion	15451 mm
Momentum acceptance	5%
Horizontal angle acceptance	±20 mr
Vertical angle acceptance	±70 mr

2.4 Grand Raiden spectrometer and focal plane detector system

Forward particles are momentum-analyzed by the Grand Raiden (GR) spectrometer, which is consist of two quadrupoles (Q1 and Q2), one sextuple (SX), one multipole (MP) and three dipole magnets (D1, D2 and DSR), as shown in Fig. 2.13 [54]. Table 2.4 shows a summary of GR specification [54]. With a large momentum dispersion and small magnification, high resolving power is achieved. In addition, with a small vertical magnification, the vertical size of the focal plane of GR is less than 3 cm, which helps to reduce the vertical size of focal plane detector and thus reduce the background [54]. At the focal plane of GR, a detector system consisting of two vertical drift chambers (VDCs) and two plastic scintillators (PLs) is placed along the direction of the focal plane. Two PLs are mainly used to generate the event trigger for data acquisition system (DAQ) and identify the scattered particles, while two VDCs are used to measure the the particle trajectory. In following part we introduce the focal
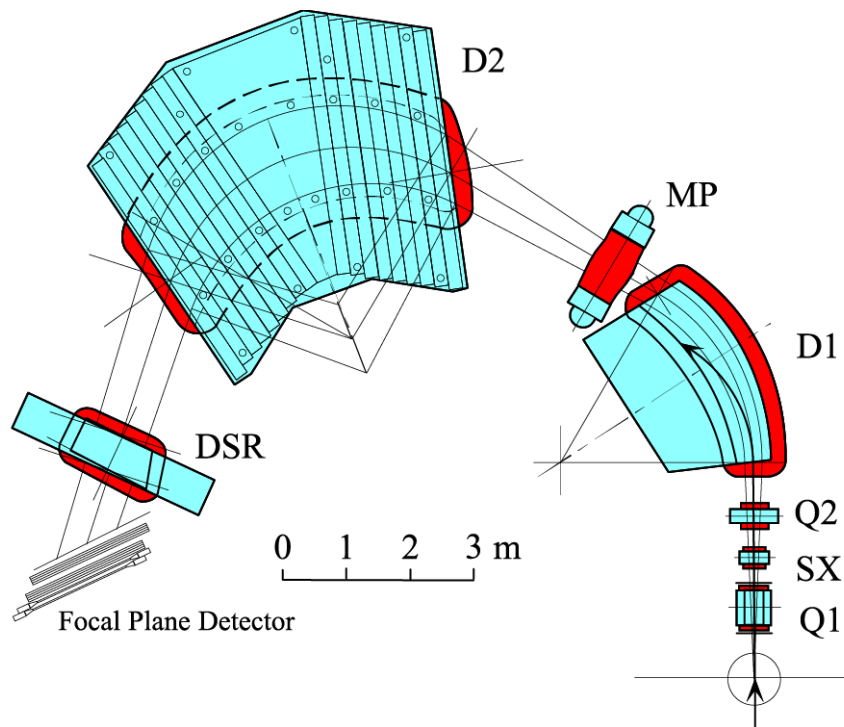
Figure 2.13: Schematic layout of the Grand Raiden spectrometer is shown. It consists of two quadrupoles, one sextuple, one multipole and three dipole magnets [54].

plane detector system.

From ion optics, in the first order the horizontal position of a particle at focal plane (x_{FP}) can be written as:

$$x_{\text{FP}} = < x|\delta > \delta + < x|x > x_0, \tag{2.1}$$

where $\delta = \frac{p-p_0}{p_0}$ is the momentum deviation from center trajectory. $< x|x >$ is the horizontal magnification and $< x|\delta >$ is the momentum dispersion. x_0 is the horizontal position of reaction point at target. Other terms in the first order are designed to be zero for GR. The typical size of beam spot is around 1 mm at the target position. The magnification and dispersion is -0.417 and 15451 mm, respectively. For example, for two particles with δ differs 0.1%, the position difference at the focal plane would be around 15 mm from the first term in Eq. 2.1, while the second term is in the order of sub-millimeter. As a result, the horizontal position is mainly determined by the momentum of the particle:

$$x_{\text{FP}} = < x|\delta > \delta. \tag{2.2}$$

Therefore, we can construct the momentum from the position at the focal plane. In order to obtain the position at the focal plane of GR, two sets of VDCs are used to measure the trajectory of the particles. In addition, two PLs are used to generate the event trigger of DAQ and particle identification.

Table 2.5: Grand Raiden plastic scintillator specifications

Scintillation material	BC408
PMT	HAMAMATSU H1161
Active area	1200 mm×120 mm
Thickness	3 + 10 mm
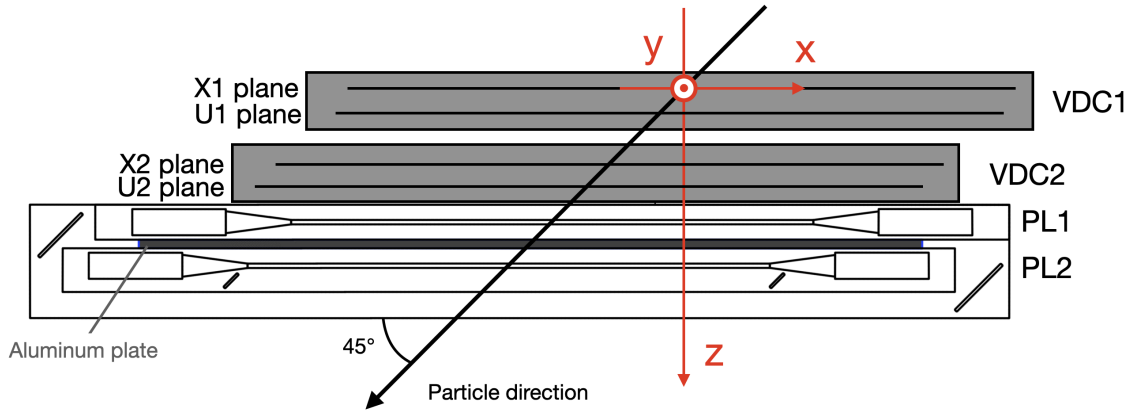
Figure 2.14: A top view of plastic scintillators and vertical drift chambers at GR focal plane is shown.

2.4.1 Plastic Scintillators

Plastic scintillators (PL) with the size of 1200 mm×120 mm and several thickness (1, 3, 5 and 10 mm) are available in WS Course, RCNP. In E552 experiment, we used 3 mm +10 mm combination to detect the deuteron and proton with 392 and 230 MeV incident energies. Table 2.5 shows the specification of PL at GR focal plane.

Figure 2.14 shows a top view of PLs and VDCs at GR focal plane. Photons were collected at left and right PMTs for both PLs. Analogue signals from PMTs were separated into two lines, one was sent to discriminators to generated logic signals and recorded in TDC (time-to-digital converter), another one was sent to QDC (charge-to-digital converter). In present experiment, CAEN V1190 and Mesytec "MQDC-32" were used as TDC and QDC, respectively. By these two lines, timing and energy informations were recorded. The coincidence of logic signals from two PLs were used as the "GR trigger", a part of the event trigger for DAQ, in order to reduce the background. The details of the DAQ logic and electronic circuits are presented in Sec 2.6. Due to the large reaction cross section of p+H scattering and large amount of hydrogen atoms in PL, secondary particle from reaction at PL1 can hit PL2 and cause fake coincidence. To suppress this, an aluminum plate with 10 mm thickness was insert between two PLs in addition. At 230 and 392 MeV incident energies, all particles that we are interested (protons and deuterons) can penetrate both PLs.
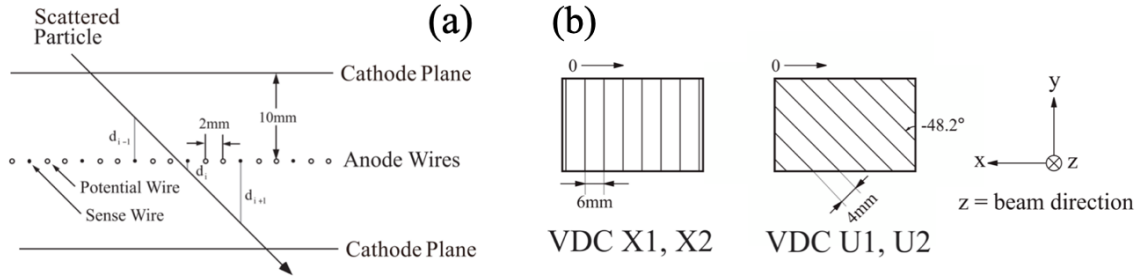
Figure 2.15: Panel (a) shows a schematic view of the X-plane structure of VDCs. Panel (b) shows the wire configuration of two VDCs, as well as the coordinate definition.

Table 2.6: Vertical drift chamber specifications

Wire configuration	X (0°), U (-48.2°)
Active area	1150 mm×120 mm
Number of sense wires	192 (X), 208 (U)
Anode-cathode gap	10 mm
Anode wire spacing	2 mm
Sense wire spacing	6 mm (X), 4 mm (U)
Anode sense wires	$\emptyset$ 20 μm gold-plated beryllium-copper wire
Cathode film	10 μm-thick carbon-aramid film
Applied voltage	-5.4 kV (cathode), -0.3 kV (potential), 0 V (sense)
Gas mixture	Argon (71.4%)+Iso-butane (28.6%)+Iso-propyl-alcohol
Entrance and exit window	12.5 μm aramid film
Digitizer	CAEN V1190

2.4.2 Vertical drift chamber

Two vertical drift chambers (VDCs) are placed at the upstream of PLs parallel as shown in Fig. 2.14. Each VDC consists of two anode wire planes (X and U). Each anode wire plane is sandwiched by two cathode planes, as shown in panel (a) of Fig. 2.15 [34]. Panel (a) in Fig. 2.15 shows a schematic view of the X-plane structure. Two potential wires with 2 mm spacing are placed between every sense wire, in order to keep high electric field around potential wire. High voltage of -5.4 kV and -0.3 kV (relative to sense wires) were applied to the cathode planes and the potential wires, respectively. Panel (b) in Fig. 2.15 shows the wire configuration of VDCs. The spacing between sense wires is 6 mm and 4 mm for X and U plane, respectively. Wires in X-plane are placed vertically, while that in U-plane have a angle of 48.2° to the vertical direction. This configuration helps to obtain the best resolution along horizontal axis, which is critical for momentum reconstruction as discussed above.

Table 2.6 shows a summary of VDC specifications. A mixture gas consisting of argon, iso-butane and iso-propyl-alcohol was filled in VDCs. While argon gas serves as a working gas for electron source, the iso-butane serves as the quencher. In addition, iso-propyl-alcohol is mixed to reduce a gain loss due to aging effect. The electrons
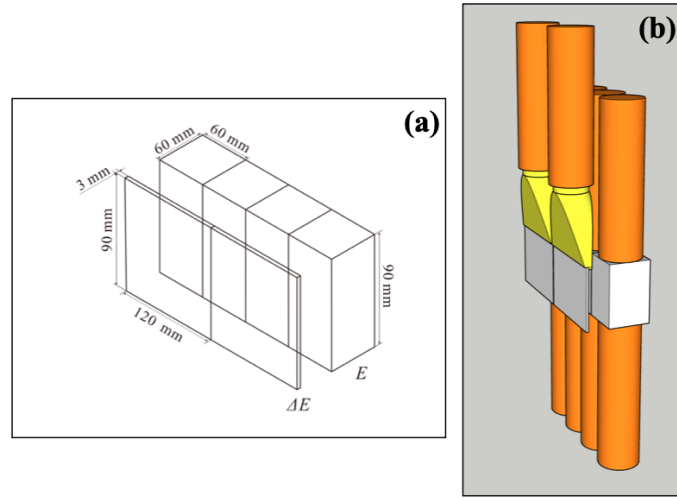
Figure 2.16: A schematic view of HODO is shown. Panel (a) shows the size of scintillation material [34]. Panel (b) shows the schematic view with light guide and PMT.

from the gas are ionized when a charged particle passes through VDC, and drift to the sense wire. Due to electron avalanche, large amount of electrons are produced and collected at the sense wires. After amplified and discriminated, the signal generated was digitized by CAEN V1190 and thus the the hit information was recorded in DAQ. Analysis of VDCs is discussed in Chap. 3.

2.5   Proton hodoscope detector

To measure the backward particles in (p, Nd) reactions ($N = p$ or n), we develop a detector system named "BAckward Nucleon Detector" (BAND), placing around the scattering chamber. BAND consists of a proton hodoscope detector (HODO) and a neutron detector named Beihang-Osaka university Stack Structure Solid organic Scintillator (BOS4). We introduce HODO in this section. Introduction of BOS4 is included in Appendix C.

In E552 experiment we aim at measuring proton with kinetic energy up to around 100 MeV at several backward angles. We use two layers of plastic scintillators to identify proton and determine its energy. Since we measured the proton at several scattering angles, we designed a holder frame system to install BAND onto the rotational base of the Large Acceptance Spectrometer (LAS). In addition, we design a rail system for HODO in order to maximize the covering angular range without any interference with the scattering chamber and other devices in the beam line. We firstly introduce the detector itself in subsection 2.5.1 and then show the holder frame and rail system in subsection 2.5.2.

Table 2.7: HODO specifications

Scintillation material	BC408
PMT type	HAMAMATSU H2431-02T (dE) and H7195 (E)
Size of dE	$120 \times 90 \times 3$ (W×H×T, in mm) × 2 (pieces)
Size of E	$60 \times 90 \times 60$ (W×H×T, in mm) × 4 (blocks)
Total active area	240×90 (mm^2)
Horizontal angular acceptance	$26°$
Total number of readout (PMT)	10

2.5.1 Hodoscope detector

Figure 2.16 shows the schematic view of HODO and Table 2.7 shows a summary of the specifications of HODO, where "W", "H" and "T" denote the width, height and thickness of the detector, respectively. Two segments with a thickness of 3 mm and four segments with a thickness of 60 mm form the dE-E hodoscope for the sake of particle identification. Fish-tail type light guide is used to collect the light from scintillation material to a round shape photo-multiplier tube (PMT) for dE, while the PMTs are glued directly to the scintillation material for E. In order to compensate the position dependence of the obtained pulse height, two readouts are used for E counters. The distance from the target position to the center of dE and counters is 459 and 519 mm, respectively. Each dE and E blocks cover around $\pm 7°$ and $\pm 3.3°$ horizontally.

2.5.2 Holder frame and rail system

For accurate angular measurement and easy operation during beam time, we designed a holder frame system to install BAND on LAS rotational base. Figure 2.17 shows a photo and a schematic view of BAND including the holder frame. HODO was placed close to SC. Two sliding rails enable HODO to move in the red arrow direction, so that the interference with the flange or the "wing" of the scattering chamber can be avoided.

With BAND system installed, the LAS rotation angle has some realistic constraint. Figure 2.18 shows the top view of BAND on LAS in two angular settings as examples. In the case GR was at most forward angle (6.4 degree), BAND went to the most backward angle. HODO was shifted to forward side (center at around 146 degree) to avoid the interference with the "wing" of the scattering chamber. In the case GR was at most backward angle (16.1 degree), BAND went to the most forward angle. HODO was shifted to backward side (center at around 120 degree) to avoid the interference with the flange of the scattering chamber.

2.6 Data acquisition system

In this section, we firstly introduce briefly the whole data acquisition system (DAQ) used in E552 in subsection 2.6.1. Secondly, we introduce the event trigger logic in subsection 2.6.2. Thirdly, we present the circuit diagram of our unique setup, HODO,
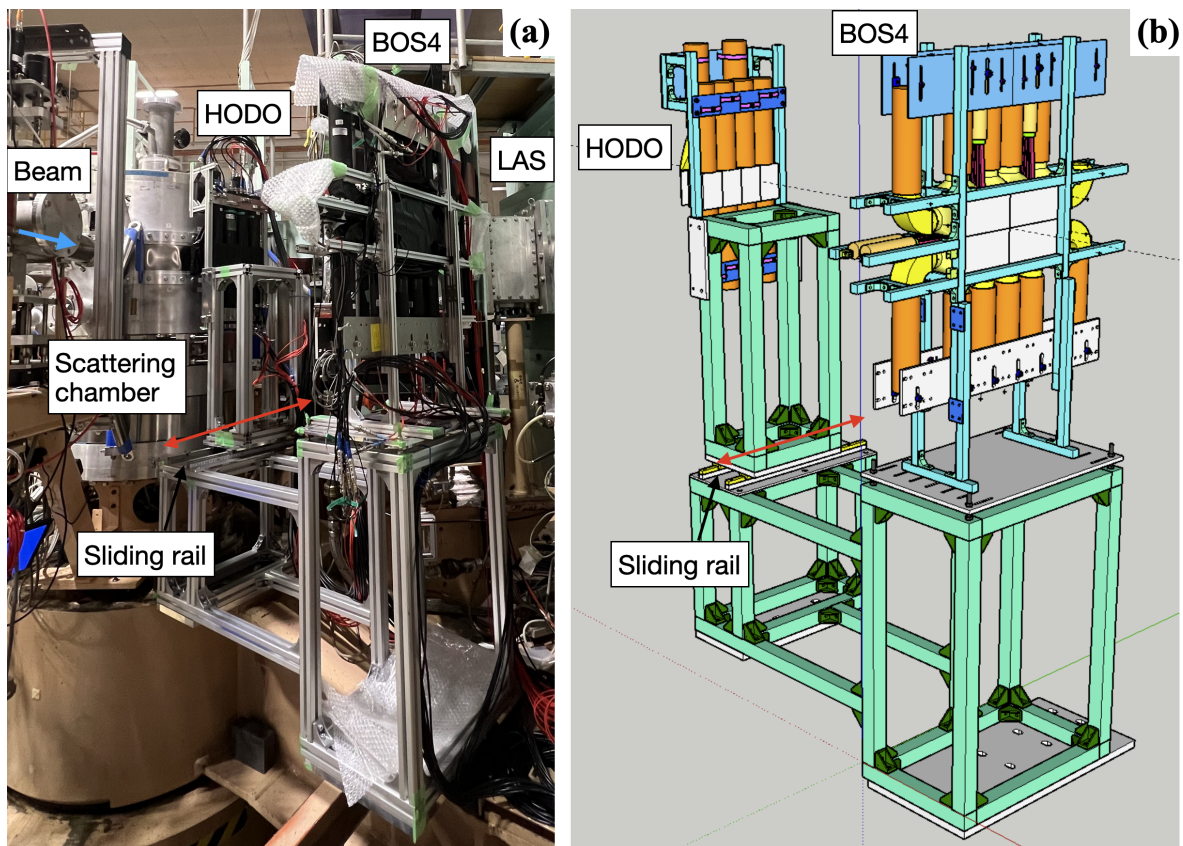
Figure 2.17: A photo and a schematic view of BAND is shown in panel (a) and panel (b), respectively.
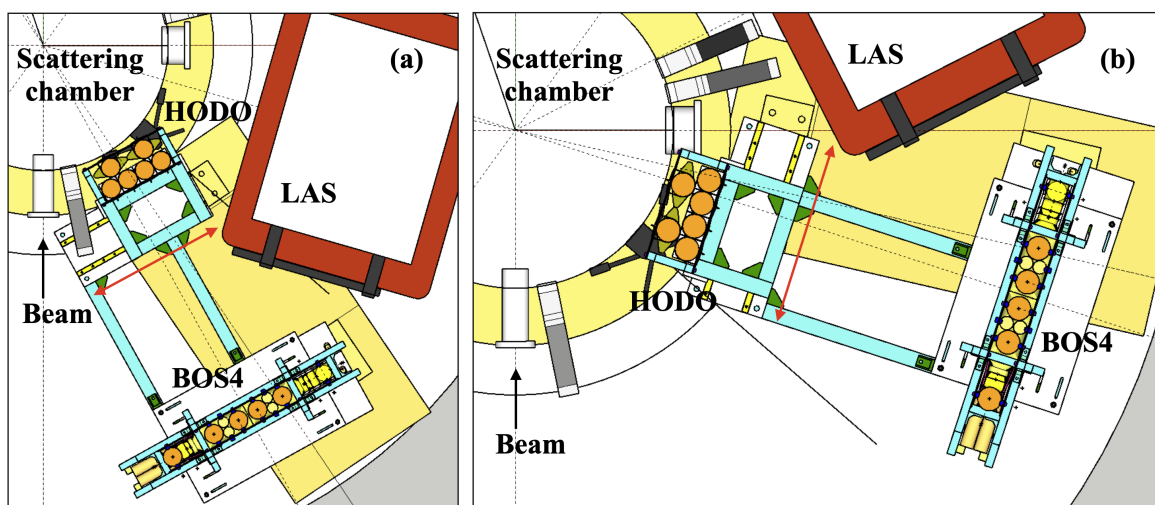
Figure 2.18: The top view of BAND on LAS is shown for HODO center at 146° and 120° in panel (a) and panel (b), respectively.

in subsection 2.6.3.

2.6.1 Introduction

Data acquisition system (DAQ) is used to handle the signal generated in the detector, digitize and save it into a computer. In E552 experiment, two types of signal were generated and recorded: logic signals with timing information and analogue signals with energy information.

For VDCs, the drift time was recorded and then converted into drift length. We analyzed the drift length and reconstructed the particle trajectory via tracking analysis. Combined with GR optics analysis, we obtained the position of the particle at the focal plane and reconstructed the momentum of the particle.

For plastic scintillators at GR focal plane and near scattering chamber, the analogue signal from each PMT was divided into two lines: one was fed into the discriminator to generate the logic signal, which contained the timing information and was used for event trigger, discussed in subsection 2.6.2; another one was recorded by QDC (charge-to-digital converter) or ADC (analogue-to-digital converter) and analyzed to obtain energy information. The timing information was used to obtain the time of flight of the particle. With the energy information and the time of flight, the particle was identified.

In addition, we obtained the angular information from the geometry of the detector and spectrometer. With particle identification of forward deuterons and backward protons, together with their energy and angular information, we reconstructed the missing mass spectrum of (p, pd) reactions.

In parallel, scaler information of Beam Line Polarimeters (BLP) and Faraday cup was also recorded and used to obtain the beam charge. Combining the number of detected events, efficiencies, target thickness and beam charge, we evaluated the triple differential cross section.

The DAQ in WS Course was under development for a faster speed of data transfer. Originally a FERA based system was used and now a VME based system is under development. In order to confirm the newly build system, both FERA and VME system were used simultaneously during E552 for commissioning purpose. The comparison between two system was used to confirm the validity of the new system. During E552, event mismatch happened sometimes. Those events were excluded in present analysis and detail discussion is not included in this thesis.

2.6.2 Event trigger logic

In E552, we aim at measuring the forward going deuterons (by GR) and backward going protons or neutrons (by BAND) in coincidence. Because the coincident rate of interested channel is low compared with the counting rate in each detector and the data processing speed of DAQ is limited, it is desirable to use the event trigger system to increase the DAQ efficiency of coincidence measurement. In this subsection we present the event trigger logic in E552. Firstly we introduce briefly the trigger logic for particles going to GR.
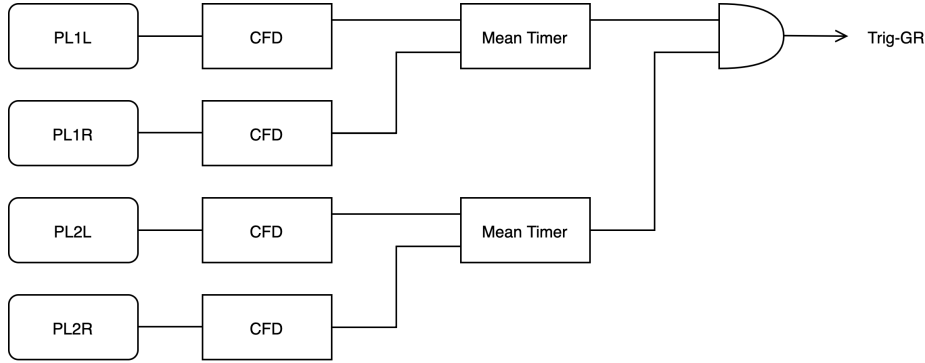
Figure 2.19: The trigger logic for particles going to GR is shown.

Figure 2.19 shows the trigger logic for particles going to GR. "PL1L" to "PL1R" represent the signal from left and right PMT of GR PL1, respectively (similar for "PL2L" and "PL2R"). The signal was fed into a Constant Fraction Discriminator (CFD) and then sent to a Mean Timer. The mean time of left and right PMT helps to reduce the position dependence in the timing as well as reduce the electronic noise in single PMT. The coincidence of the mean time of PL1 and PL2 was used as the trigger for particles going to GR, named as "Trig-GR".

Figure 2.20 shows the BAND trigger logic. Only HODO part is discussed explicitly, and BOS4 part is omitted. "E1" to "E4" denote the signals from different E counters. "U" and "D" denote the signals from the PMTs of the E counter at upper and lower side, respectively. "dE1" and "dE2" denote the single from the dE detectors. The signal of each PMT was fed to a leading edge discriminator and then for pair PMTs the coincidence was required. After that the "OR" of logic signal of each detector (including BOS4) was used as BAND trigger, denoted as "Trig-BAND".

The trigger mode of WS DAQ was selected depending on the measurement. In a singlet measurement using only GR (such as proton elastic scattering), "GR single mode" was used where only "Trig-GR" can be accepted by DAQ. In a coincidence measurement (such as (p, pd) reactions), the coincident mode was used.

Figure 2.21 shows the trigger logic of coincident mode of GR DAQ. In the coincident mode, the coincidence of "Trig-GR" and "Trig-BAND" was checked in the highest priority. While DAQ is ready for data processing, if a coincident trigger comes, DAQ will process the data as a "COIN event". If no coincident trigger comes, but only Trig-GR (or Trig-BAND) comes, DAQ will process the data for every n-th (or m-th) events, as a GR single (or BAND single). An event register was used to record the source of each event.

The sampling rate (m and n) was decided based on the counting rate of different trigger, which depended on the beam intensity and the target thickness.

2.6.3 Circuit of proton detector

In the E552 experiment, we detected backward protons by the unique detector, HODO. We present the circuit diagram of HODO part in the following sections. Figure 2.22 shows the circuit diagram of HODO.
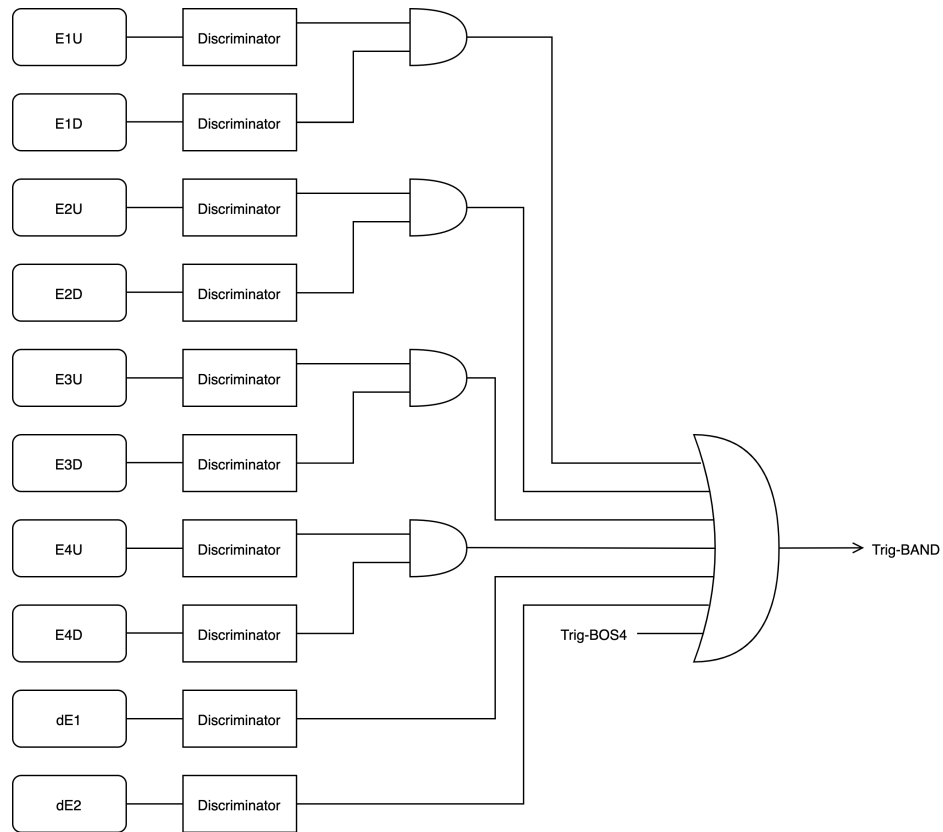
Figure 2.20: The trigger logic for particles going to BAND is shown.
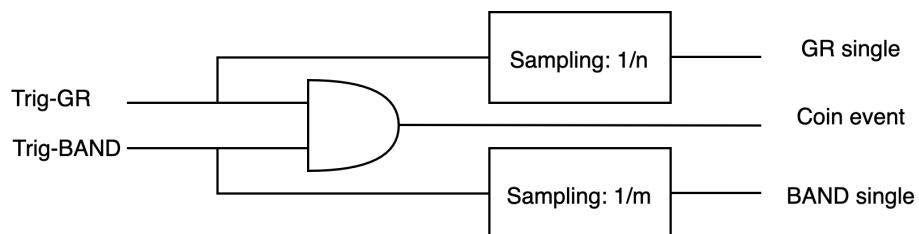
Figure 2.21: The trigger logic of the coincident mode of GR DAQ is shown.
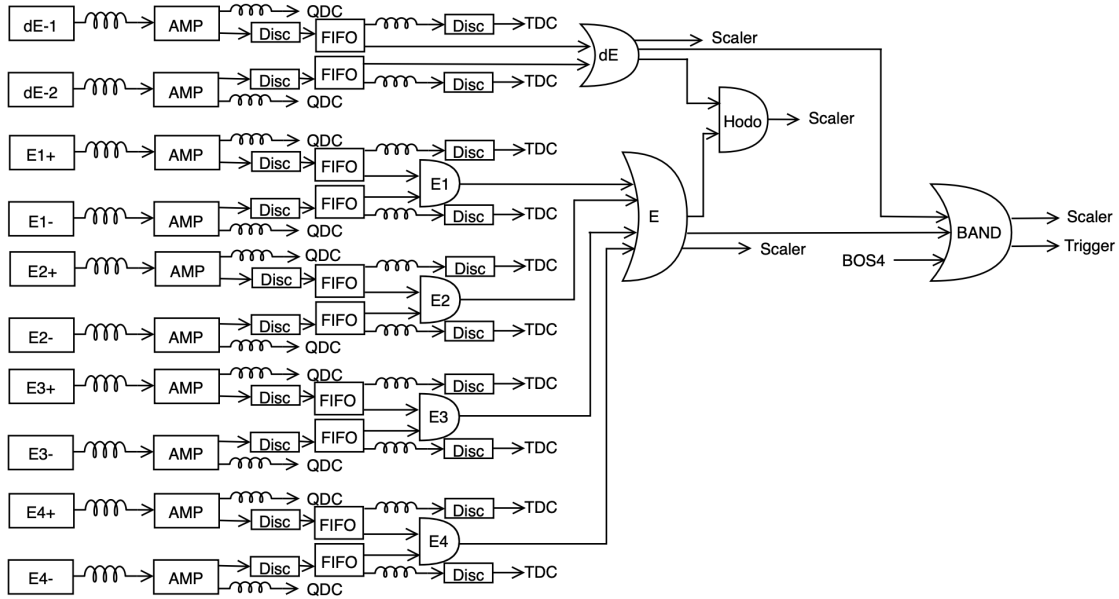
Figure 2.22: The circuit diagram of HODO is shown. "dE-1", "dE-2", "E1+" and etc. denote the signals from each PMT. "+" and "-" denote the upper and lower PMT of a E block, respectively. "AMP", "Disc"and "FIFO" denote amplifier, discriminator and Fan-In-Fan-Out modules, respectively.

Anode outputs of each PMT was sent to the "amplifier" (AMP) to increase the signal to noise ratio. After that, one output of the AMP was sent to QDC (charge-to-digital converter). In E552 we used "Mesytec MQDC32". Another output was sent to a discriminator to generated a logic signal. For a detector with two readouts (E blocks), the coincidence of both readout was required. The logic signal of all detectors were sent to TDC (time-to-digital converter), ("CAEN V1190" in E552). The "OR" was made from all backward detectors (including BOS4) and used as "BAND trigger". In addition, the logic signals of "dE", "E", "HODO" and "BAND" were sent to a "scaler" module.

2.7   Summary of measurement

Table 2.8 shows the data summary of E552 experiment. The first column shows the incident beam energy (T_{b}). The second and third columns show the deuteron and proton scattering angles, respectively. The first and second values show the center angle and coverage, respectively. The momentum of the central trajectory (P_{GR}) is shown in the fourth column in the table. GR has momentum acceptance around 5%, thus the coverage is roughly ±2.5%. In each angular settings, several magnetic rigidity settings of GR were used to cover whole deuteron momentum range. The largest P_{GR} cover the region of (p, d) low-lying states, which helps in the calibration of GR spectrometer and detectors. We distributed most of the time to perform measurement in the region with the highest cross section at certain angular setting, which was near the recoilless condition, while for other region we measured shortly to determine the

Table 2.8: Data summary

T_{b} [MeV]	θ_d [°]	θ_p [°]	P_{GR} [MeV/c]	Time [hour]
392	6.4±1	146.0±13	1225	0.5
			1187	1.4
			1143	1.7
			1095	1.6
	16.1±1	120.5±13	1209	0.1
			1195	0.5
			1149	2.0
			1102	2.0
			1053	1.0
			991	0.3
230	6.4±1	146.0±13	909	0.3
			875	1.6
			840	3.5
			806	4.3
			768	0.6
	8.7±1	136.7±13	909	0.6
			875	0.7
			840	2.7
			806	2.3
			768	0.2
	15.0±1	123.4±13	908	0.2
			877	0.2
			845	0.2
			811	3.0
			778	2.3
			744	0.2
	16.1±1	120.5±13	908	0.2
			877	0.2
			845	0.2
			811	1.2
			778	2.2
			744	0.2

tail component.

Reference measurement with other targets is not included in the table. In total, we run E552 experiment for 4.5 days with 392 MeV proton beam and 6 days with 230 MeV proton beam, including commissioning.

Chapter 3

Data Analysis

We present the data analysis of (p, pd) channel in E552 experiment in this chapter. We measured $^{16}\mathrm{O}(p, pd)^{14}\mathrm{N}$ reactions at two incident energies, 230 and 392 MeV, and measured deuterons and protons in coincidence at several angular settings. There are two main goals of data analysis: one is to obtain the excitation energy spectra of $^{16}\mathrm{O}(p, pd)^{14}\mathrm{N}$ reactions; another is to evaluate the triple differential cross section of reaction populating to the second excited state of $^{14}\mathrm{N}$ ($E_{\mathrm{ex}} = 3.9$ MeV, $J^{\pi} = 1^{+}$).

From the energies and scattering angles of deuterons and protons, we constructed the excitation energy spectrum of $^{14}\mathrm{N}$ via missing mass method. We present the energy analysis for forward and backward particles in Sec. 3.1 and 3.2, respectively. At the end of Sec. 3.2, we present the summary of excitation energy spectra of $^{16}\mathrm{O}(p, pd)^{14}\mathrm{N}$.

From the scaler data, we evaluated beam charge, several efficiencies and so on. After that we present the triple differential cross section. The scaler analysis is presented in Sec. 3.3 and the summary of triple differential cross section is presented at the end.

3.1 Grand Raiden analysis

We present the analysis for forward going particles detected via Grand Raiden (GR) spectrometer in this section. There are two main species of particles detected by GR in E552 experiment: proton from elastic scattering and deuteron from (p, d) reactions. Firstly we present the particle identification using dE-TOF method in subsection 3.1.1. Secondly we present the tracking and optics analysis for GR in subsection 3.1.2 and 3.1.3, aiming to obtain the position at the focal plane and scattering angle after the target, from the VDC tracking information. Thirdly, we used the position of the particle at the focal plane to construct the momentum and discuss the calibration in subsection 3.1.4. After that we present the excitation energy spectra of (p, d) reactions at several targets and discuss the performance of GR energy analysis in subsection 3.1.5. At the end we discuss the beam energy fluctuation with time in subsection 3.1.6.

3.1.1 Particle identification

In present experiment, all protons and deuterons pass through both layers of GR focal plane plastic scintillators. Based on the Bethe-Bloch formula, the energy deposition

of a charged particle in scintillators is approximately proportional to the square of its charge and inversely proportional to the square of velocity. In addition, the time-of-flight (TOF) of a particle in certain path is inversely proportional to its velocity. Note that GR has a momentum acceptance of 5%, certain momentum of particles were selected by GR. Therefore, from dE-TOF two dimensional plot, we can separate different particles (in E552, mainly proton, deuteron and triton) with different mass and velocities.

In this subsection we present the particle identification (PI) for particles detected via GR by dE-TOF method. We firstly performed a correction on the charge of GR plastic scintillators (PLs), to reduce the position dependence.

Panel (a) and (d) in Fig. 3.1 shows the charge distributions of the left and right PMT of GR PL1 and PL2, respectively. Due to the attenuation in scintillator, the light collected by the PMT depends on the position of the particle path. Conventionally the total charge of a plastic scintillator is obtained from the geometrical average of two ends, to minimize the position dependence:

$$Q_{\mathrm{PL1}} = \sqrt{Q_{\mathrm{PL1L}} \times Q_{\mathrm{PL1R}}} \ , \tag{3.1}$$

$$Q_{\mathrm{PL2}} = \sqrt{Q_{\mathrm{PL2L}} \times Q_{\mathrm{PL2R}}} \ , \tag{3.2}$$

where Q_{PL1L}, Q_{PL1R}, Q_{PL2L} and Q_{PL2R} are the charge of left and right PMT of PL1 and PL2, recorded in QDC (charge-to-digital converter). The pedestal has been subtracted. Panel (b) and (e) in Fig. 3.1 show the charge and position distributions of GR PL1 and PL2, respectively. The horizontal axis is the timing difference between the left and the right PMT, showing the horizontal position of the particle path at PL. Because the scintillator is long, the geometrical average of charge still depends on the position. Correction with a quadratic function was applied to remove the position dependence. Panel (c) and (f) in Fig. 3.1 show the corrected charge and position distributions. Compared with that in panel (b) and (e), the correlation in panel (c) and (f) is smaller. Even though we still see remaining correlation at the corner, we ignored them at this moment because the efficiency of VDC tracking is bad at that region and we restrict the analysis in certain range where the corner is not included (discussed in subsection 3.3.2).

Panel (a) and (b) in Fig. 3.2 show the charge (Q) and the time-of-flight (TOF_{GR}) distributions of PL1 and PL2, where the TOF_{GR} is the timing difference between the ring frequency signal (RF) timing (T_{RF}) and GR trigger (Trig-GR) timing ($T_{\mathrm{Trig\text{-}GR}}$). When a Trig-GR was accepted by data acquisition system (DAQ), it was used as the common stop in the TDC (time-to-digital-convertor) and the timing of Trig-GR was also recorded in the TDC. Therefore, from the timing difference between RF and Trig-GR, we obtained the time-of-flight of the particle from target to GR PL (with an unknown but fixed offset):

$$TOF_{\mathrm{GR}} = T_{\mathrm{RF}} - T_{\mathrm{Trig\text{-}GR}} \ . \tag{3.3}$$

The selection of deuterons are shown in red squares in panel (a) and (b). Because Q is related with the energy deposition of particles in PL and TOF is related with the time of flight of particles from the target position to PLs, we call this method
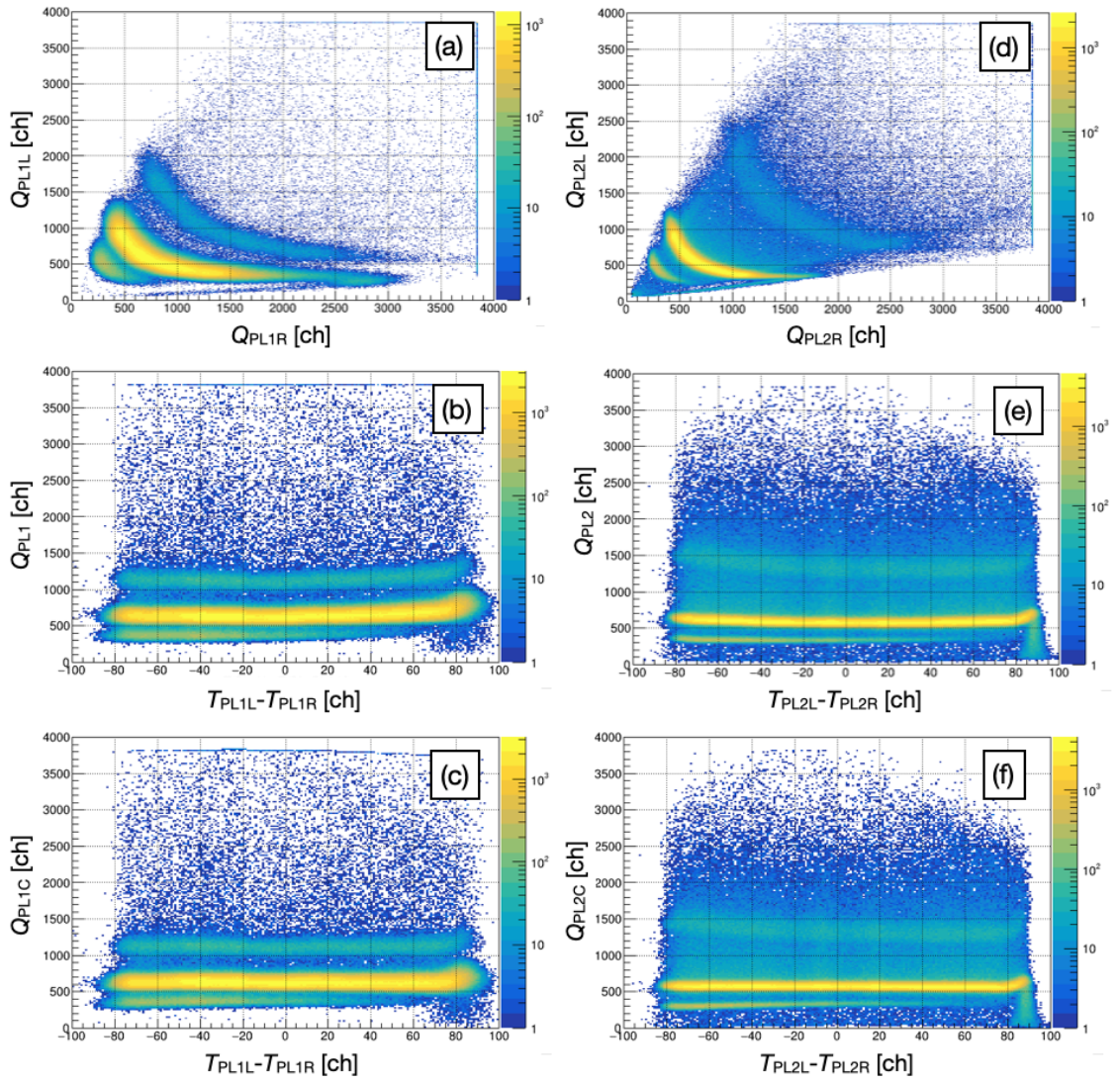
Figure 3.1: Panel (a) shows the charge distributions of the left and right PMTs of GR PL1; Panel (b) shows the charge and position distribution of PL1; Panel (c) shows the corrected charge and position distribution of PL1; Panel (d), (e) and (f) are figures for GR PL2 with the same definition.
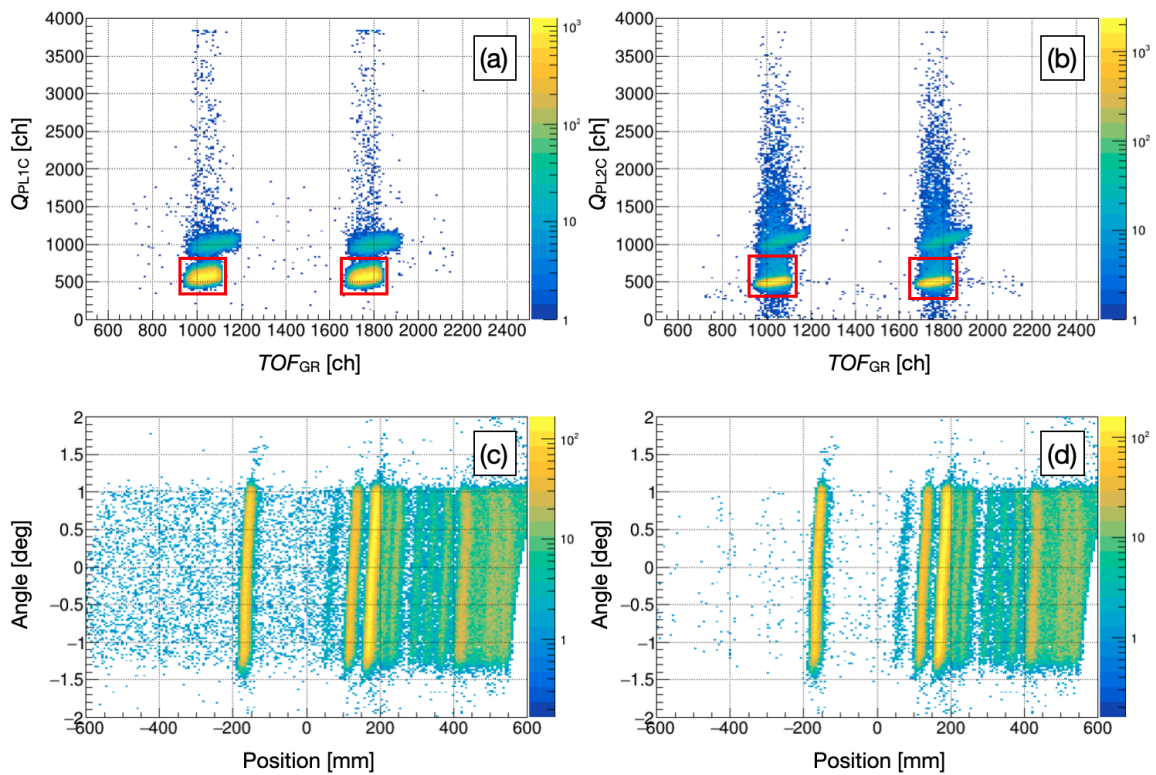
Figure 3.2: Panel (a) and (b) show the charge and time-of-flight distributions of PL1 and PL2, respectively. The red squares represent the PI selection (for deuterons). Panel (c) and (d) show the angle and position distributions at GR focal plane before and after applying PI selection, respectively.
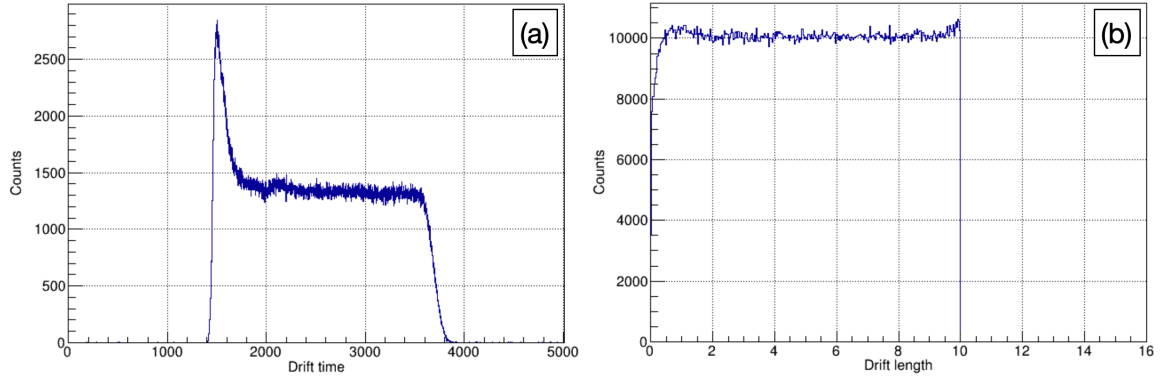
Figure 3.3: Panel (a) shows the drift time distribution of X1 plane. Panel (b) shows the drift length converted from drift time.

as dE-TOF PI method. Because the RF signal was down-scaled by a factor two, we observed two bunches of RF timing. The "OR" of two squares in panel (a) were used as the particle identification (PI) condition in dE-TOF of PL1, denoted as "PI_1" and similarly in panel (b) for PL2, denoted as "PI_2". The "AND" of PI_1 and PI_2 was used as deuteron PI, denoted as "PI_d".

Panel (c) in Fig. 3.2 shows the angle and position distribution (from VDC tracking and after optics correction, discussed in subsection 3.1.3) at GR focal plane before applying PI_d with thin ice target as an example. Position at the focal plane is linearly related to the momentum of deuteron. Thus different lines represent different final states of $^{16}O(p,d)^{15}O$ reactions. Large amount of background can be seen between discrete lines. As a comparison, after applying PI_d, as shown in panel (d), the remaining background is much less, indicating most of the background were removed by the PI selection.

In short, we performed PI for protons and deuterons detected via GR by dE-TOF method for PL1 and PL2 separately and the "AND" of two PI conditions was used as the PI for protons or deuterons.

3.1.2 Tracking analysis

Forward particle is momentum-analyzed by GR in a dispersive mode, where the position at the focal plane depends on the momentum deviation from the central trajectory. Two VDCs were used to construct the particle trajectory. The drift time of electrons to sense wires was recorded in TDC and converted into drift length.

Figure 3.3 shows the drift time and drift length distribution of X1 plane as an example. Because the gradient of the electric field is steep near the sense wires, the drift velocity of electrons changes drastically there, as can be seen in panel (a) that there is a shape peak. The drift length was converted from the drift time by polynomial functions, and a uniform drift-length distribution was obtained as shown in panel (b).

With the drift length of each plane, the hit position at each plane was calculated. With "X" and "U" position at two VDCs, the "X track" and "U track" were obtained by assuming a straight line. Figure 3.4 shows the principle of tracking analysis. X
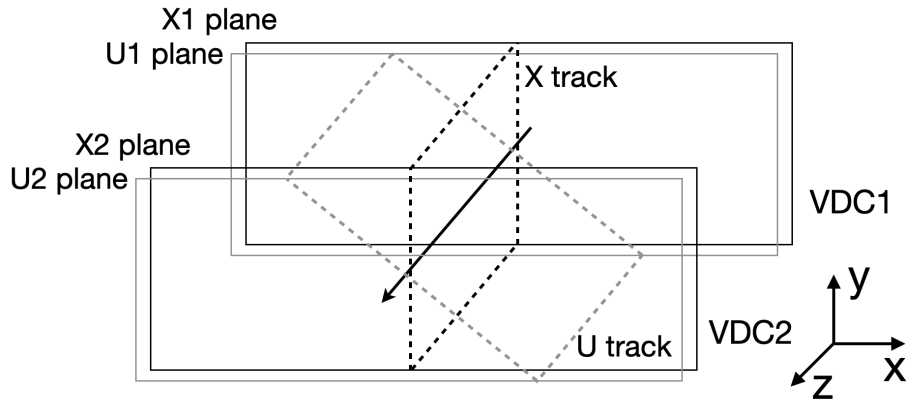
Figure 3.4: Panel (a) shows the drift time distribution of X1 plane. Panel (b) shows the drift length converted from drift time.
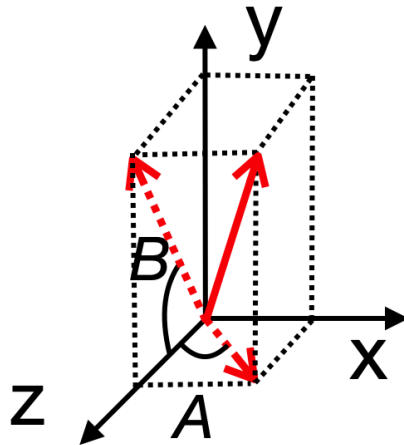
Figure 3.5: The coordinate for particles detected at GR focal plane is shown. A and B represents the horizontal angle and vertical angle, respectively.

planes and U planes are shown by black and grey frames, respectively. "X track" and "U track" are illustrated by black and grey dashed frames, respectively. With the "X track" and "U track", we determined the particle trajectory. The tracking analysis was performed using an analyzer developed by Dr. Furuno [55].

From the trajectory we obtained horizontal and vertical position of the particle. Horizontal and vertical angles were also obtained from the derivative of horizontal and vertical position to z-position, respectively. Figure 3.5 shows the definition of the coordinate. Red solid arrow represents the direction of a particle as an example. Two red dash arrows represent the projections to z-x and z-y plane and the derivatives to z-axis are defined as horizontal (A) and vertical angle (B), respectively.
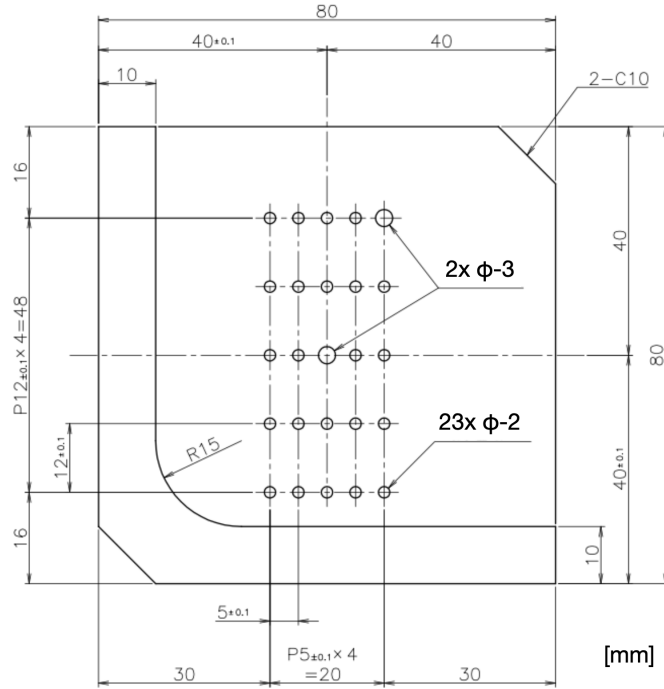
Figure 3.6: Figure shows the schematic view of the sieve slit used in E552 experiment.

3.1.3 Optics analysis

From the trajectory we performed optics analysis aiming to obtain the scattering angle after reaction at the target position and the momentum of the particle. As we shown in Eq. 2.2, horizontal position at the focal plane depends linearly on the momentum deviation δ. However, due to higher-order effects, it is also related on the angle and position at target. In addition, the angle measured at focal plane is not only depends on the scattering angle after target but also coupled with momentum and thus position. It is found that the correlation between horizontal variables (X and A) and vertical variables (Y and B) was negligible in present data, so we present the analysis for horizontal variables only.

To simplify, we started from the obtained observables from VDC tracking analysis, mainly X and A, and performed phenomenological optics correction to obtain x_{FP} and A_{TA} (horizontal angle at the target), where we assume the position at the focal plane x_{FP} depends only on momentum deviation after optics correction.

We used the data of proton elastic scattering on carbon target with a sieve slit at the entrance of GR to perform optics correction and present in following part. Figure 3.6 shows the schematic view of the sieve slit used in E552 experiment. In total 25 holes were prepared on an aluminum plate with a thickness of 5 mm. The angle spacing in horizontal and vertical direction is 0.5 and 1.2 degree, respectively, calculated from the geometry.

Figure 3.7 shows the horizontal angle position distribution of a run with proton elastic scattering on carbon target with the sieve slit, as an example. We started from A_1 and X_1, where A_1 is the horizontal angle at GR focal plane and X_1 is the horizontal
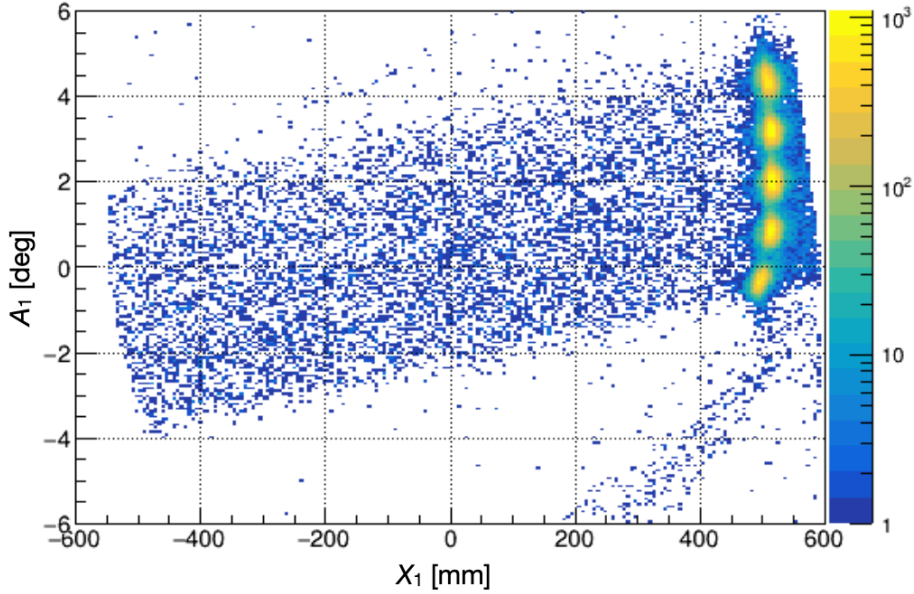
Figure 3.7: Angle and position distributions of p+C elastics scattering data with the sieve slit are shown.

position at X1 plane of VDC1. The data were taken at 15° of GR center. The scattering angle difference of different holes in the sieve slit was negligibly small, compared with the angle of GR center, which means the scattering angle after target was very close to the angle of GR center (see Eq. 3.13 for details). Therefore, for certain incident energy and GR center angle, the elastic scattered protons have identical momentum. As shown in Fig. 3.7, we see five clusters with similar X_1, which means the momentum of protons in these five clusters are similar. Five clusters have different A_1, which is due to five rows of holes in the sieve slit.

During the experiment, we adjusted the magnetic setting of GR to scan the elastic scattered protons in the whole momentum acceptance. We selected the elastic scattering region in each run (for example, $400 \leq X_1 \leq 600$ mm region for data in Fig. 3.7) and merged the data. Figure 3.8 shows the horizontal angle and position distribution of the merged data of p+C elastic scattering with the sieve slit at 230 MeV (a-e) and 392 MeV incident energy (f).

Panel (a) shows the "raw" distribution without optics correction, as the starting point of optics correction. Six rows show six runs with slightly different magnetic settings of GR, and five clusters in each row show particles passing through holes with different horizontal angles at sieve slit with a space of 0.5 degree. The phenomenological optics correction is summarized in following equations:

$$A_2 = (P_1^{\text{opt}} + P_2^{\text{opt}} \times X_1) \times A_1 \, , \tag{3.4}$$

$$A_3 = A_2 - (P_3^{\text{opt}} + P_4^{\text{opt}} \times X_1) \, , \tag{3.5}$$

$$X_2 = X_1 + (P_5^{\text{opt}} + P_6^{\text{opt}} \times X_1) \times A_3 + P_7^{\text{opt}} \times A_3^2 \, , \tag{3.6}$$

$$X_3 = X_2 + P_8^{\text{opt}} \times A_3 \, , \tag{3.7}$$
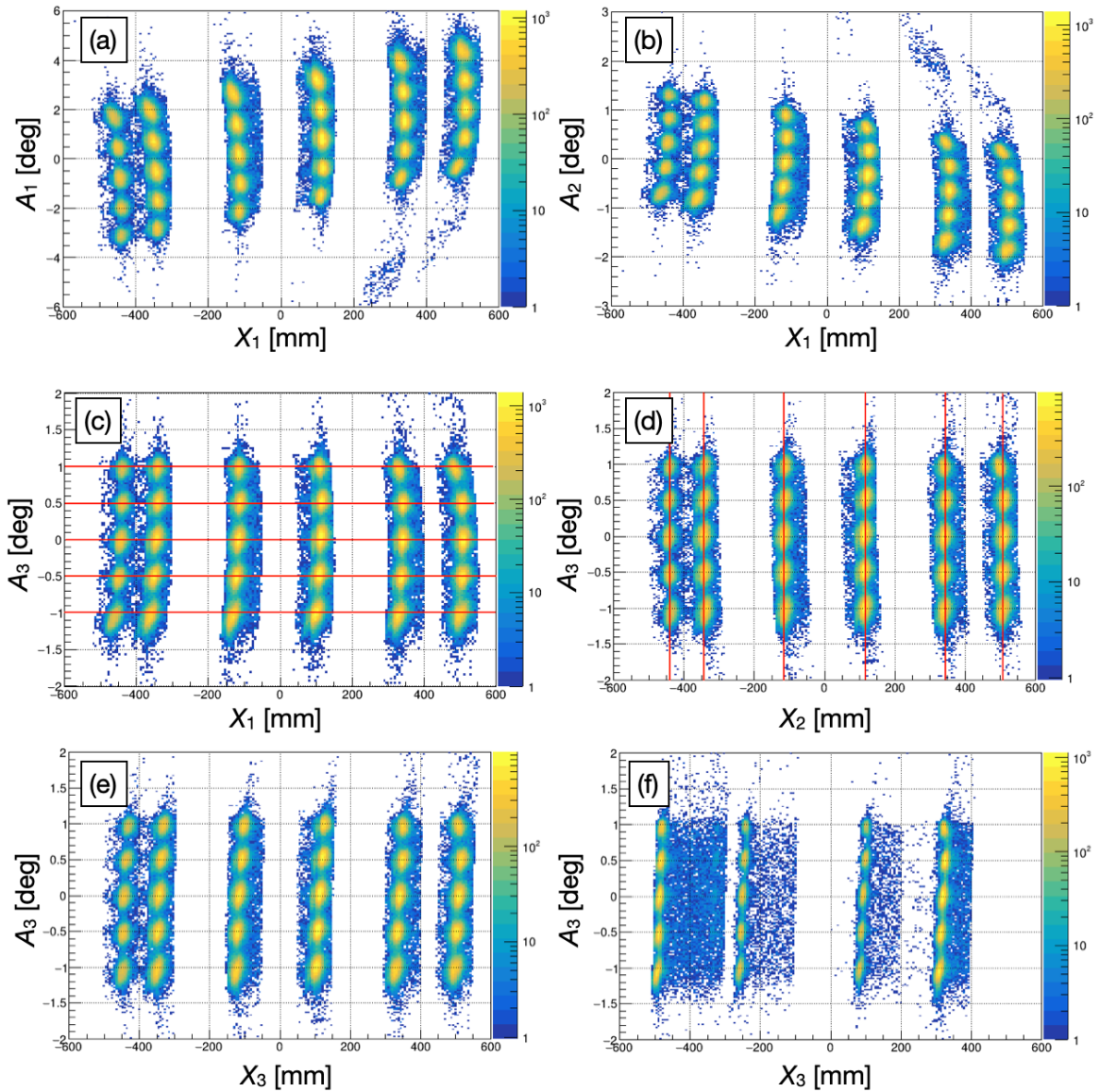
Figure 3.8: Horizontal angle and position distributions are shown for proton elastic scattering data with carbon target and the sieve slit. Panel (a-e) show the distributions at different steps of data at 230 MeV incident energy. Panel (f) shows the distributions at the final step of data at 392 MeV incident energy.

Before the optics correction, fitting with a gaussian function was performed for each run and each cluster, and the center value of angle and position was obtained.

Optics correction step 1

Firstly, we corrected the magnification term ($<a|a>$ in conventional optics matrix element). The averaged angle spacing (ΔA_{run}) was calculated for each run and a factor (M_{run}) was used to corrected the observed spacing to the spacing of the sieve slit ($0.5°$):

$$M_{\mathrm{run}} = -0.5/\Delta A_{\mathrm{run}} , \tag{3.8}$$
$$A_2 = M_{\mathrm{run}} \times A_1 . \tag{3.9}$$

From the design of GR and previous analysis of experimental data at GR, the angle magnification of GR is negative, which is also confirmed by present data. Therefore, a negative sign appears in Eq. 3.8. It is found that this factor has a linear position dependence ($M = M(X_1)$). Two parameter P_1^{opt} and P_2^{opt} were assumed and obtained from linear fitting ($M = P_1^{\mathrm{opt}} + P_2^{\mathrm{opt}} \times X_1$) on factor position correlation. Therefore, the first step in optics correction is shown in Eq. 3.4. Here P_1^{opt} can be regarded as the first order matrix element, $<a|a>$ (angle magnification), while P_2^{opt} can be considered as the second order $<a|ax>$ term. As a result, panel (b) of Fig. 3.8 shows the A_2 and X_1 distributions, where the angle spacing of each cluster becomes 0.5 degree.

Optics correction step 2

In the second step, we aligned the center clusters in each run. In panel (b) of Fig. 3.8, a linear correlation between A_2 and X_1 can be seen for center clusters. Parameter P_3^{opt} and P_4^{opt} was assumed and obtained from the linear fitting:

$$A_2 = P_3^{\mathrm{opt}} + P_4^{\mathrm{opt}} \times X_1 , \tag{3.10}$$

where A_2 and X_1 is the center from gaussian fitting for center clusters. Therefore, in the second step we corrected the angle with Eq. 3.5. As a result, shown in panel (c) of Fig. 3.8, five holes of each magnetic setting are align at the angle of holes at sieve slit ($0, \pm0.5$ and ±1 degree), as shown by the red lines for reference. Up here, the angle (A_3) is now independent with the position. Here, P_3^{opt} can be regarded as the angle offset, which may come from the VDC alignment or analyzer definition. P_4^{opt} is the first order $<a|x>$ term (ignoring the sign).

Optics correction step 3

In the third step, the angle dependence of the position was corrected. As shown in panel (c) of Fig. 3.8, we see clear correlation between position and angle at least up to the second order. A quadratic function was used to fit the position angle correlation ($X_1 = P_0^{XA} + P_1^{XA} \times A_3 + P_2^{XA} \times A_3^2$), and parameters P_1^{XA} and P_2^{XA} obtained from the quadratic fitting were found to have a correlation with position itself ($P_1^{XA} = P_1^{XA}(X_1)$ and $P_2^{XA} = P_2^{XA}(X_1)$), which implies the necessity of including higher order correction. Therefore, a position dependence of P_1^{XA} was included, and the parameters P_5^{opt} and
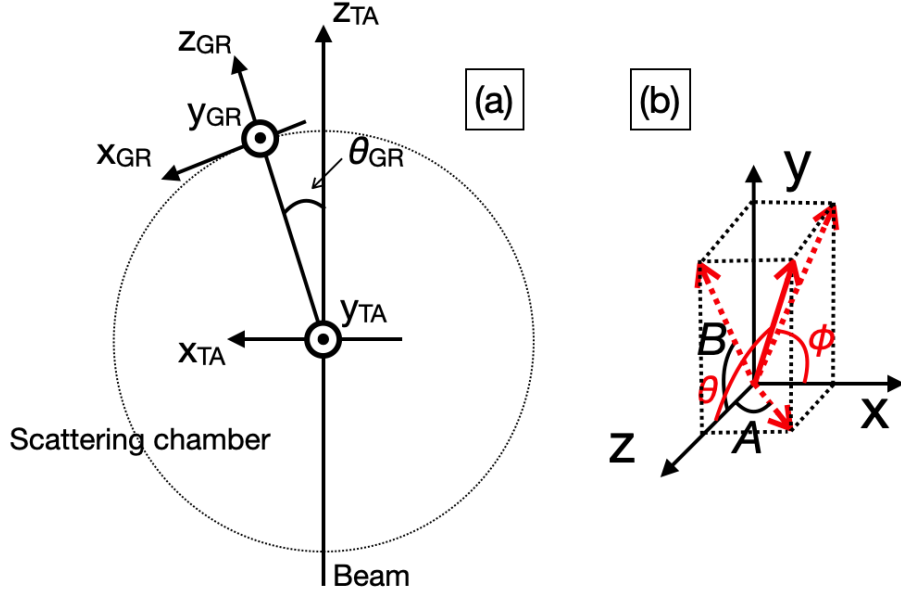
Figure 3.9: Panel (a) shows the definition of the coordinate at the entrance of GR and at the target position. Panel (b) shows the relationship of horizontal and vertical angle A and B with polar and azimuthal angle θ and ϕ.

P_6^{opt} were assumed and obtained from the linear fitting of P_1^{XA} versus position:

$$P_1^{XA} = P_5^{\text{opt}} + P_6^{\text{opt}} \times X_1 \ . \tag{3.11}$$

Because we restricted the correction up to the second order, we didn't include the position dependence of P_2^{XA}. Thus the average of P_2^{XA} was used as P_7^{opt} simply. As a result, we applied the correction in the third step with Eq. 3.6. Here P_5^{opt}, P_6^{opt} and P_7^{opt} corresponds to $< x|a >$, $< x|ax >$ and $< x|aa >$ term, respectively. As a result, panel (d) in Fig. 3.8 shows the distributions after the third step correction. Vertical straight lines are shown (as red lines) as references to confirm that there are no angle dependence of position remaining after correction.

Optics correction step 4

Figure 3.9 shows the definition of the coordinate at GR entrance and target position and the relationship between horizontal angle A, vertical angle B and polar angle θ, azimuthal angle ϕ. For the coordinate at target, the z direction is defined by beam direction and x-axis is along horizontal direction and points to GR side. Then y-axis is in vertical direction and points up. The coordinate at the GR entrance is rotated from the coordinate at target with y-axis to anti-clock direction, with θ_{GR} (the center angle of GR). Panel (b) is the geometrical relationship between A, B and θ, ϕ in polar coordinate.

We consider that after optics correction, A_3 represents the horizontal angle at the entrance of GR, thus we can obtain the horizontal angle at target by:

$$A_{\text{TA}} = \theta_{\text{GR}} + A_3 \ . \tag{3.12}$$

Vertical angle B is calibrated roughly by linear function and we simply have $B_{\mathrm{TA}} = B_{\mathrm{GR}}$. From panel (b) of Fig. 3.9, we obtain:

$$\theta_{\mathrm{TA}} = \arctan(\sqrt{(\tan A_{\mathrm{TA}})^2 + (\tan B_{\mathrm{TA}})^2}) \ , \tag{3.13}$$

$$\phi_{\mathrm{TA}} = \arctan(\frac{\tan B_{\mathrm{TA}}}{\tan A_{\mathrm{TA}}}) \ . \tag{3.14}$$

At certain angle of GR center (for example $\theta_{\mathrm{GR}} = 15°$), B_{TA} is much smaller than A_{TA}. Therefore, simply we have $\theta_{\mathrm{TA}} \approx A_{\mathrm{TA}}$ and $\phi_{\mathrm{TA}} \approx 0$.

From the kinematics, the momentum of proton after elastic scattering depends on the scattering angle $\theta_{\mathrm{TA}} \approx A_{\mathrm{TA}} = \theta_{\mathrm{GR}} + A_3$. Therefore, if the position after correction (X_3) depends only on the momentum of the particle, the relation with A_3 should remain. Therefore, the correlation between A_3 and X_2 was added back by the parameter P_8^{opt}, which was obtained from kinematic calculation and X_3 was obtained by Eq. 3.7. As a result, panel (e) in Fig. 3.8 shows the final distributions of A_3 and X_3) for proton elastic scattering data on carbon target with the sieve slit at 230 MeV.

Similar procedures were applied to obtain parameters for the data at 392 MeV, as the final distributions shown in panel (f) in Fig. 3.8. It was found that optics correction parameters (P_i^{opt}, $i = 0 \sim 7$) for data at 230 and 392 MeV were close to each other. Thus for a sake of simplicity and consistency, we used the average of each parameter at two incident energies for both energies for further analysis.

It should be noted that all parameters in the correction except P_8^{opt} were obtained from the minimum-chi-square fitting.

3.1.4 Momentum calibration

The momentum of the particle can be reconstructed from the position at the focal plane, as:

$$\delta = \frac{x_{\mathrm{FP}}}{< x|\delta >} \ , \tag{3.15}$$

where $< x|\delta >$ is the momentum dispersion of GR and δ is the momentum deviation from the central trajectory, defined as:

$$\delta = \frac{p - p_0}{p_0} \ , \tag{3.16}$$

where p_0 is the momentum of the central trajectory and p is the momentum of the particle. Thus, we have:

$$p = (\frac{x_{\mathrm{FP}}}{< x|\delta >} + 1) \cdot p_0 \ . \tag{3.17}$$

After optics correction, we consider $x_{\mathrm{FP}} = X_3$. Assuming a constant dispersion, we obtained it using proton elastic scattering data on carbon target with the sieve slit. Then we reconstructed the momentum of the proton and compared with calculation, and found that the residual has a second order correlation with the position. This

is consistent with the previous knowledge that the GR dispersion has a second order effect (in position). In order to have a better momentum construction, we corrected the second order effect by following equation:

$$X_4 = P_0^{\text{disp}} + P_1^{\text{disp}} \cdot X_3 + P_2^{\text{disp}} \cdot X_3^2 \;, \tag{3.18}$$

$$x_{\text{FP}} = X_4 \;, \tag{3.19}$$

where X_4 is corrected from X_3 and used as x_{FP} to reconstruct the momentum of the particle. The calibration of GR was check by (p, d) spectrum and discussed in the following section.

3.1.5 Confirmation of energy calibration

With the momentum and the scattering angle information of a deuteron, we can calculate the excitation energy of (p, d) reactions, which can be used to confirm the calibration. Related equations are presented in Sec. A.1 of Appendix A. Because E552 and E481 experiments were performed together as a campaign, most of the setup is the same. We analyzed E481 data with the same manner. In E552 experiment we used mainly ^{16}O and ^{12}C target, with which the (p, d) spectra covered limited region of VDC, making it difficult to check the higher order effect of the dispersion and calibration. However, in E481 calcium targets were used, whose (p, d) spectra covers much wider region of VDC, offering a good examination of GR calibration. Therefore, using calcium (p, d) spectra we examined the calibration of GR and present in this part.

Panel (a) in Fig. 3.10 shows the angle position distribution of deuteron from $^{\text{nat}}$Ca(p, d). The ^{39}Ca excitation energy spectrum is shown in panel (b). Several significant states were used and fitted by gaussian function to determine the center energy. The energy difference compared with the excitation energy listed in level scheme is shown in panel (c) as residual. Beam energy was adjusted to make the average of residual as 0 MeV. The error bar shows the uncertainty of peak center in the fitting. We can see that for spectrum covering 6.5 MeV region, the maximum discrepancy is around 30 keV.

Similar analysis was performed for ^{44}Ca(p, d) data as well and shown in panel (d), (e) and (f) in Fig. 3.10. With a larger coverage up to 9 MeV, the maximum discrepancy is around 120 keV. However, there is no remaining second order effect.

Since the energy resolution of the (p, pd) excitation energy spectrum is mainly determined by proton energy determination, we conclude that present energy calibration for GR is sufficient.

3.1.6 Beam energy fluctuation

As mentioned in subsection 3.1.5, the beam energy was adjusted to satisfy the average of residual as 0 MeV. This is because we observed significant beam energy fluctuation with time. Even though some other fluctuation such as magnetic field fluctuation and beam position fluctuation (together with non-uniformity of target) might also affect the offset of excitation energy, we consider the beam energy fluctuation is the main source and thus we introduced an offset of beam energy and determined it from data.
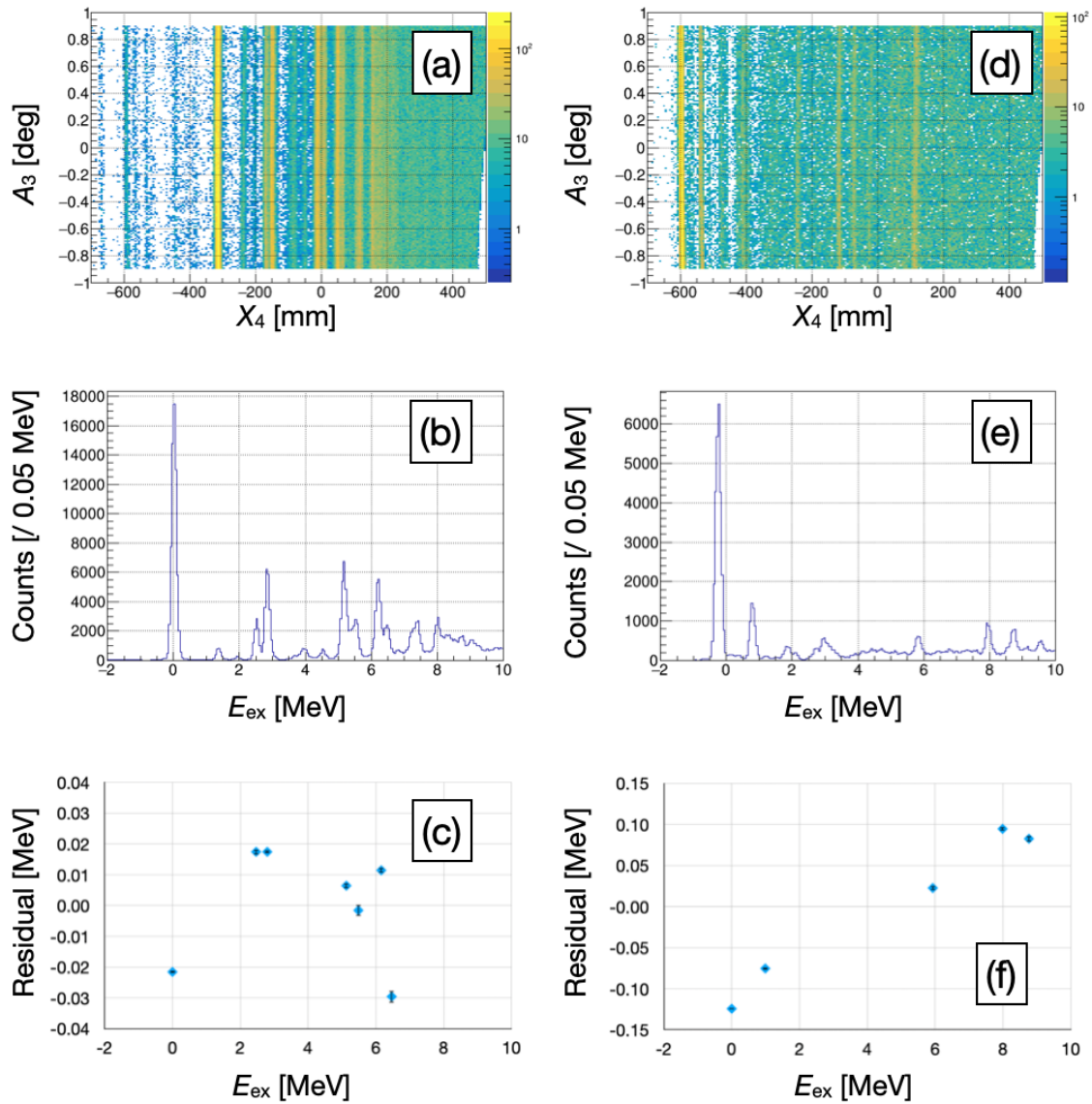
Figure 3.10: Panel (a) and (d) show the angle position distributions, after optics correction. Panel (b) and (e) show the excitation energy spectra of (p, d) reaction. Panel (c) and (f) show the difference of peak center and excitation energy in level scheme. Left side three panels are for $^{nat}Ca(p, d)$ and right side for $^{44}Ca(p, d)$.
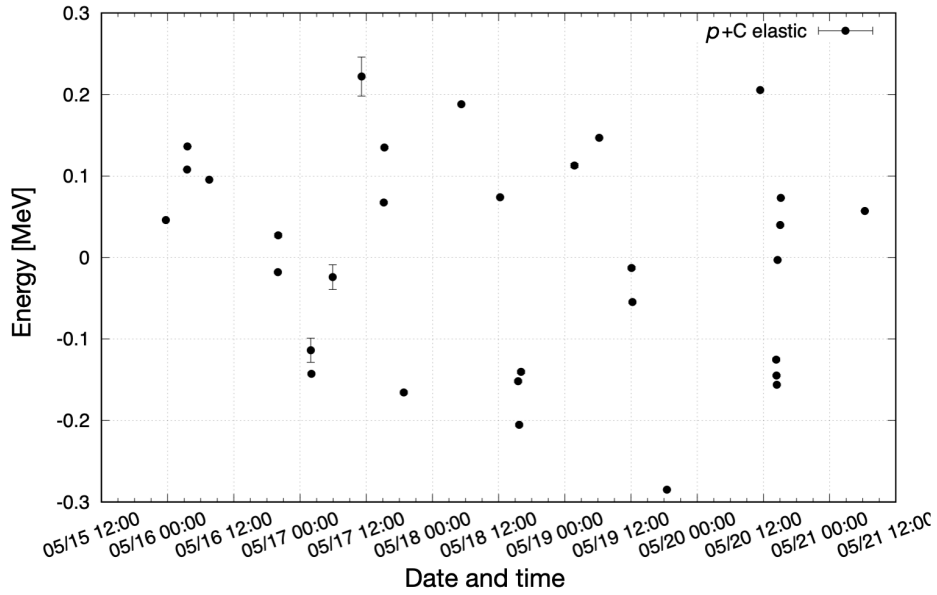
Figure 3.11: Proton elastic scattering energy on carbon target with small collimator in front of GR is shown. The error bar shows the uncertainty of the peak center determination in the gaussian fitting on the ground state peak. The calculation assumed a constant beam energy.

Figure 3.11 shows the beam energy fluctuation at 230 MeV. Data of proton elastic scattering on carbon target with the small collimator was used to minimized the effect of energy loss in target. In the calculation, a constant beam energy was assumed and we checked the excitation energy of the elastic scattering peak, which was expected to be at 0 MeV. A gaussian function was assumed to fit the elastic scattering peak, with the uncertainty of the peak center determination in the fitting shown as error bars. We observed a random fluctuation over time, with around 200 keV. Therefore, we determined the beam energy from the data run by run, namely using the discrete states in the spectrum.

3.2 Proton hodoscope analysis

We performed coincidence measurement for $^{16}O(p, pd)^{14}N$ reactions and used missing mass method to obtain the excitation energy of ^{14}N. Forward deuterons going to GR were analyzed and discussed previously in Sec. 3.1. In this section we present the analysis for backward protons, which were detected by the proton hodoscope (HODO), consisting of two layers of plastic scintillators.

High energy protons (around 25-90 MeV) which penetrated the first layer and stop in the second layer were categorized as "penetrating proton", and detected by both dE and E counters. The energy of a penetrating proton was determined by the E counters, where most of the energy was deposited. Low energy protons (around 16-24 MeV) which stopped in the first layer were categorized as "stopping proton". The energy of a stopping proton was determined by the dE counters.

We present the particle identification (PI) in subsection 3.2.1 and energy calibra-
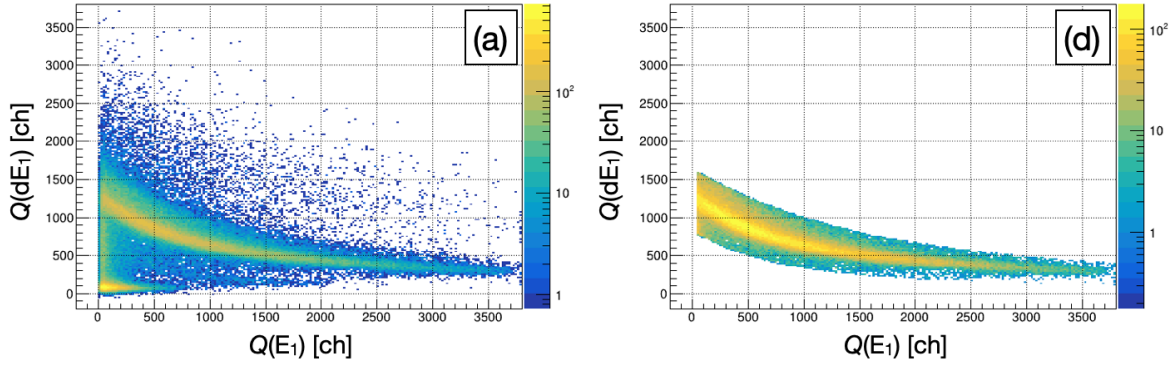
Figure 3.12: The correlation of dE-E is shown. Panel (a) and (b) shows the distribution without and with PI selection, respectively.

tion in subsection 3.2.2. Thereafter we discuss the method to subtract accidental background in subsection 3.2.3. Finally we present the energy spectra of $^{16}\text{O}(p, pd)^{14}\text{N}$ reactions in subsection 3.2.4.

3.2.1 Particle identification

Firstly we present the particle identification (PI) for the proton. We applied two methods to select protons. The first method called dE-E PI uses the energy deposition correlation in the first and the second layer. Thus this method was used only for penetrating protons. The second method called E-TOF PI uses the energy deposition and the timing correlation in a single detector. Thus it was applied for both penetrating and stopping protons.

Firstly we show the dE-E PI method, where dE represents the energy deposition in the first layer (dE block) and E represents the energy deposition in the second layer (E block). Panel (a) in Fig. 3.12 show the distributions of charge collected by the first and second layers for penetrating events. $Q(\text{dE}_1)$ and $Q(\text{E}_1)$ represents the charge collected in dE_1 and E_1 block, respectively. The charge is related with the energy deposition, and thus we called this as dE-E PI method. Clear proton locus was seen and selection was made for the locus as shown in panel (b) of Fig. 3.12.

Secondly we present the E-TOF PI method, where E represents the energy deposition in a detector, and TOF represents the time-of-flight (TOF) from target to the same detector. TOF is calculated from the timing difference between the detector and RF signal, which was corrected to have only one bunch.

Panel (a) and (c) in Fig. 3.13 show the E and TOF distributions of E_1 and dE_1 block, respectively. Except the proton locus, we see a deuteron locus nearby, which is difficult to identify in dE-E correlation, as shown in Fig. 3.12. Panel (b) and (d) in Fig. 3.13 show the selected protons in E_1 and dE_1 block, respectively. In addition, we can see the penetrating events in panel (c) as well, which was confirmed by the PI from E-TOF of E_1 block.
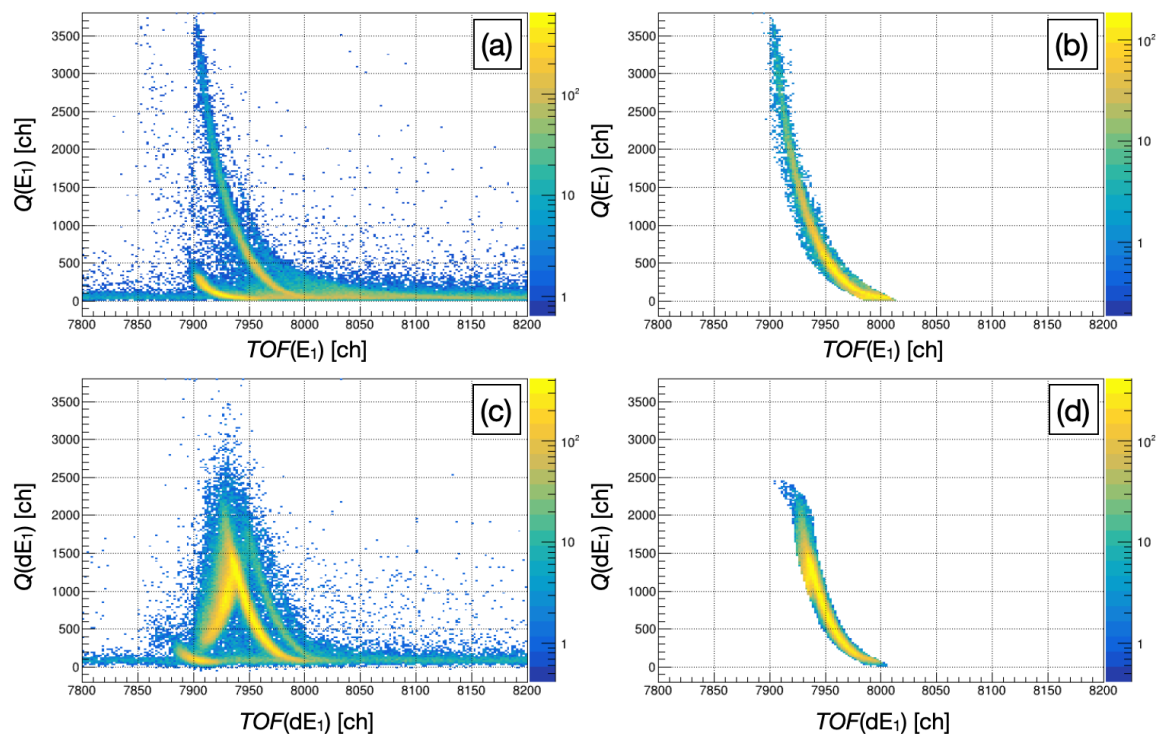
Figure 3.13: The distributions of E and TOF are shown. Panel (a) and (b) show the distributions without and with the PI selection for E_1 block, respectively. Panel (c) and (d) show the distributions without and with PI selection for dE_1 block, respectively.

Table 3.1: Angle summary of HODO

θ_{GR}	$\theta_{\mathrm{dE_1}}$	$\theta_{\mathrm{dE_2}}$	$\theta_{\mathrm{E_1}}$	$\theta_{\mathrm{E_2}}$	$\theta_{\mathrm{E_3}}$	$\theta_{\mathrm{E_4}}$ [deg]
6.4	154.0±6.9	139.6±7.5	155.4±3.3	149.2±3.3	142.7±3.0	136.0±3.2
8.7	144.7±6.9	130.3±7.5	146.1±3.3	139.9±3.3	133.4±3.0	126.7±3.2
15.0	130.4±7.3	115.8±7.3	133.4±3.3	126.7±3.3	120.1±3.3	113.5±3.2
16.1	127.5±7.3	112.9±7.3	130.5±3.3	123.8±3.3	117.2±3.3	110.7±3.3

3.2.2 Calibration

Because there are several materials between the target and the detector, the energy response of the detector is complicated and non-linear. Also due to a large solid angle of the detector, it is difficult to prepare mono-energetic proton for energy calibration. During E552 experiment, we performed a measurement for p+d elastic scattering using a CD_2 target, with deuterons detected via GR and protons detected by HODO. Even thought we obtained only a few energy points, these data were useful to confirm the energy range. After the confirmation, we perform phenomenological calibration for HODO to obtain the response function based on the discrete state of (p, pd) spectrum.

Firstly we used one E block (E_3) as a reference and adjusted the gain of other three E blocks by a linear function:

$$Q_c(E_i) = P_{0,i}^{\mathrm{gain}} + P_{1,i}^{\mathrm{gain}} \cdot Q(E_i), \ (i = 1, 2, 4) \ , \tag{3.20}$$

where $Q(E_i)$ is the original channel number in QDC (after pedestal subtraction) and $Q_c(E_i)$ is the channel number after adjustment. After adjustment, all four E blocks were expected to have a common response function. A global polynomial function up to the third order was use to calibrate four E blocks:

$$T_p(E_i) = P_0^{\mathrm{HODO}} + P_1^{\mathrm{HODO}} \cdot Q_c(E_i) + P_2^{\mathrm{HODO}} \cdot Q_c^2(E_i) + P_3^{\mathrm{HODO}} \cdot Q_c^3(E_i) \ , \tag{3.21}$$

where T_p is proton kinetic energy and P_i^{HODO} are free parameters. Similar procedure was applied to dE blocks, but without adjustment at the beginning.

Panel (a) in Fig. 3.14 shows the distributions of proton kinetic energy and excitation energy as an example. Equations to obtain the excitation energy are presented in subsection A.2.2 of Appendix A. Here proton energy is obtained from E_2 counter. The aim of proton energy calibration is to make the correlation straight. Black and blue dots represent for the data from different magnetic settings of GR. Panel (b) shows the correlation between charge measured in E_2 counter and deuteron kinetic energy. A straight red dashed line is shown for eye-guide. Before calibration, the correlation is not straight, especially at small proton energy region. Panel (c) shows the distributions of proton energy after calibration and deuteron kinetic energy. We see the correlation is straight.

In addition, we confirmed the angle of HODO using the CD_2 data with the alignment before the experiment. Table 3.1 shows a summary of HODO angle in different settings, where the first value denotes the center angle and the second one denotes the acceptance.
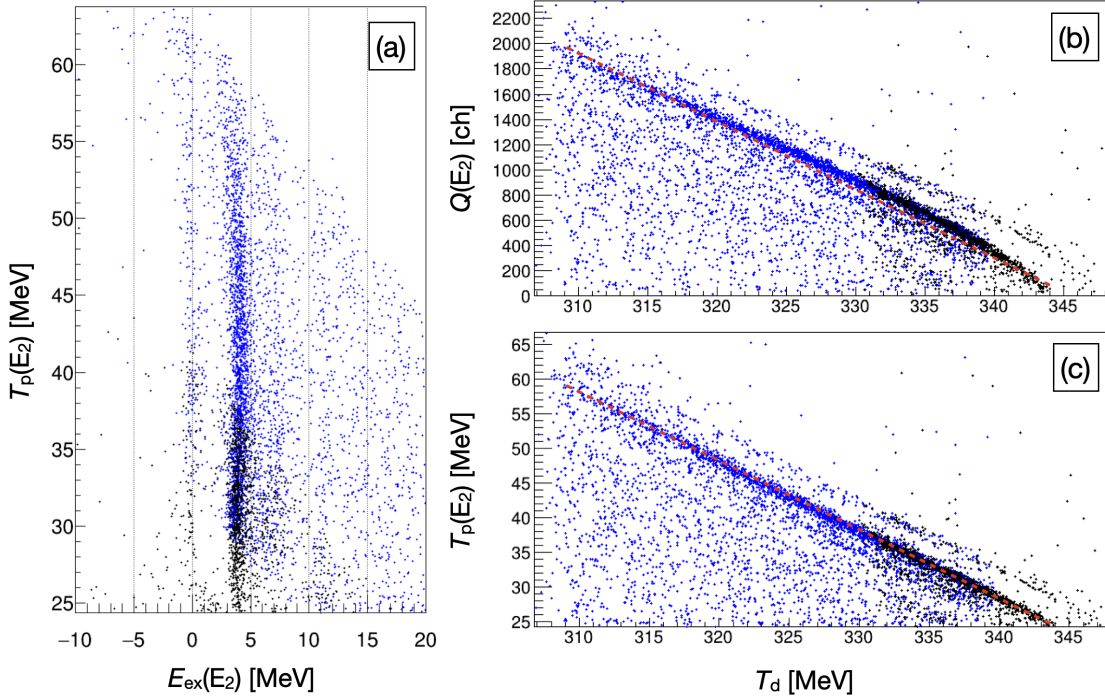
Figure 3.14: The distributions of proton kinetic energy and excitation energy are shown in panel (a). The distributions of proton and deuteron kinetic energy are shown in panel (b) and (c) before and after proton energy calibration, respectively.

3.2.3   Accidental background subtraction

For the data at 230 MeV incident energy, we see huge amount of accidental background due to large counting rate of HODO. Therefore, we investigated the distribution of accidental coincident events and subtracted it.

Figure 3.15 shows the coincident timing of E_1 block at 392 MeV and 230 MeV in panel (a) and (b) as examples. The coincident timing of E_1 ($t_{\mathrm{COIN}}(E_1)$) was calculated from the timing difference between E_1 and GR. Besides the real coincident peak at the center, we observed several side bunches near by, because the coincident width of BAND and GR was large. While the amount accidental coincident events was small for the data at 392 MeV, as shown in panel (a), the amount of that at 230 MeV shown in panel (b) was large.

In order to obtain the amount of accidental background in the real coincident peak (No.3), we fitted all six peaks (No.1-6) with gaussian function:

$$N_i = \frac{A_i}{\sqrt{2\pi}\sigma_i} e^{-\frac{(t_{\mathrm{COIN}} - t_i)^2}{2\sigma_i^2}} \,, \tag{3.22}$$

and obtained the amplitude (A_i) and center (t_i) of each peak. Then in the A_i versus t_i plot ($A_i = f(t_i)$), we fitted four points with the second order polynomial function:

$$A_i = f(t_i) = P_0^{\mathrm{COIN}} + P_1^{\mathrm{COIN}} t_i + P_2^{\mathrm{COIN}} t_i^2, \ \ i = 1, 4, 5, 6, \tag{3.23}$$
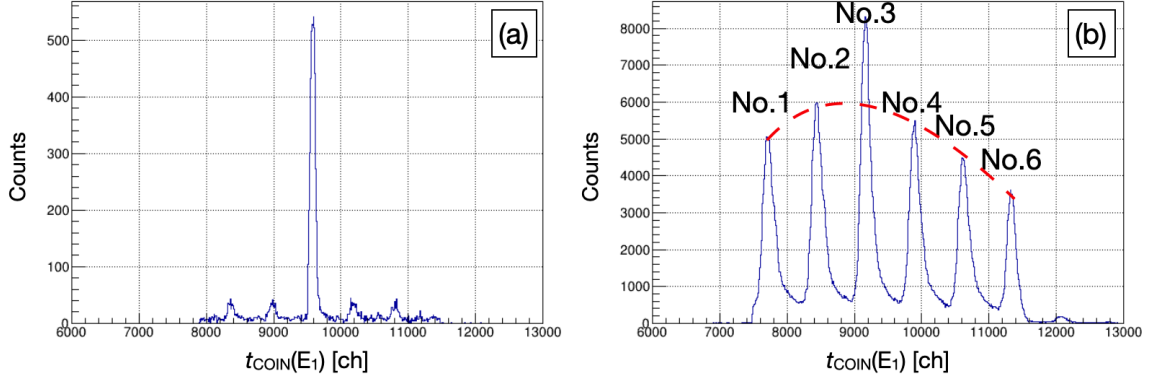
Figure 3.15: Panel (a) and (b) show the coincident timing distributions of the data at 392 and 230 MeV incident energy, respectively.
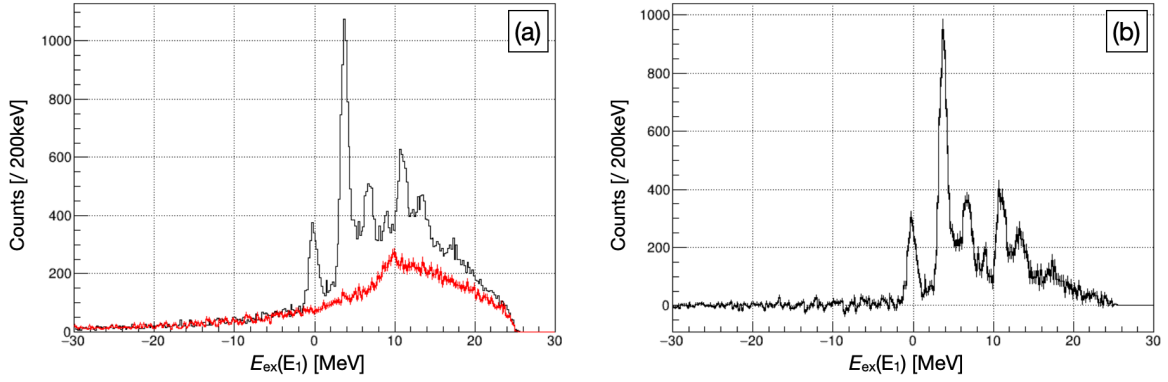
Figure 3.16: Panel (a) shows the excitation energy spectrum of ^{14}N for real coincident bunch as black histogram and the scaled accidental bunch as red histogram of 230 MeV and GR angle at 6.4 degree. The proton was measured by E1 block. Panel (b) shows the spectrum after accidental background subtraction.

where P_0^{COIN}, P_1^{COIN} and P_2^{COIN} were parameters and obtained from the quadratic fitting. We exclude the second peak to estimate the accidental background shape because of the possible mixture of real coincident event in the second bunch. Thereafter we calculated the accidental background amplitude in the real coincident peak by interpolating using:

$$A_3 = f(t_3) = P_0^{\mathrm{COIN}} + P_1^{\mathrm{COIN}}t_3 + P_2^{\mathrm{COIN}}t_3^2 \, , \qquad (3.24)$$

where t_3 is the center of the gaussian fitting for main coincident peak (No.3).

We applied the same proton PI selection with E-TOF method in accidental bunches and scaled the accidental background distribution in the fourth peak (No.4) by a factor $R = A_3/A_4$, where A_3 was obtained from Eq. 3.24 and A_4 was obtained from gaussian fitting (Eq. 3.22). Panel (a) in Fig. 3.16 shows the excitation energy spectrum calculated with proton energy from E_1 block and deuteron energy, with the black histogram for the distribution in real coincident bunch (No.3) and the red histogram for scaled distribution in accidental coincident bunch (No.4). Panel (b) shows the resulting
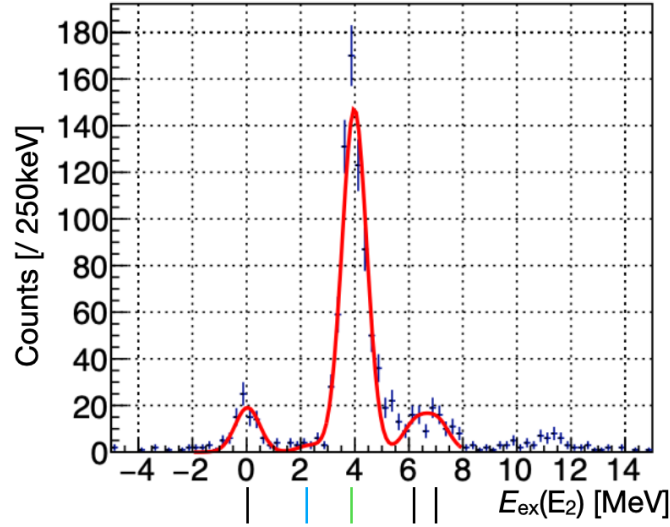
Figure 3.17: Figure shows the excitation energy spectrum of ^{14}N at 392 MeV incident energy and $\theta_{\mathrm{GR}} = 6.4°$ by blue symbols, as well as the fitting by the red line.

spectrum after the subtraction with red histogram from black histogram. At $E_{\mathrm{ex}} < 2$ MeV region, we see almost no background remaining. Therefore, we concluded that the accidental background was removed reasonably.

3.2.4 Excitation energy spectrum

After PI and calibration, we calculated the excitation energy of ^{14}N, equation is presented in Appendix A. For data at 230 MeV incident energy, we subtracted the accidental background as discussed above in subsection 3.2.3. For data at 392 MeV, because the amount of accidental background is negligibly small, background subtraction was not necessary. We applied multi-gaussian fitting for the range of [-2,8] MeV, with a common energy offset (x_{os}) and a common shape (σ):

$$f(x) = \sum_{i=1}^{5} \frac{A_i}{\sqrt{2\pi}\sigma} e^{-\frac{(x+x_{\mathrm{os}}-x_i)^2}{2\sigma^2}} \quad , \tag{3.25}$$

where $f(x)$ denotes the function with 5 gaussian and was used in the fitting. A_i is the amplitude of the i-th peak. σ and x_{os} is the common sigma and energy offset, respectively. Five states were assumed in the fitting with excitation energy of 0, 2.313, 3.948, 6.204 and 7.029 MeV (as x_i, $i = 1 \sim 5$).

Figure 3.17 shows an example of the excitation energy spectrum of ^{16}O$(p, pd)^{14}$N at 392 incident energy and GR center angle (θ_{GR}) 6.4°. The multi-gaussian fitting in the range of -2 to 8 MeV is shown as by the red line. The fitting parameters are summarized in Table 3.2. Five vertical lines at bottom show five excited states that were assumed in the fitting, where the blue and green ones indicate two states of our interest, $E_{\mathrm{ex}} = 2.313$ MeV, $J^\pi = 0^+$ and $E_{\mathrm{ex}} = 3.948$ MeV, $J^\pi = 1^+$, respectively.

One of the goal in data analysis is to obtain the ratio of cross sections of reactions

Table 3.2: Fitting result

Name	Value	Uncertainty	Name	Value	Uncertainty
x_{ox}	-0.03	0.02	σ	0.455	0.016
A_1	22	2	A_2	3.3	1.3
A_3	168	7	A_4	14	3
A_5	15	3			
$\chi^2/ndf = 91.2/32$					

Table 3.3: Spectrum summary

T_{b}[MeV]	θ_d	P_{GR} [MeV/c]	Figure
392	6.4°	1143	3.18
		1187	3.19
	16.1°	1102	3.20
		1149	3.21
230	6.4°	806	3.22
		840	3.23
		875	3.24
	8.7°	806	3.25
		840	3.26
		875	3.27
	15.0°	811	3.28
		778	3.29
		845	3.30
	16.1°	811	3.31
		778	3.32
		845	3.33

populating to these two states. We considered the multi-gaussian fitting was reasonable and thus we obtained the ratio from the fitting result, namely "A_2" and "A_3". The detail is presented in Sec. 4.1.

We present a summary of all spectra of $^{16}\text{O}(p, pd)^{14}\text{N}$ reactions at two incident energies and several deuteron scattering angles. At incident energy (T_{b}) of 392 and 230 MeV, we measured deuterons at scattering angles (θ_d) from 6.4° to 16.1°, and several magnetic settings (represented by P_{GR}, the momentum of the central trajectory of GR). We measured protons in coincidence by HODO, where each detector has different angle at the center (from beam direction, θ_{E_i} or θ_{dE_i}). Then the excitation energy was obtained for each blocks (denoted as $E_{\text{ex}}(\text{E}_i)$ or $E_{\text{ex}}(\text{dE}_i)$).

Table 3.3 shows the summary of spectrum with different kinematics conditions. The angle summary of backward detector HODO can be found in Table 3.1.
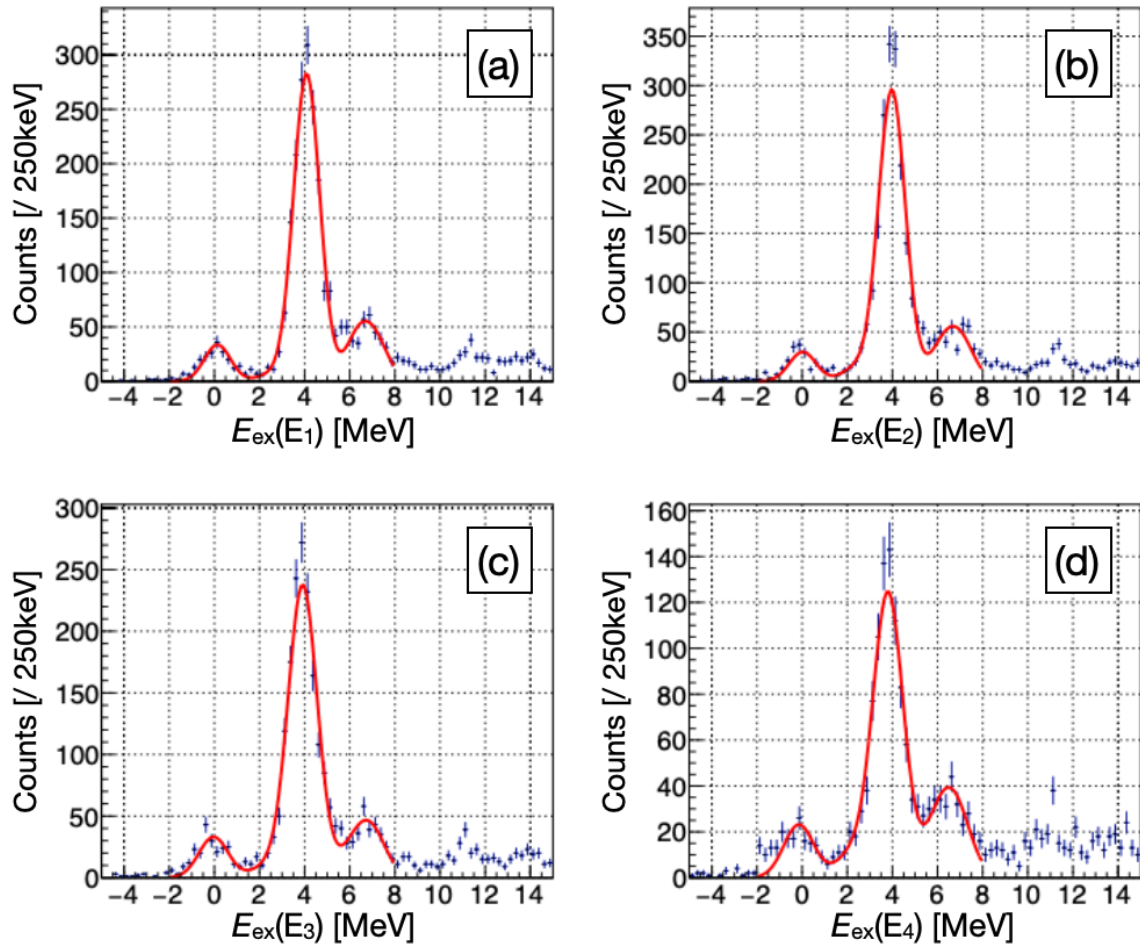
Figure 3.18: Excitation energy spectra at $T_b = 392$ MeV, $\theta_d = 6.4°$, $P_{GR} = 1143$ MeV/c are shown.
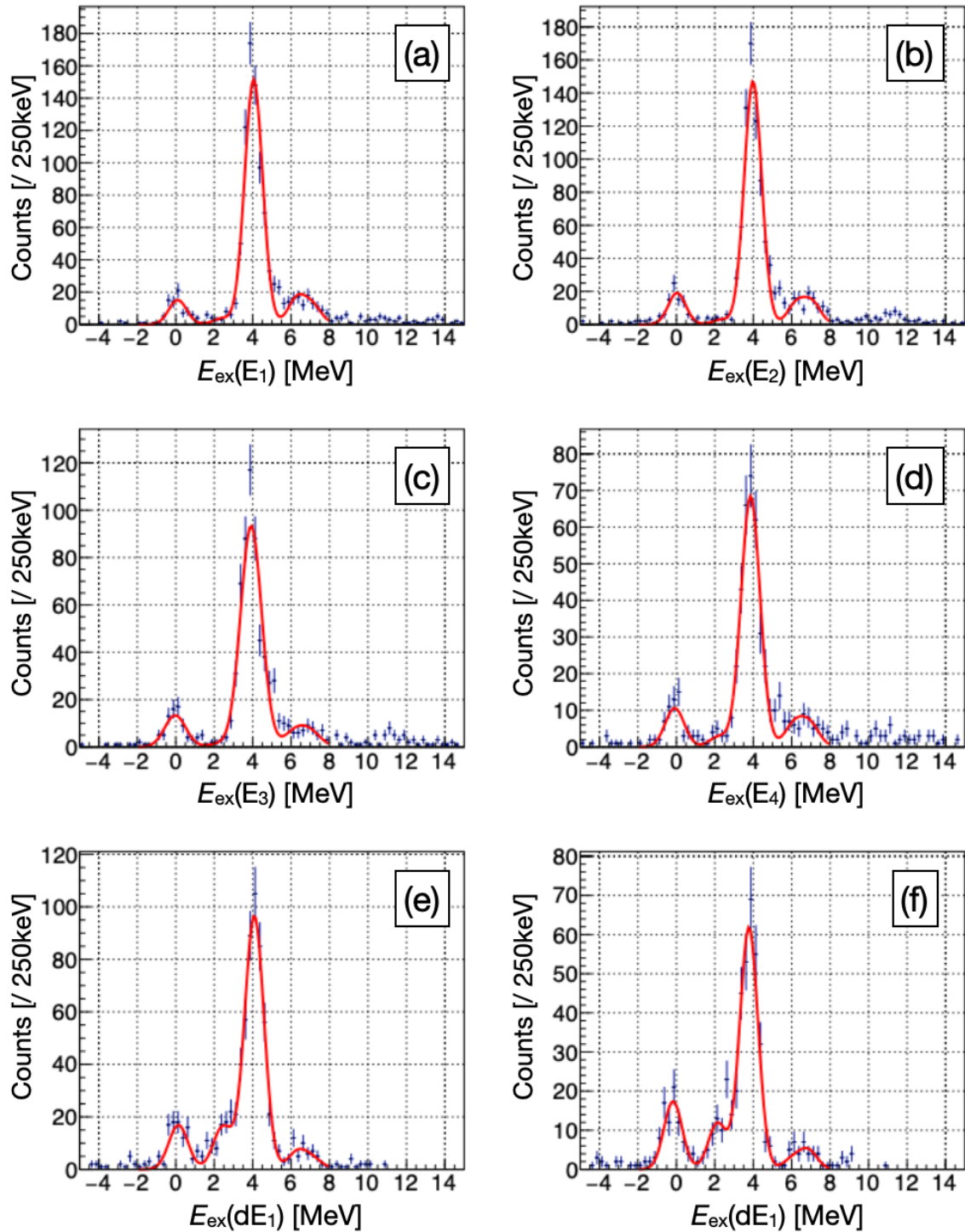
Figure 3.19: Excitation energy spectra at $T_{\mathrm{b}} = 392$ MeV, $\theta_d = 6.4°$, $P_{\mathrm{GR}} = 1187$ MeV/c is shown.
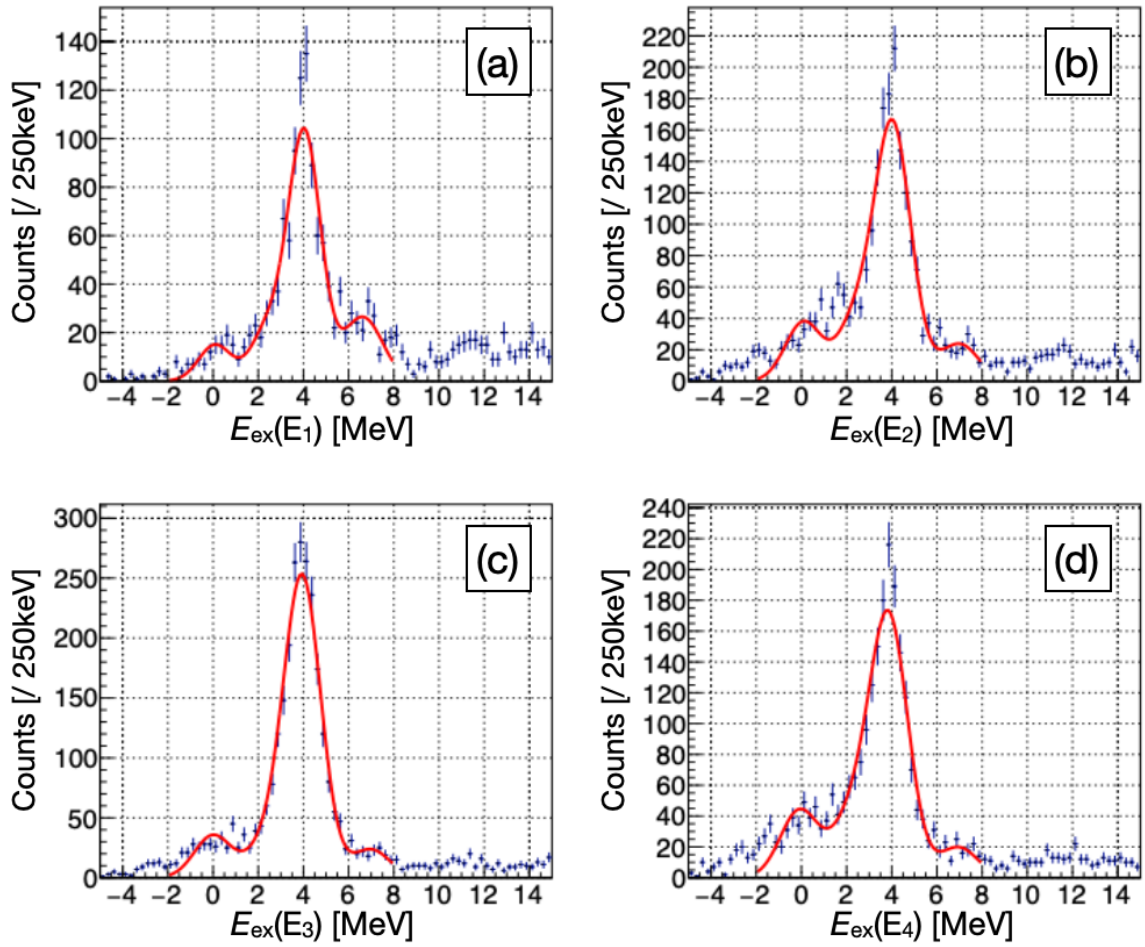
Figure 3.20: Excitation energy spectra at $T_b = 392$ MeV, $\theta_d = 16.1°$, $P_{GR} = 1102$ MeV/c are shown.
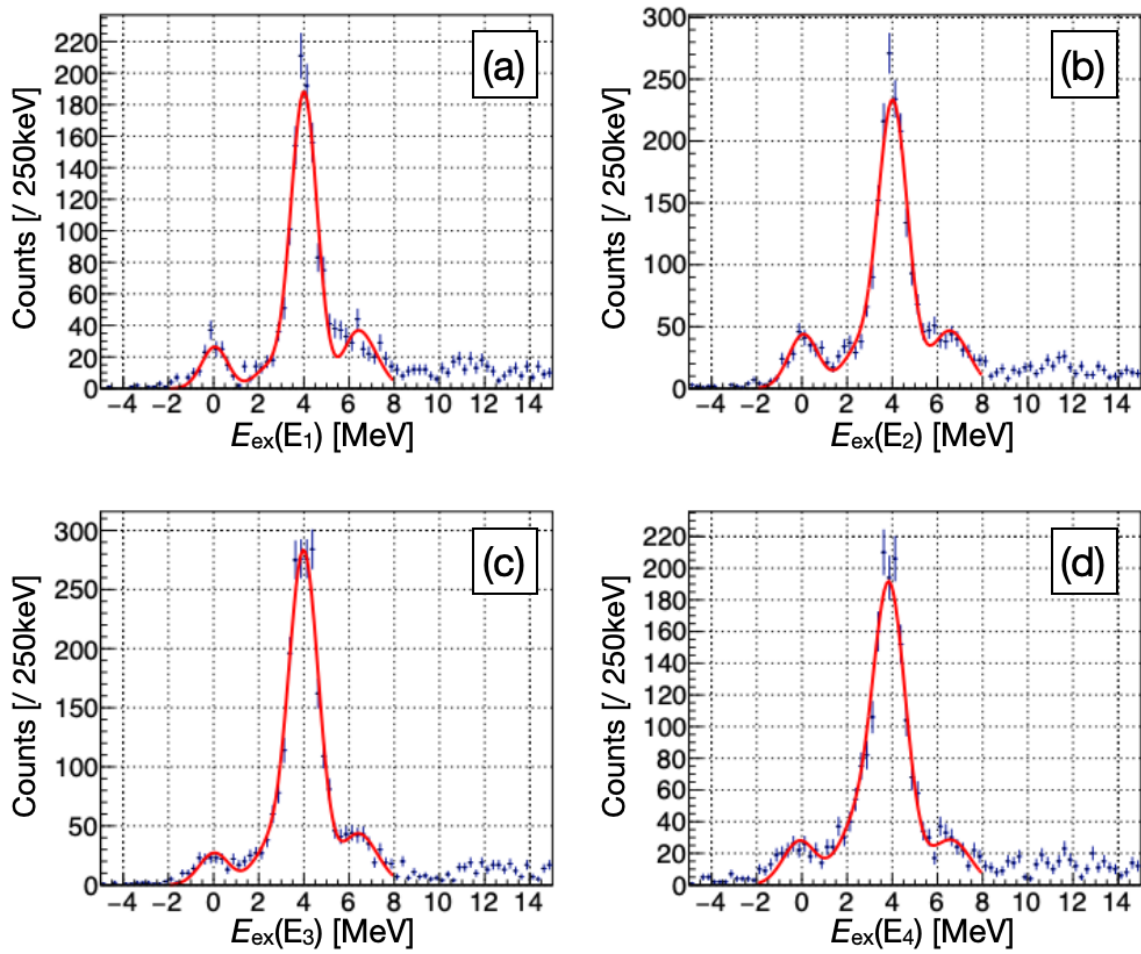
Figure 3.21: Excitation energy spectra at $T_{\rm b} = 392$ MeV, $\theta_d = 16.1°$, $P_{\rm GR} = 1149$ MeV/c are shown.
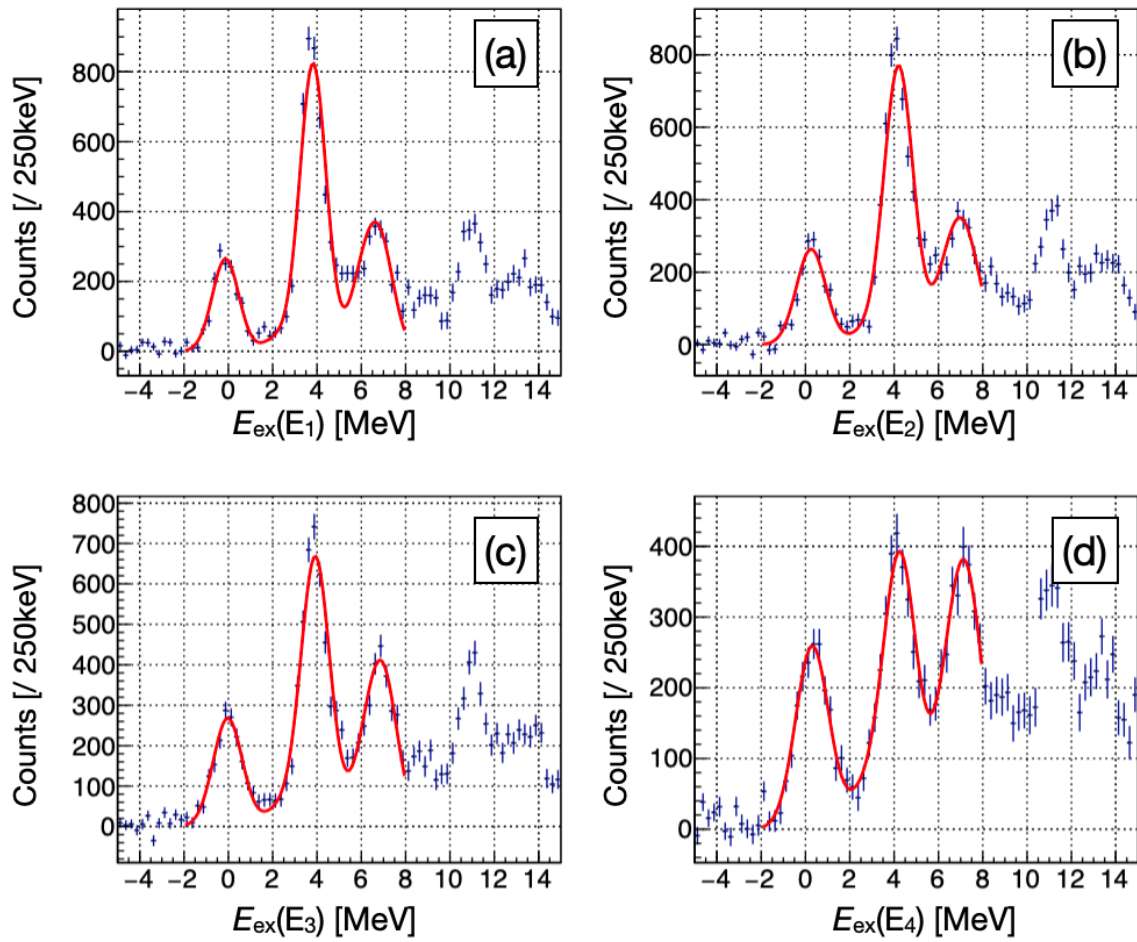
Figure 3.22: Excitation energy spectra at $T_{\mathrm{b}} = 230$ MeV, $\theta_d = 6.4°$, $P_{\mathrm{GR}} = 806$ MeV/c are shown.
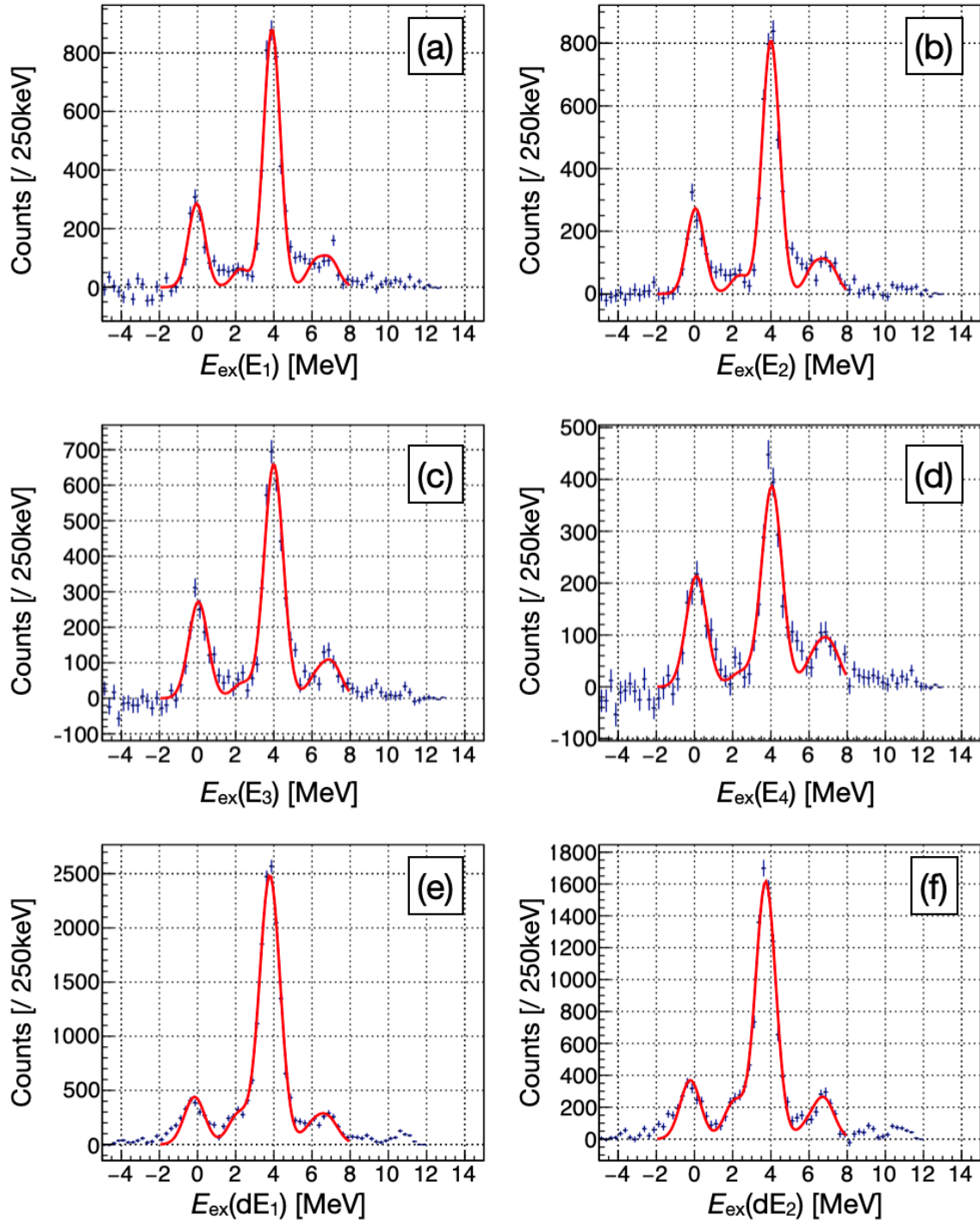
Figure 3.23: Excitation energy spectra at $T_b = 230$ MeV, $\theta_d = 6.4°$, $P_{GR} = 840$ MeV/c are shown.
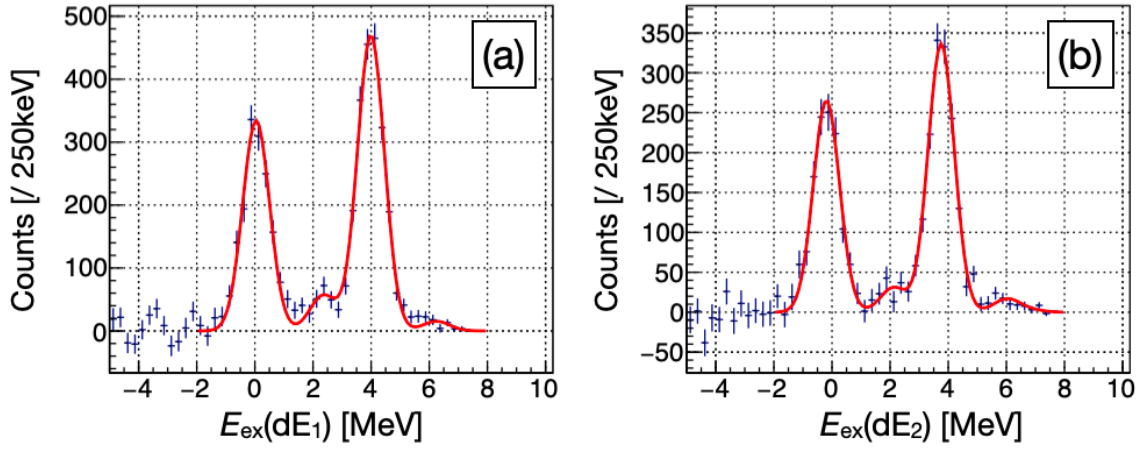
Figure 3.24: Excitation energy spectra at $T_{\mathrm{b}} = 230$ MeV, $\theta_d = 6.4°$, $P_{\mathrm{GR}} = 875$ MeV/c are shown.
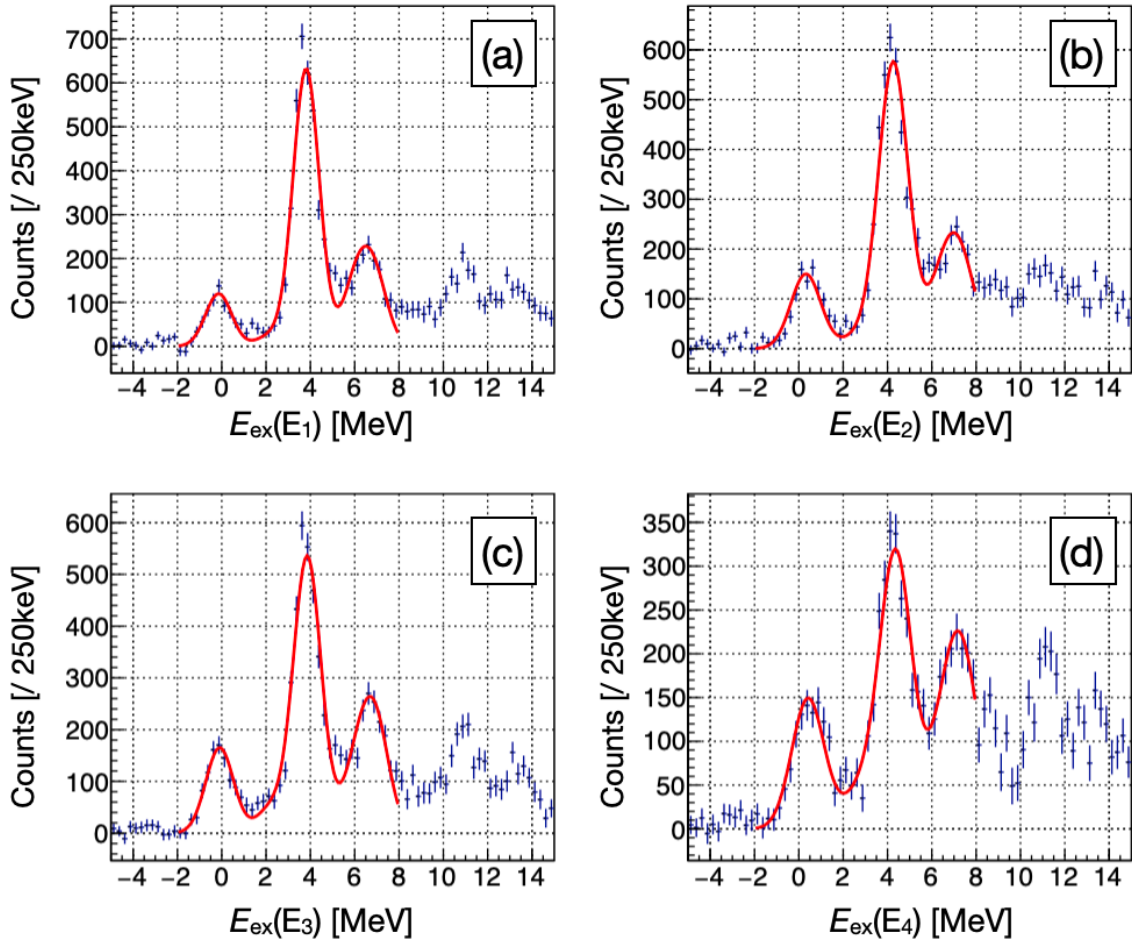
Figure 3.25: Excitation energy spectra at $T_{\mathrm{b}} = 230$ MeV, $\theta_d = 8.7°$, $P_{\mathrm{GR}} = 806$ MeV/c are shown.
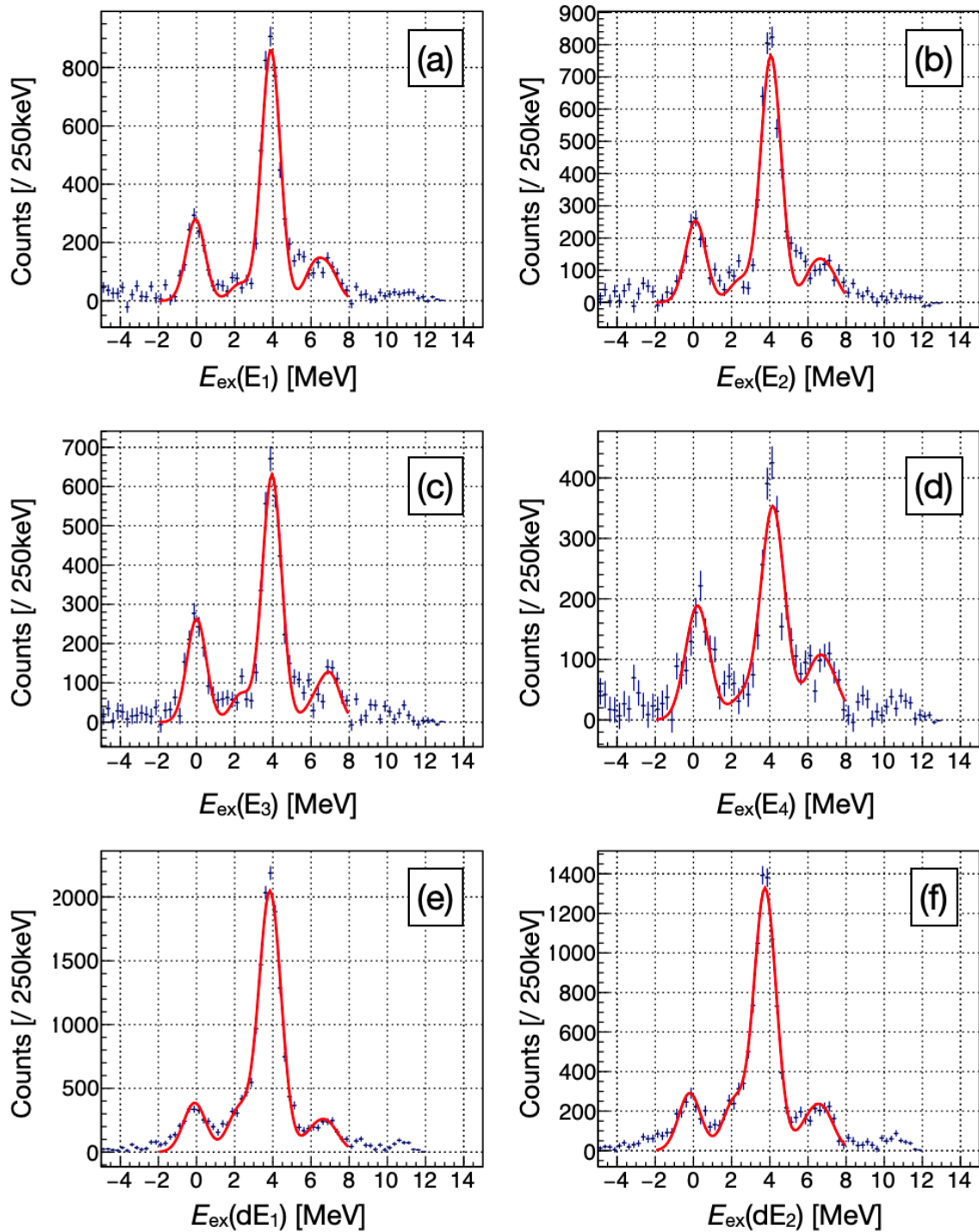
Figure 3.26: Excitation energy spectra at $T_b = 230$ MeV, $\theta_d = 8.7°$, $P_{GR} = 840$ MeV/c are shown.
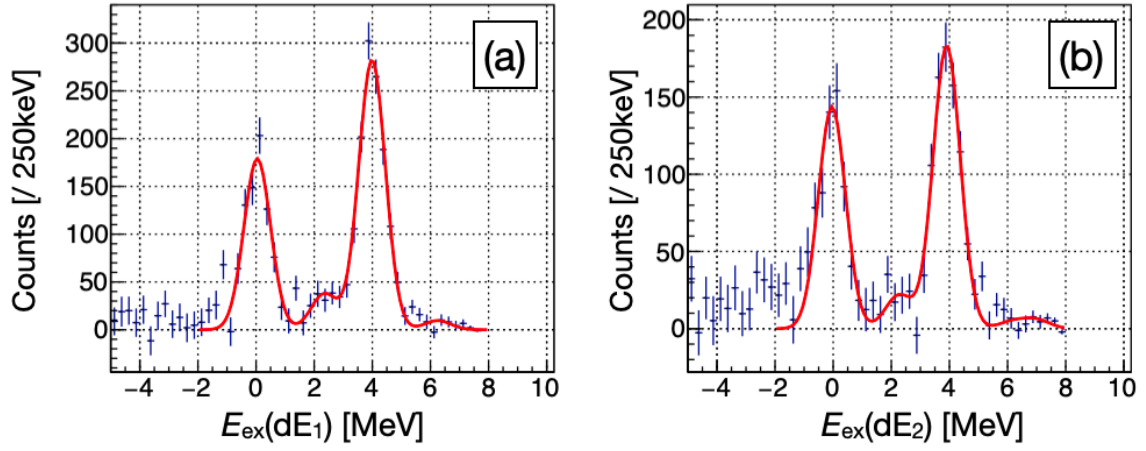
Figure 3.27: Excitation energy spectra at $T_b = 230$ MeV, $\theta_d = 8.7°$, $P_{GR} = 875$ MeV/c are shown.
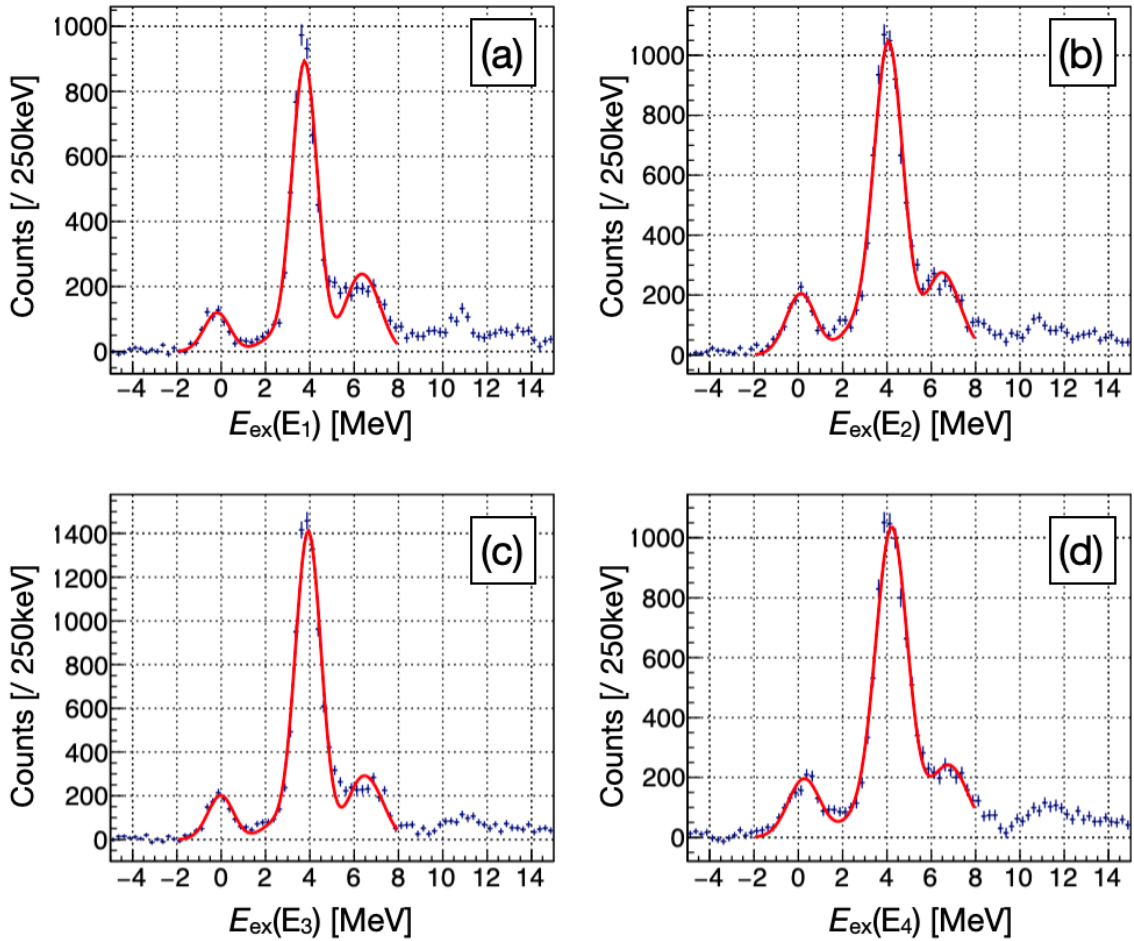
Figure 3.28: Excitation energy spectra at $T_b = 230$ MeV, $\theta_d = 15.0°$, $P_{GR} = 811$ MeV/c are shown.
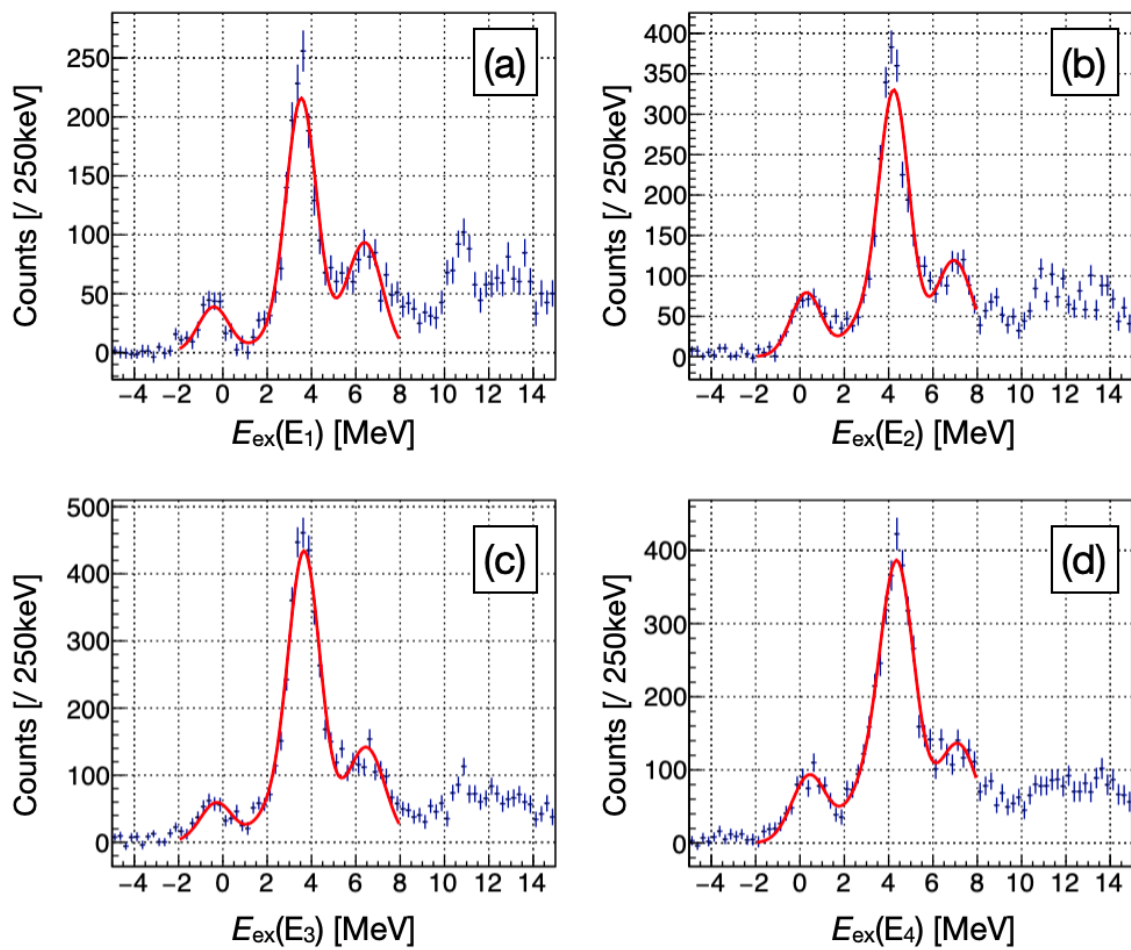
Figure 3.29: Excitation energy spectra at $T_{\rm b}$ = 230 MeV, θ_d = 15.0°, $P_{\rm GR}$ = 778 MeV/c are shown.
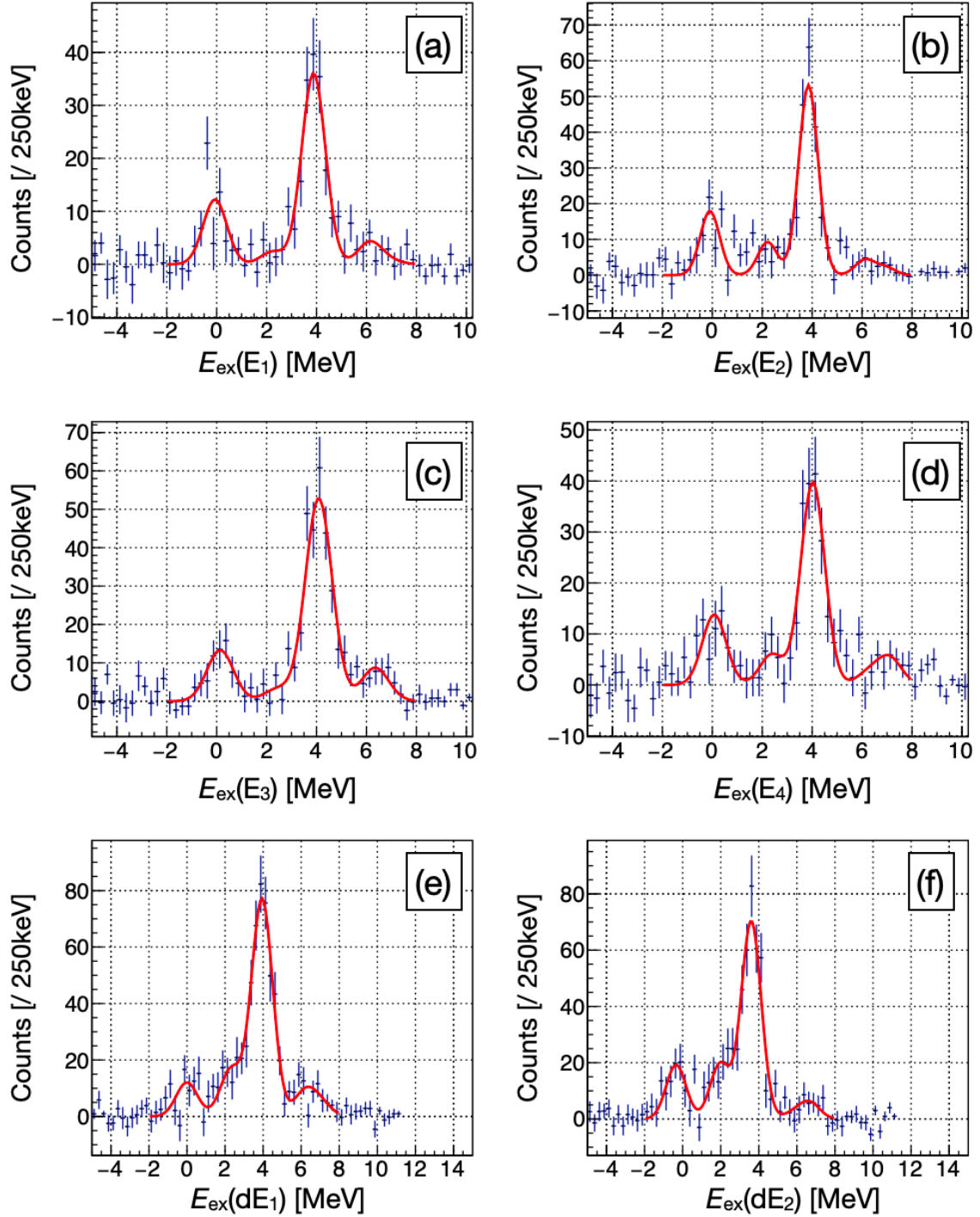
Figure 3.30: Excitation energy spectra at $T_b = 230$ MeV, $\theta_d = 15.0°$, $P_{GR} = 845$ MeV/c are shown.
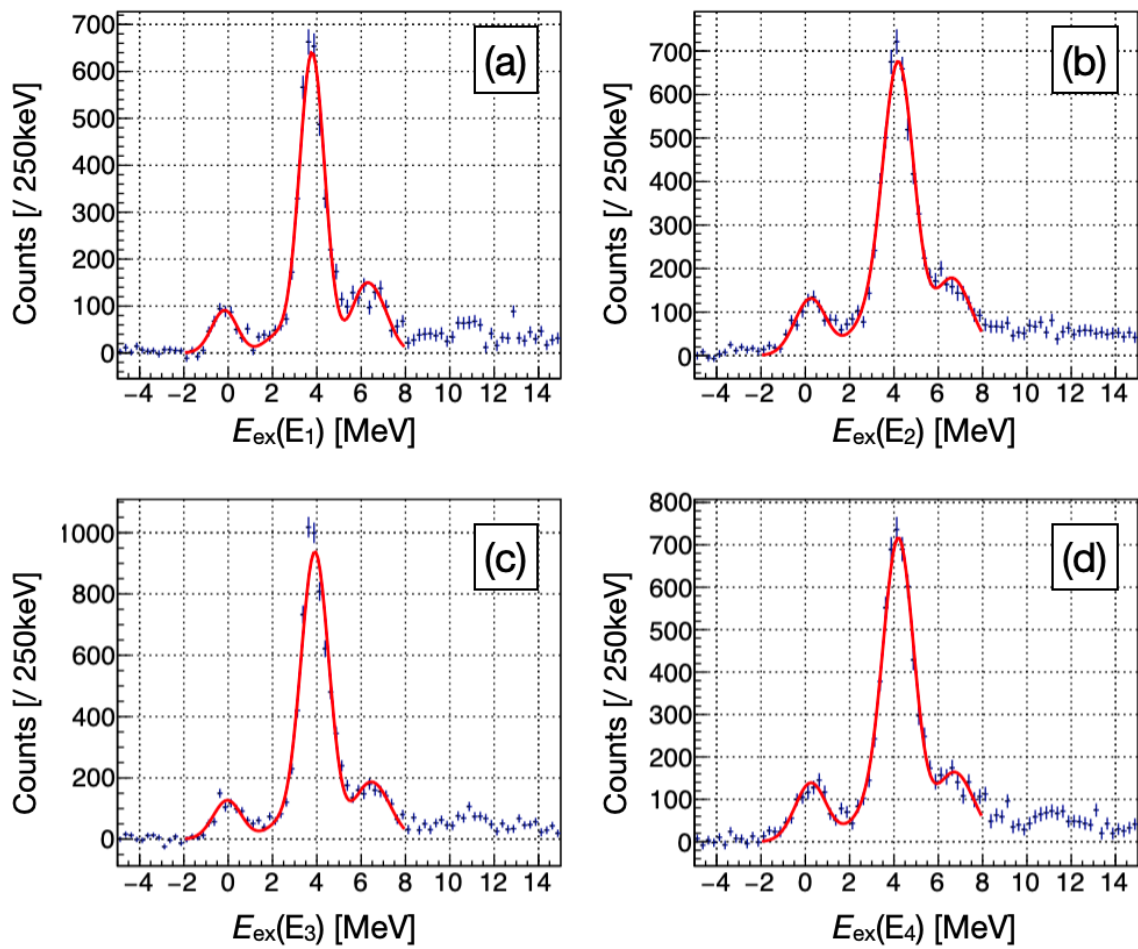
Figure 3.31: Excitation energy spectra at $T_{\rm b}$ = 230 MeV, θ_d = 16.1°, $P_{\rm GR}$ = 811 MeV/c are shown.
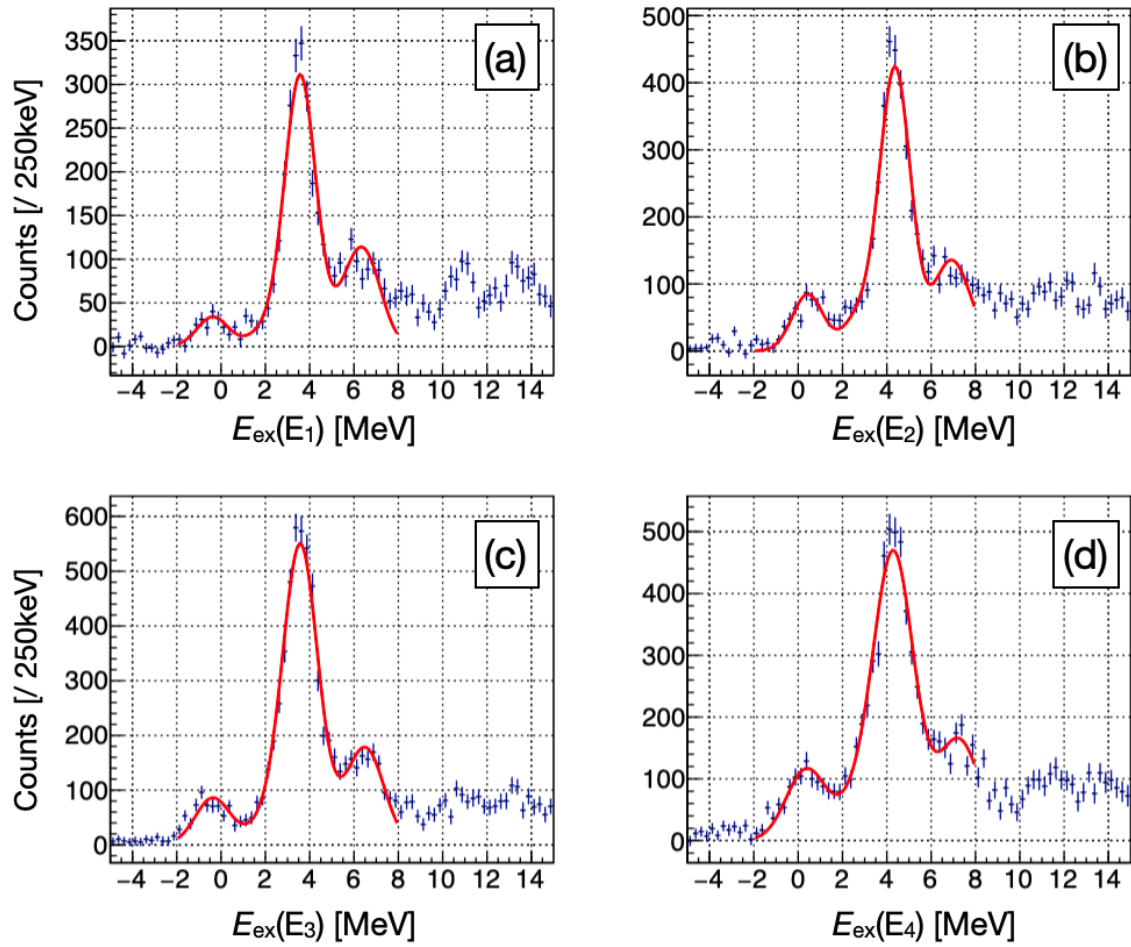
Figure 3.32: Excitation energy spectra at $T_{\mathrm{b}} = 230$ MeV, $\theta_d = 16.1°$, $P_{\mathrm{GR}} = 778$ MeV/c are shown.
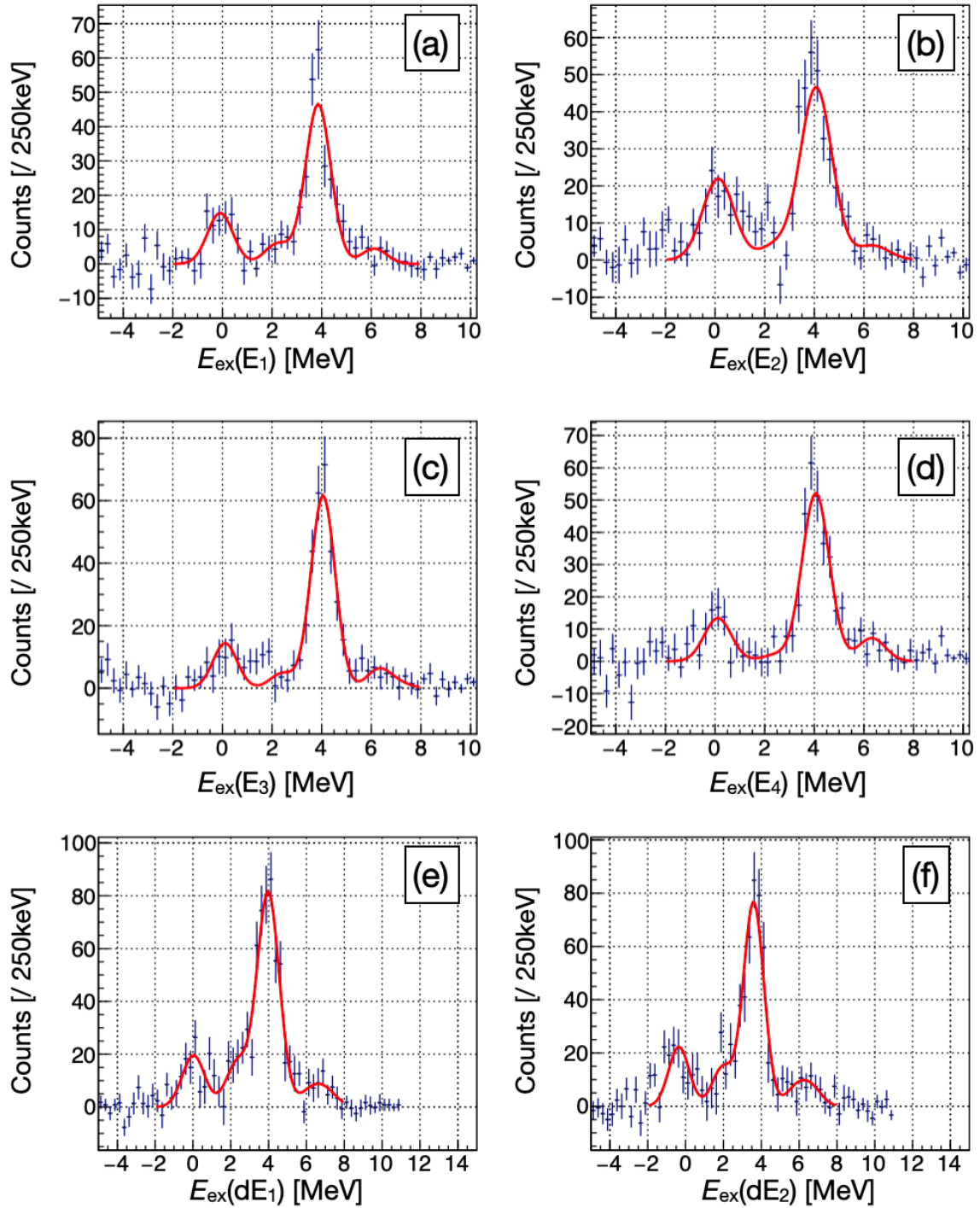
Figure 3.33: Excitation energy spectra at $T_{\mathrm{b}} = 230$ MeV, $\theta_d = 16.1°$, $P_{\mathrm{GR}} = 845$ MeV/c are shown.

3.3   Scaler analysis

In Sec. 3.1 and 3.2 we have presented how we obtained the excitation energy spectra from deuteron and proton analysis. In this section we discuss how we analyzed the scaler data, and obtained the triple differential cross section of (p, pd) reaction populating to $E_{\text{ex}} = 3.948$ MeV, $J^\pi = 1^+$ state.

In the first subsection 3.3.1 we discuss the analysis of the beam current monitor. After checking the response of several beam current monitors, we used the wall Faraday cup (WallFc) to calculate the beam current and use the Beam Line Polarimeter (BLP) to monitor the transmission efficiency from BLP to WallFc.

In the second subsection 3.3.2, we present the evaluation of the total efficiency of particles detected via Grand Raiden (GR) spectrometer, which includes particle identification (PI) efficiency and VDC efficiency.

In the third subsection 3.3.3 we discuss the DAQ efficiency, mainly from the DAQ live time.

After that we present the result of the measurement of $p+^{12}$C elastic scattering cross section, to verify present scaler analysis in subsection 3.3.4.

Then, we present the analysis of proton elastic scattering on thin ice target in subsection 3.3.5. Comparison has been made between measurements for two channels, $p+$H and $p+$O elastic scattering, and consistent result of the thickness of thin ice target was obtained.

In subsection 3.3.6, we evaluated the efficiency of backward protons and concluded that it is close to 100%.

Finally we present the result of triple differential cross sections of ^{16}O(p, pd) reactions in subsection 3.3.7.

3.3.1   Beam current

As presented in Chap. 2, two sets of Beam Line Polarimeter (BLP) and the Wall Faraday cup (WallFc) were prepared to monitor the beam current. While BLPs were placed upstream of the scattering chamber (SC), WallFc was placed downstream of SC. A Faraday Cup in SC (ScFc) was used for calibration purpose. During physics measurement, ScFc was moved out from the beam line and the unreacted beam particles were transported to WallFc via Grand RAiden Forward beam line (GRAF) and collected there. In this part we present the analysis of BLP and WallFc. The aim of this analysis is to obtain the number of beam particle at SC.

BLP1 and BLP2 monitor beam intensities by detecting two protons from $p+$H elastic scattering at a thin Aramid target in coincidence. In the calibration run, we inserted the Faraday cup at the scattering chamber (ScFc) to measure beam current directly, which was considered as the reference. Then, the calibration factor k_{BLP1} and k_{BLP2} is defined as:

$$k_{\text{BLP1}} = N_{\text{BLP1}}/Q_{\text{ScFc}} \, , \tag{3.26}$$

$$k_{\text{BLP2}} = N_{\text{BLP2}}/Q_{\text{ScFc}} \, , \tag{3.27}$$

where N_{BLP1} and N_{BLP2} denotes the total counts measured by BLP1 and BLP2 in a
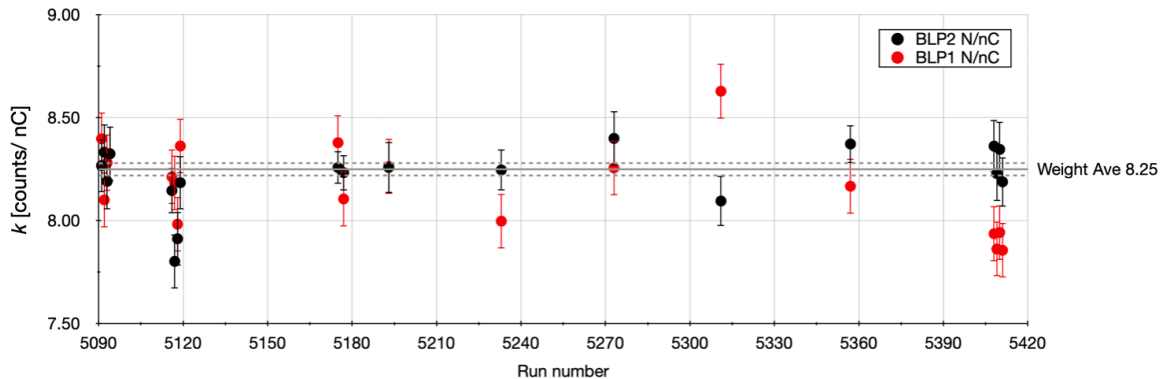
Figure 3.34: BLP calibration factor is shown as a function of run number, which can be regarded as time line. No clear dependence on the time of the factor is obaserved. Red and black dots are for BLP1 and BLP2, respectively.

run and Q_{ScFc} denotes the charge integral from beam current measured by ScFc.

Figure 3.34 shows the calibration result at 230 MeV as an example, where calibration factor for BLP1 and BLP2 is shown by red and black symbols, respectively. The error bar shows the statistical uncertainty. The weighted average was calculated for BLP2 and shown in grey solid line. The grey dash line shows the one-sigma-width of the weighted average, used as the uncertainty of the calibration factor in further analysis. We checked this calibration with all available data and concluded that we didn't observe time dependence of the calibration factor, showing no irradiation effect. In addition, calibration data with several beam currents (from 1 to 22 nA) were checked and we concluded that the calibration factor has no dependence on beam current.

After BLP calibration, we checked the WallFc without target and ScFc in the beam line. Beam charge calculated from BLP was used as a reference by assuming the transmission from BLP to the target position was unchanged. Then we evaluated the transmission efficiency of beam line from the target to WallFc (GRAF line). Figure 3.35 shows the transmission efficiency at 230 MeV with several targets as an example. For thin ice and carbon target, the transmission efficiency is close to that of empty target, while for thick ice target, which has a thickness of one order larger than others, the efficiency is slightly smaller than others. This is considered due to the increase of beam emittance by the multiple Coulomb scattering of beam particle in a thick target.

During the measurement for physics run, we kept using BLPs and WallFc to monitor the beam current and we aimed to know the total number of beam particles at SC. In the case of normal operation, the transmission efficiency from BLP to WallFc is high enough, thus we can use either of them to determine the number of beam particles at SC. However, in the data of physics runs in E552 experiment, significant beam loss before SC was observed in some of runs (discussed in Appendix D) and the transmission efficiency was small. Therefore, we used the beam charge obtained by WallFc as the beam charge at SC and the possible transmission efficiency loss of GRAF was considered as a source of systematic uncertainty.
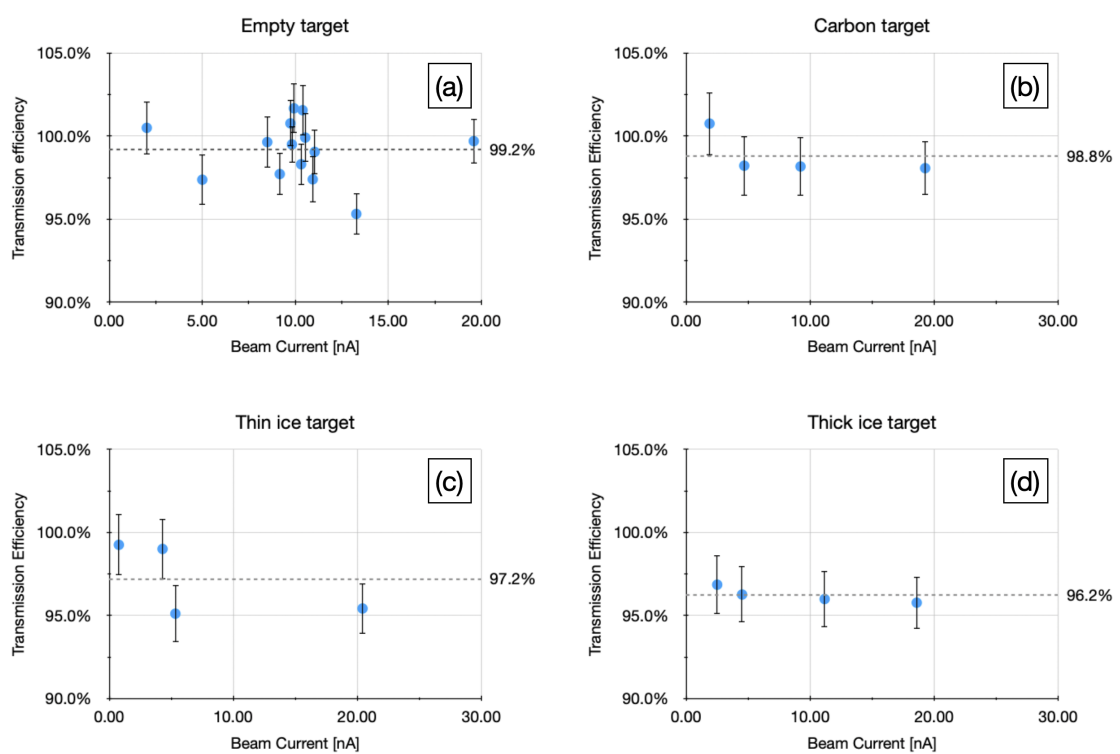
Figure 3.35: Panel (a), (b), (c) and (d) shows the transmission efficiency in calibration data with empty, carbon, thin ice and thick ice target, respectively.

3.3.2   Detection efficiency of forward particle

Forward going particles were momentum-analyzed by GR and detected by focal plane detectors. Since the coincidence of PL1 and PL2 was used as event triggers, we are not able to evaluate the detection efficiency of PL1 and PL2. It was assumed that all charged particles that passed through PLs gave signals in PLs. Such assumption is considered to be reasonable for a high energy charge particle passing through a plastic scintillator.

The total efficiency of forward particles detected by GR includes three parts (detection efficiency assumed as 100% and omitted): particle identification (PI) efficiency in PL1 (ϵ_{PI1}), PI efficiency in PL2 (ϵ_{PI2}) and tracking efficiency in VDC (ϵ_{VDC}). Because three parts are independent of each other, we evaluated the efficiency of each part from other two:

$$\epsilon_{\mathrm{PI1}} = \frac{N(G_{\mathrm{PI1}} \cap G_{\mathrm{PI2}} \cap G_{\mathrm{VDC}})}{N(G_{\mathrm{PI2}} \cap G_{\mathrm{VDC}})} \ , \tag{3.28}$$

$$\epsilon_{\mathrm{PI2}} = \frac{N(G_{\mathrm{PI1}} \cap G_{\mathrm{PI2}} \cap G_{\mathrm{VDC}})}{N(G_{\mathrm{PI1}} \cap G_{\mathrm{VDC}})} \ , \tag{3.29}$$

$$\epsilon_{\mathrm{VDC}} = \frac{N(G_{\mathrm{PI1}} \cap G_{\mathrm{PI2}} \cap G_{\mathrm{VDC}})}{N(G_{\mathrm{PI1}} \cap G_{\mathrm{PI2}})} \ , \tag{3.30}$$

where G_{PI1} and G_{PI2} denotes the PI selection via dE-TOF method in PL1 and PL2 respectively (as presented in subsection 3.1.1). G_{VDC} denotes the condition of good tracking in VDC analysis. The $N(G_{\mathrm{PI1}} \cap G_{\mathrm{PI2}} \cap G_{\mathrm{VDC}})$ means the number of events requiring all three conditions, and similar definition for the denominator with two conditions required. Then we obtained the total detection efficiency of forward particle (ϵ_{GR}):

$$\epsilon_{\mathrm{GR}} = \epsilon_{\mathrm{PI1}} \times \epsilon_{\mathrm{PI2}} \times \epsilon_{\mathrm{VDC}} \ . \tag{3.31}$$

We investigated the efficiency position dependence by making several segments along horizontal direction at PL2 as $\epsilon = f(x_{\mathrm{PL2}})$, where x_{PL2} is the horizontal position obtained from the timing difference of left and right PMT of PL2 ($x_{\mathrm{PL2}} = T_{\mathrm{PL2L}} - T_{\mathrm{PL2L}}$). We used the position information from timing of PL2, instead of the horizontal position obtained from VDC analysis. Otherwise the discussion is biased on good tracking events in VDC analysis.

Figure 3.36 shows the position dependence of the efficiency of each part as well as the overall detection efficiency. The data of (p,d) reaction at the continuous region (high excitation energy region of (p,d)) is shown as an example. The PI1 efficiency (ϵ_{PI1}, red symbols) is close to 100% at the center position of PL, while the PI2 efficiency (ϵ_{PI2}, green symbols) is slightly smaller. This is because when reaction between particle and nuclei in PL1 (mainly hydrogen) occurs, the energy and direction of the particle may changes drastically. The decrease of PI1 and PI2 at the corner was understood as a result of the remaining position dependence of the charge, as shown in Fig 3.1.

Drastic drop of VDC efficiency (ϵ_{VDC}, blue) at the corner was also seen, which is related with the treatment of tracking analysis, especially for the two-hit (hit number = number of fired wires) event. According to the discussion in following sections, we
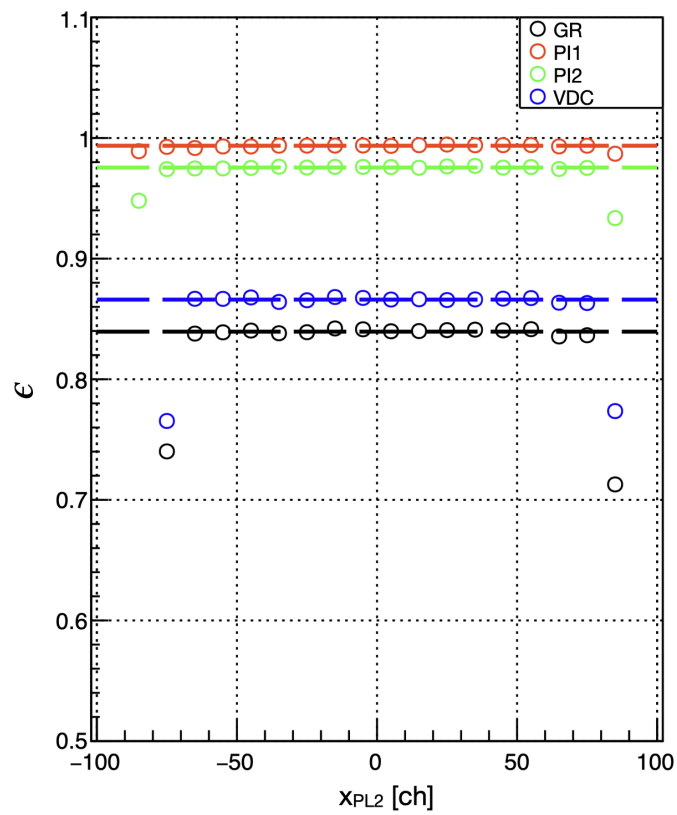
Figure 3.36: The efficiency of PI1, PI2, VDC and GR is shown as a function of horizontal position at PL2 with red, green, blue and black circles, respectively. The dash line shows the average efficiency in a range of $(-70 \leq x_{\mathrm{PL2}} \leq 80$ ch$)$.

Table 3.4: Forward particle detection efficiency

Particle	ϵ_{PI1}	ϵ_{PI2}	ϵ_{VDC}	ϵ_{GR}
Proton	$98 \sim 99\%$	$97 \sim 99\%$	$60 \sim 77\%$	$60 \sim 75\%$
Deuteron	$\sim 99\%$	$96 \sim 97\%$	$83 \sim 88\%$	$80 \sim 85\%$

are interested in the center region of GR momentum acceptance. Therefore, we chose the flat efficiency region for further analysis. For the flat region, the average efficiency was evaluated and shown as dash lines in Fig. 3.36.

Table 3.36 shows the summary of typical detection efficiency of forward particle. In the case that huge background in GR PL was observed, we applied additional gate to exclude background for efficiency estimation, in order to avoid an underestimate of VDC efficiency. The detail is discussed in Appendix D.

3.3.3   DAQ efficiency

While the DAQ processing the data for an event, it cannot receive next events. This causes certain "dead time" in DAQ. We calculate the DAQ "live time" ϵ_{live} as conventional method:

$$\epsilon_{\mathrm{live}} = N_{\mathrm{acc}}/N_{\mathrm{req}} \ , \tag{3.32}$$

where N_{acc} and N_{req} represents the accepted and requested number of GR triggers in a run.

Because we used two sets of electronics (VME and FERA) in parallel for commissioning purpose, we compared the data taken by two sets and truncated the data when two sets were inconsistent. Since the scaler information was recored run by run, for the run truncated, we simply applied a correction factor as "correlation efficiency", ϵ_{corr}, and included it in DAQ efficiency. The detail comparison is not be discussed in this thesis. ϵ_{corr} was simply calculated from the fraction of consistent data to the whole data in a run, and the total DAQ efficiency is defined as:

$$\epsilon_{\mathrm{DAQ}} = \epsilon_{\mathrm{live}} \times \epsilon_{\mathrm{corr}} \ . \tag{3.33}$$

3.3.4   Cross section of proton carbon scattering

During the experiment, we measured the proton elastic scattering on carbon target from time to time as a reference to confirm the performance of detectors as well as data taking system. Because we evaluated the thickness of ice targets from the proton elastic scattering data, we firslty evaluated the cross section of p+C elastic scattering from present data and compared with some reference, as a confirmation of experimental system and data analysis.

Differential cross section of proton elastic scattering is written as:

$$\frac{d\sigma}{d\Omega} = \frac{N_{\mathrm{GR}}}{N_{\mathrm{b}} N_{\mathrm{t}} \epsilon_{\mathrm{GR}} \epsilon_{\mathrm{DAQ}} \Delta\Omega} \ , \tag{3.34}$$

Table 3.5: Cross section of $p+^{12}C$ elastic scattering

Energy [MeV]	θ_{LAB}	$d\sigma/d\Omega_{\text{meas}}$ [mb/sr]	error [mb/sr]	$d\sigma/d\Omega_{\text{ref}}$ [mb/sr]
230	6.4°	423.4	0.6	411.8
	8.7°	329.3	0.9	310.6
	15.0°	62.4	0.2	63.1
	16.1°	50.3	0.2	43.9
392	6.4°	718	11	640
	16.1°	14.5	0.2	9.4

where N_{GR} is the total number of detected elastically scattered protons. N_{b} is the number of beam particles, calculated from beam charge Q_{b} (obtained from WallFc as discussed in subsection 3.3.1) and the charge magnitude unit (e_0) with:

$$N_{\text{b}} = Q_{\text{b}}/e_0 \ . \tag{3.35}$$

N_{t} is the number of target nuclei, calculated from target thickness t:

$$N_{\text{t}} = t/\cos\theta_{\text{t}} \cdot N_{\text{A}}/M \ , \tag{3.36}$$

where θ_{t} is the target tilted angle, N_{A} is Avogadro number and M is molecular mass of the target. ϵ_{GR} and ϵ_{DAQ} is the total efficiency of particles detected via GR (here proton) and the efficiency of DAQ, respectively. $\Delta\Omega$ is the solid angle of GR acceptance.

For elastic scattering channel, because the cross section is large, we used weak beam for measurements to avoid large dead time in DAQ. As a consequence, the DAQ live time was high ($> 90\%$). Considering the beam charge determination, we can obtain the beam charge at the scattering chamber from BLP or WallFc depending on different assumptions. We separate the discussion for elastic scattering data at 230 and 392 MeV.

For $p+C$ elastic scattering data at 230 MeV incident energy, the transmission efficiency from BLP to WallFc was high, as 99% in average. Therefore, the difference of beam charge at scattering chamber determined with two methods is small and we used WallFc to determine the beam charge.

For $p+C$ elastic scattering data at 392 MeV incident energy, the transmission efficiency from BLP to WallFc was low, as $60 \sim 80\%$. We found the correlation between proton background and beam loss, indicating the beam loss before the scattering chamber (SC) (details discussed in Appendix D). In addition, we investigated HODO responds and make an effort to use HODO as a beam current monitor around SC. Unfortunately, we found that HODO was also affected by the amount of proton background and correlated with the beam loss, as a result we concluded that HODO is not able to be used as an independent beam current monitor.

Therefore, we used the WallFc to determine the beam charge at SC, by assuming the transmission efficiency from SC to WallFc was 100%. The difference between BLP and WallFc is treated as systematic uncertainty (as discussed in Appendix D).

Table 3.5 shows the summary of the cross section of $p+^{12}C$ in present measurement together with the one from reference (Dirac Global [56]). The errors of the measurement
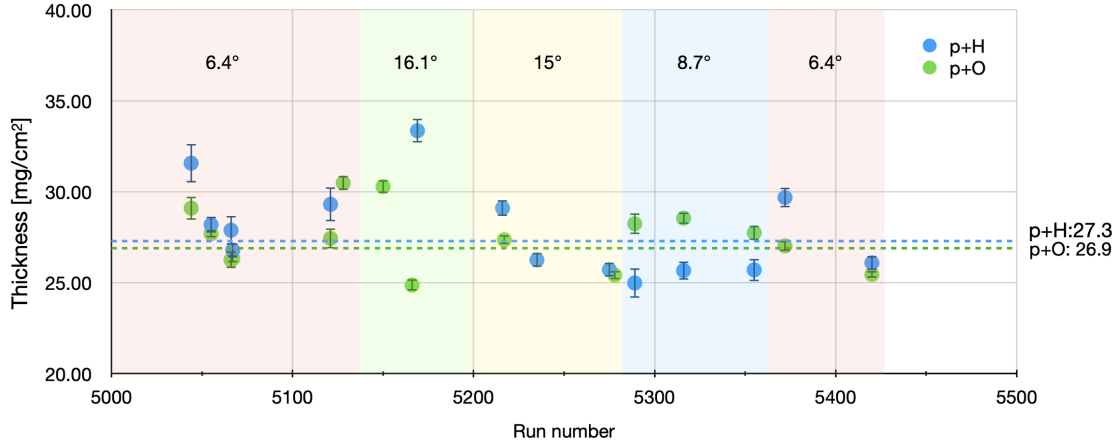
Figure 3.37: Thin ice target thickness measurement at 230 MeV is shown. Blue and green symbols show the estimation using p+H and p+O channel, respectively. The dashed lines show the average of measurements. Shadow areas shows different proton scattering angles.

includes only the statistical uncertainty. The systematic uncertainty from beam charge determination was estimated as 2% and 20% in maximum for results at 230 and 392 incident energy, respectively. The result of present measurement is roughly consistent with that in reference, showing that the measurement and analysis is reliable.

3.3.5 Thickness of ice targets

We analyzed the proton elastic scattering on thin ice target and we used the cross section from the reference to evaluate the thickness of the target:

$$N_{\mathrm{t}} = \frac{N_{\mathrm{GR}}}{N_{\mathrm{b}}\epsilon_{\mathrm{GR}}\epsilon_{\mathrm{DAQ}}\Delta\Omega \frac{d\sigma}{d\Omega}} \; , \tag{3.37}$$

$$t = \frac{N_{\mathrm{t}}\cos\theta_{\mathrm{t}}M}{N_{\mathrm{A}}} \; . \tag{3.38}$$

Figure 3.37 shows the determined thickness of thin ice target thickness at 230 MeV. Blue and green symbols show the estimation using p+H and p+O channel, respectively. Shadow areas show the measurements at different proton scattering angles. The dashed lines show the average of measurements, where both of measurement gave a roughly consistent result of 27 mg/cm². In addition, no clear time dependence was observed, indicating the thickness of the ice target was stable.

Some of the possible reasons which may cause the fluctuation of the thickness measured at different runs have been checked and discussed in the following part. Figure 3.37 shows results at different GR angles as the shadow areas with different colors, where we didn't observe global shift for measurement at the same angle, showing that the fluctuation was not from the angular distribution of cross section we used. The fluctuations of results of p+H and p+O didn't have clear correlations, which indicates that a common beam transmission efficiency or DAQ efficiency fluctuation

is less likely as a cause of the fluctuation. One of remaining reason considered is the background and cut condition for the elastic scattering peak. Especially for p+H channel, the background from p+O channel mixed in the peak region of p+H. Therefore, we considered the result from p+O is more reliable.

In short, we evaluated the thickness of thin ice target was as 26.9±0.1 and 14.1±0.1 mg/cm^2 at 230 and 392 MeV incident energies, respectively. The values shows the result of p+O channel with only statistical uncertainty is included.

3.3.6 Efficiency of backward protons

In this subsection we discuss the efficiency of backward protons, detected by proton hodoscope (HODO). The total efficiency of proton ϵ_p is written as:

$$\epsilon_p = \epsilon_{\text{det}} \cdot \epsilon_{\text{PI}} , \tag{3.39}$$

where we considered the detection efficiency ϵ_{det} and particle identification (PI) efficiency (ϵ_{PI}) were both 100%.

As we discussed in subsection 3.2.1, depending on energy, we separated protons as two categories: "penetrating proton" as protons penetrating the dE counter and stopping at E counters and "stopping proton" as protons stopping at the dE counter. For penetrating protons, both PI methods, dE-E and E-TOF, can be applied. For stopping protons, only E-TOF method can be applied. Therefore, we used E-TOF PI for both penetrating and stopping protons for consistency in further analysis.

Detection efficiency of protons

Firstly we discuss the detection efficiency. Because dE blocks covered larger solid angle than E blocks, from geometry all penetrating protons which were detected by E blocks passed through dE blocks. With penetrating proton as denominator, we checked the detection efficiency of dE blocks.

Figure 3.38 shows the excitation energy spectrum of (p, pd) reaction at 392 MeV incident energy and 6.4° deuteron scattering angle as an example. Protons were measured by the E_1 block and E-TOF PI was applied. Black histogram shows the spectrum with E-TOF PI of the E_1 block and red histogram shows the spectrum with the same PI and anti-gate of the dE_1 block coincident timing. Panel (a) and panel (b) shows the same spectra with linear and logarithmic scale in vertical axis, respectively. We see that there is no structure for red histogram at around 4 MeV, which means all penetrated protons (from (p, pd) reaction to $^{14}N_{3.95}^{1+}$ final state and measured by E_1) gave signals in dE_1.

We integrated the number of events in $2 < E_{\text{ex}} < 6$ MeV region for black and red histogram, and calculated the ratio:

$$\frac{N^{\text{red}}_{2<E_{\text{ex}}<6}}{N^{\text{black}}_{2<E_{\text{ex}}<6}} = 1\% . \tag{3.40}$$

This shows the detection efficiency of dE_1 is larger than 99%. The 1% difference from 100% is considered as mainly due to the background in the denominator (penetrating
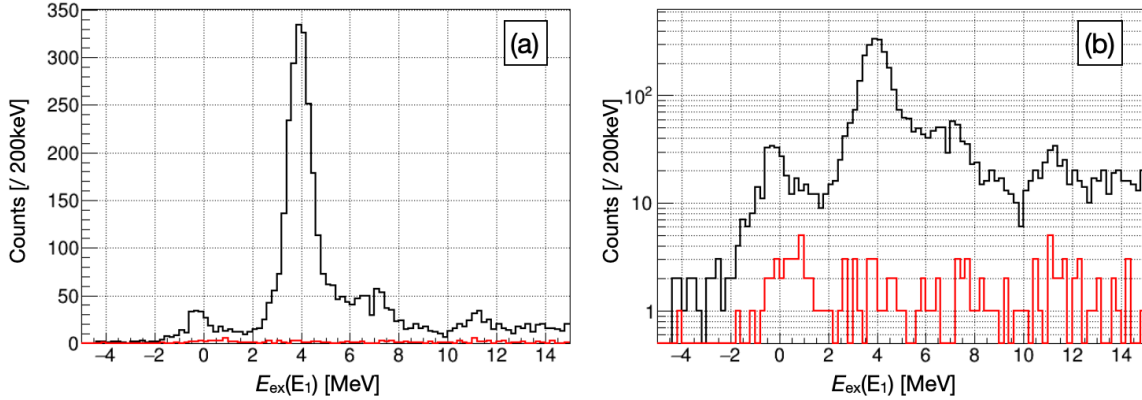
Figure 3.38: Figure shows the excitation energy spectrum of (p, pd) reaction at 392 MeV incident energy and 6.4° deuteron scattering angle. Protons were measured by the E_1 block and E-TOF PI was applied. Black histogram shows the spectrum with with E-TOF PI of the E_1 block and red histogram shows the spectrum with the same PI and anti-gate of the dE_1 block coincident timing. Panel (a) and panel (b) shows the same spectrum with linear and logarithmic scale in vertical axis, respectively.

protons measured by E_1), because only random distribution is seen in the red histogram in Fig. 3.38.

Therefore, we concluded that the detection efficiency of proton is close to 100% and the possible inefficiency was treated as systematic uncertainty.

PI efficiency of protons with E-TOF method

Secondly we discuss the PI efficiency of E-TOF method. For penetrating events, both E-TOF and dE-E PI methods can be applied. Therefore, we used penetrating protons with dE-E PI as denominator to check the PI efficiency of E-TOF method.

Figure 3.39 shows the excitation energy spectrum of (p, pd) reaction at 392 MeV incident energy and 6.4° deuteron scattering angle as an example. Black histogram shows the spectrum with dE-E PI of the E_1 block and red histogram shows the spectrum with the same PI and anti-gate of E-TOF PI of the E_1 block. We see that there is almost no events remaining for red histogram, indicating the efficiency of E-TOF PI selection is 100%

In short, we investigated the detection efficiency of dE_1, which is nearly 100%, so we assumed the detection efficiency of E blocks were also nearly 100%. We also investigated the PI efficiency of E_1, which is 100% and thus we assumed the PI efficiency of dE blocks was also 100%. Therefore, we concluded that the total efficiency of both penetrating and stoping protons is nearly 100%.
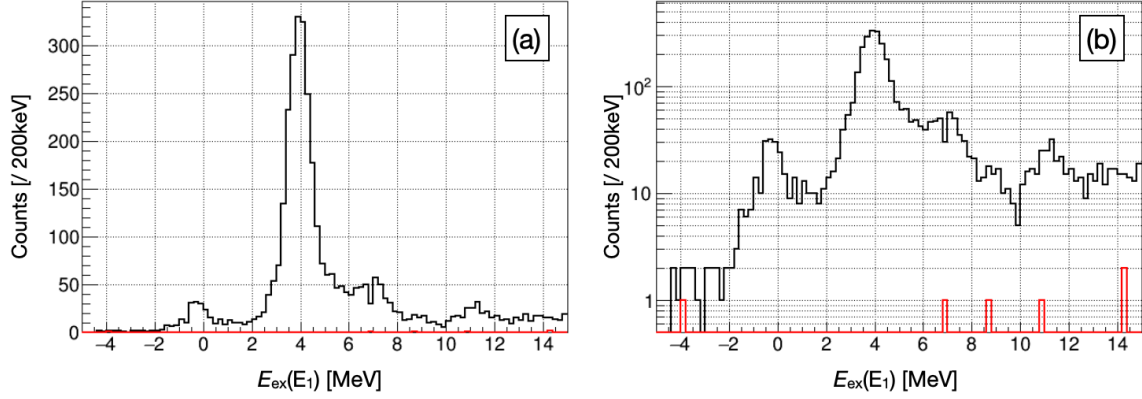
Figure 3.39: Figure shows the excitation energy spectrum of (p, pd) reaction at 392 MeV incident energy and 6.4° deuteron scattering angle. Protons were measured by the E_1 block and dE-E PI was applied. Black histogram shows the spectrum with with dE-E PI of the E_1 block and red histogram shows the spectrum with the same PI and anti-gate of E-TOF PI of the E_1 block. Panel (a) and panel (b) shows the same spectrum with linear and logarithmic scale in vertical axis, respectively.

3.3.7 Triple differential cross section

Triple differential cross section of (p, pd) reaction can be written as:

$$\frac{d^3\sigma}{d\Omega_d d\Omega_p dT_d} = \frac{N_{(p, pd)}}{N_b N_t \epsilon_{GR} \epsilon_{DAQ} \epsilon_p \Delta\Omega_d \Delta\Omega_p \Delta T_d} \tag{3.41}$$

where N_b, N_t, ϵ_{GR}, and ϵ_{DAQ} have the same definition in Eq. 3.34. T_d is the kinetic energy of deuteron. $N_{(p, pd)}$ is the total number of events within the range of $T_d \pm \frac{1}{2}\Delta T_d$ for a certain final state of (p, pd) reaction. We aim at the first 1+ excited state of ^{14}N with E_{ex}=3.95 MeV and thus we integrate the count from 2 to 6 MeV in the excitation energy spectrum. ϵ_p is the proton detection efficiency and set as 100% based on the discussion in subsection 3.3.6. Ω_p is the solid angle for proton detection, which varies for different detectors of HODO depending on the geometry. Ω_p is the solid angle for deuteron detection, restricted by the collimator size of GR.

Figure 3.40 shows the triple differential cross section for (p, pd) reaction populating to ^{14}N$^{1+}_{3.95}$ state at different angles. Panel (a) and (b) shows the data at $\theta_d = 6.4°$ and panel (c) and (d) shows the data at $\theta_d = 16.1°$. Symbols with different color shows the data with protons measured by different detectors of HODO. Filled and empty symbols shows the data of penetrating and stopping protons measured by E and dE blocks, respectively.

It should be noted that, only statistical uncertainty is shown in the figures and the maximum systematic uncertainty for results at 230 and 392 MeV was roughly estimated as 10% and 30%, respectively.
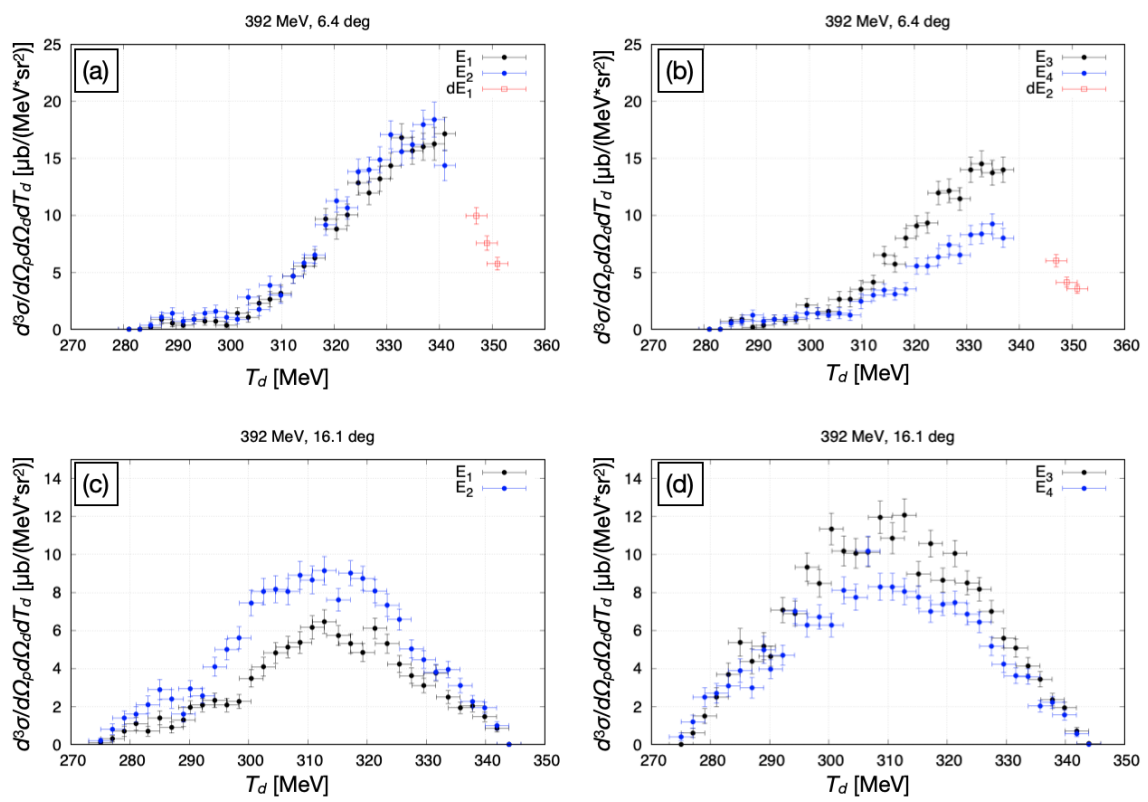
Figure 3.40: Figure shows the triple differential cross section for (p, pd) reaction populating to $^{14}N^{1+}_{3.95}$ state at different angles.
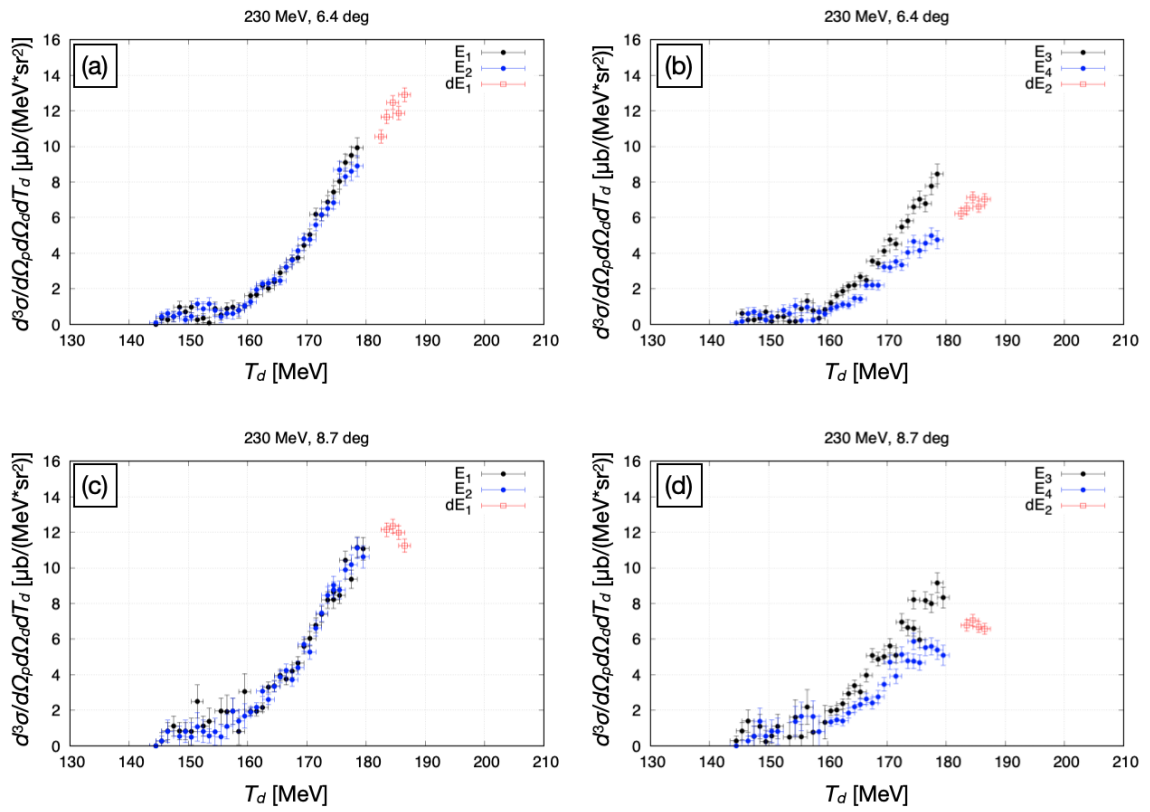
Figure 3.41: Figure shows the triple differential cross section for (p, pd) reaction populating to $^{14}N^{1+}_{3.95}$ state at different angles.
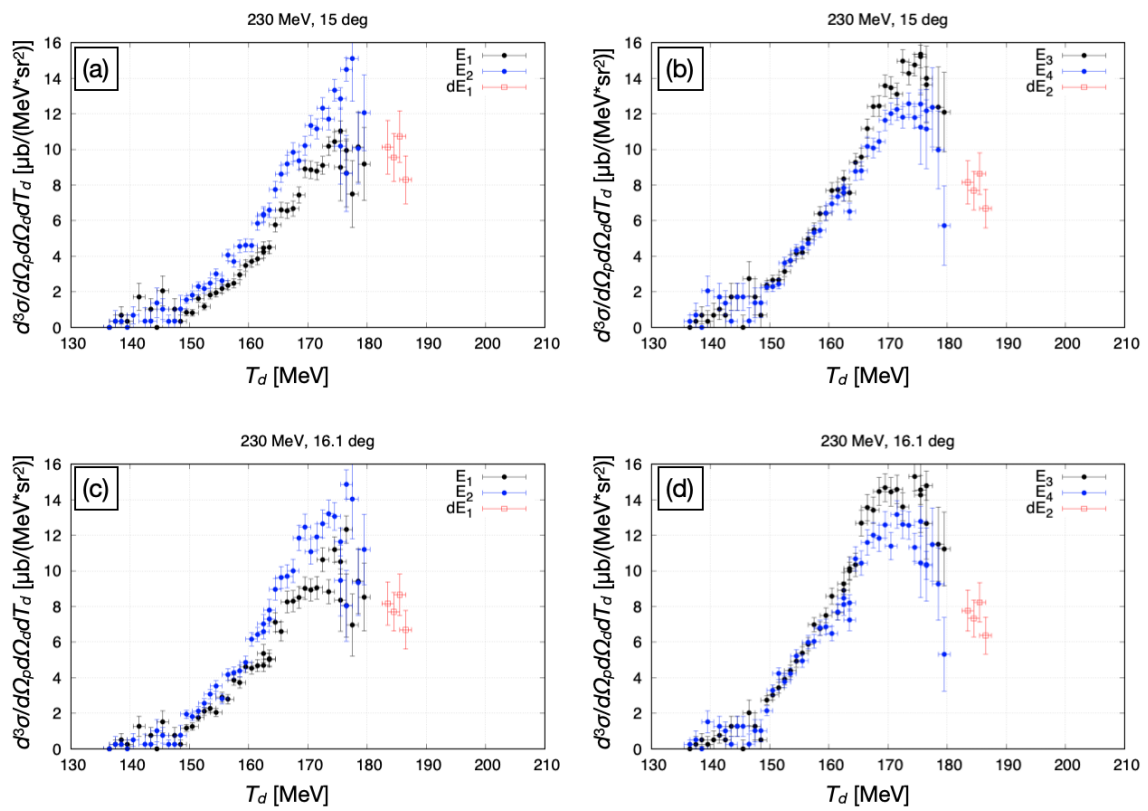
Figure 3.42: Figure shows the triple differential cross section for (p, pd) reaction populating to ${}^{14}N^{1+}_{3.95}$ state at different angles.

Chapter 4

Result Discussion

As presented in Chap. 3, we obtained mainly two experimental results, the excitation energy spectra of ^{16}O$(p, pd)^{14}$N reactions and the triple differential cross sections of reaction populating to ^{14}N$^{1^+}_{3.95}$ state. In this chapter we discuss the first result and present the related conclusions.

In the first Sec. 4.1 we present the discussion based on the cross section ratio of reactions populating to ^{14}N$^{0^+}_{2.31}$ and ^{14}N$^{1^+}_{3.95}$ states. With the confirmation of kinematics calculation as well as the stability check of the cross section ratio at recoilless condition, we present a summary of all available cross section ratios extracted from the excitation energy spectra. In the second Sec. 4.2 we interpret how tensor interactions change the cross section ratio. We also discuss the effect of reaction mechanism, in Sec. 4.3.

4.1   Cross section ratio

The missing mass spectra of ^{16}O$(p, pd)^{14}$N reactions at incident energies of 230 and 392 MeV and deuteron scattering angles from 6.4 to 16.1 degrees are summarized in Table 3.3. From kinematics, when the recoil ^{14}N has zero-momentum and the deuteron is detected at forward scattering angle, the momentum transfer is identical to the internal momentum of picked-up neutron. With different final states of ^{14}N, pn pairs with different spin and isospin (S, T) were studied. We aim at studying the momentum dependence of correlated pn pair with (1,0) and (1,0) configurations. As discussed in Fig. 1.13 in Chap. 1, from the final state of ^{14}N, we know that $(0, 1)$ and $(1, 0)$ pairs corresponds to ^{14}N$^{0^+}_{2.31}$ and ^{14}N$^{1^+}_{3.95}$ final states, respectively. We define the cross section ratio (R_{cs}) of reaction populating to ^{14}N$^{0^+}_{2.31}$ and ^{14}N$^{1^+}_{3.95}$ states as:

$$R_{cs} = \int_{\Delta T_d} \frac{d^3\sigma(^{14}\mathrm{N}^{0^+}_{2.31})}{d\Omega_d d\Omega_p dT_d} dT_d / \int_{\Delta T_d} \frac{d^3\sigma(^{14}\mathrm{N}^{1^+}_{3.95})}{d\Omega_d d\Omega_p dT_d} dT_d \tag{4.1}$$

In the first subsection 4.1.1 we present a confirmation of reaction calculation and then present a summary of the settings which covers the recoilless condition.

In the second subsection 4.1.2 we present the deduced cross section ratio with the selection of recoilless condition.
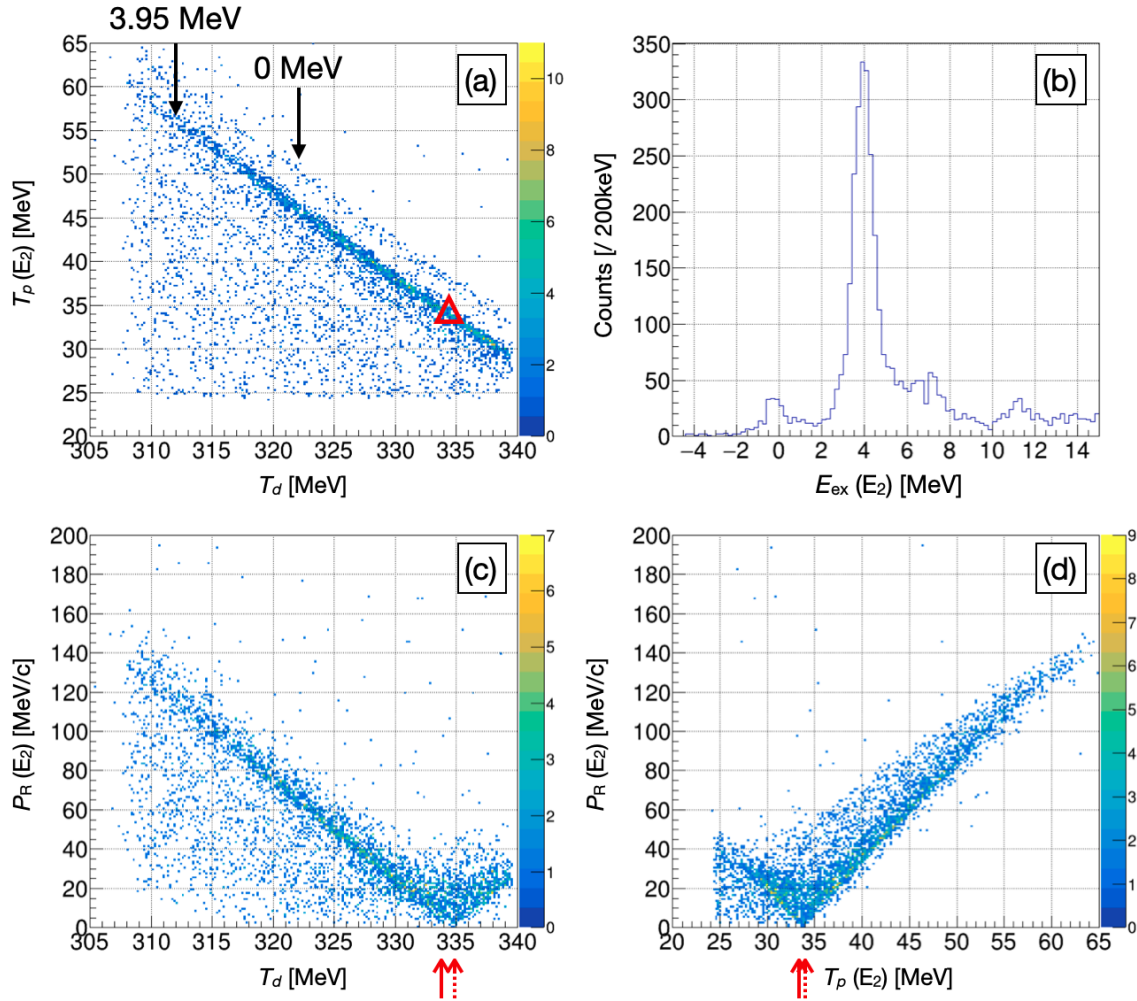
Figure 4.1: Panel (a) shows the scatter plot between the kinetic energy of protons and deuterons at $T_{\rm b} = 392$ MeV, $\theta_d = 6.4°$, $\theta_p = 149.2°$. Panel (b) shows the corresponding excitation energy spectrum. Panel (c) and (d) shows the scatter plots between residual momentum and proton and deuteron kinetic energy.

4.1.1   Recoilless condition

In this subsection we aim at selecting the condition where physics discussion is simple. We firstly show a confirmation of kinematics calculation and then summarize the recoilless condition for the following discussion.

Figure 4.1 shows several scatter plots and the corresponding excitation spectrum of the data at $T_{\rm b} = 392$ MeV, $\theta_d = 6.4°$, $\theta_p = 149.2°$ as examples. In this setting, the recoilless condition is covered by E_2 block (considering proton angle and energy). Panel (a) shows the scatter plot between the kinetic energy of deuterons (T_d) and protons ($T_p(E_2)$, obtained from E_2 block). We see the most intensive line, which is the $^{14}N_{3.95}^{1^+}$ state and another line at the right side, which is $^{14}N_0^{1^+}$ ground state. Red triangle shows the region of recoilless condition. The corresponding excitation energy spectrum is shown in panel (b).

Panel (c) and (d) shows the scatter plots between residual (^{14}N) momentum ($P_{\rm R}$)

Table 4.1: Recoilless condition summary

T_{b}	θ_d	θ_p	T_d	T_d	P_{GR}	Hodo
MeV	degree	degree	MeV	MeV	MeV/c	
392	6.4	149.2	334.3	33.8	1143	E_2
					1187	E_2
392	16.1	113.2	309.1	59.0	1143	E_4
230	6.4	148.9	187.9	18.2	840	dE_1
230	8.7	139.0	185.6	20.5	840	dE_1
230	15.0	116.4	179.9	30.2	811	E_4
230	16.1	113.0	173.7	32.4	811	E_4

and proton and deuteron kinetic energy. The residual momentum is calculated from proton and deuteron energy and angle, with energy and momentum conservation law (equations are presented in Appendix A). From the kinematic calculation, the recoilless conditions for $^{14}\mathrm{N}^{1^+}_{3.95}$ state and $^{14}\mathrm{N}^{0^+}_{2.31}$ state are $\theta_d = 6.4°$, $\theta_p = 149.1°$, $T_d = 333.7$ MeV, $T_p = 33.6$ MeV and $\theta_d = 6.4°$, $\theta_p = 149.3°$, $T_d = 334.9$ MeV, $T_p = 34.1$ MeV, respectively. From panel (c) and (d) we see the recoilless point, the cross point of the "check mark", appears at the position consistent with the kinematics calculation. Solid and dashed red arrows indicate the kinetic energies of deuterons (in panel (c)) and protons (in panel (d)) at recoilless condition of $^{14}\mathrm{N}^{1^+}_{3.95}$ and $^{14}\mathrm{N}^{0^+}_{2.31}$ states, respectively.

In addition, we see the width of different sides of the correlation from recoilless point in panel(c) and (d) is asymmetric. For a square shape of detector, similar size in vertical direction would cover different solid angle due to $d\Omega = \sin\theta d\theta d\phi$. At present condition, $\theta_p > 90°$, so the larger θ corresponds to smaller $\sin\theta$ and the solid angle covered by the detector is larger. From kinematic calculation, larger T_d (and smaller T_p) corresponds to larger θ_p. Therefore, we conclude that the observed asymmetric shape comes from geometry and kinematics.

Table 4.1 shows the summary of recoilless condition for incident energies and deuteron scattering angles that we have measured. The excitation energy of $^{14}\mathrm{N}$ is assumed as 3.13 MeV, the average of two states of our interest. We pick up the data which covers the recoilless condition, and discuss the ratio in following part.

4.1.2 Ratio at recoilless condition

In this subsection we present the kinematic selection for the excitation energy spectrum covering the recoilless condition and then present the cross section ratio deduced from the fitting in the spectrum. Since the difference between two excited state is small, the kinematics of reactions populating to them are similar. Therefore, the discussion on the ratio of cross section of two states is free from the systematic uncertainty of efficiencies, number of beam proton and so on. As we shown in Fig. 3.17 and Eq. 3.25 in Chap. 3, from fitting we obtained the amplitude of several low-lying states (A_i), where the second and third one (A_2 and A_3) is the amplitude of the peak at 2.31 and

Table 4.2: Ratio summary

| T_b | θ_d | P_{rel} | R_{cs} | error |
MeV	degree	fm^{-1}		
392	6.4	1.29	0.017	0.005
230	6.4	0.94	0.064	0.009
230	15.0	1.22	0.048	0.017
230	16.1	1.26	0.08	0.03

3.95 MeV, respectively. Therefore, we extracted the cross section ratio from:

$$R_{cs} = \frac{A_2}{A_3} \tag{4.2}$$

Figure 4.2 shows the data at 392 MeV, $\theta_{GR} = 6.4°$ and $P_{GR} = 1143$ MeV/c as an example. Left panel shows the correlation between proton and deuteron kinetic energy. Panel (a) shows the full acceptance data at this setting. Red triangle shows the position of the recoilless condition. In this setting, deuteron energy range restricts the range of observation. In some case the limit comes from proton energies. We make a selection with $K_1 \leq T_d - T_p \leq K_2$ (K_1 and K_2 as the upper and lower limit), which helps to avoid the distortion of spectrum shape due to proton and deuteron energy limitation. Panel (c) and (e) shows the example of selection with different K_1 and K_2. Right panels show the corresponding excitation energy spectra. Fitting with gaussian function (Eq. 3.25) was performed and the result is shown in the spectrum. The ratio R_{cs} was obtained for different K_1 and K_2. As a result, we find that the cross section ratio (R_{cs}) in the second and third condition is close to each other, but the first one is deviated. This is considered as because the first condition covers region far from recoilless condition, and the second and third one cover mainly recoilless condition.

Figure 4.3 shows the data at 392 MeV, $\theta_{GR} = 6.4°$ and $P_{GR} = 1187$ MeV/c, which has an overlap with $P_{GR} = 1143$ MeV/c setting near the recoilless condition. The definition and selection is the same as that in 4.2. We see that at the same region, we obtained consistent ratio from measurement at different magnetic setting. This confirms the stability of ratio at recoilless condition. An additional confirmation is that the ratio at 392 MeV, 6.4 degree is close to that at 392 MeV, 8.7 degree ($R = 0.023$), measured at another experiment E443 [33].

Table 4.2 shows a summary of ratio at data where suitable selection cover recoilless condition can be applied. In some of the data we observe large distortion of spectrum shape and consider it is not suitable to include for present discussion (for example, panel (d) in Fig. 3.20).

4.2 Effects of tensor interactions

In this section we investigate the role of tensor interactions in changing the cross section ratio between $^{14}N_{2.31}^{0^+}$ and $^{14}N_{3.95}^{1^+}$ final states at different momentum transfer. We discuss the ratio obtained from data at 6.4 degree, with 230 and 392 MeV incident
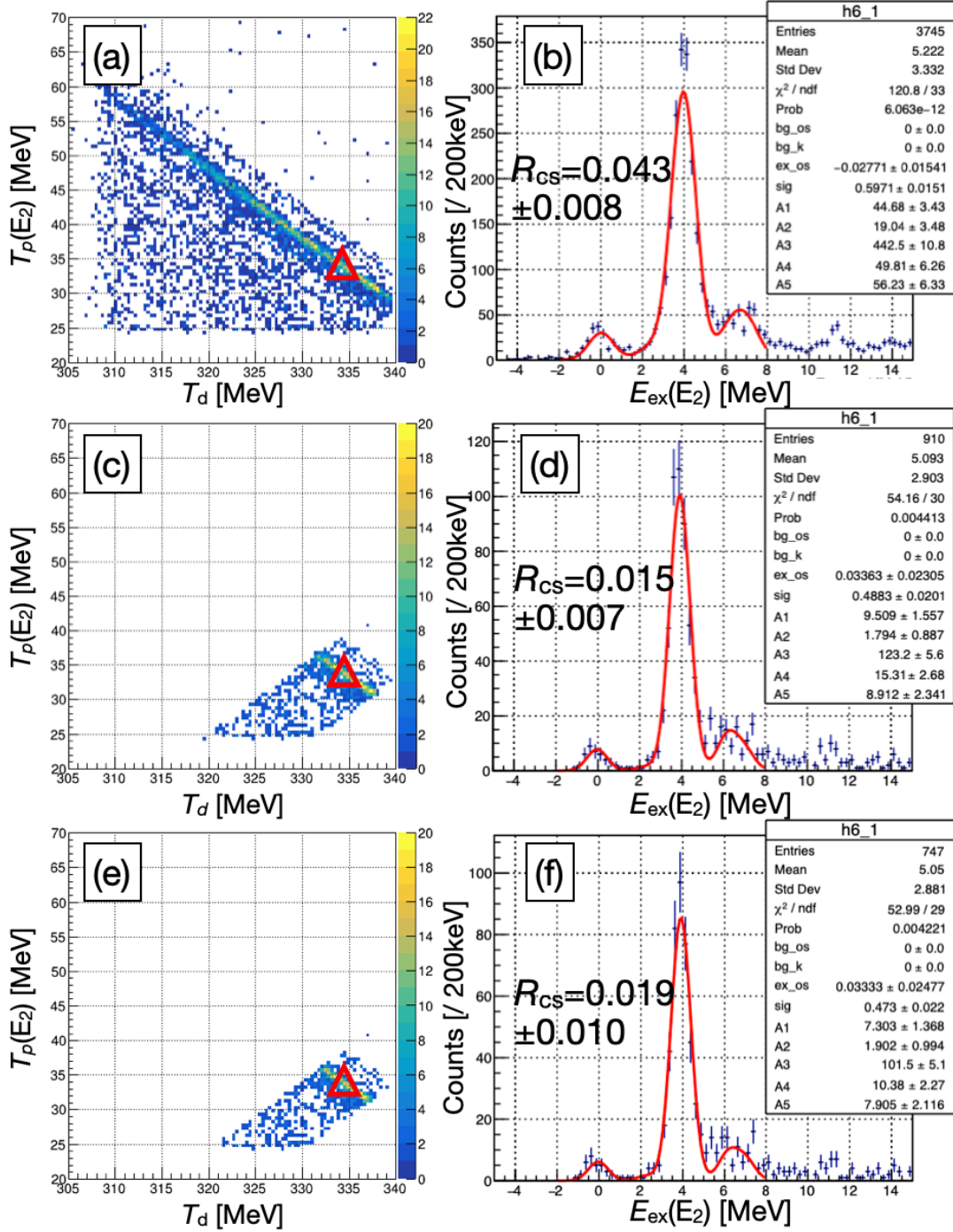
Figure 4.2: Figure shows the proton and deuteron kinetic energy correlation as well as the corresponding spectrum: panel (a) and (b): full acceptance; panel (c) and (d): $295 \leq T_d - T_p \leq 307$ MeV; panel (e) and (f): $296 \leq T_d - T_p \leq 306$. The data at 392 MeV, $\theta_{\mathrm{GR}} = 6.4°$ and $P_{\mathrm{GR}} = 1143$ MeV/c is shown as an example.
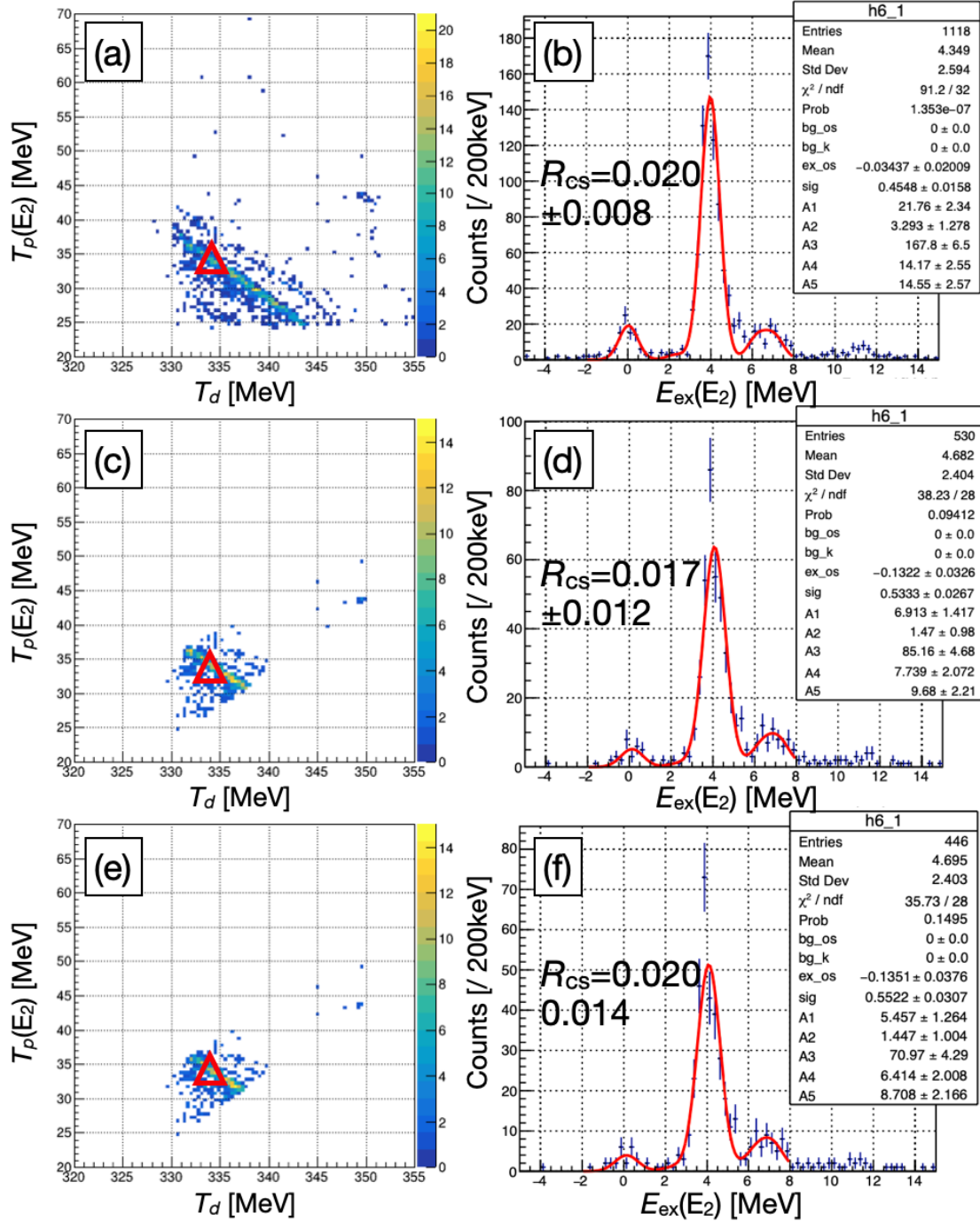
Figure 4.3: See Fig. 4.2 for definition. The data at 392 MeV, $\theta_{\mathrm{GR}} = 6.4°$ and another magnetic setting $P_{\mathrm{GR}} = 1187$ MeV/c is shown as an example.
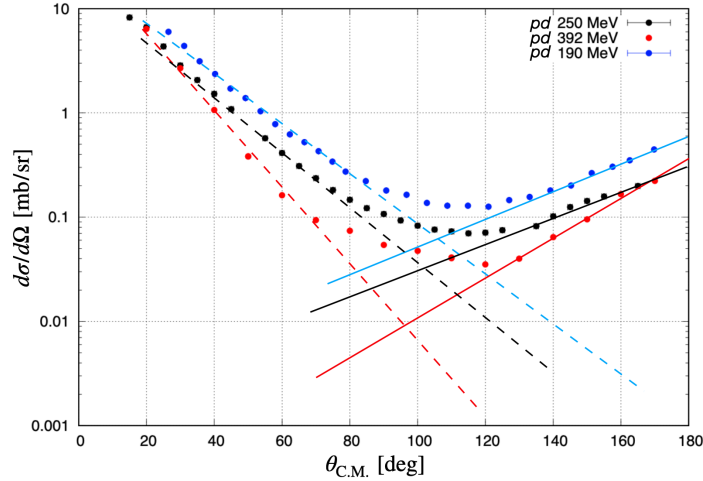
Figure 4.4: Angular distribution of $p + d$ scattering cross section is shown for the data at three incident energies: 250 MeV [57] in black, 392 MeV [45] in red and 190 MeV [43] in blue symbols, respectively. Soild and dash lines are simply extrapolation from the backward and forward peak, respectively.

energies, where we can safely assume that the pick-up mechanism is the main reaction mechanism and other reaction mechanisms are minimal.

In the first subsection 4.2.1 we discuss the experimental approach, high-momentum transfer (p, pd) reaction with deuterons detected at forward scattering angles, which is in favor of pick-up mechanism. Based on this mechanism, we probe the high-momentum pn pair selectively. In the second subsection 4.2.2 we present a discussion of the spin and isospin (S, T) character of the pn pair in $^{16}O(p, pd)^{14}N$ reactions. From the conservation of spin and isospin, we obtain the spin and isospin character of pn pair in the initial state, by selecting the finial state of ^{14}N. With different (S,T) configuration, we are able to distinguish tensor interactions and central interactions. In the third subsection 4.2.3, we present a method to calculate the ratio between the amount of pn pairs with different configurations. It is shown that we can extract the contribution of tensor interactions from the ratio. Finally, we present the importance of tensor interactions from this analysis.

4.2.1   Pick-up mechanism

Figure 4.4 shows the angular distribution of $p+d$ elastic cross section at several incident energies [43, 45, 57]. The backward peak was understood as the pick-up mechanism [46], where neutrons inside deuteron match the momentum of incident protons, then deuterons are emitted at forward scattering angles, corresponding to the backward scattering angles of proton. In such a mechanism, the internal momenta of picked-up neutron equal to the momentum transfer in the reaction.

For (p, pd) reactions, if the recoil particle has zero-momentum (recoilless condition), the total momentum of pn pair can be considered as also zero, which means the momentum of correlated proton is opposite to the neutron. As a result, the relative

Table 4.3: Spin and isospin character of pn pairs

Initial state ^{16}O: (J^π, T)	Pair in initial state pn: (S,T)	Final state ^{14}N: (J^π, T), E_{ex} [MeV]	d: (S,T)
$(0^+, 0)$	$(1,0)$	$(1^+, 0)$, 3.95	$(1,0)$
$(0^+, 0)$	$(0,1)$	$(0^+, 1)$, 2.31	$(1,0)$

momentum (P_{rel}) of pn pair is indicated by the momentum transfer ($\vec{q}$) of the reaction:

$$P_{\text{rel}} = |\vec{q}| \, , \tag{4.3}$$

Detail explanation is presented in Appendix A.

Angular distribution of $p + d$ scattering cross section is shown for the data at three incident energies: 250 MeV [57] in black, 392 MeV [45] in red and 190 MeV [43] in blue symbols, respectively. We simply extrapolate the forward and backward peak by dash and solid lines, representing the contribution from knock-out and pick-up mechanism, respectively. Deuteron scattering angle $\theta_d = 6.4°$ corresponds to center of mass angle $\theta_{\text{CM}} = 167°$, where we can simply assume the reaction is dominated by the pick-up mechanism. Therefore, for the comparison of two cross section ratios at deuteron scattering $\theta_d = 6.4°$, we consider it is free from the effect of reaction mechanism.

4.2.2   Spin and isospin character of proton-neutron pair

As we have discussed in Chap. 1, we can pin down the spin and isospin (S,T) configuration of a pn pair in the initial state in ^{16}O from the spin-parity of the final state of ^{14}N. Figure 1.13 shows a schematic view of the mechanism of ^{16}O$(p,pd)^{14}$N reactions [33]. Table 4.3 shows a summary of (S,T) configuration of the pn pair probed in ^{16}O$(p,pd)^{14}$N reactions.

As discussed in Chap. 1, while central interactions contribute to both (1,0) and (0,1) pairs, tensor interactions contribute only to (1,0) pairs. In the following section we discuss the contribution from different interactions to pairs with different configuration.

4.2.3   Relative momentum distribution and tensor contribution

In this part we discuss the relative momentum distribution of zero-total-momentum (back-to-back) nucleon pairs and investigate the contribution of tensor interactions from theoretical studies.

Figure 4.5 shows the relative momentum distribution of two-nucleon pair from calculations with the linked and number conserving cluster expansion with correlated wave functions [41]. The distribution was calculated for both pn and pp pairs, as shown in solid and dash line in Fig. 4.5, respectively. The horizontal axis is momentum (P_{rel}) of two nucleons in a pair and the vertical axis is the density ($n(P_{\text{rel}}, P_{\text{total}} = 0)$) of the pair with the back-to-back condition (total momentum (P_{total}) of the pair is zero). We see that the difference of pn and pp becomes larger for the $P_{\text{rel}} > 1.5\text{fm}^{-1}$, which is understood as effects of tensor interactions. The insert shows the ratio R_{pN} which is
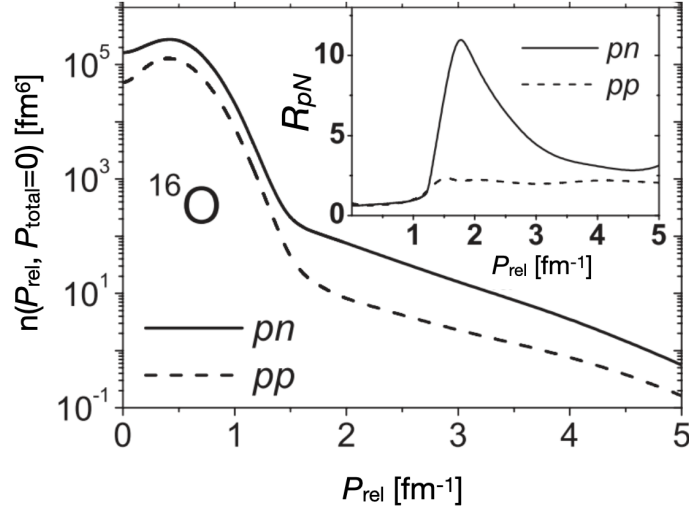
Figure 4.5: The relative momentum distribution is shown for ^{16}O with a condition of back-to-back nucleons, in solid and dash line for pn and pp pair, respectively. The inset shows the ratio of total density to the density with only central correlations, see text for detail information. The figure is from Ref. [41].
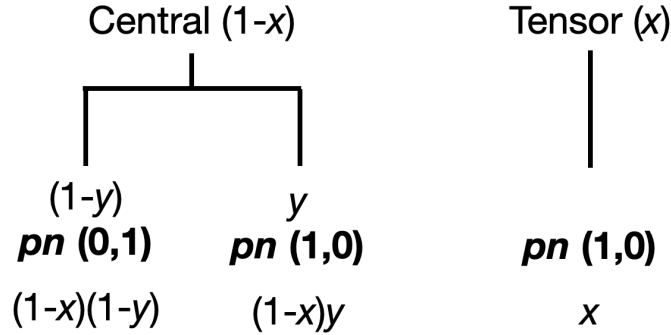
Figure 4.6: A simple illustration for the contribution of central and tensor interactions to pn pair with different spin and isospin configurations.

obtained from:

$$R_{pN} = \frac{n_{pN}(P_{\text{rel}}, P_{\text{total}} = 0)}{n_{pN}^{\text{central}}(P_{\text{rel}}, P_{\text{total}} = 0)} \tag{4.4}$$

where n_{pN} is the total density and n_{pN}^{central} is the corresponding density calculated with only central correlations. The ratio R_{pN} shows the contribution of other than central interactions, which is tensor interactions. We see from above 1 fm^{-1}, R_{pN} increases rapidly and reaches the maximum at around 2 fm^{-1}, where $R_{pN} \sim 10$. Around 2 fm^{-1}, the amount of central interactions in relative momentum distribution is around 10%, ands the tensor contribution is around 90%.

In the following part, we present a model to investigate how tensor tensor interactions change the cross section ratio.

We focus on the pn pair, so that we can compare to the measurement of (p, pd)

reactions directly. Because tensor interactions contribute to only (1,0) channel and central interactions contribute to both, the probability of finding a (1,0) pair and (0,1) pair would change if tensor contributions change.

We illustrate the effect of central and tensor interactions on pn pairs in Fig. 4.6. First of all we assume the relative momentum distribution is dominated by tensor and central interactions only. We assume the contribution of tensor interactions to the distribution is $x = x(P_{\rm rel})$ depending only on $P_{\rm rel}$, then we simply have the contribution of central interactions, as $(1 - x)$. Since tensor interactions only contribute to $S = 1$ state, the amount of pn pair with (1,0) configuration from tensor interactions is proportional to x. Meanwhile, the central interactions contribute to both (1,0) and (0,1) pairs, we assume the fraction of central contribution to (1,0) and (0,1) pairs is y and $(1 - y)$, respectively. With the illustration in Fig. 4.6, we can calculate the pair ratio of amount between (0,1) and (1,0) pairs:

$$R_N(P_{\rm rel}) = \frac{N_{(0,1)}(P_{\rm rel})}{N_{(1,0)}(P_{\rm rel})} = \frac{(1 - y)(1 - x)}{y(1 - x) + x} \ , \tag{4.5}$$

where R_N is defined as the ratio of probability of finding a pn pair with (0,1) and (1,0) configuration. $N_{(0,1)}(P_{\rm rel})$ and $N_{(1,0)}(P_{\rm rel})$) represents the probability of finding (0,1) and (1,0) pair with certain relative momentum in ^{16}O ground state. We consider that y is a constant but x has a relative momentum dependence, due to effects of different interactions. Therefore, $R_N(P_{\rm rel})$ is also a function of relative momentum.

We consider the differential cross section of $^{16}{\rm O}(p, pd)^{14}{\rm N}^{1+}_{3.95}$ reaction is governed by the free space $p + d$ scattering since the incident energy is much larger than the binding energy of "d+^{14}N" system. Taking into account the expression in [46, 58] and two-body final state differential cross section, we assume the triple differential cross section can be written as:

$$\frac{d^3\sigma(^{14}{\rm N}^{1+}_{3.95})}{d\Omega_d d\Omega_p dT_d} = F_{1+} \cdot N_{(1,0)}(P_{\rm rel}) \cdot N_d(P_{\rm rel}) \ , \tag{4.6}$$

$$\frac{d^3\sigma(^{14}{\rm N}^{0+}_{2.31})}{d\Omega_d d\Omega_p dT_d} = F_{0+} \cdot N_{(0,1)}(P_{\rm rel}) \cdot N_d(P_{\rm rel}) \ , \tag{4.7}$$

where F_{1+} and F_{0+} is the kinematic and phase space factor of reaction populating $^{14}{\rm N}^{1+}_{3.95}$ and $^{14}{\rm N}^{0+}_{2.31}$ final states, respectively. N_d denotes the momentum distribution of deuteron. We note that the final state is similar, except small difference of excitation energy. Thus we assume the kinematic and phase space factor is similar for two states. In addition, deuteron momentum distribution is the same for two channels. Therefore, taking a ratio between Eq. 4.6 and 4.7 there are only $N_{(1,0)}$ and $N_{(0,1)}$ terms remaining. In other words, the cross section ratio can be approximated by the pair ratio:

$$R_{\rm cs} \ \sim \ R_{\rm N} \tag{4.8}$$

We compare the cross section ratio at $\theta_d = 6.4°$ and $T_{\rm b} = 392$ and 230 MeV, which corresponds to $P_{\rm rel} = 1.29$ fm^{-1} and 0.94 fm^{-1}, respectively. Figure 4.7 shows the $x - y$ correlation with certain $R_{\rm cs}$. Red line indicates the correlation with $R_{\rm cs}(P_{\rm rel} = 1.29) = 0.017$ and blue line indicates the correlation with $R_{\rm cs}(P_{\rm rel} = 0.94) = 0.066$.
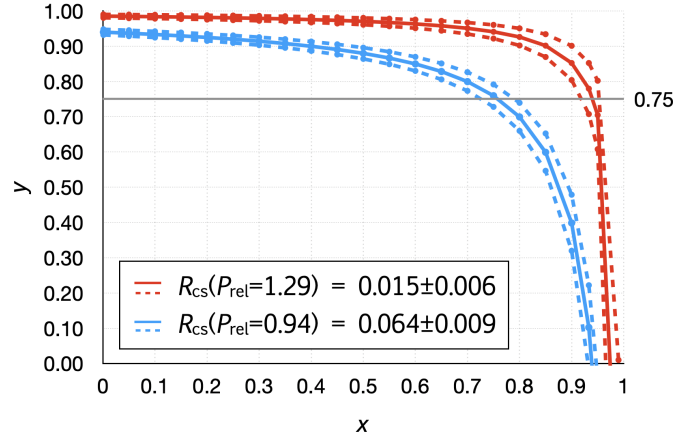
Figure 4.7: Figure shows x and y correlation with certain cross section ratio.

Table 4.4: Cross section ratio and tensor contributions

T_{b}	θ_d	P_{rel}	R_{cs}	error	$x(P_{\mathrm{rel}})$
MeV	degree	fm^{-1}		stat.	if $y = 0.75$
230	6.4	0.94	0.064	0.009	76%
392	6.4	1.29	0.015	0.006	94%

Dash lines show the upper and lower limit of R_{cs} with statistics uncertainty taken into account.

It should be noted that y is the central contribution to (1,0) pair, considered as a constant. x is the tensor contribution of our interest. From Fig. 4.7 we see that with a constant value of y, the increase of x from small P_{rel} to large P_{rel} leads to the decrease of R_{cs} (except y is very large).

Since central interactions contribute to different spin and isospin channels equally, one can make reasonable assumption with $y = 0.75$ (based on the spin triplet and singlet). Therefore, we obtain the tensor contribution $x(P_{\mathrm{rel}} = 0.94) = 76\%$ and $x(P_{\mathrm{rel}} = 1.29) = 94\%$, as summarized in Table 4.4. We see that the change of tensor contribution is responsible to the change of ratio at different momentum, which is consistent with the theoretical finding that tensor interactions induced short-range nucleon pairs with high-relative-momentum. In addition, the difference shows large tensor contributions in most possible value of P_{rel}.

As a short summary of this section, from above calculation, we conclude that the observed ratio difference at the same forward scattering angle of neutrons and different incident energies and momentum transfer is an effect of tensor interactions.

Table 4.5: Ratio at similar momentum transfer

$T_{\rm b}$ MeV	θ_d degree	$\theta_{\rm CM}$ degree	$R_{\rm cs}^{\rm exp}$	$R_{\rm cs}^{\rm exp}$ error	$P_{\rm rel}$ fm^{-1}	$x(P_{\rm rel})$	$R_{\rm cs}^{\rm cal}$	$R_{\rm cs}^{\rm cal}$ error
75	37.5	104.5	0.36	0.05	1.18	88%	0.030	0.008
230	15.0	149.2	0.048	0.017	1.22	91%	0.026	0.008
230	16.1	147.0	0.08	0.03	1.26	93%	0.019	0.008
392	6.4	166.6	0.015	0.007	1.29	94%	0.015	0.007
392	8.7	161.8	0.02	0.001	1.37	98%	0.004	0.007

4.3   Investigation of reaction mechanism

Another important question to this experiment is how does the reaction mechanism affect the ratio we observed. We have illustrated how tensor interactions change the cross section ratio at different relative momentum, with the data at the same deuteron scattering angle, where we assumed the reaction is dominated by pick-up mechanism.

To check effects other than tensor interactions, we compare the ratio at similar relative momentum but different incident energies and deuteron scattering angles, as summarized in the left part of Table 4.5. Using the x value shown in Table 4.4, we simply interpolate to obtain $x(P_{\rm rel} = 1.22) = 91\%$ and $x(P_{\rm rel} = 1.26) = 93\%$. In addition, we include the result from [33] and [48], which was taken at $T_{\rm b} = 392$ MeV, $\theta_d = 8.7$ ° and $T_{\rm b} = 75$ MeV, $\theta_d = 37.5$ °, respectively. For data at $T_{\rm b} = 392$ MeV, $\theta_d = 8.7$ °, $x(P_{\rm rel} = 1.37)$ is from extrapolate as 98%. The sixth and seventh columns in Table. 4.5 show the relative-momentum and corresponding tensor contribution obtain from simple interpolation (or extrapolation for $P_{\rm rel} = 1.37$). We obtained the calculated cross section ratio ($R_{\rm cs}^{\rm cal}$), assuming there is no effect from reaction mechanism (knock-out), as summarized in the last two columns of Table 4.5.

Figure 4.8 shows the experimental and calculated cross section ratios in filled and open symbols, respectively. Panel (a) shows the result at 392 and 230 MeV incident energies in blue and red symbols, respectively. Because we assume no effects from knock-out mechanism in the calculation, the difference between calculation and experimental results shows the effect of knock-out mechanism (shown in arrows). We see that at larger angle the effect becomes larger.

Panel (b) of Fig. 4.8 includes another result at $T_{\rm b} = 75$ MeV in green symbols [48]. We see the experimental result goes to around one third, which is understood due to at large scattering angles of deuterons, the reaction is dominated by knock-out mechanism. In the knock-out domain region, since the relative-momentum is no longer connected with the "momentum transfer" in pick-up reaction, the cross section ratio is independent of relative-momentum. From simple counting, because (0,1) is spin singlet and (1,0) is spin triplet, the ratio becomes one third.

We see that at larger scattering angles, the experimental cross section ratios are larger than that from calculation. It should be noted that, at the same incident energy, larger scattering angle corresponds to larger momentum transfer and thus larger contribution is expected from tensor interactions. One would expect the cross section ratio becomes smaller due to tensor interactions. However, at larger scattering angle
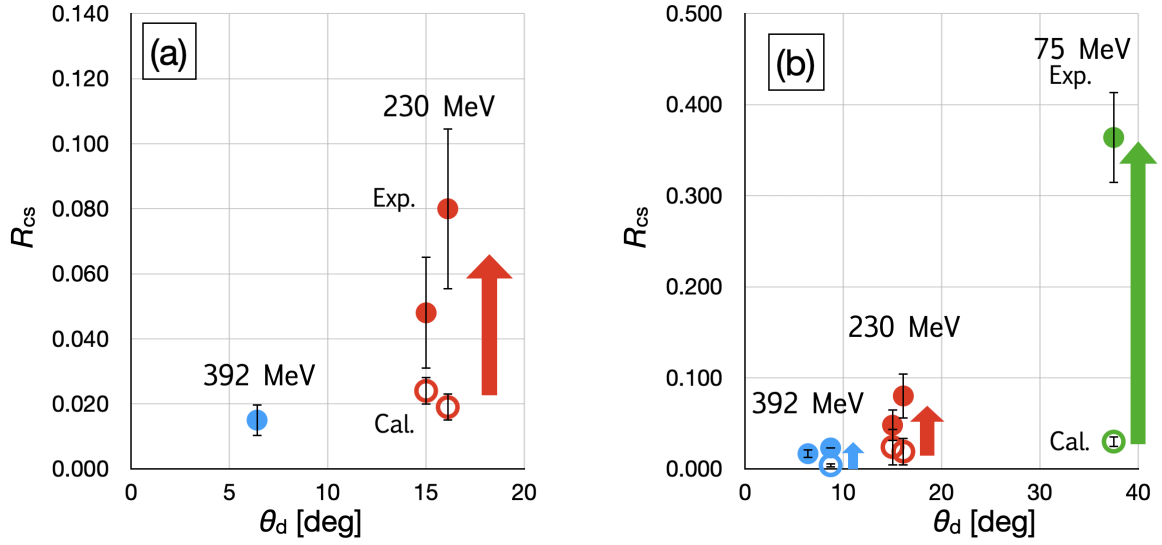
Figure 4.8: Figure shows the cross section ratio at different scattering angle of deuterons with similar relative momentum. Blue symbols show R_{cs} at $T_b = 392$ MeV. Red symbols show R_{cs} at $T_b = 230$ MeV. Filled symbols show the cross section ratio obtained from data. Open symbols show the cross section ratio calculated from P_{rel} assuming no knock-out mechanisms effects. Panel (a) shows results at $T_b = 230$ and 392 MeV. Panel (b) shows results in larger range including data at from Ref. [33] and [48].

due to the effect of competing reaction mechanism, the observed cross section might become larger.

In short, we investigate the effect of reaction mechanism, using the data at similar relative momentum region. Consistent with our understanding that the effect of competing reaction mechanism decreases the observed reduction of cross section ratio from small to large relative momentum due to tensor interactions. Therefore, it is desirable to measure deuterons at as much as forward angle and discuss the effect systematically at the same angle.

h6_1	
Entries	910
Mean	5.093
Std Dev	2.903
χ^2 / ndf	54.16 / 30
Prob	0.004413
bg_os	0 ± 0.0
bg_k	0 ± 0.0
ex_os	0.03363 ± 0.02305
sig	0.4883 ± 0.0201
A1	9.509 ± 1.557
A2	1.794 ± 0.887
A3	123.2 ± 5.6
A4	15.31 ± 2.68
A5	8.912 ± 2.341
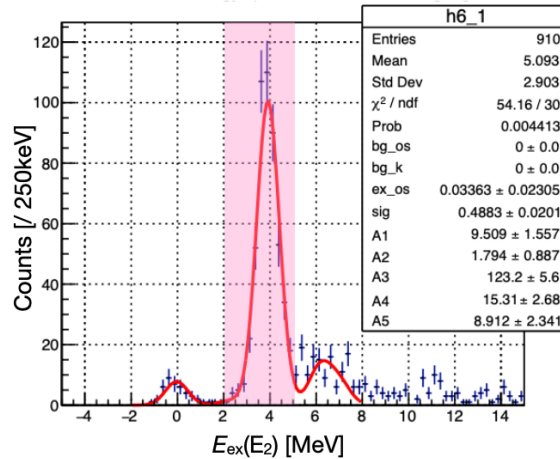
Figure 4.9: Figure shows the excitation energy spectrum of ^{14}N at $T_{\mathrm{b}} = 392$ MeV, $\theta_d = 6.4°$, $P_{\mathrm{GR}} = 1143$ MeV/c and $295 \leq T_d - T_p \leq 307$ MeV as an example. A integral is made in the region from 2 to 5 MeV as shown in red shadow area.

4.4   Systematic uncertainty

Because we discuss the result based on the relative value (cross section ratio), the uncertainty of absolute value (such as beam intensity, target thickness and so on) is canceled out. Because the cross section of ^{14}N$^{0+}_{2.31}$ final state is small and the energy resolution was not small enough to separate two states, we determined the ratio by fitting. Therefore, the remaining systematic uncertainty of experimental results might come from the fitting. In this section we present a discussion on the systematic uncertainty of ratio determination via fitting.

4.4.1   Discrepancy at the peak center

First we present an investigation of the discrepancy at the peak center region. As it can be seen in the right panels of Fig. 4.2 and 4.3, the fitting at the peak center of ^{14}N$^{1+}_{3.95}$ state is smaller than the data. We check the difference of the amplitude between fitting and integrating. Because the amplitude of ^{14}N$^{0+}_{2.31}$ peak is small, we fix it with the value from fitting in this investigation.

Figure 4.9 shows the excitation energy spectrum of ^{14}N at $T_{\mathrm{b}} = 392$ MeV, $\theta_d = 6.4°$, $P_{\mathrm{GR}} = 1143$ MeV/c and $295 \leq T_d - T_p \leq 307$ MeV as an example. We integraled the region from 2 to 5 MeV and obtained 128.3 counts. The amplitude of ^{14}N$^{0+}_{2.31}$ peak is 1.8 counts. Thus we obtained 126.5 counts for ^{14}N$^{1+}_{3.95}$ peak from integrating. Since the amplitude is 123.2 from fitting, the difference between fitting and integrating is around 3%, which is much smaller than the statistical uncertainty.

We also checked other data and it is found that the discrepancy of fitting at the peak center is negligible compared with the statistical uncertainty. We conclude that the small discrepancy of fitting and data at the peak center does not affect the discussion and conclusion.
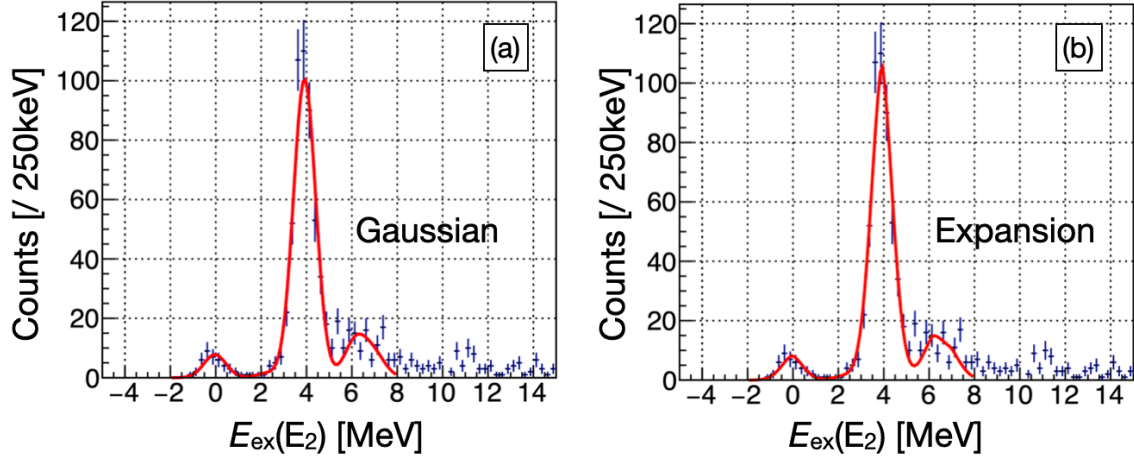
Figure 4.10: Figure shows the excitation energy spectrum of ^{14}N at $T_{\rm b} = 392$ MeV, $\theta_d = 6.4°$, $P_{\rm GR} = 1143$ MeV/c and $295 \leq T_d - T_p \leq 307$ MeV as an example. Fitting with gaussian function and the first order expansion is shown in panel (a) and (b), respectively.

4.4.2 Peak shape investigation

Secondly we investigate the peak shape.

As it can be seen in the right panels of Fig. 4.2 and 4.3, the fitting reproduced the peak shape for both left and right side well, which indicates the assumption of fitting functions is reasonable, regarding the symmetric shape of peaks in excitation energy spectra.

We investigate the systematic uncertainty with different fitting functions:

$$f(x) = \sum_{i=1}^{5} \frac{A_i}{\sqrt{2\pi}\sigma} \cdot (1 + b|x + x_{\rm os} - x_i|)e^{-\frac{(x+x_{\rm os}-x_i)^2}{2\sigma^2}}, \tag{4.9}$$

where b denotes the first order distortion parameter from gaussian function and other parameters share the same definition with that in Eq. 3.25.

Figure 4.10 shows the excitation energy spectrum of ^{14}N at $T_{\rm b} = 392$ MeV, $\theta_d = 6.4°$, $P_{\rm GR} = 1143$ MeV/c and $295 \leq T_d - T_p \leq 307$ MeV as an example. Fitting with gaussian function and the first order expansion is shown in panel (a) and (b), respectively. The fitting with two functions are similar. The obtained result is summarized in Table 4.6. χ^2 and NDF denote the total chi-square and the number of degree of freedom in the fitting, respectively. The reduced chi-square (χ^2/NDF) of two fitting is the same. The difference of cross section ratio ($R_{\rm cs}$) obtained from two fitting is much smaller than the statistical uncertainty. We have also checked other data and obtained similar conclusion.

As a result, we conclude that the systematic uncertainty that we have investigated is negligible compared with the statistical uncertainty and does not affect the discussion and conclusion.

Table 4.6: Results of fitting with two functions

Name	Gaussian	Expansion
χ^2/NDF	$54.16/30$	$52.9/29$
A_2	1.8 ± 0.9	2.0 ± 1.1
A_3	123 ± 6	150 ± 22
R_{cs}	0.015 ± 0.007	0.013 ± 0.008

Chapter 5

Summary and perspectives

Demands of understanding nuclear tensor interactions become more and more urgent, because of the rapidly developing knowledge of nuclei far from the stability line. New methods to investigate effects of tensor interactions in nuclei have been developed with high-energy proton experiments, namely (p,d) and (p,pd) reactions. Those studies reveal an existence of high-momentum nucleons due to the short-range nature of tensor interactions. The recent experiment [33] has shown an important evidence of high-momentum nucleons in ^{16}O nucleus. However, two questions are raised for understanding it clearly.

One of the questions is the change of the contribution of tensor interactions on the nucleon momentum. Tensor interactions contribute to the relative-momentum $(P_{\text{rel}} = \frac{1}{2}|\vec{P}_p - \vec{P}_n|)$ distribution of pn pairs at around 2 fm^{-1} of relative-momentum in maximum. Observing the change of tensor contributions as expected by theoretical studies has basic importance to confirm effects of tensor interactions. The other question is a complication of extracting the real momentum distribution from experimental cross sections. Contribution of two main reaction mechanisms, pick-up and knock-out, depends on the scattering angles of deuterons. Only in pick-up mechanism the relative-momentum of correlated pairs is related with the momentum transfer. Although experiments were performed in the pick-up domain region, where extraction of momentum distribution is reasonably expected, no proof has been made. It is thus important to study the reaction in regions where other reactions mechanism may contribute to the cross sections.

We have measured ^{16}O$(p,pd)^{14}$N reactions at 230 and 392 MeV incident energies and several scattering angles of deuterons systematically. Self-supported thin ice targets were used as ^{16}O targets. With thin ice targets, no background from contaminant was observed. A plastic scintillator array called "HODO" was developed and used to measure backward going protons in coincidence with forward going deuterons measured by Grand Raiden spectrometer. From the energies and scattering angles of protons and deuterons, we reconstructed the missing mass spectra of ^{16}O$(p,pd)^{14}$N and extracted the cross sections to ^{14}N$^{0+}_{2.31}$ and ^{14}N$^{1+}_{3.95}$ states, which correspond to a pn pair with $(S,T) = (0,1)$ and $(1,0)$ configurations, respectively. Because tensor interactions contribute to $(1,0)$ pairs selectively, the cross section ratio of two final states was used as an indicator of contribution of tensor interactions. We extracted the cross section ratio of two states with recoilless condition (total momentum of pn pair is also zero), where

the relative-momentum in the pair is identical with the momentum transfer. We discussed the incident energies and scattering angles dependence of the ratio at different and similar momentum transfer, respectively, and obtain mainly two conclusions.

With present data, for the first time we are able to discuss the cross section ratio at different momentum transfer but the same scattering angle of deuterons, where the discussion is free from the influence of competing reaction mechanism. The cross section ratio decreases with factor four from momentum transfer 0.94 to 1.29 fm^{-1}. A simple model predicts that the tensor contribution for pn pair momentum distribution at around 1.3 fm^{-1} is around 94%.

Present data also enable for the first time the comparison for cross section ratio at similar momentum transfer but different deuteron scattering angles, where effects from tensor interactions are expected to be similar. A clear difference between expected ratio and observed ratio is found and the difference increases with deuteron scattering angles. We concluded that the effect of competing reaction mechanism (knock-out) decreases the observed effect from tensor interactions. With a simple calculation, we found that due to the effect of competing reaction mechanism, the ratio could increase with a factor 2 or 3 from deuteron scattering angle 6.4° to 16°, which is comparable with the effect of tensor interactions if considering the transfer momentum difference at the same incident energy and varying the angle similarly.

We have shown effects of tensor interactions and competing mechanism separately, which confirms present experimental approach is a powerful tool to isolate and investigate tensor interactions experimentally. More studies are demanded to answer several questions. In the following, we discuss the perspective for future studies.

Present studies confirms tensor interactions are changing the cross section ratios at different momentum transfer. The importance of tensor interaction in inducing high-momentum nucleons is shown by the preference on (1,0) pn pair. With real reaction calculations, such as distorted-wave impulse-approximation (DWIA), the strength of tensor interactions in ^{16}O could be compared with that in deuteron directly. Such quantitative discussion may fed back to structure model with explicit treatment for tensor interactions.

In order to analyze experimental data via DWIA, accurate differential cross section is required. Present data at 230 MeV incident energy suffers from huge proton background in GR detectors and possible beam loss before the scattering chamber, thus large systematic uncertainty remains for present results. In addition due to materials between the target and proton detector, low energy proton could not be measured, thus the shape of differential cross section is not well constrained for data at 230 MeV incident energy. More detailed investigation and new measurement would help to pin down these questions.

As shown by several calculations, tensor interactions would have maximum effect at around 2 fm^{-1}. From present study, it is desirable to investigate the effect of tensor interactions at small scattering angle of deuterons. For instance, setting $\theta_d = 6.4°$, one would need $T_{\rm b} = 1$ GeV to reach 2 fm^{-1}. At such high energy, the yield of coincident measurements would be much smaller than that in present experiment, making big challenge for detector systems. In addition, higher accuracy is demanded for new measurements. At relative momentum region around 2 fm^{-1}, the cross section ratio is expected to be smaller due to tensor interactions. From this sense the accuracy
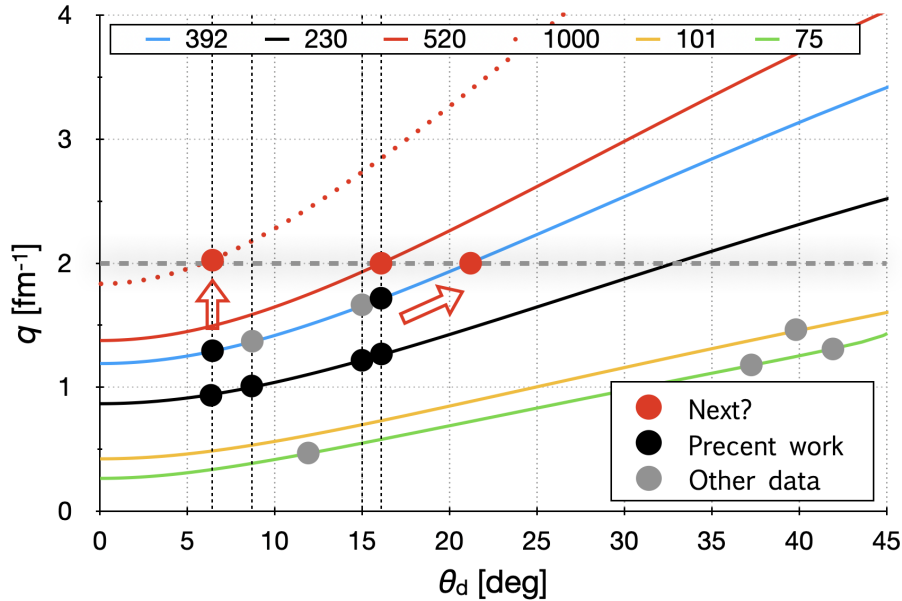
Figure 5.1: Momentum transfer of ^{16}O(p, pd) reaction is shown for various incident energies and scattering angles of deuteron.

of cross section ratio becomes important for new measurements. On the other hand, the smaller cross section demands for higher beam current, challenging the proton detectors placed near by scattering chamber. As a result, both energy resolution and background suppression should be considered carefully for proton detectors in future measurements.

One possibility is to consider measuring the reaction at larger deuteron scattering angles so that with smaller incident energy the 2 fm^{-1} could be approached. For example at $\theta_d = 16.1°$, one need $T_b = 520$ MeV to cover the momentum region with $\theta_d = 6.4°$ and $T_b = 1$ GeV. Figure 5.1 shows the momentum transfer of ^{16}O(p, pd) reaction with recoilless condition. However, the effect of competing reaction mechanism should be understood quantitatively for a reasonable discussion. Large distortion was found in the spectra at $T_b = 392$ MeV and $\theta_d = 15.0°$ and $16.1°$, but not found in that at $T_b = 230$ MeV with the same deuteron scattering angles. More investigation would help to understand the complexity of reaction mechanisms and advise for new measurements.

Another direction is to pin down the cross section ratio at small incident energy and deuteron scattering angles. Such measurement is important to complete the mapping of cross section ratio at different momentum regions as well.

Besides the investigation on tensor interactions in ^{16}O, it is also very interesting to explore the study to heavier nuclei such as ^{40}Ca and ^{48}Ca. In addition, study of tensor interactions in exotic nuclei is of highly importance in the future. Since the contribution of tensor interactions are strongest in $N = Z$ nuclei and decrease in nuclei far from the stability line, systematic studies of nuclear structure from stability line to far from stability line are important. Changes of magic numbers in neutron-rich nuclei and unexpected mixing of the wave-functions in nuclei far from stability line would be

signs of importance of tensor interactions in nuclei.

Acknowledgement

I feel fortunate to have received support from many individuals throughout my doctoral studies. I would like to take this opportunity to express my sincere gratitude to everyone, even though words may fall short in conveying the depth of my appreciation.

My grateful thank goes first and foremost to my supervisor, Prof. Isao Tanihata. Recently, I came across an article outlining the qualities of a good supervisor, and I was not surprised to discover that Prof. Tanihata embodies nearly all the characteristics listed [59]. No matter how much I express, I cannot fully convey my gratitude to him. Still, I want to take this opportunity to thank him, especially for the time he has invested and the encouragement he has provided.

Prof. Tanihata always found time to discuss with me, no matter how busy he was. These discussions were crucial in aligning my work and studies towards the goal, as illustrated in Fig. 5.2. My path to the goal has been winding and zigzagged, and the conversations with Prof. Tanihata work as turning point to make my path converged toward the goal. He always immediately identifies the key points of my questions in whatever the fields, such as detector techniques, data analysis, the essence of physics and so on. Moreover, he dedicated a significant amount of time to meticulously proofread my thesis, enhancing its scientific quality and readability.

Prof. Tanihata demanded strictness from me while consistently providing encouragement. I vividly recall an occasion when we went out to take photos of the Milky Way for the first time. After I set my camera near the Great Wall, a powerful gust of wind sent my camera tumbling down to the base, several meters below the wall. I managed to retrieve my camera utilizing the limited tools at our disposal. Before I could even lament my camera, he offered words of encouragement, saying, 'Now, I believe you can conduct experiments successfully.' He was never stingy with encouragement, countless times reassuring me that I was the best when I doubted myself.
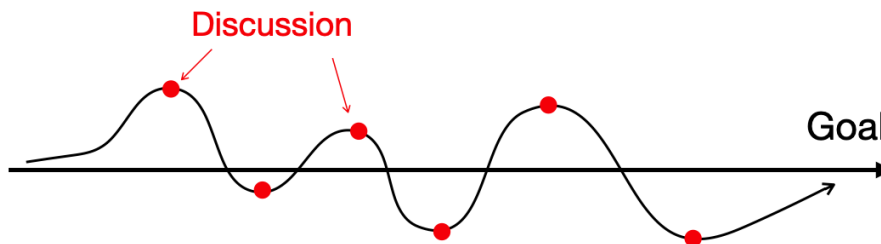

Figure 5.2: My path to the goal has been winding and zigzagged. The dicussions with Prof. Tanihata make my path turn back to a correct direction.

I extend my sincere thanks to Prof. Satoru Terashima, my "second supervisor" and my most important collaborator in doctoral study. He is an experimental expert, and the present study is a continuation of his research. It is my good fortune to have his guidance and collaboration. Throughout the entire process, from preparing and conducting the experiment to analyzing the data, I felt like an advance guard and I could explore and engage in anything I found interesting, with the confidence that Prof. Terashima had a firm grasp on everything and would assist in resolving any challenges I encountered. Without his devoted supports, I wouldn't have been able to complete data analysis, results discussion, and thesis writing within a year after the experiment.

I am deeply grateful to Prof. Nori Aoi for agreeing to become my official supervisor. Prof. Aoi established a conducive research environment for me, enabling me to concentrate fully in learning and research without distractions. When I discussed with Prof. Aoi, he posed seemingly simple yet challenging questions. Contemplating how to address his questions always inspired me and deepen my understanding.

I would like to express my sincere appreciation to Prof. Ong Hooi Jin. Prof. Ong has taken care of me in both research and daily life since I came to Japan. His meticulous work attitude and endless patience towards others have become my role model.

Special thanks to all referees of this thesis – Prof. Nori Aoi, Prof. Astushi Tamii, Prof. Takatsugu Ishikawa and Prof. Shinsuke Ota and Prof. Kenichi Yoshida, for fruitful discussions and invaluable comments on this thesis.

Thanks are due to the Scholarship of Graduate School of Science, Daiyukyo Foundation of Interational Exchange Assistance & Resaerch, RCNP and Chinese Government Scholarship for the financial supports during my studying in Japan. Without these supports, I would not be able to concentrate fully on my study and reseach.

I would like to thank all the collaborators of RCNP-E552 and E481 experiments, for their great contributions to perform both experiments successfully. Special thanks to Prof. Atsushi Tamii, Nobuyuki Kobayashi, and others for their dedicated efforts in various developments at WS course, RCNP. Acknowledgments to Prof. Takahiro Kawabata and his team for the development of the cool target system and allowing us to use it. Appreciation to Mr. Hidemoto Yoshida for his support in various aspects such as detector development, experiment preparation and so on. Thanks to Dr. Dinh Trong Tran for his contributions to preparing and maintaining the cool target system. Gratitude to Dr. Tatsuya Furuno for his work on the development of electronics and analyzer. Thank Xiaodong Xu, Bingshui Gao, Zhichao Zhang, Bingfeng Lv, JunBing Ma, Yutian Li, Jiawei Cai, Yuya Honda, He Wang, Juzo Zenihiro, Masanori Dozono, Shigno Ogio, YiMing Gao, Jacob Bekker, and others for their outstanding efforts during the experiments. Furthermore, I extend my appreciation to the RCNP Ring Cyclotron staff for delivering the stable proton beams throughout the experiments, particularly for their remarkable achievement in providing the 230 MeV proton beam for the first time.

I have been studied at RCNP, Osaka University for 6 years. I want to express my sincere gratitude to all professors, staffs and lab mates at RCNP and professors and staffs at the Graduate School of Science, Osaka University. Their support and companionship have made my study enjoyable. I would like to extend my thanks to my friends in Japan, with whose accompany I have had a happy and fruitful life in

Japan.

I owe a special debt of gratitude to my dear family. Thank my beloved mother for the 100% trust, supports and love that enable me to pursue my interests in a foreign country. I extend my heartfelt thanks to my girlfriend, Dr. Yijie Hu. I started my doctoral course from April, 2020. Due to the pandemic and some realistic reasons, our experiment was postponed for two years and finally conducted on April and May, 2023. Without her, I would never have expected to finish my doctoral study at this momentum. She is the source of my courage.

At the end, to myself, thanks for the days and nights.

Appendix A

Reaction kinematics

In this appendix we present the relevant formulas for two-body and three-body final state reactions in Sec. A.1 and A.2, respectively. Formulas for two-body final state reactions were used mainly in the momentum calibration of GR analysis. Formulas for three-body final state reactions were used both in the design of the experiment and data analysis.

A.1   Two-body reaction

The two-body kinematic can be described in Fig. A.1 within the laboratory system (LAB). Here "A" and "B" represent the target nucleus and recoil nucleus, respectively, while "a" and "b" denote the projectile nucleus and projectile-like nucleus. The angle θ_b and θ_B signify the polar angles of "b" and "B" in LAB, respectively. From the momentum conservation, two-body final state reaction is always coplanar, thus the reaction plane can rotate freely along beam direction and we can ignore the azimuth angle.

In relativity, the total energy E can be expressed as

$$E = T + M \ , \tag{A.1}$$

where T is kinematic energy, M is the mass of a particle, which is the sum of the
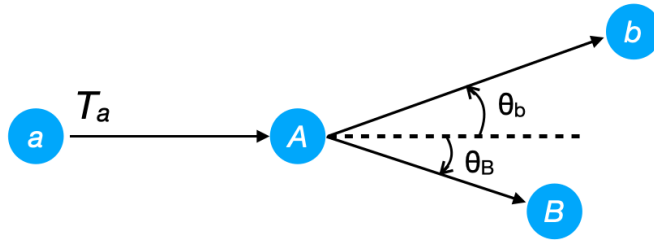
Figure A.1: Two-body Kinematics.

ground state mass M_{gs} and excitation energy E_{ex}:

$$M = M_{\mathrm{gs}} + E_{\mathrm{ex}} . \tag{A.2}$$

The total energy can be also expressed as:

$$E^2 = P^2 + M^2 , \tag{A.3}$$

where P is the magnitude of momentum vector ($P = |\vec{P}|$).

Here we use natural unit, with:

$$\hbar = c = 1 . \tag{A.4}$$

From the conservation law of energy and momentum, we obtain:

$$E_a + E_A = E_b + E_B , \tag{A.5}$$
$$\vec{P_a} + \vec{P_A} = \vec{P_b} + \vec{P_B} . \tag{A.6}$$

Using the polar angles, the equation of momentum conservation can be written as:

$$P_a = P_b \cdot \cos\theta_b + P_B \cdot \cos\theta_B , \tag{A.7}$$
$$P_b \cdot \sin\theta_b = P_B \cdot \sin\theta_B . \tag{A.8}$$

With all M known (including the excitation energy of particle "B"), at certain incident energy T_a and scattering angle θ_b, we can solve the equations and obtain all unknown variables:

$$P_b = \frac{-C_2 \pm \sqrt{C_2^2 - 4C_1 C_3}}{2C_1} , \tag{A.9}$$

with:

$$C_0 = P_a^2 + M_B^2 - M_b^2 - (E_a + E_A)^2 , \tag{A.10}$$
$$C_1 = 4P_a^2 \cos\theta_b{}^2 - 4(E_a + E_A)^2 , \tag{A.11}$$
$$C_2 = -4P_a \cos\theta_b \cdot C_0 , \tag{A.12}$$
$$C_3 = C_0^2 - 4M_b^2(E_a + E_A)^2 . \tag{A.13}$$

The momentum transfer in a transfer reaction is defined as the difference between the momentum of outgoing detected particle "b" and incident particle "a" as $\vec{q} = \vec{P_b} - \vec{P_a}$, and is identical with the internal momentum of picked-up nucleon. Therefore, in a pick-up reaction, the internal momentum of picked-up nucleon is indicated by the momentum transfer.

In the experiment, based on the incident energy and scattering angle of particle "b", as well as the excitation energy of low-lying discrete states of residual nuclei "B", we obtained the momentum of "b". We adjusted the magnetic rigidity of GR to cover this momentum. With discrete states measured, we calibrated the position of particles at GR focal plane to momentum, as shown in subsection 3.1.4.

A.2 Three-body reaction

In this section we present the formulas for the three-body final state reaction $A(a, bc)B$. In the first subsection A.2.1 we discuss a special condition where the recoil particle has zero momentum. In such cases, the kinematics becomes similar to that of the two-body final state reaction. Then we present the formulas for experimental case in subsection A.2.2.

A.2.1 Non-recoil case

With the same definition as in Sec. A.1 and one additional outgoing particle "c", we rewrite the equations of conservation laws:

$$E_a + E_A = E_b + E_c + E_B \ , \tag{A.14}$$
$$\vec{P_a} + \vec{P_A} = \vec{P_b} + \vec{P_c} + \vec{P_B} \ . \tag{A.15}$$

In the recoilless condition, particle "B" is at rest:

$$P_B = 0 \tag{A.16}$$
$$T_B = 0 \ . \tag{A.17}$$

Then we have:

$$E_a + M_A = E_b + E_c + M_B \ , \tag{A.18}$$
$$\vec{P_a} + \vec{P_A} = \vec{P_b} + \vec{P_c} \ . \tag{A.19}$$

The kinematics becomes similar with that of two-body final state. Similarly with all mass known and certain incident energy and polar angle of particle "b", we can calculate all unknown variables:

$$P_b = \frac{-C_2 \pm \sqrt{C_2^2 - 4C_1C_3}}{2C_1} \ , \tag{A.20}$$

with:

$$D_1 \ = M_A + M_a - M_B + T_a \ , \tag{A.21}$$
$$D_2 \ = D_1^2 - M_c^2 + M_b^2 - T_a^2 - 2T_aM_a \ , \tag{A.22}$$
$$C_1 \ = D_1^2 - \cos{\theta_b}^2(T_a^2 + 2T_aM_a) \ , \tag{A.23}$$
$$C_2 \ = -D_2 \cos\theta_b \sqrt{T_a^2 + 2T_aM_a} \ , \tag{A.24}$$
$$C_3 \ = D_1^2 M_b^2 - \frac{K_2^2}{4} \ . \tag{A.25}$$

Specially for ^{16}O$(p, pd)^{14}$N reaction with deuteron at small polar angle, the reaction is dominated by pick-up mechanism and can be illustrated in Fig. A.2. Similarly the momentum transfer $\vec{q}$ in the reaction is identical with the internal momentum of picked-
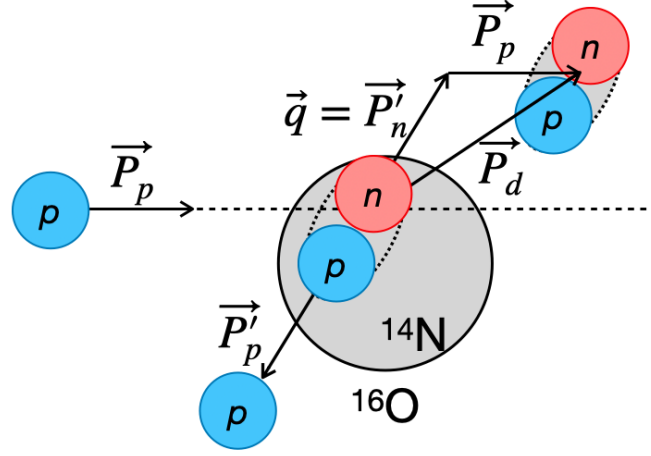
Figure A.2: Figure shows an illustration of (p, pd) reactions.

up neutron $\vec{P'_n}$:

$$\vec{q} = \vec{P'_n} \tag{A.26}$$

In addition, in the recoilless condition, we have:

$$P_B = 0 \, , \tag{A.27}$$

$$P_{\text{total}} = |\vec{P'_p} + \vec{P'_n}| = 0, \tag{A.28}$$

where $\vec{P'_p}$ is the internal momentum of outgoing proton and P_{total} is the total momentum of $p - n$ pair. Therefore, we obtain:

$$\vec{P'_p} = -\vec{P'_n} = -\vec{q} \, . \tag{A.29}$$

The relative momentum (P_{rel}) is defined as the momentum of one nucleon in the center of mass of two-nucleon system and we obtain the relationship between P_{rel} and $\vec{q}$:

$$P_{\text{rel}} = \frac{1}{2}|\vec{P'_n} - \vec{P'_p}| = |\vec{q}| \tag{A.30}$$

We see that in the recoilless condition, via (p, pd) reactions we are able to probe the $p - n$ pair with certain relative momentum $(P_{\text{rel}} = |\vec{q}|)$ and zero total momentum $(P_{\text{total}} = |\vec{P'_n} + \vec{P'_p}| = 0)$. Therefore, pick-up dominated (p, pd) reactions at the recoilless condition provide a unique tool to study the high-relative-momentum nucleon pair selectively.

Based on the equations presented above and the relative momentum that we aimed to measure, we determined the incident energy and scattering angles when designing the experiment.

A.2.2   Experimental case

Here we present the equation for reconstructing the excitation energy spectrum from the scattering angle and energy of protons and deuterons in both data analysis and Monte Carlo simulation. In the experiment, the residual particle ^{14}N possesses certain momentum. By measuring protons and deuterons simultaneously, we can reconstruct the missing mass of residual nuclei, as well as its momentum.

We define the forward going particle detected by GR as "scatter particle" (sca), and the backward going particle detected by HODO as "recoil particle" (rec). The undetected residual particle is called "residual particle" (res).

From GR analysis we obtained the momentum (P_{sca}, from Eq. 3.17 in subsection 3.1.4) and the polar angle (θ_{sca}, the same with θ_{TA} of Eq. 3.13 in subsection 3.1.3) of the scatter particle (deuteron). From HODO analysis, we obtained the kinetic energy (T_{rec}, the same with T_p of Eq. 3.21 in subsection 3.2.2) of the recoil particle (proton). We obtain the momentum of recoil particle:

$$P_{\text{rec}} = \sqrt{(T_{\text{rec}} + M_{\text{rec}})^2 - M_{\text{rec}}^2} \ . \tag{A.31}$$

The polar angle (θ_{rec}) of recoil particle is approximated by the angle from the beam direction to the center of each detector of HODO ($\theta_{\text{dE}_{1,2}}$ or $\theta_{\text{E}_{1\sim4}}$, summarized in Table 3.1).

From momentum conservation we have:

$$\vec{P}_{\text{b}} + \vec{P}_{\text{TA}} = \vec{P}_{\text{sca}} + \vec{P}_{\text{rec}} + \vec{P}_{\text{res}} \ , \tag{A.32}$$

where, $\vec{P}_{\text{b}}$ and $\vec{P}_{\text{TA}}$ denote the momentum of beam and target particle respectively.

Because the detectors for protons and deuterons were set at the same (horizontal) plane and the (vertical) acceptance of detectors is small, we ignore the azimuth angle (coplanar) and rewrite Eq. A.32 in beam direction and transverse direction:

$$P_{\text{b}} = \cos\theta_{\text{sca}} \cdot P_{\text{sca}} + \cos\theta_{\text{rec}} \cdot P_{\text{rec}} + P_{\text{Z,res}} \ , \tag{A.33}$$

$$P_{\text{T,res}} = |\sin\theta_{\text{sca}} \cdot P_{\text{sca}} - \sin\theta_{\text{rec}} \cdot P_{\text{rec}}| \ , \tag{A.34}$$

where $P_i = |\vec{P}_i|$ denotes the magnitude of momentum vector. $P_{\text{Z,res}}$ and $P_{\text{T,res}}$ denote the momentum of residual particle in beam and transverse direction, respectively.

We obtain the momentum of residual particle (P_{res}):

$$P_{\text{res}} = \sqrt{P_{\text{Z,res}}^2 + P_{\text{T,res}}^2} \ . \tag{A.35}$$

We confirmed the consistency of calculation by checking the recoilless condition ($P_{\text{res}} = 0$) in subsection 4.1.1 of Chap. 4.

From energy conservation we have:

$$E_{\text{b}} + E_{\text{TA}} = E_{\text{sca}} + E_{\text{rec}} + E_{\text{res}} \ , \tag{A.36}$$

where we obtain the total energy of residual particle (E_{res}). The "missing mass" of

residual particle is:

$$M_{\text{miss}} = \sqrt{E_{\text{res}}^2 - P_{\text{res}}^2}, \tag{A.37}$$

which is also the sum of the ground state mass M_{gs} and excitation energy E_{ex}. Therefore, we obtain the excitation energy of residual particle:

$$E_{\text{ex}} = M_{\text{miss}} - M_{\text{gs}} . \tag{A.38}$$

Data including low-lying discrete states of ^{14}N from (p, pd) reactions were used to perform energy calibration in HODO analysis, as presented in subsection 3.2.2.

Appendix B

Monte Carlo simulation

During preparing the proposal of RCNP-E552 experiment, we performed Monte Carlo simulation to investigate the energy resolution of excitation energy spectrum. We optimized the target tilted angle and target thickness, with a compensation between yield and energy resolution. In this appendix we present the Monte Carlo simulation and discuss the target effect on the energy resolution of the excitation energy spectrum.

In the first Sec. B.1, we present the effect of interaction between particles and materials and relevant formulas. In the simulation, we considered the energy loss and multiple scattering and ignored the energy straggling. Formulas and parameters are presented in Sec. B.1. In the second Sec. B.2, we present the method of generating reaction events, including the assumed momentum distribution of residual particle. In the third Sec. B.3, we present the assumption of particle detection. After that we present the excitation energy spectra in Sec. B.4 and discuss the effect of target in Sec. B.5, respectively.

B.1 Interaction in material

Before reaction, incident protons interact with target material (ice). After reaction, deuterons and protons also have interaction with target material. In addition, outgoing protons need to pass through several material before reaching plastic scintillators. Because the interaction of charge particles with material, the energy and angles of particles may changed. For effects of interactions of proton and deuteron with materials, we mainly consider three aspects. In the first subsection B.1.1, we discuss the treatment of energy loss. In the second subsection B.1.2, we present the effect of energy straggling. In the third subsection B.1.3, we present the treatment of multiple scattering.

B.1.1 Energy loss

Range (R) is defined as the distance of a particle losing all its energy in a material. The range of charged particle with atomic number Z, mass number A and kinetic energy

E_{in} is given as [60] :

$$R(E_{\text{in}}) = a \frac{A}{Z^2} (\frac{E_{\text{in}}}{A})^\gamma + bA \; , \tag{B.1}$$

where a, b and γ are parameters depending on the particle and material. In the case that the particle pass through a small distance d, the remaining energy (E_{r}) is:

$$E_{\text{r}} = E_{\text{in}} - \Delta E \; , \tag{B.2}$$

where ΔE is the energy loss of the particle. The range of the particle with energy E_{r} is then:

$$R(E_{\text{r}}) = a \frac{A}{Z^2} (\frac{E_{\text{r}}}{A})^\gamma + bA = R(E_{\text{in}}) - d \tag{B.3}$$

The remaining energy is obtained by:

$$E_{\text{r}} = (\frac{Z^2 A^{\gamma-1}}{a} (R(E_{\text{in}}) - d - bA))^{\frac{1}{\gamma}} \tag{B.4}$$

$$= (E_{\text{in}}^\gamma - \frac{d}{a} Z^2 A^{\gamma-1})^{\frac{1}{\gamma}} \tag{B.5}$$

Therefore, we obtained the energy loss (ΔE) in distance d:

$$\Delta E = E_{\text{in}} - E_{\text{r}} = E_{\text{in}}(1 - (1 - \frac{d}{R(E_{\text{in}}) - bA})^{\frac{1}{\gamma}}) \; . \tag{B.6}$$

With the range known, we can evaluate the energy loss in certain distance. In the following parts, we present the fitting of the range formula of protons and deuterons in several materials.

It is found that if we use a global function to fit the range of particles with small energy (sub and few MeV) and large energy (tens and hundreds MeV), the range formula reproduces the range at large energy region well but has large discrepancy at low energy region. Therefore, we separate the fitting in two regions. For the low energy part, we fit the range from 0 to 35 MeV. For the high energy part, we fit the range from 10 to 220 MeV. We keep the overlap region so that two functions connect smoothly.

Figure B.1 shows the proton and deuteron range in ice as well as the fitting. Panel (a) and (b) show the range of low and high energy proton, respectively. Panel (c) and (d) show the range of low and high energy deuteron, respectively. The range data are obtained from the "Physical Calculator" of "LISE++" program [61].

After emitted from the ice target, forward-going deuterons went into GR and were momentum-analyzed by GR. Because the scattering chamber and spectrometer are under vacuum, there is no need to consider other energy loss of deuterons. However, backward-going protons need to pass through the stainless membrane, air and materials covering the plastic scintillators before depositing all remaining energy in the scintillation material and thus we consider the energy loss of protons after emitted from the target. Because the thickness of membrane is the main part of the materials, we consider only the energy loss in stainless steel for protons after target. We use a
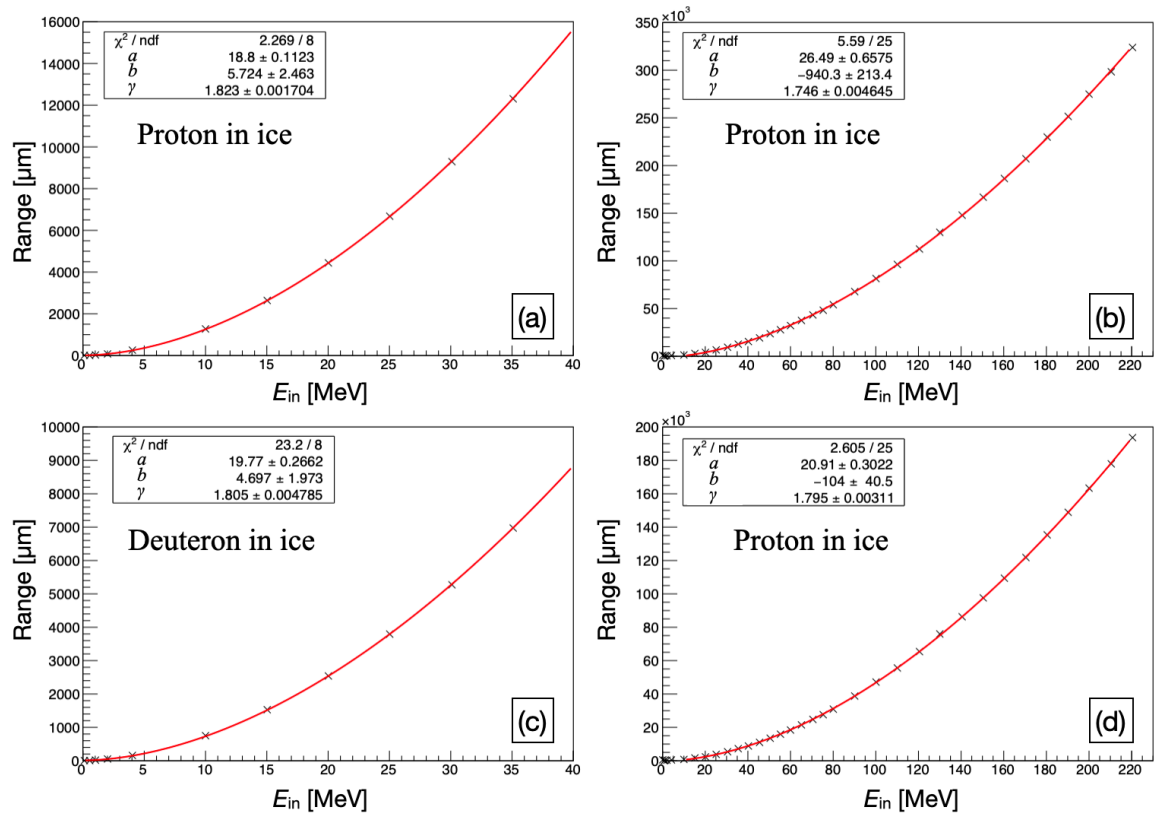
Figure B.1: Figure shows the proton and deuteron range in ice. Cross symbols show the range data obtained from "LISE++" [61] and red lines shows the fitting of range formula with parameters shown in the frame. Panel (a) and (b) show the range of low and high energy proton, respectively. Panel (c) and (d) show the range of low and high energy deuteron, respectively.
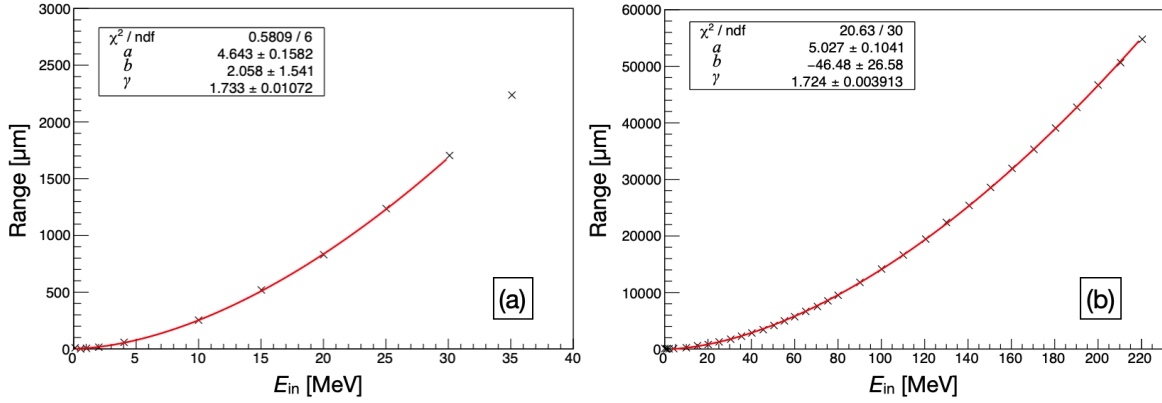
Figure B.2: Figure shows the proton range in stainless steel. Cross symbols show the range data obtained from "LISE++" [61] and red lines shows the fitting of range formula with parameters shown in the frame. Panel (a) and (b) show the range of low and high energy proton, respectively.

Table B.1: Summary of range parameters

Particle	Energy [MeV]	Material	a	b	γ
Proton	0-40	ice	18.8	5.7	1.823
Proton	10-220	ice	26.5	-940	1.746
Deuteron	0-40	ice	19.8	4.7	1.805
Deuteron	10-220	ice	20.9	-104	1.795
Proton	0-30	stainless steel	4.64	2.1	1.733
Proton	10-220	stainless steel	5.03	-46	1.724

typical type of stainless steel $Cr_8Fe_{74}Ni_{18}$ with a density of 8 g/cm^3.

Figure B.2 shows the proton range in stainless steel as well as the fitting. Panel (a) and (b) show the range of low and high energy proton, respectively.

Obtained parameters are summarized in Table B.1. In the simulation, we use the range formula with listed parameter to calculate the range of protons and deuterons in ice and stainless steel. For the range in ice, we used different parameters for energy bellow and above 40 MeV. For the range in stainless steel, we used different parameters for energy bellow and above 20 MeV.

The distance that protons and deuterons go through in ice target is calculated with the target tilted angle (θ_t), proton and deuteron scattering angles (θ_p and θ_d) and reaction point (z_{reac}). Figure B.3 shows the illustration of the energy loss in the ice target. The target tilted angle (θ_t) is defined within 0 to 90 degree. The effective target thickness (t_{eff}) is obtained by:

$$t_{eff} = t/\cos\theta_t \ , \tag{B.7}$$

where t is the target thickness. The reaction point (z_{reac}) is assumed as uniformly distributing from 0 to t_{eff} in the simulation. The incident protons go through the ice target with a distance z_{reac}. The outgoing protons go through the ice target with a
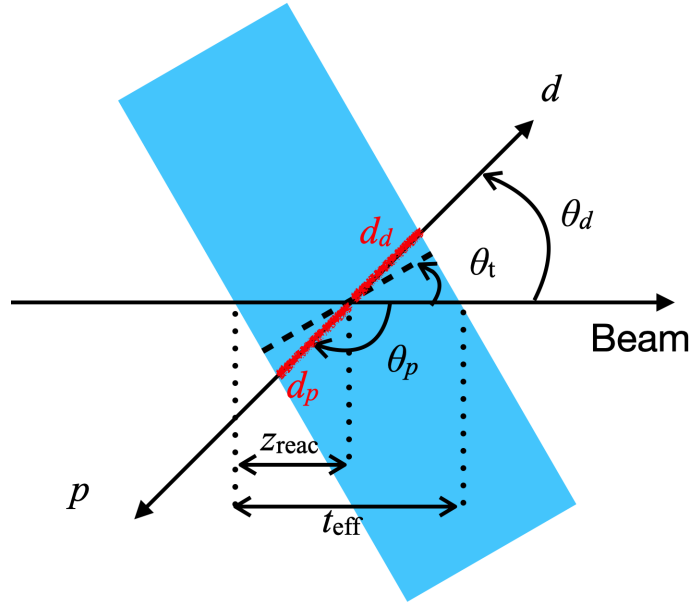
Figure B.3: Figure shows the illustration of energy loss of protons and deuterons in the ice target.

distance d_p:

$$d_p = z_{\text{reac}} \left| \frac{\cos \theta_{\text{t}}}{\cos (\theta_p + \theta_{\text{t}})} \right| . \tag{B.8}$$

The outgoing deuterons go through the ice target with a distance d_d:

$$d_d = (t_{\text{eff}} - z_{\text{reac}}) \left| \frac{\cos \theta_{\text{t}}}{\cos (\theta_d - \theta_{\text{t}})} \right| . \tag{B.9}$$

For the distance of proton passing through the membrane, it was taken as the thickness of the membrane (400 μm).

With the initial energy of particle, distance in material and range, we calculate the energy loss for each step by Eq. B.6.

B.1.2   Energy straggling

The energy loss has fluctuations, which is called straggling. The energy straggling causes the spread of energy of particle and thus affects the energy resolution of spectrum. We calculated the energy straggling (σ_{s}) of protons and deuterons in a thickness of 10 mg/cm² ice by using "LISE++" program [61], as summarized in Table B.2. We see that for both small and high energy protons and deuterons in ice, the energy straggling is less than 30 keV. Considering the typical spread of incident energy is larger 100 keV (in σ), we ignored the energy straggling of particles in materials in the simulation.

Table B.2: Energy straggling in ice

Particle	Energy [MeV]	σ_{s} [keV]
Proton	200	28
	20	26
Deuteron	200	13
	20	13

B.1.3   Multiple scattering

A charged particle transversing a medium is deflected by many small angle scatters, which is called multiple scattering [62]. For many small-angle scatters the net scattering and displacement distributions are Gaussian. Define:

$$\theta_0 = \frac{1}{\sqrt{2}}\theta_{\mathrm{space}}^{\mathrm{rms}} \; , \tag{B.10}$$

where θ_0 is the root mean square width in plane and $\theta_{\mathrm{space}}^{\mathrm{rms}}$ is the root mean square width in space. θ_0 is given by Ref. [63]:

$$\theta_0 = \frac{13.6 \text{ MeV}}{\beta c p} Z \sqrt{x/X_0}[1 + 0.038\ln(x/X_0)] \; , \tag{B.11}$$

where p, βc, and Z are the momentum, velocity and charge number of the incident particle. x and X_0 is the thickness of the scattering medium and radiation length. The radiation length for ice is 36.08 g/cm^2 or 39.31 cm [64], which is much larger than the thickness of the ice target. Therefore, we can ignore the logarithmic term. We obtained $\theta_{\mathrm{space}}^{\mathrm{rms}}$ [65]:

$$\theta_{\mathrm{space}}^{\mathrm{rms}} \approx 101.2 \frac{T + M}{T(T + 2M)} Z \sqrt{x} \; , \tag{B.12}$$

where T and M are the kinetic energy and mass of the particle. Here we use natural unit. For x in unit mg/cm^2, we obtain the angular spread in unit mrad.

We determine the proton scattering angle by the center angle of fired detector in HODO, which has large acceptance. Thus the uncertainty of proton scattering angle is large. Because the angular spread caused by membrane is much smaller than the angular uncertainty, we ignore it and consider the angular spread caused by the ice target only.

B.2   Event generator

We used functions in "TGenPhaseSpace" class of "CERN ROOT" to generate final state particles [66]. With assumed incident energy, we firstly generated a random number for reaction point and calculated the energy loss of incident proton in certain distance of ice target. Thereafter we defined the initial state four momentum and generate three particles final states with certain masses. For the final state of ^{16}O$(p, pd)^{14}$N,

Table B.3: Weight of final state

Excitation energy	Weight
0 MeV	0.08
2.31 MeV	0.02
3.95 MeV	0.4
7-17 MeV	0.5
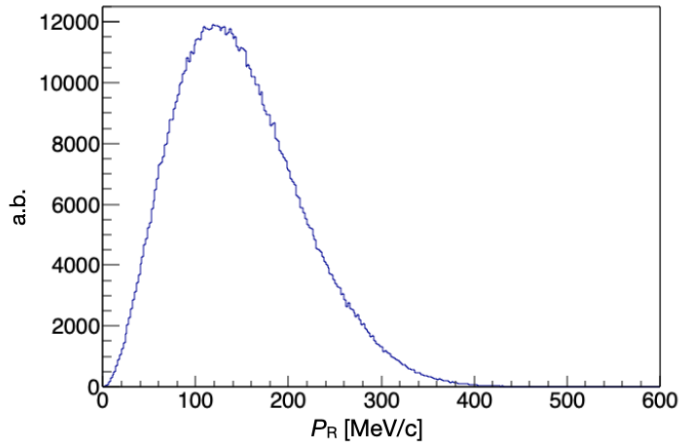
Figure B.4: Figure shows the residual momentum distribution in the simulation.

we consider the excitation of ^{14}N only. Because we are interested mainly in the ^{14}N$^{0^+}_{2.31}$ and ^{14}N$^{1^+}_{3.95}$ states, we assumed the excitation energy of ^{14}N is distributed in certain weight based on the result in Ref. [33], as summarized in Table B.3. We also assumed a continuum at high excitation energy region (7-17 MeV).

After generating final states particles, we made selection to restrict the angular acceptance of proton and deuterons. We also restrict the distribution of residual momentum by a gaussian:

$$P_{\mathrm{R}} \leq |\mathrm{Gauss}(P_0, \sigma_P)| \,, \tag{B.13}$$

where P_0 and σ_P denote the center and width parameter of the gaussian function. In the simulation we assumed $P_0 = 0$ and $\sigma_P = 100$ MeV/c based on the results in Ref. [33]. Figure B.4 shows the residual momentum distribution after restriction.

We obtained the four momentum of all three particles in final states. For outgoing protons and deuterons, energy loss and multiple scattering in ice target are evaluated. In addition, the energy loss of protons in stainless steel is calculated. As a result, we obtain the ideal energies and angles of protons and deuterons.

B.3 Detection of particles

After considering the energy loss in materials and angle spread in ice target, we obtained the energy and angle of particles at detector position. In this section we discuss the

detection of deuterons and protons in subsection B.3.1 and B.3.2, respectively.

B.3.1   Detection of deuterons

Deuterons are detected by the Grand Raiden spectrometer (GR). From the optics of GR, considering the first order, we have:

$$x_{\text{FP}} = <x|\delta> \cdot \delta + <x|x> \cdot x_0 \; , \tag{B.14}$$

where x_{FP} and x_0 denotes the position of the particle at the focal plane and at the target position. $<x|x>$ and $<x|\delta>$ denote the horizontal magnification and momentum dispersion of GR, respectively. δ is the momentum deviation defined as:

$$\delta = \frac{P - P_0}{P_0} \; , \tag{B.15}$$

where P and P_0 is the momentum of the particle and the central trajectory of GR.

We have the resolution of momentum of the particle as:

$$\sigma_P = |\frac{P_0}{<x|\delta>}| \sqrt{\sigma_x^2 + (<x|x> \cdot \sigma_{x_0})^2} \; , \tag{B.16}$$

where σ_x and σ_{x_0} are the position resolution at focal plane and and position spread at target. Since $T = \sqrt{P^2 + M^2} - M$, we have:

$$\sigma_T = \frac{P}{\sqrt{P^2 + M^2}} \cdot \sigma_P \; , \tag{B.17}$$

where σ_T denotes the resolution (in sigma) of kinetic energy (T).

The position resolution of VDC is around 0.15 mm in σ. The horizontal magnification is around -0.4. The typical beam size is around 1 mm in FWHM, which corresponds to 0.42 mm in sigma. The dispersion of GR ($<x|\delta>$) is around 1.5×10^4 mm. Therefore, we estimated the energy resolution (σ_T) for deuteron detection is 3 and 6 keV in sigma for the momentum (P) of 600 and 850 MeV/c, respectively. Because the energy resolution of deuterons is much better than protons, we assumed a constant $\sigma_T \sim 5$ keV in the simulation.

The angle for deuteron can be reconstructed by optics analysis. Because the uncertainty of angle determination for deuterons is much smaller than that of protons, we ignored the angular resolution of deuteron detection ($\sigma_\theta = 0$).

B.3.2   Detection of protons

After penetrating membrane, protons are detected by HODO. We considered four blocks of E counters.

The ideal polar angle of a proton determined which E counter the proton was detected, and the measured proton polar angle was then determined by the center angle of the E counter.

The measured kinetic energy of protons was assumed as the ideal kinetic energy folded by a gaussian function with σ_p.

From the respond of plastic scintillators, we assumed:

$$\sigma_p \propto \sqrt{E} \ , \tag{B.18}$$

where E denotes the energy deposited in the plastic scintillator. Based on the result of HODO test, we assumed $\sigma_p = 0.5$ MeV at 50 MeV (1%). Therefore, we assumed $\sigma_p = 0.07\sqrt{E}$ in the simulation. As examples, for $E = 10$ MeV, $\sigma_p = 0.22$ MeV; for $E = 90$ MeV, $\sigma_p = 0.66$ MeV. In addition, in some of simulation we also assumed 1.5% resolution at 50 MeV, which corresponds to $\sigma_p = 0.11\sqrt{E}$.

As a result, we obtained measured energies and angles for both protons and deuterons in the simulation.

B.4 Excitation energy spectrum

We calculated the excitation energy of residual ^{14}N with measured energies and angles of protons and deuterons, by equations presented in Appendix A. Figure B.5 shows an excitation energy spectrum obtained from the simulation as an example. In this example, the condition is:

- Incident energy: $T_b = 250$ MeV;

- Incident energy fluctuation: $\sigma_b = 100$ keV;

- Target thickness: $t = 10$ mg/cm^2;

- Target tilted angle: $\theta_t = 45°$;

- Proton energy resolution at 50 MeV: $\frac{\sigma_p}{50MeV} = 1\%$;

- Deuteron energy resolution: $\sigma_d = 5$ keV;

We perform fitting on the spectrum and obtain the energy resolution in the spectrum is $\sigma = 0.39$ MeV in this example. In the following part, we discuss the effect of target on this resolution by changing the condition of simulation.

B.5 Effects of target

In order to determine the angle and thickness of target, we investigated the effect of target tilted angle and thickness on the energy resolution in excitation energy spectra and present in this section. In the first subsection B.5.1 we show the effect of target tilted angle and in the second subsection B.5.2 we discuss the effect of target thickness. In the last subsection B.5.3 we present the conclusion of target tilted angle and thickness determination.
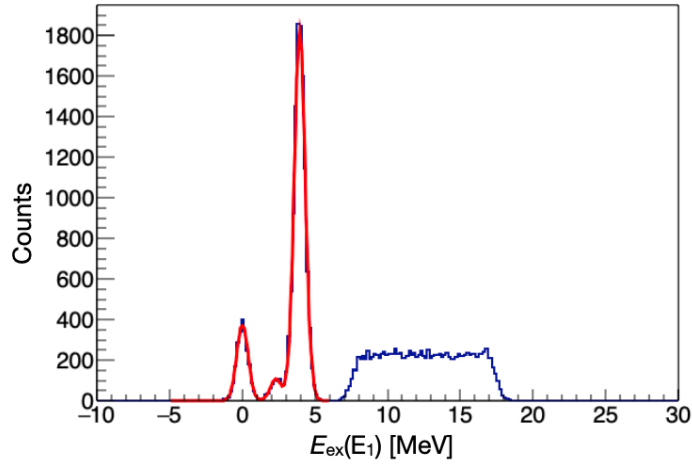
Figure B.5: Figure shows an excitation energy spectrum obtained from the simulation as an example.
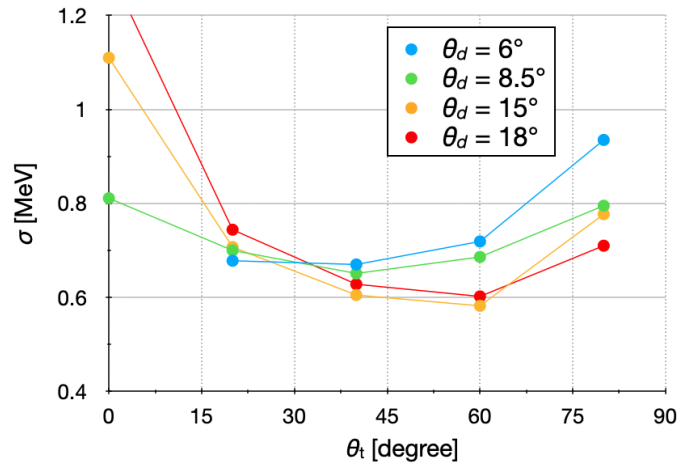
Figure B.6: Figure shows obtained energy resolution with various target tilted angle.

B.5.1   Target tilted angle

For different target tilted angle (θ_t), the distance of outgoing protons and deuterons passing through the ice target is different. In order to check the effect of θ_t, we perform simulation with large target thickness $t = 100$ mg/cm^2 where the difference of energy resolution with different θ_t is significant.

Figure B.6 shows obtained energy resolution with various target tilted angles. Different colors show the energy resolution of different angular settings. In each setting the center angle of HODO (θ_p) is adjusted to match deuteron angle (center of GR, θ_d) in order to cover the recoilless condition, as summarized in Table B.4. The angular setting in the simulation is slightly different from that in the experiment, because we adjusted the angular setting during the preparation of the experiment based on some realistic conditions. However, the difference is small and thus we consider the discussion will not change drastically. We obtained the optimized θ_t for each setting where

Table B.4: Angular settings in the simulation

Set	θ_d	θ_p	optimized θ_{t}
1	$6° \pm 1°$	$151° \pm 2°$	$30°$
2	$8.5° \pm 1°$	$140° \pm 2°$	$40°$
3	$15° \pm 1°$	$117° \pm 2°$	$60°$
4	$18° \pm 1°$	$108° \pm 2°$	$60°$
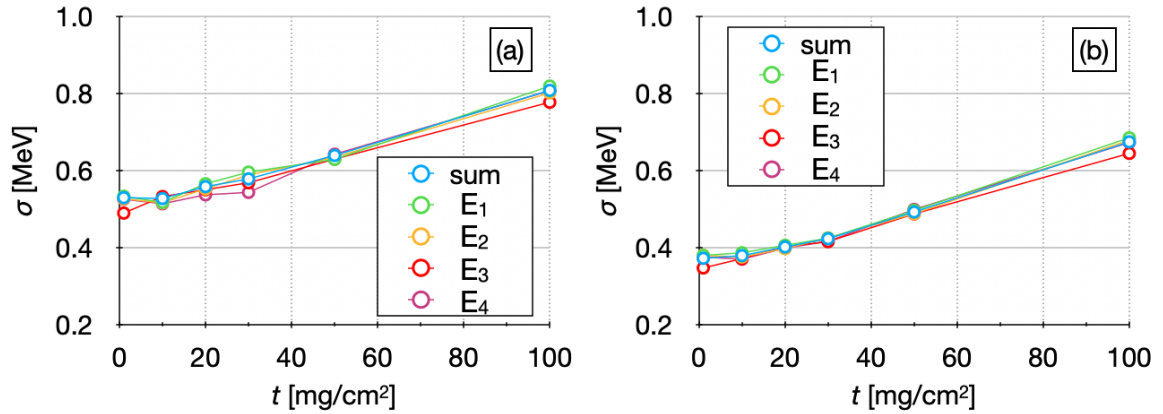
Figure B.7: Figure shows obtained energy resolution with various target thickness. Panel (a) and (b) shows the result with assuming proton energy resolution 1.5% and 1% at 50 MeV, respectively.

σ is minimum.

The condition in the simulation is:

- Incident energy: $T_{\mathrm{b}} = 250$ MeV;

- Incident energy fluctuation: $\sigma_{\mathrm{b}} = 100$ keV;

- Target thickness: $t = 100$ mg/cm^2;

- Proton energy resolution at 50 MeV: $\frac{\sigma_p}{50 MeV} = 1\%$;

- Deuteron energy resolution: $\sigma_d = 5$ keV;

For incident energy of 392 MeV, the tendency and optimized θ_{t} are similar. We used the optimized θ_{t} and checked the effect of thickness.

B.5.2 Effects of target thickness

In the following part we present the investigation of thickness effect with the optimized target tilted angle summarized in Table B.4.

Figure B.7 shows obtained energy resolution with various target thickness as examples. Panel (a) and (b) shows the result with assuming proton energy resolution 1.5% and 1% at 50 MeV, respectively. Different colors shows the resolution in spectra obtained from different E blocks. The blue one shows the sum of all four blocks.
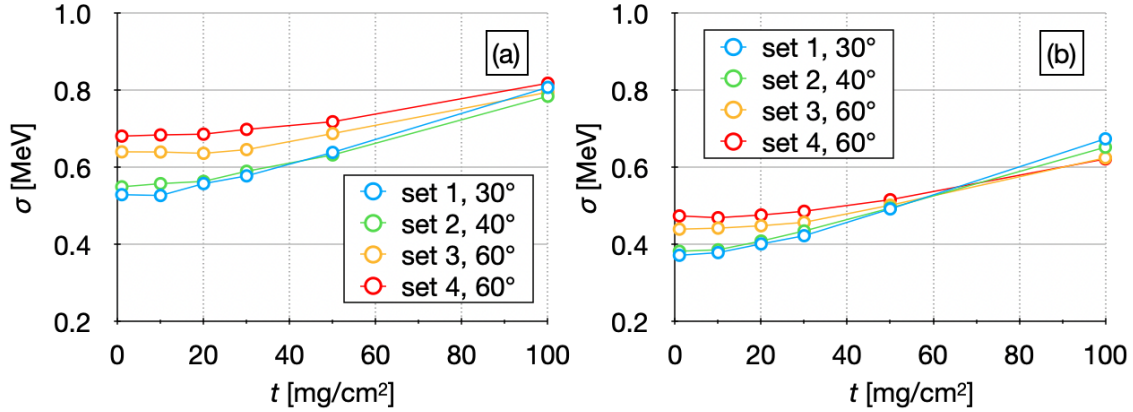
Figure B.8: Figure shows obtained energy resolution with various target thickness. Panel (a) and (b) shows the result with assuming proton energy resolution 1.5% and 1% at 50 MeV, respectively. For different angular settings, different target tilted angle were used.

They have very small differences, so we discuss the resolution in the sum spectrum for simplification.

The condition in the simulation is:

- Incident energy: $T_b = 237$ MeV;

- Incident energy fluctuation: $\sigma_b = 100$ keV;

- Target tilted angle: $\theta_t = 30°$;

- Proton energy resolution at 50 MeV: $\frac{\sigma_p}{50MeV} = 1.5\%$ for (a) and 1% for (b);

- Deuteron energy resolution: $\sigma_d = 5$ keV;

In panel (a) of Fig. B.7, we see that even with $t = 0$ mg/cm^2, $\sigma \sim 0.5$ MeV. In panel (b), with better proton energy resolution, the energy resolution in spectrum is much better. It should be noted that with $\sigma < 0.5$ MeV, two states of our interested can be identified by eye. This means in the case we can achieve good energy resolution for proton detection, it is much helpful to use target with thickness $t < 40$ mg/cm^2.

Figure B.8 shows obtained energy resolution with various target thickness as examples. Panel (a) and (b) shows the result with assuming proton energy resolution 1.5% and 1% at 50 MeV, respectively. Different colors shows the resolution in spectra obtained from angular settings. Here only the resolution in the sum spectra is shown. The condition in the simulation is:

- Incident energy: $T_b = 237$ MeV;

- Incident energy fluctuation: $\sigma_b = 100$ keV;

- Target tilted angle: $\theta_t = 30°, 40°, 60°, 60°$ for set 1-4;

- Proton energy resolution at 50 MeV: $\frac{\sigma_p}{50MeV} = 1.5\%$ for (a) and 1% for (b);

- Deuteron energy resolution: $\sigma_d = 5$ keV;

B.5.3 Conclusion

Based on the effect of target tilted angle on energy resolution and the consideration of the risk and consumed time in changing target tilted angle, we decided to fix the target tilted angle at 45° during the measurement. Based on the effect of target thickness on energy resolution and the yield estimation, we decided to use an ice target with around 20 mg/cm^2 for (p, pd) channel.

Appendix C

Neutron detector

Based on the existing neutron detector used in E443 [33], which is called Beihang-Osaka university Stack Structure Solid organic Scintillator (BOS4) [67], we upgraded the BOS4 detector to measure (p, nd) reaction channel in E552 experiment. Even though in this thesis we do not discuss the (p, nd) reaction channel, we present the introduction of the upgrade of BOS4 detector here as an appendix, because designing, constructing and testing BOS4 detector is a part of the work of my doctoral study. The main point of the upgrade is adding 6 new readouts to reduce the uncertainty of interaction point of neutron and scintillation material, so as to improve the energy resolution. We firstly present a brief introduction on BOS4 in Sec. C.1 and then present the main upgrade in Sec. C.2.

C.1 Basic idea of the neutron detector

Conventionally, neutron is detected by scintillators due to the large cross section of $p + n$ scattering. A trade is always made between the distance and solid angle of the detector. For a shorter distance, the solid angle is larger for a detector with the same active area. However, the background around the scattering chamber is roughly inverse proportional to the square of distance. In addition, neutron detector measure the time of flight to determine the kinetic energy of neutron. Thus with certain timing resolution, the longer flight path improves the energy resolution of neutron. To compensate these considerations, BOS4 was designed to cover relatively large solid angle with moderate distance, size and cost, at the same time have the ability to detect neutrons with sufficient energy resolution and efficiency.

Due to the Grand RAiden Forward mode (GRAF), the beam dump is positioned 25 m downstream of the scattering chamber (SC), resulting in a significantly lower background level around SC compared to using a beam dump in SC. However, even with GRAF, the background (mainly gamma (γ)) near SC is still high and a special technique of neutron-gamma ($n - \gamma$) discrimination is used in BOS4.

To discriminate neutron and γ-rays with similar energy, BOS4 takes the use of the range difference of the secondary particles. After interacted with scintillation material, the secondary particles of neutrons are protons, while that of γ-rays are electrons. Panel (a) of Fig. C.1 shows the range of electrons and protons in plastic scintillator as
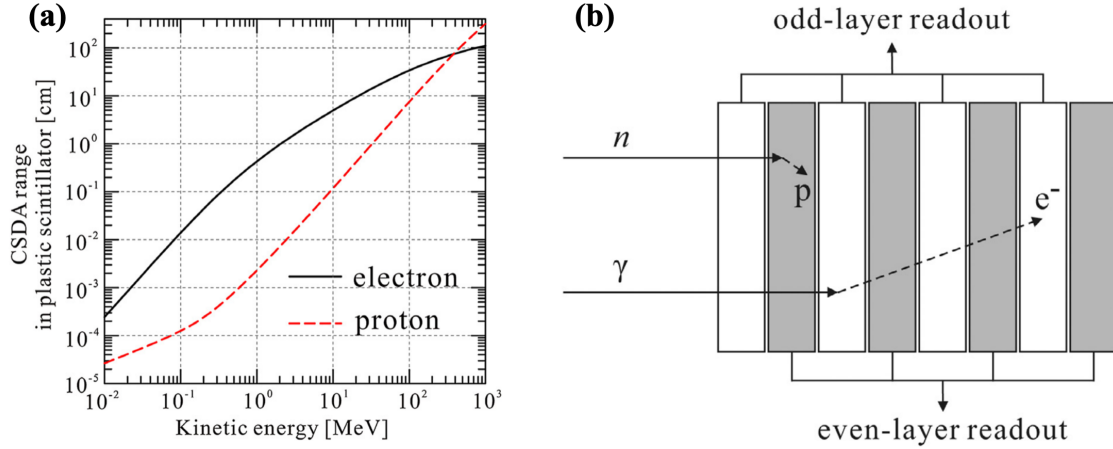
Figure C.1: Panel (a) shows the range difference of electron and proton in plastic scintillator. Panel (b) shows illustration of the $n - \gamma$ discrimination of BOS4. [67]

a function of kinetic energy [67]. At around few tens MeV kinetic energy of our interest, the range of electrons is around two order larger than that of protons. The thickness of each layer of BOS4 was carefully so that most of the secondary protons produced by neutrons stop at the layer where interaction occurs, while in a contrary, the secondary electrons produced by γ-rays can penetrate several layers, as shown in Panel (b) of Fig. C.1. Therefore, from the difference of readout from different layers, BOS4 is able to identify neutron from gamma ray. Details about the $n-\gamma$ discrimination was presented in Ref. [67].

C.2   Main upgrade of the neutron detector

In this section we firstly introduce the configuration of origin BOS4 and then present that of upgraded BOS4.

Figure C.2 shows the schematic view of the light guide in Panel (a) and the arrangement of plastic scintillators in Panel (b) [67] before upgrade. The odd and even layers are segmented into four and two plates, respectively. The odd layers are connected by the specially design light guid (shown in Panel (a) of Fig. C.2) to the PMTs placed vertically, while the even layers to that horizontally. A light guide connects to one segment and 8 layers to one PMT, and on the other side another light guide connects these plastic scintillator to another PMT. Symmetric readout helps to determine the interaction position from time difference of pair PMTs. With horizontal and vertical readout, two dimensions of the interaction point are determined. However, in the particle direction, the original BOS4 cannot determine where the interaction occurs, thus there is large uncertainty in the flight path due to the total thickness of the detector (80 mm). Therefore, we add additional readout to distinguish interaction point at the first or second half in the particle direction, so that the flight path uncertainty is smaller.

Panel (a) of Fig. C.3 shows a schematic view of upgraded BOS4. Additional light guides and PMTs (marked by black dash frames) are used to reduce the flight path
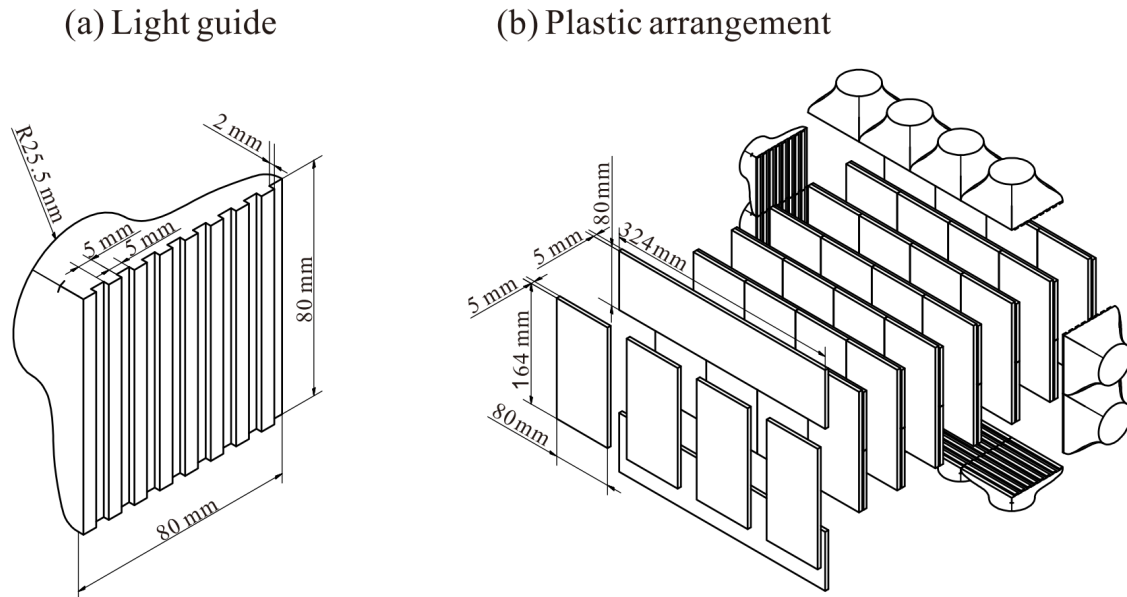
(a) Light guide   (b) Plastic arrangement

Figure C.2: The schematic view of BOS4 before upgrade is shown. Panel (a) shows the schematic view of the light guide. Panel (b) shows the arrangement of plastic scintillators of BOS4. [67]

uncertainty into a half. Panel (b) of Fig. C.3 shows a photo of additional light guide and PMT. Each light guide connects to four layers. Panel (c) of Fig. C.3 shows a photo of the front part of the light guide where it is connected with the plastic scintillators. Because each light guide connects to two segments, small gap was made and filled by Al sheet, to avoid the light leakage between nearby segments via the light guide. In addition, small Al blocks were inserted as a spacer and reflector to avoid the light leakage among layers.

We also upgraded the holder frame for BOS4 accordingly. Photo and design of the whole BAND system (including BOS4 and HODO) are presented in Fig. 2.17 in Chap. 2.

Table C.1 shows the comparison of the specifications of original and upgraded BOS4. As a comparison with the original BOS4 used in E443 experiment, the upgraded BOS4 was placed roughly twice farther. Together with additional readout, the energy resolution of neutron detection is expected to be improved by a factor of two. At the same time, we increased the target thickness by one order of magnitude, where the energy resolution will not change based on the simulation. The yield loss, due to the smaller solid angle, is then compensated by using a thicker ice target for (p, nd) channel.

As a result, after upgrade and optimization, we expected the energy resolution of neutrons detected by BOS4 to be improved by a factor of two, while at the same time, the yield was similar, compared with the E443 experiment.
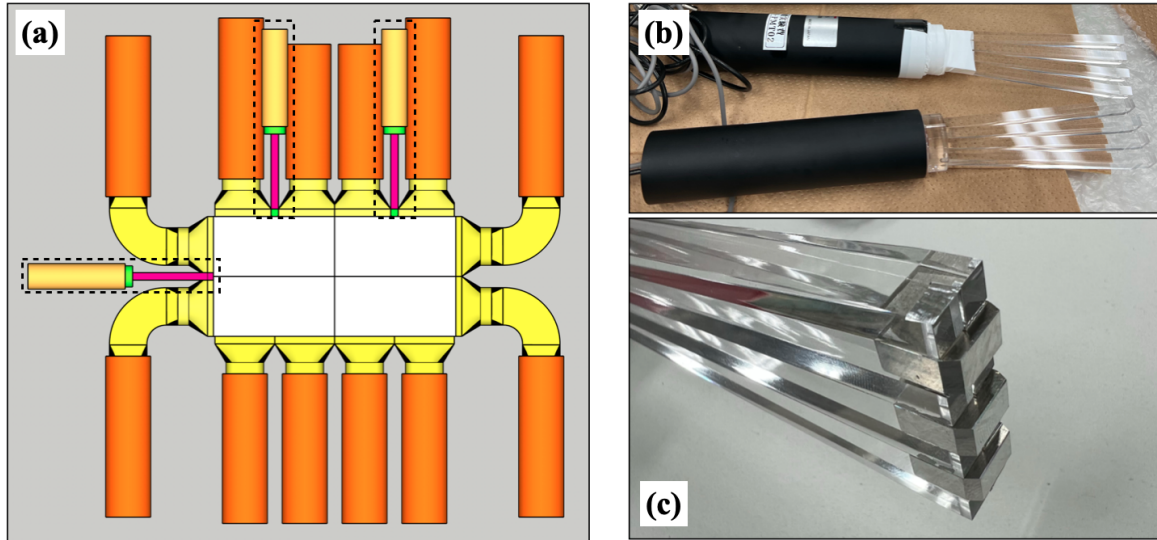
Figure C.3: A schematic view of upgraded BOS4 is shown in panel (a). New light guides and PMTs are marked by black dash frames. Panel (b) shows a photo of new light guides and PMTs. Panel (c) shows a photo of the front part of light guide to avoid light leakage between segments.

Table C.1: BOS4 specifications

Specification	Original BOS4 in E443	Upgraded in E552
Scintillation material	BC408	same
PMT type	H7195, H6410, E5859	addition: H7415
Size of odd layer	80 × 164 × 5 × 4 (W×H×T×segments)	same
Size of even layer	324 × 80 × 5 × 2 (W×H×T×segments)	same
Total active area	320×160 (mm^2)	same
Thickness	80 mm	2×40 mm
Horizontal angular acceptance	±12°	±6.7°
Vertical angular acceptance	±6°	±3.3°
Flight length	70 cm	132 cm
Total number of readout	12	12+6

Appendix D

Proton background and beam loss

We observed significant proton background in the plastic scintillators (PLs) at the focal plane of Grand Raiden (GR) spectrometer. From the analysis of hit pattern and time-of-flight of the background, we identified the source point of the proton background, around the "QM9S" magnet in Fig. 2.3.

In this appendix we discuss the considerations regarding the proton background from QM9S. In Sec. D.1 we provide a brief introduction to the background. In Sec. D.2 we outline the method used to eliminate the background when estimating the VDC tracking efficiency. In Sec. D.3 we present the connection between the amount of the background and beam intensity fluctuation.

D.1   Overview

Figure D.1 shows the scatter plot of charge and time-of-flight distribution detected in GR focal plane plastics (PLs). Panels (a) and (b) show the distributions in PL1 without and with VDC tracking condition, respectively, while panels (c) and (d) show those in PL2. In panel (b) and (d) where good VDC tracking condition is required, deuteron and triton loci are seen, with a small amount of proton in addition. However, in panels (a) and (c) where no requirement for VDC tracking, additional loci are seen. It is considered as proton background from backside (opposite from spectrometer side). From the hitting pattern and time-of-flight of the background, we identified the source point of this background at the upstream of the scattering chamber [68], roughly around "QM9S" magnet as shown in Fig. D.2.

Because the background can be handled properly and does not affect the result and conclusion in this thesis, we skip the detail investigation about the background and discuss mainly the treatment of the background. For simplification, we call this proton background in GR plastics from the backside as "the background" in this appendix.

D.2   Tracking efficiency estimation

In this section we discuss the treatment of the background when estimating the tracking efficiency of VDC. As presented in subsection 3.3.2, we estimated the VDC tracking

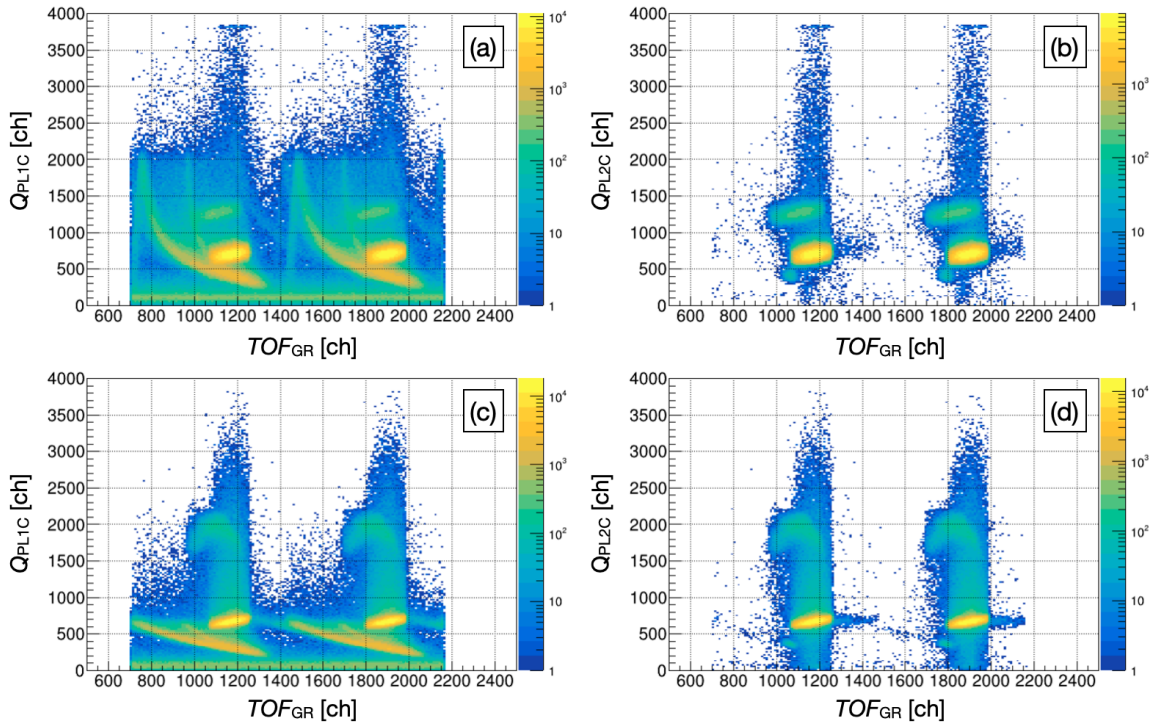**Figure D.1:** Figure shows the scatter plot of charge and time-of-flight distribution detected by PL1 (panels (a) and (b)) and PL2 (panels (c) and (d)). Panels (a) and (c) show the distributions without VDC tracking condition, while (b) and (d) show the distributions with VDC tracking condition.
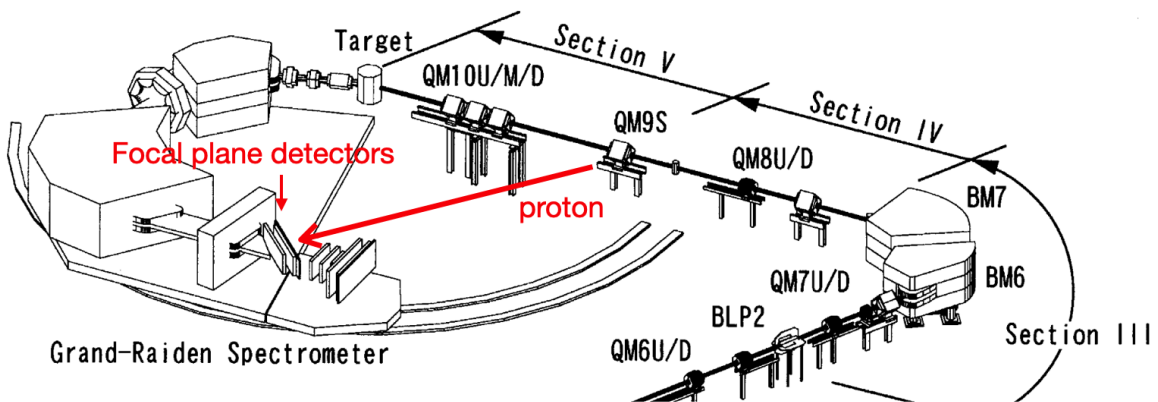

Figure D.2: Figure shows the source point of the proton background. The figure is from Ref. [50].
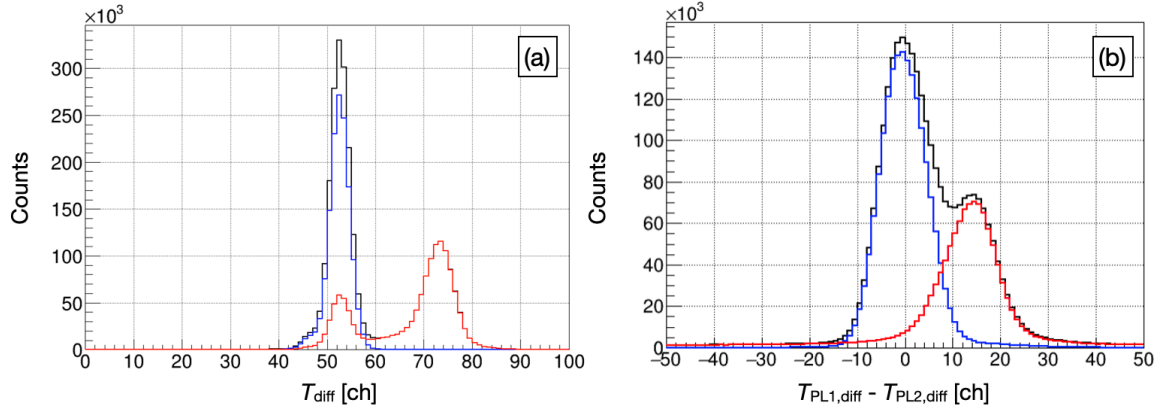
Figure D.3: Panel (a) and (b) show the distribution of timing difference and position difference between PL1 and PL2, respectively. Black, blue and red histograms show the distribution of total, VDC good tracking and no VDC good tracking events, respectively.

efficiency by using the particle identification (PI) of PL1 and PL2 as denominator, as shown in Eq. 3.30. Therefore, we should remove the background in the denominator.

Since we found that most of the background cannot have good tracking in VDC analysis, we use VDC tracking condition to check the distribution of the background. Panel (a) of Fig. D.3 shows the timing difference distribution between two plastics at GR focal plane. The timing of each plastics are calculated from the average timing of PMTs at both side:

$$T_{\text{PL1}} = \frac{1}{2}(T_{\text{PL1L}} + T_{\text{PL1R}}) \,, \tag{D.1}$$

$$T_{\text{PL2}} = \frac{1}{2}(T_{\text{PL2L}} + T_{\text{PL2R}}) \,, \tag{D.2}$$

$$T_{\text{diff}} = T_{\text{PL1}} - T_{\text{PL2}} \,, \tag{D.3}$$

Black histogram shows the timing difference distribution of all events, where two peaks are observed. Because the momentum acceptance of GR is small and the distance between two plastics is small, in normal operation we observed only one peak. The additional peak is considered as from the background and consistent with the hypothesis that the background came from the opposite direction of GR. Blue histogram shows the timing difference distribution with good VDC tracking, where only one peak is observed. Red histogram shows the distribution without good VDC tracking, where two peaks appear. The peak at around 50 to 60 channel is considered as from particles coming from GR side (but inefficient in VDC tracking) and another one at around 70 to 80 channel is from the backside background.

From the timing difference distribution we have a separation between the real signal (coming from GR) and the background. Therefore, we restrict the timing difference within safe region (in this example from 30 to 62 channel) to remove the background.

Panel (b) of Fig. D.3 shows the position difference measured by two plastics at GR focal plane. The position at each plastic is obtained from the timing difference between
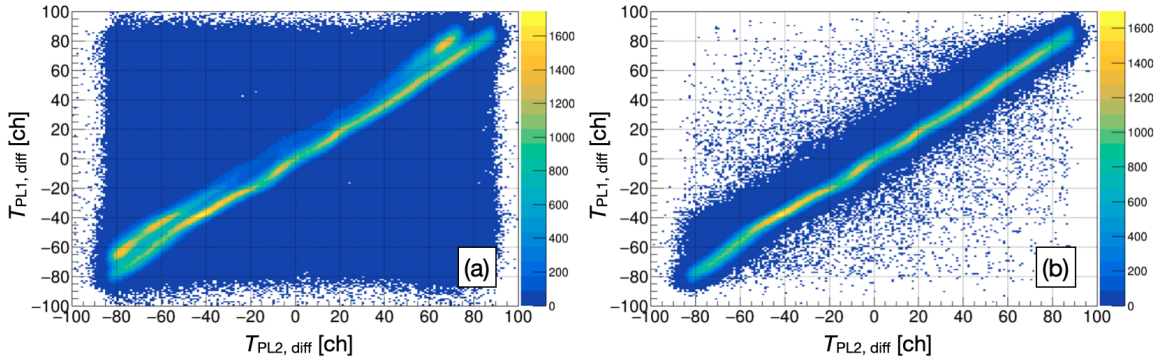
Figure D.4: Figure shows the scatter plots of position distribution at PL1 and PL2. Panel (a) and (b) show the distribution without and with timing difference restriction, respectively.

left and right readouts:

$$T_{\text{PL1, diff}} = T_{\text{PL1L}} - T_{\text{PL1R}} \ , \tag{D.4}$$

$$T_{\text{PL2, diff}} = T_{\text{PL2L}} - T_{\text{PL2R}} \ . \tag{D.5}$$

Black histogram shows the position difference distribution of all events, where two peaks are observed. Blue histogram shows the position difference distribution with restricting the timing difference in the reasonable range ($30 \leq T_{\text{diff}} \leq 62$). We observed only one peaks, which is consistent with particles coming from the same direction (from GR). Red histogram shows the distribution of remaining events, where we see another peak. As result, we separated the real signal (from GR) and the background (from backside) by selecting a proper range of the timing difference.

Figure D.4 shows the scatter plots of position distribution at two plastics. Panel (a) shows the distribution of all events, where two lines are observed. One line shows the particles coming from GR side, while the other one shows the background from different angles. Panel (b) shows the distribution of events with the restriction in timing difference distribution, where only one line remains. We see that with the restriction the amount of remaining background is two orders smaller than the signals.

We applied the restriction on the timing difference when estimating the VDC tracking efficiency. As a result, we obtained similar VDC tracking efficiency for all data of (p,d) channel regardless the background condition.

D.3   Beam charge at scattering chamber

As discussed in subsection 3.3.1, we determined the beam current by wall Faraday cup (WallFc). At the same time we check the beam current evaluated from Beam Line Polarimeters (BLPs) and monitor the transmission efficiency from BLP to WallFc.

To investigate the possible effect of the background, we performed scaler analysis in each run to check the beam condition. In the following part we present an example of good beam condition and then an example of bad beam condition, where some part
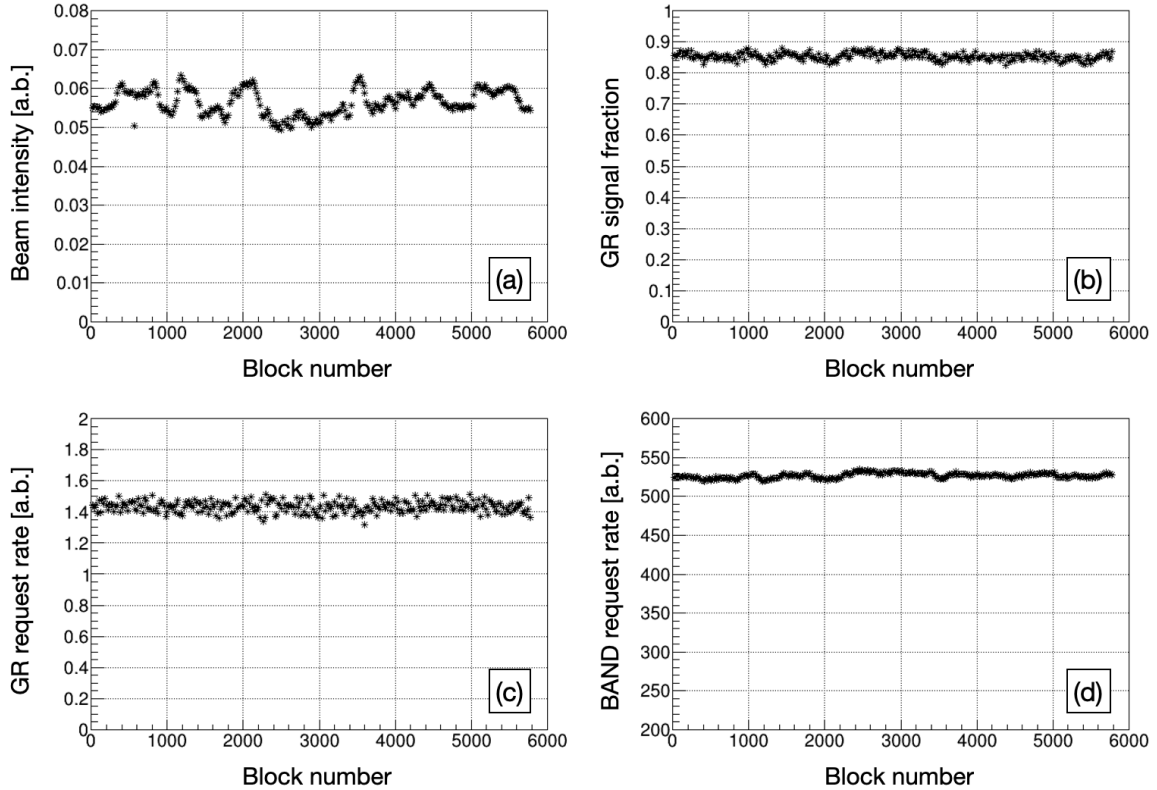
Figure D.5: Figure shows several scatter plots in scaler analysis to check the beam condition. Horizontal axis is the block number. Panel (a) shows the variation of beam intensity. Panel (b) shows the variation of GR signal fraction. Panel (c) and (d) show the variations of GR request trigger and BAND request trigger normalized by beam intensity, respectively.

of beam hit the upstream of scattering chamber (SC) and caused the background.

The data were transferred block by block depending on the size. Typical number of events is 83 events per block in precent data. We calculated the increase of scaler data for each 20 blocks for enough statistics.

Figure D.5 shows several scatter plots in scaler analysis to check the beam condition. Firstly we show an example of data with good beam condition. Horizontal axis is the block number. Panel (a) shows the variation of beam intensity. Beam intensity is calculated from the number of increased counts in the scaler of WallFc divided by that of a clock. For simplification we shows the arbitrary unit (a.b.) only to present the fluctuation. Panel (b) shows the variation of GR signal fraction, defined as the fraction of number of GR signal (events within the timing difference restriction discussed in Sec. D.2) to the total GR events. The fraction is around 90% in this example showing the amount of the background is small and stable. Panel (c) and (d) show the variations of GR request trigger and BAND request trigger normalized by beam intensity, respectively. Despite the fluctuation in beam intensity, the GR and BAND request trigger rates remained stable, indicating that the beam condition did not fluctuate significantly.
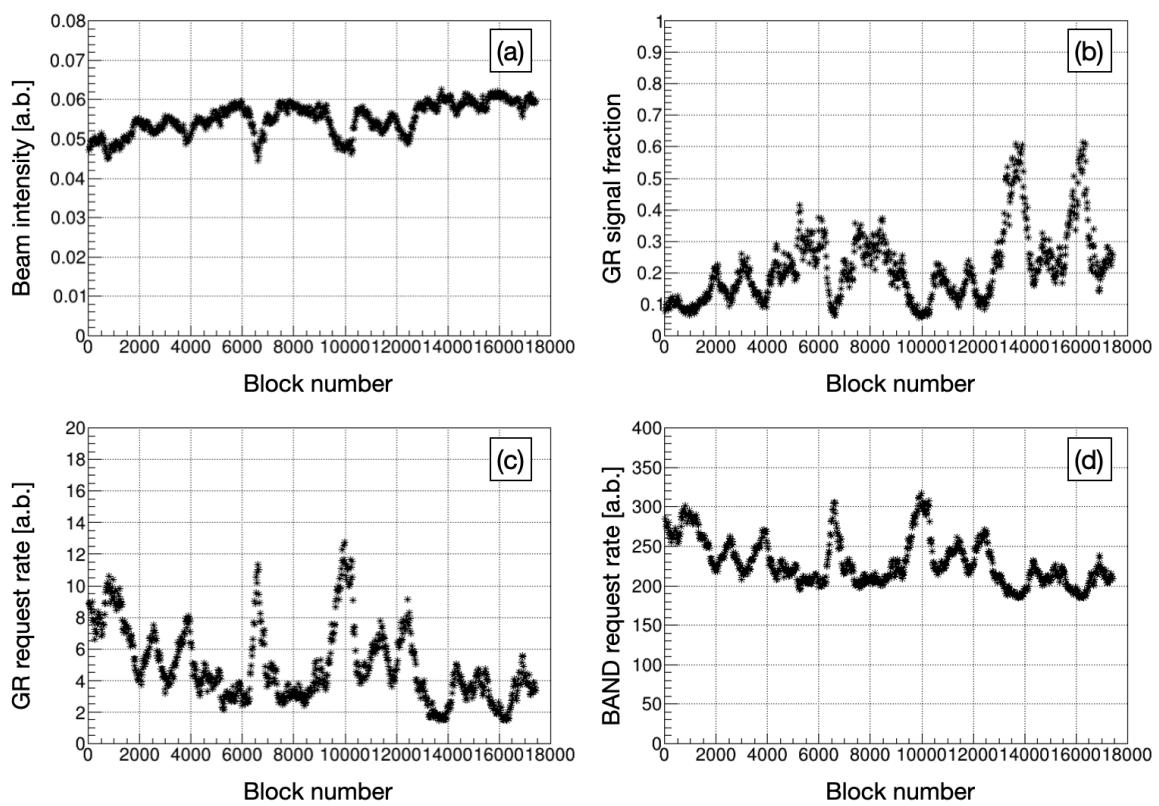
Figure D.6: Figure shows a example of bad beam condition. The definition is the same with Fig. D.5.
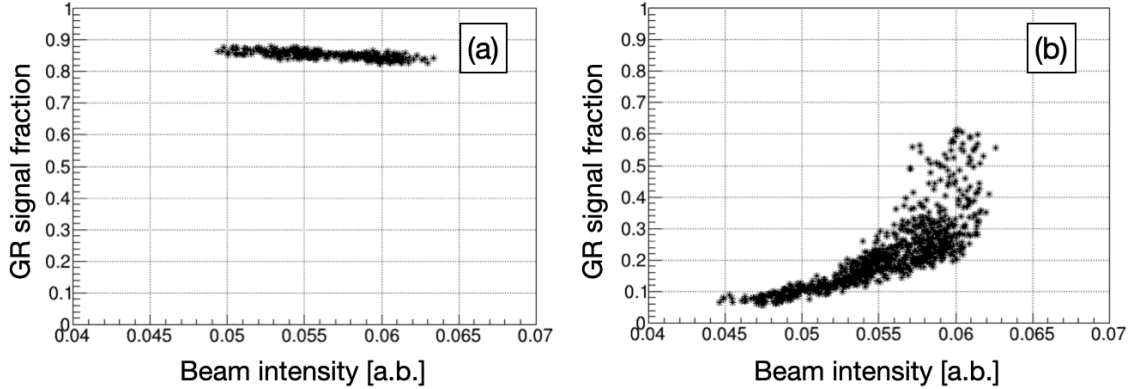
Figure D.7: Figure shows the scatter plots of the distributions of GR signal fraction and beam intensity in panel (a) and (b) for data with good and bad beam condition, respectively.

Figure D.6 shows another example with bad beam condition, with the same definition with Fig. D.5. From panel (b) of Fig. D.6 we see the fraction was small and fluctuating very much. In addition, we see in panels (c) and (d) that the requested rate of GR and BAND were also fluctuating.

Figure D.7 shows the scatter plots of distributions of GR signal fraction and beam intensity in panel (a) and (b) for data with good and bad beam condition, respectively. While in panel (a) the fluctuation of GR signal fraction is small, the fluctuation of GR signal fraction is large in panel (b). With smaller beam intensity, the GR signal fraction is smaller, which indicates the amount of the background is larger. The correlation between GR signal fraction and beam intensity is consistent with the case that some part of the beam hit at the upstream of SC and caused the background.

Therefore, we determined the beam intensity at SC by WallFc instead of BLP. BLPs are then used as a monitor to check the transmission efficiency. In data at 230 MeV incident energy, typical transmission efficiency is above 90%. Some of data has small transmission efficiency but the fraction of these data in total data is small. In data at 392 MeV incident energy, typical transmission efficiency is around 70 to 80 %. Therefore, we consider present result with scaler analysis, namely the absolute value of differential cross section might have around 10% and 30% systematics uncertainty in maximum at 230 and 392 MeV, respectively.

In short, we conclude that detailed investigation is needed to discuss the absolute cross section, where the systematic uncertainty should be treated carefully and properly.

Bibliography

[1] A. Bohr and B. R. Mottelson, *World Sci.* (1998).

[2] R. Machleidt, (1985).

[3] M. Naghdi, Physics of Particles and Nuclei **45**, 924 (2014), arXiv:0702078 [nucl-th] .

[4] R. Machleidt, in *Advances in Nuclear Physics* (Springer US, 1989) pp. 189–376.

[5] M. S. Fayache, L. Zamick, and B. Castel, Phys. Rep. **290**, 201 (1997).

[6] T. E. Ericson, Nucl. Physics, Sect. A **416**, 281 (1984).

[7] R. Machleidt, K. Holinde, and C. Elster, The bonn meson-exchange model for the nucleon-nucleon interaction (1987).

[8] M. Garçon and J. W. Van Orden (Springer, Boston, MA, 2001) pp. 293–378, arXiv:0102049 [nucl-th] .

[9] K. Ikeda, T. Myo, K. Kato, and H. Toki, in *Lect. Notes Phys.*, Vol. 818 (2010) pp. 165–221.

[10] G. Colò, H. Sagawa, S. Fracasso, and P. F. Bortignon, Physics Letters, Section B: Nuclear, Elementary Particle and High-Energy Physics **646**, 227 (2007).

[11] D. J. Mercer, T. N. Taddeucci, L. J. Rybarcyk, X. Y. Chen, D. L. Prout, R. C. Byrd, J. B. McClelland, W. C. Sailor, S. Delucia, B. Luther, D. G. Marchlenski, E. Sugarbaker, E. Gülmez, C. A. Whitten, C. D. Goodman, and J. Rapaport, Phys. Rev. Lett. **71**, 684 (1993).

[12] S. C. Pieper and R. B. Wiringa, Annu. Rev. Nucl. Part. Sci. **51**, 53 (2001), arXiv:0103005 [nucl-th] .

[13] J. Carlson, S. Gandolfi, F. Pederiva, S. C. Pieper, R. Schiavilla, K. E. Schmidt, and R. B. Wiringa, Rev. Mod. Phys. **87**, 10.1103/RevModPhys.87.1067 (2015), arXiv:1412.3081 .

[14] T. Myo, S. Sugimoto, K. Kato, H. Toki, and K. Ikeda, Prog. Theor. Phys. **117**, 257 (2007).

[15] T. Myo, A. Umeya, H. Toki, and K. Ikeda, Phys. Rev. C - Nucl. Phys. **84**, 1 (2011).

[16] T. Myo, A. Umeya, H. Toki, and K. Ikeda, Phys. Rev. C - Nucl. Phys. **86**, 10.1103/PhysRevC.86.024318 (2012).

[17] D. T. Tran, H. J. Ong, G. Hagen, T. D. Morris, N. Aoi, T. Suzuki, Y. Kanada-En'Yo, L. S. Geng, S. Terashima, I. Tanihata, T. T. Nguyen, Y. Ayyad, P. Y. Chan, M. Fukuda, H. Geissel, M. N. Harakeh, T. Hashimoto, T. H. Hoang, E. Ideguchi, A. Inoue, G. R. Jansen, R. Kanungo, T. Kawabata, L. H. Khiem, W. P. Lin, K. Matsuta, M. Mihara, S. Momota, D. Nagae, N. D. Nguyen, D. Nishimura, T. Otsuka, A. Ozawa, P. P. Ren, H. Sakaguchi, C. Scheidenberger, J. Tanaka, M. Takechi, R. Wada, and T. Yamamoto, Nat. Commun. **9**, 1 (2018).

[18] O. Sorlin and M. G. Porquet, Nuclear magic numbers: New features far from stability (2008), arXiv:0805.2561 .

[19] T. Otsuka and D. Abe, Mean field properties of exotic nuclei and the tensor force (2007).

[20] T. Otsuka, T. Suzuki, R. Fujimoto, H. Grawe, and Y. Akaishi, Physical Review Letters **95**, 1 (2005).

[21] R. Schiavilla, R. B. Wiringa, S. C. Pieper, and J. Carlson, Phys. Rev. Lett. **98**, 10.1103/PhysRevLett.98.132501 (2007).

[22] W. Horiuchi and Y. Suzuki, Physical Review C - Nuclear Physics **76**, 024311 (2007).

[23] R. B. Wiringa, R. Schiavilla, S. C. Pieper, and J. Carlson, Phys. Rev. C - Nucl. Phys. **89**, 24305 (2014).

[24] T. Neff, H. Feldmeier, and W. Horiuchi, Phys. Rev. C - Nucl. Phys. **92**, 10.1103/PhysRevC.92.024003 (2015).

[25] T. Neff and H. Feldmeier, Nucl. Phys. A **713**, 311 (2003).

[26] I. Korover, N. Muangma, O. Hen, R. Shneor, V. Sulkosky, A. Kelleher, S. Gilad, D. W. Higinbotham, E. Piasetzky, J. W. Watson, S. A. Wood, P. Aguilera, Z. Ahmed, H. Albataineh, K. Allada, B. Anderson, D. Anez, K. Aniol, J. Annand, W. Armstrong, J. Arrington, T. Averett, T. Badman, H. Baghdasaryan, X. Bai, A. Beck, S. Beck, V. Bellini, F. Benmokhtar, W. Bertozzi, J. Bittner, W. Boeglin, A. Camsonne, C. Chen, J. P. Chen, K. Chirapatpimol, E. Cisbani, M. M. Dalton, A. Daniel, D. Day, C. W. De Jager, R. De Leo, W. Deconinck, M. Defurne, D. Flay, N. Fomin, M. Friend, S. Frullani, E. Fuchey, F. Garibaldi, D. Gaskell, R. Gilman, O. Glamazdin, C. Gu, P. Gueye, D. Hamilton, C. Hanretty, J. O. Hansen, M. Hashemi Shabestari, T. Holmstrom, M. Huang, S. Iqbal, G. Jin, N. Kalantarians, H. Kang, M. Khandaker, J. Lerose, J. Leckey, R. Lindgren, E. Long, J. Mammei, D. J. Margaziotis, P. Markowitz, A. Marti Jimenez-Arguello, D. Meekins, Z. Meziani, R. Michaels, M. Mihovilovic, P. Monaghan,

C. Munoz Camacho, B. Norum, Nuruzzaman, K. Pan, S. Phillips, I. Pomerantz, M. Posik, V. Punjabi, X. Qian, Y. Qiang, X. Qiu, A. Rakhman, P. E. Reimer, S. Riordan, G. Ron, O. Rondon-Aramayo, A. Saha, E. Schulte, L. Selvy, A. Shahinyan, S. Sirca, J. Sjoegren, K. Slifer, P. Solvignon, N. Sparveris, R. Subedi, W. Tireman, D. Wang, L. B. Weinstein, B. Wojtsekhowski, W. Yan, I. Yaron, Z. Ye, X. Zhan, J. Zhang, Y. Zhang, B. Zhao, Z. Zhao, X. Zheng, P. Zhu, and R. Zielinski, Phys. Rev. Lett. **113**, 10.1103/PhysRevLett.113.022501 (2014), arXiv:1401.6138 .

[27] E. Piasetzky, M. Sargsian, L. Frankfurt, M. Strikman, and J. W. Watson, Phys. Rev. Lett. **97**, 10.1103/PhysRevLett.97.162504 (2006).

[28] R. Subedi, R. Shneor, P. Monaghan, B. D. Anderson, K. Aniol, J. Annand, J. Arrington, H. Benaoum, F. Benmokhtar, W. Boeglin, J. P. Chen, S. Choi, E. Cisbani, B. Craver, S. Frullani, F. Garibaldi, S. Gilad, R. Gilman, O. Glamazdin, J. O. Hansen, D. W. Higinbotham, T. Holmstrom, H. Ibrahim, R. Igarashi, C. W. De Jager, E. Jans, X. Jiang, L. J. Kaufman, A. Kelleher, A. Kolarkar, G. Kumbartzki, J. J. LeRose, R. Lindgren, N. Liyanage, D. J. Margaziotis, P. Markowitz, S. Marrone, M. Mazouz, D. Meekins, R. Michaels, B. Moffit, C. F. Perdrisat, E. Piasetzky, M. Potokar, V. Punjabi, Y. Qiang, J. Reinhold, G. Ron, G. Rosner, A. Saha, B. Sawatzky, A. Shahinyan, S. Širca, K. Slifer, P. Solvignon, V. Sulkosky, G. M. Urciuoli, E. Voutier, J. W. Watson, L. B. Weinstein, B. Wojtsekhowski, S. Wood, X. C. Zheng, and L. Zhu, Science (80-.). **320**, 1476 (2008).

[29] M. Duer, O. Hen, E. Piasetzky, H. Hakobyan, L. B. Weinstein, M. Braverman, E. O. Cohen, D. Higinbotham, K. P. Adhikari, S. Adhikari, M. J. Amaryan, J. Arrington, A. Ashkenazi, J. Ball, I. Balossino, L. Barion, M. Battaglieri, V. Batourine, A. Beck, I. Bedlinskiy, A. S. Biselli, S. Boiarinov, W. J. Briscoe, W. K. Brooks, S. Bueltmann, D. Bulumulla, V. D. Burkert, F. Cao, D. S. Carman, A. Celentano, G. Charles, T. Chetry, G. Ciullo, L. Clark, B. A. Clary, P. L. Cole, M. Contalbrigo, O. Cortes, V. Crede, R. Cruz-Torres, A. D'Angelo, N. Dashyan, R. De Vita, E. De Sanctis, M. Defurne, A. Deur, C. Djalali, G. Dodge, R. Dupre, H. Egiyan, A. El Alaoui, L. El Fassi, P. Eugenio, R. Fersch, A. Filippi, T. A. Forest, G. Gavalian, Y. Ghandilyan, S. Gilad, G. P. Gilfoyle, K. L. Giovanetti, F. X. Girod, E. Golovatch, R. W. Gothe, K. A. Griffoen, L. Guo, N. Harrison, M. Hattawy, F. Hauenstein, K. Hafidi, K. Hicks, M. Holtrop, C. E. Hyde, Y. Ilieva, D. G. Ireland, B. S. Ishkhanov, E. L. Isupov, K. Joo, M. L. Kabir, D. Keller, G. Khachatryan, M. Khachatryan, M. Khandaker, A. Kim, W. Kim, A. Klein, F. J. Klein, I. Korover, S. E. Kuhn, L. Lanza, G. Laskaris, P. Lenisa, K. Livingston, I. J. MacGregor, C. Marchand, N. Markov, B. McKinnon, S. Mey-Tal Beck, T. Mineeva, M. Mirazita, V. Mokeev, R. A. Montgomery, A. Movsisyan, C. Munoz-Camacho, B. Mustapha, S. Nadeeshani, P. Nadel-Turonski, S. Niccolai, G. Niculescu, M. Osipenko, A. I. Ostrovidov, M. Paolone, E. Pasyuk, M. Patsyuk, A. Papadopoulou, K. Park, D. Payette, W. Phelps, O. Pogorelko, J. Poudel, J. W. Price, S. Procureur, Y. Prok, D. Protopopescu, M. Ripani, A. Rizzo, G. Rosner, P. Rossi, F. Sabatié, A. Schmidt, C. Salgado, B. A. Schmookler, R. A. Schumacher, E. P. Segarra, Y. G. Sharabian, G. D. Smith, D. Sokhan, N. Sparveris, S. Stepanyan, S. Strauch, M. Taiuti, J. A. Tan, M. Ungaro, H. Voskanyan, E. Voutier, D. P.

Watts, X. Wei, N. Zachariou, J. Zhang, X. Zheng, and Z. W. Zhao, Nature **560**, 617 (2018).

[30] H. J. Ong, I. Tanihata, A. Tamii, T. Myo, K. Ogata, M. Fukuda, K. Hirota, K. Ikeda, D. Ishikawa, T. Kawabata, H. Matsubara, K. Matsuta, M. Mihara, T. Naito, D. Nishimura, Y. Ogawa, H. Okamura, A. Ozawa, D. Y. Pang, H. Sakaguchi, K. Sekiguchi, T. Suzuki, M. Taniguchi, M. Takashina, H. Toki, Y. Yasuda, M. Yosoi, and J. Zenihiro, Phys. Lett. Sect. B Nucl. Elem. Part. High-Energy Phys. **725**, 277 (2013).

[31] C. L. Guo, *Probing effects of tensor interactions in nuclei via 16O and 12C(p, d) reaction*, Ph.D. thesis, Beihang University, Beijing, China.

[32] X. Wang, *Studying the high-momentum neutron in nuclei by $^{16}O(p,d)$ transfer reactions*, Master's thesis, Osaka University, Osaka, Japan.

[33] S. Terashima, L. Yu, H. J. Ong, I. Tanihata, S. Adachi, N. Aoi, P. Y. Chan, H. Fujioka, M. Fukuda, H. Geissel, G. Gey, J. Golak, E. Haettner, C. Iwamoto, T. Kawabata, H. Kamada, X. Y. Le, H. Sakaguchi, A. Sakaue, C. Scheidenberger, R. Skibiński, B. H. Sun, A. Tamii, T. L. Tang, D. T. Tran, K. Topolnicki, T. F. Wang, Y. N. Watanabe, H. Weick, H. Witała, G. X. Zhang, and L. H. Zhu, Phys. Rev. Lett. **121**, 10.1103/PhysRevLett.121.242501 (2018), arXiv:1811.02118 .

[34] Y. Lei, *Probing the Tensor Interactions in Nuclei*, Ph.D. thesis, Beihang University (2018).

[35] S. G. Terashima, H. J. Ong, I. Tanihata, and M. Fukuda, in *Proceedings of 13th International Conference on Nucleus-Nucleus Collisions*, July (2020).

[36] L. Lapikás, Nuclear Physics, Section A **553**, 297 (1993).

[37] K. Gottfried, Annals of Physics **21**, 29 (1963).

[38] J. G. Zabolitzky and W. Ey, Physics Letters B **76**, 527 (1978).

[39] K. I. Blomqvist, W. U. Boeglin, R. Böhm, M. Distler, R. Edelhoff, I. Ewald, R. Florizone, J. Friedrich, R. Geiges, J. Jourdan, M. Kahrau, M. Korn, H. Kramer, K. W. Krygier, V. Kunde, M. Kuss, A. Liesenfeld, K. Merle, R. Neuhausen, E. A. Offermann, T. Pospischil, M. Potokar, A. W. Richter, A. Rokavec, G. Rosner, P. Sauer, S. Schardt, A. Serdarevic, B. Vodenik, I. Sick, S. Sirca, A. Wagner, T. Walcher, and S. Wolf, Physics Letters, Section B: Nuclear, Elementary Particle and High-Energy Physics **424**, 33 (1998).

[40] K. Miki, A. Tamii, N. Aoi, T. Fukui, T. Hashimoto, K. Hatanaka, T. Ito, T. Kawabata, H. Matsubara, K. Ogata, H. J. Ong, H. Sakaguchi, S. Sakaguchi, T. Suzuki, J. Tanaka, I. Tanihata, T. Uesaka, and T. Yamamoto, Few-Body Syst. **54**, 1353 (2013).

[41] M. Alvioli, C. Ciofi Degli Atti, and H. Morita, Phys. Rev. Lett. **100**, 1 (2008).

[42] K. Sekiguchi, H. Sakai, H. Sakai, H. Witała, H. Witała, W. Glöckle, J. Golak, J. Golak, M. Hatano, H. Kamada, H. Kato, Y. Maeda, J. Nishikawa, A. Nogga, T. Ohnishi, H. Okamura, N. Sakamoto, S. Sakoda, Y. Satou, K. Suda, A. Tamii, T. Uesaka, T. Wakasa, and K. Yako, Phys. Rev. C - Nucl. Phys. **65**, 340031 (2002).

[43] K. Sekiguchi, H. Witała, T. Akieda, D. Eto, H. Kon, Y. Wada, A. Watanabe, S. Chebotaryov, M. Dozono, J. Golak, H. Kamada, S. Kawakami, Y. Kubota, Y. Maeda, K. Miki, E. Milman, A. Ohkura, H. Sakai, S. Sakaguchi, N. Sakamoto, M. Sasano, Y. Shindo, R. Skibiński, H. Suzuki, M. Tabata, T. Uesaka, T. Wakasa, K. Yako, T. Yamamoto, Y. Yanagisawa, and J. Yasuda, Phys. Rev. C **96**, 064001 (2017).

[44] K. Sekiguchi, Y. Wada, J. Miyazaki, H. Witała, M. Dozono, U. Gebauer, J. Golak, H. Kamada, S. Kawase, Y. Kubota, C. S. Lee, Y. Maeda, T. Mashiko, K. Miki, A. Nogga, H. Okamura, T. Saito, H. Sakai, S. Sakaguchi, N. Sakamoto, M. Sasano, Y. Shimizu, R. Skibiński, H. Suzuki, T. Taguchi, K. Takahashi, T. L. Tang, T. Uesaka, T. Wakasa, and K. Yako, Phys. Rev. C - Nucl. Phys. **89**, 64007 (2014).

[45] A. Tamii, M. Dozono, K. Fujita, K. Hatanaka, E. Ihara, T. Kaneda, H. Kuboki, Y. Maeda, H. Matsubara, T. Ohta, H. Okamura, H. Sakai, Y. Sakemi, Y. Satou, K. Sekiguchi, K. Suda, M. Takechi, Y. Tameshige, H. Tanabe, N. Uchigashima, T. Uesaka, T. Wakasa, and K. Yako, AIP Conf. Proc. **915**, 765 (2007).

[46] G. F. Chew and M. L. Goldberger, Phys. Rev. **77**, 470 (1950).

[47] T. Myo, H. Toki, and K. Ikeda, Progress of Theoretical Physics **121**, 511 (2009).

[48] J. Y. Grossiord, M. Bedjidian, A. Guichard, M. Gusakow, J. R. Pizzi, T. Delbar, G. Grégoire, and J. Lega, Physical Review C **15**, 843 (1977).

[49] S. Cohen and D. Kurath, Nuclear Physics, Section A **141**, 145 (1970).

[50] T. Wakasa, K. Hatanaka, Y. Fujita, G. P. Berg, H. Fujimura, H. Fujita, M. Itoh, J. Kamiya, T. Kawabata, K. Nagayama, T. Noro, H. Sakaguchi, Y. Shimbara, H. Takeda, K. Tamura, H. Ueno, M. Uchida, M. Uraki, and M. Yosoi, Nucl. Instruments Methods Phys. Res. Sect. A Accel. Spectrometers, Detect. Assoc. Equip. **482**, 79 (2002).

[51] N. Kobayashi, K. Miki, T. Hashimoto, C. Iwamoto, A. Tamii, N. Aoi, M. P. Carpenter, K. Hatanaka, J. Isaak, E. Ideguchi, S. Morinobu, S. Nakamura, and S. Noji, Eur. Phys. J. A **55**, 1 (2019).

[52] T. Kawabata, H. Akimune, H. Fujimura, H. Fujita, Y. Fujita, M. Fujiwara, K. Hara, K. Hatanaka, K. Hosono, T. Ishikawa, M. Itoh, J. Kamiya, M. Nakamura, T. Noro, E. Obayashi, H. Sakaguchi, Y. Shimbara, H. Takeda, T. Taki, A. Tamii, H. Toyokawa, N. Tsukahara, M. Uchida, H. Ueno, T. Wakasa, K. Yamasaki, Y. Yasuda, H. P. Yoshida, and M. Yosoi, Nucl. Instruments Methods Phys. Res. Sect. A Accel. Spectrometers, Detect. Assoc. Equip. **459**, 171 (2001), arXiv:0012002 [nucl-ex] .

[53] N. Kobayashi, private communication.

[54] M. Fujiwara, H. Akimune, I. Daito, H. Fujimura, Y. Fujita, K. Hatanaka, H. Ikegami, I. Katayama, K. Nagayama, N. Matsuoka, S. Morinobu, T. Noro, M. Yoshimura, H. Sakaguchi, Y. Sakemi, A. Tamii, and M. Yosoi, Nucl. Instruments Methods Phys. Res. Sect. A Accel. Spectrometers, Detect. Assoc. Equip. **422**, 484 (1999).

[55] T. Furuno, private communication.

[56] E. D. Cooper, S. Hama, and B. C. Clark, Phys. Rev. C - Nucl. Phys. **80**, 34605 (2009).

[57] K. Hatanaka, Y. Shimizu, D. Hirooka, J. Kamiya, Y. Kitamura, Y. Maeda, T. Noro, E. Obayashi, K. Sagara, T. Saito, H. Sakai, Y. Sakemi, K. Sekiguchi, A. Tamii, T. Wakasa, T. Yagita, K. Yako, H. P. Yoshida, V. P. Ladygin, H. Kamada, W. Glöckle, J. Golak, A. Nogga, and H. Witała, Phys. Rev. C - Nucl. Phys. **66**, 440021 (2002).

[58] N. K. Timofeyuk and R. C. Johnson, Theory of deuteron stripping and pick-up reactions for nuclear structure studies (2020).

[59] A. Lee, C. Dennis, and P. Campbell, Nature 2007 447:7146 **447**, 791 (2007).

[60] D. Allan, Treatise Heavy-Ion Sci. 10.1007/978-1-4615-8103-1/COVER (1985).

[61] O. B. Tarasov and D. Bazin, Lise ++ site.

[62] M. Tanabashi, K. Hagiwara, K. Hikasa, K. Nakamura, Y. Sumino, F. Takahashi, J. Tanaka, K. Agashe, G. Aielli, C. Amsler, M. Antonelli, D. M. Asner, H. Baer, S. Banerjee, R. M. Barnett, T. Basaglia, C. W. Bauer, J. J. Beatty, V. I. Belousov, J. Beringer, S. Bethke, A. Bettini, H. Bichsel, O. Biebel, K. M. Black, E. Blucher, O. Buchmuller, V. Burkert, M. A. Bychkov, R. N. Cahn, M. Carena, A. Ceccucci, A. Cerri, D. Chakraborty, M. C. Chen, R. S. Chivukula, G. Cowan, O. Dahl, G. D'Ambrosio, T. Damour, D. de Florian, A. de Gouvêa, T. DeGrand, P. de Jong, G. Dissertori, B. A. Dobrescu, M. D'Onofrio, M. Doser, M. Drees, H. K. Dreiner, D. A. Dwyer, P. Eerola, S. Eidelman, J. Ellis, J. Erler, V. V. Ezhela, W. Fetscher, B. D. Fields, R. Firestone, B. Foster, A. Freitas, H. Gallagher, L. Garren, H. J. Gerber, G. Gerbier, T. Gershon, Y. Gershtein, T. Gherghetta, A. A. Godizov, M. Goodman, C. Grab, A. V. Gritsan, C. Grojean, D. E. Groom, M. Grünewald, A. Gurtu, T. Gutsche, H. E. Haber, C. Hanhart, S. Hashimoto, Y. Hayato, K. G. Hayes, A. Hebecker, S. Heinemeyer, B. Heltsley, J. J. Hernández-Rey, J. Hisano, A. Höcker, J. Holder, A. Holtkamp, T. Hyodo, K. D. Irwin, K. F. Johnson, M. Kado, M. Karliner, U. F. Katz, S. R. Klein, E. Klempt, R. V. Kowalewski, F. Krauss, M. Kreps, B. Krusche, Y. V. Kuyanov, Y. Kwon, O. Lahav, J. Laiho, J. Lesgourgues, A. Liddle, Z. Ligeti, C. J. Lin, C. Lippmann, T. M. Liss, L. Littenberg, K. S. Lugovsky, S. B. Lugovsky, A. Lusiani, Y. Makida, F. Maltoni, T. Mannel, A. V. Manohar, W. J. Marciano, A. D. Martin, A. Masoni,

J. Matthews, U. G. Meißner, D. Milstead, R. E. Mitchell, K. Mönig, P. Molaro, F. Moortgat, M. Moskovic, H. Murayama, M. Narain, P. Nason, S. Navas, M. Neubert, P. Nevski, Y. Nir, K. A. Olive, S. Pagan Griso, J. Parsons, C. Patrignani, J. A. Peacock, M. Pennington, S. T. Petcov, V. A. Petrov, E. Pianori, A. Piepke, A. Pomarol, A. Quadt, J. Rademacker, G. Raffelt, B. N. Ratcliff, P. Richardson, A. Ringwald, S. Roesler, S. Rolli, A. Romaniouk, L. J. Rosenberg, J. L. Rosner, G. Rybka, R. A. Ryutin, C. T. Sachrajda, Y. Sakai, G. P. Salam, S. Sarkar, F. Sauli, O. Schneider, K. Scholberg, A. J. Schwartz, D. Scott, V. Sharma, S. R. Sharpe, T. Shutt, M. Silari, T. Sjöstrand, P. Skands, T. Skwarnicki, J. G. Smith, G. F. Smoot, S. Spanier, H. Spieler, C. Spiering, A. Stahl, S. L. Stone, T. Sumiyoshi, M. J. Syphers, K. Terashi, J. Terning, U. Thoma, R. S. Thorne, L. Tiator, M. Titov, N. P. Tkachenko, N. A. Törnqvist, D. R. Tovey, G. Valencia, R. Van de Water, N. Varelas, G. Venanzoni, L. Verde, M. G. Vincter, P. Vogel, A. Vogt, S. P. Wakely, W. Walkowiak, C. W. Walter, D. Wands, D. R. Ward, M. O. Wascko, G. Weiglein, D. H. Weinberg, E. J. Weinberg, M. White, L. R. Wiencke, S. Willocq, C. G. Wohl, J. Womersley, C. L. Woody, R. L. Workman, W. M. Yao, G. P. Zeller, O. V. Zenin, R. Y. Zhu, S. L. Zhu, F. Zimmermann, P. A. Zyla, J. Anderson, L. Fuller, V. S. Lugovsky, and P. Schaffner, Review of Particle Physics (2018).

[63] G. R. Lynch and O. I. Dahl, Nucl. Inst. Methods Phys. Res. B **58**, 6 (1991).

[64] R. L. Workman and Others (Particle Data Group), PTEP **2022**, 083C01 (2022).

[65] H. J. Ong, private communication (2019).

[66] Root reference documentation.

[67] L. Yu, S. Terashima, H. J. Ong, P. Y. Chan, I. Tanihata, C. Iwamoto, D. T. Tran, A. Tamii, N. Aoi, H. Fujioka, G. Gey, H. Sakaguchi, A. Sakaue, B. H. Sun, T. L. Tang, T. F. Wang, Y. N. Watanabe, and G. X. Zhang, Nucl. Instruments Methods Phys. Res. Sect. A Accel. Spectrometers, Detect. Assoc. Equip. **866**, 118 (2017).

[68] S. Terashima, private communication (2023).